8-2020

Geomorphic History of the Grand Staircase Region of the Colorado Plateau: Understanding Arroyo Cut-Fill Dynamics, Erosion Rates, and Wildfire

Kerry E. Riley
Utah State University

GEOMORPHIC HISTORY OF THE GRAND STAIRCASE REGION OF THE COLORADO PLATEAU: UNDERSTANDING ARROYO CUT-FILL DYNAMICS, EROSION RATES, AND WILDFIRE

by

Kerry E. Riley

A dissertation submitted in partial fulfillment
of the requirements for the degree

of

DOCTOR OF PHILOSOPHY

in

Geology

Approved:

_____	_____
Tammy Rittenour, Ph.D. Major Professor	Justin DeRose, Ph.D. Committee Member
_____	_____
Joel Pederson, Ph.D. Committee Member	Joe Wheaton, Ph.D. Committee Member
_____	_____
Patrick Belmont, Ph.D. Committee Member	Janis L. Boettinger, Ph.D. Acting Vice Provost of Graduate Studies

UTAH STATE UNIVERSITY
Logan, Utah

2020

ABSTRACT

Geomorphic History of the Grand Staircase Region of the Colorado Plateau:

Understanding Arroyo Cut-Fill Dynamics, Erosion Rates, and Wildfire

by

Kerry E. Riley, Doctor of Philosophy

Utah State University, 2020

Major Professor: Dr. Tammy Rittenour
Department: Geology

> "…we left behind a long line of cliffs, many hundred feet high, composed of orange and vermilion sandstones. Have named them "Vermilion Cliffs".
>
> … I looked back and saw the morning sun shining in splendor on their painted faces. The salient angles were on fire, and the retreating angles were buried in shade."
>
> John Wesley Powell, 1869

Most streams in the Southwest United States are ephemeral and can be sensitive to climate change given the delicate balance between sediment supply and discharge. These streams undergo rapid geomorphic change because of the semi-arid climate, high sediment supply, and flashy hydrology. At the turn of the 20th century, many streams in the region rapidly incised into their floodplains forming arroyos stimulating questions regarding the cause of such widespread synchronous channel change. Arroyos are a

geomorphic form where a channel is entrenched into fine-grained cohesive alluvium with near vertical channel banks. This dissertation investigates Holocene and late Pleistocene geomorphic change in catchments draining the Grand Staircase region of the Colorado Plateau in southern Utah with the goal of understanding how climate variability and sediment supply influence channel change, landscape evolution, and wildfire history. Methods and datasets used include field descriptions of stratigraphy and sedimentology, geospatial analysis, optically stimulated luminescence and radiocarbon dating, cosmogenic nuclide ^{10}Be concentrations of modern, Holocene, and Pleistocene alluvium, and alluvial charcoal derived fire records. Synchronous regional arroyo entrenchments support climate influenced channel change, while systematic changes in longitudinal profile concavity support autogenic controls on arroyo entrenchment. Modern cosmogenic ^{10}Be concentrations record high spatial variability in erosion rates throughout the study area, in part attributed to lithologic-controlled steepness and differential erosion related to cliff retreat along the White Cliffs and headward drainage expansion along the Pink Cliffs. Paleo-cosmogenic ^{10}Be inventories from Holocene alluvium suggest climate changes during the Holocene did not systematically influence erosion rates. Late Pleistocene erosion rates were generally faster than modern and Holocene analogues. The frequency of regionally synchronous fires increased in the late Holocene. Results support that climate-driven changes in vegetation productivity and the frequency and intensity of drought influences Holocene fire activity.

(245 pages)

PUBLIC ABSTRACT

Geomorphic History of the Grand Staircase Region of the Colorado Plateau: Understanding Arroyo Cut-Fill Dynamics, Erosion Rates, and Wildfire

Kerry E. Riley

Most streams in the southwestern United States do not flow all year, and given their delicate balance of sediment and water flow, they are sensitive to climate change. At the turn of the 20th century, many streams in the Southwest rapidly incised into their floodplains, forming arroyos with a channel entrenched into near-vertical channel banks mostly composed of sand and mud. This dissertation investigates past changes in watersheds draining the Grand Staircase region in southern Utah with the goal of understanding how changes in climate and sediment influence these types of streams. Results show sediment supply is highly variable across the study area because of different rock types and slope, with hotspots of erosion located along the White and Pink Cliffs. This conversely leads to sediment storage on low-relief benches and valleys. Fast rates of erosion and large amounts of sediment cause channels to be overloaded with sediment and unstable over time. This dissertation supports the hypothesis that channel entrenchment is caused by a combination of climate changes and internal-thresholds that control the stability of the channel. The role of climate and fire in this landscape is investigated, and results support the idea that the frequency and intensity of drought and its effect on vegetation have influenced fire activity over the past millennia.

ACKNOWLEDGMENTS

I would like to thank Dr. Tammy Rittenour for choosing me to take on this large project and for providing support throughout the process. I would also like to thank my committee members Joel Pederson, Patrick Belmont, Justin DeRose, and Joe Wheaton for their guidance and assistance throughout the entire process. I give special thanks to my dad (William), mom (Cheryl) and sister (Erin), my friends that feel like family (Keelin, Sara, Dave), and colleagues (Natalie, Daphnee, Harriet, Jim, Jen, Andy, Katie, Megan, Alex, Alexa) for their encouragement, moral support, and patience as I worked through this extended journey. I could not have done it without all of you.

Lastly, I want to dedicate this document and momentous milestone to my daughter Piper. I was almost 23 weeks pregnant and in my second year of my PhD program when my water broke. The doctors told me that it was very likely my daughter would not survive birth, die within minutes of life, or have severe developmental problems. I was hospitalized and room 411 was my new home. My friends and family really helped me during this time by sending comforts of home, decorating my room, playing me music, and even bringing me laboratory equipment, so I could continue my research. I also continued to attend my classes online. My daughter, Piper, was born on February 14th, 2014. She was approximately 3 months premature and weighed 2 pounds and 2 ounces at birth and her lowest weight was 1 pound 12 ounces. Piper remained in the NICU for about 2.5 months after birth. The hospital was too far to make the commute every day, so stayed in a guesthouse run by the hospital.

Piper came home on May 29th, 2014 and weighed 4 lb 8 oz. We maintained a heart monitor at home for about 3 months. While the heart monitor caused many false alarms, it also saved Piper's life one afternoon in May. I was in driving with a friend and Piper was in the back seat. The monitor's alarm went off and I immediately pulled the car over to check on her. When I got into the back seat, Piper was unresponsive and turning blue. My heart sunk into my belly and I saw my child's life flash right before my eyes. I immediately removed her from her car seat and tried to reestablish consciousness by pinching her leg. I tried firm back slaps over my forearm to clear her airway with no success. I then gave her two rescue breaths, which caused her lungs to fill with air and her eyes to open. I repeated the two rescue breaths and she started crying.

Piper is now 6 years old and is the joy and light of my life. While it has been a very scary and traumatic roller-coaster ride over the last 8 years, I love my daughter and what she has brought to my life. I have been teaching at Colorado Mesa University for the past two years. Some of my favorite song lyrics sum up my feelings about this process quite well.

'I am worn and bruised, but I am here at least'

`I am ready for the time that I can finally say,

This has all been wonderful, but now I 'm on my way'.

Kerry E. Riley

CONTENTS

Page

LIST OF TABLES

LIST OF FIGURES

CHAPTER I

INTRODUCTION

Historic arroyo entrenchment in the southwestern U.S.A. (Bryan, 1925), at the turn of the 20th century (AD ~1880 ± 30; Cooke and Reeves, 1976; Webb, 1985), was one of the most significant historic geomorphic events in the region, stimulating research addressing the forcing mechanisms and necessary geomorphic and climatic conditions that drive episodic channel entrenchment into valley-fill alluvium. Arroyos are an end-member channel form characterized by a channel entrenched into fine-grained cohesive valley-fill alluvium, with near vertical channel banks (arroyo walls), and a flat channel bottom. Historic arroyo entrenchment exposed 5-30 m's of Holocene alluvium and revealed several different-aged sediment packages separated by buttress unconformities. While many streams in the Southwest are currently characterized by arroyo landforms, stratigraphic records indicate that during most of the mid-late Holocene, these fluvial systems were dominated by aggradational conditions and characterized by shallow channels and floodplain accretion (e.g., Hereford, 2002; Huff and Rittenour, 2014; Nelson and Rittenour, 2014). Interestingly, in many arroyo systems, each period of aggradation and entrenchment appear to have reached approximately the same levels suggesting that a geomorphic threshold associated with channel geometry may control end-member stream grade and the timing of channel entrenchment. However,

observations of near synchronous regional cut-fill events have led to hypotheses that climate change, an allogenic forcing, may be a primary control of arroyo dynamics (Hack, 1942; Graf, 1987; Hereford, 2002). Deciphering the role of allogenic forcing versus autogenic processes on arroyo cutting and filling dynamics is needed to understand and predict channel adjustment in these dynamic stream systems.

Over 80% of streams in the southwest United States are ephemeral or intermittent (Levick, 2008) and these streams can be sensitive monitors of the effects of allogenic forcing, such as climate change, on the geomorphic response of the landscape (Bull, 1997). Settlement in the semi-arid southwest is dependent on the availability of water resources. During historic arroyo entrenchment, channel incision and floodplain abandonment led to the desertion of some communities in the region because they became disconnected from their water source. The sudden change in stream dynamics caused severe damage to agriculture and infrastructure and has resulted in land managers installing flood-control and channel stabilization measures in these dynamic stream systems (Webb and Hereford, 2001).

Climate models predict greater temperature extremes and more frequent floods and droughts under elevated greenhouse gas conditions (Diffenbaugh, 2005; Kerr, 2008). Increases in natural hazards are expected to have significant socio-economic impacts. This is especially true in the desert southwest were population centers commonly occupy geomorphically active landscapes characterized by episodic and/or catastrophic movement of sediment and infrequent high magnitude discharge events. Investigating past geomorphic response to Holocene climate change enables us to quantify the natural

range of variability in sediment transport processes and fluvial dynamics to better predict how the landscape will respond to future climate change. The goals of my dissertation are to understand how allogenic forcing, such as climate change, and autogenic processes (geomorphic thresholds) influence arroyo dynamics. Specifically, the following four chapters investigate the spatial and temporal distribution of cut-fill episodes, quantifies spatial and temporal erosion rate variability, and reconstruct fire activity in catchments draining the Grand Staircase region of the Colorado Plateau, southern Utah.

Chapter 2 reconstructs the alluvial chronostratigraphy of Johnson Wash, an ephemeral stream in southern Utah, and compares the timing of aggradation and entrenchment to other regional chronologies. The alluvial chronology of Johnson Wash had not been previously studied and increased the spatial extent of mid-late Holocene alluviation described, mapped, and dated in southern Utah. Johnson Wash is located between Kanab Creek and Kitchen Corral Wash, two watersheds where valley-fill alluvium has been previously mapped and dated (Harvey and Pederson, 2011; Harvey et al., 2011; Huff and Rittenour, 2014; Nelson and Rittenour, 2014). The chronology and stratigraphy of Johnson Wash is compared to arroyo cut-fill chronologies from these regional catchments allowing hypotheses relating to allogenic and autogenic forcing of cut-fill dynamics to be tested. Primary research questions addressed in the chapter are: What is the timing of aggradation and arroyo entrenchment in Johnson Wash, how does the reconstructed cut-fill chronology compare to other regional catchments, how does the timing of aggradation and entrenchment relate to mid-late Holocene climate, and Is there a systematic trend in aggraded versus entrenched longitudinal profiles in the region. This

manuscript is being prepared to be submitted to the journal Geologic Society of America Bulletin.

Chapter 3 investigates how erosion rates vary spatially in the topographically and lithologically diverse Grand Staircase region of the Colorado Plateau in southern Utah. This chapter seeks to increase our understanding of if and how variability in erosion rates influence the sediment supplied to the stream and arroyo cut-fill dynamics. Documenting erosion rates and sediment yields in un-gauged streams and understanding the effects of sediment supply on these dynamic streams are needed to predict future channel adjustments and manage for the impact of these channel changes on society. Detrital ^{10}Be concentrations from quartz were analyzed in samples of modern channel alluvium/colluvium from a range of catchment areas containing different rock types and topography. Research questions included: What do cosmogenic nuclide derived estimates of erosion rates tell us about processes in this transient landscape? Do ^{10}Be concentrations from channel sediment represent upstream catchment-averaged erosion rates? How do apparent erosion rates vary across catchments as rock type and cliff and bench topography varies? This manuscript was published in the journal Geology (Riley et al., 2019).

Chapter 4 inventories paleo erosion rates and compares them to reference modern erosion rates to evaluate if and how erosion rates varied with Holocene and Pleistocene climate change in Johnson Wash, Kanab Creek, and Kitchen Corral Wash. Concentrations of ^{10}Be and inferred erosion rates measured in 15 Holocene-aged samples from dated arroyo cut-fill stratigraphy and in six dated alluvial samples from late

Pleistocene terraces and pediments are compared with modern erosion rates to interpret temporal changes in landscape response to climate change over the last 100 kyr. This chapter addresses the following questions: Did climate change significantly modify denudation rates of Grand Staircase over the late Pleistocene and mid-to-late Holocene? Do paleo-erosion rates reflect the influence of lithology, topography, and transience seen in modern erosion rates? Are there relations between increased erosion rate and the timing of arroyo aggradation and entrenchment during the Holocene? This manuscript is being prepared to be submitted to the journal Quaternary Science Reviews.

Chapter 5 reconstructs decadal to millennial scale fire activity using alluvial charcoal from the four large watersheds that drain the Grand Staircase region of the Colorado Plateau in southern Utah. This chapter builds on century-scale fire reconstructions in the Southwest by extending the record of regional fire activity to the mid-Holocene, specifically adding a regional millennial-scale fire history to the few available long-term fire histories from other pinyon-juniper woodlands. Alluvial records are abundant throughout the Southwest and provide a valuable record of Holocene wildfire activity that is otherwise unavailable from other fire proxy records. Past arroyo and paleo-flood studies in the region produced hundreds of radiocarbon ages dating depositional events. In this chapter, I take advantage of the rich alluvial charcoal data to investigate how climate change has influenced regional fire activity in the west-central Colorado Plateau and provide a millennial scale record of fire from what is now dominantly pinon/juniper forest. Comparing fire records from across a large geographic region enables evaluation of the timing of synchronous periods of fire activity and the

associated climate conditions. The primary research questions for this chapter were: When were periods of increased regional fire activity in a Pinyon-Juniper Woodland during the Holocene and What is the relationship between increased regional fire activity and hyrdroclimate? This manuscript is being prepared to be submitted to the journal The Holocene.

Chapter 6, the final chapter, attempts to summarize and integrate all of the studies in this dissertation, outlines the major conclusions, and discusses future directions for this research. The four following chapters (Chapters 2-5) are the primary products of this dissertation and aim to characterize the geomorphic history of the Grand Staircase region of the Colorado Plateau.

References Cited

Bryan, K., 1925, Date of Channel Trenching (Arroyo Cutting) in the Arid Southwest: Science, v. 62, no. 1607, p. 338-344.

Bull, W. B., 1997, Discontinuous ephemeral streams: Geomorphology, v. 19, no. 3–4, p. 227-276.

Cooke, R. U., and Reeves, R. W., 1976, Arroyos and environmental change: Clarendon, Oxford.

Diffenbaugh, N. S., 2005, Sensitivity of extreme climate events to CO2-induced biophysical atmosphere-vegetation feedbacks in the western United States: Geophysical Research Letters, v. 32, no. 7.

Graf, W. L., 1987, Late Holocene sediment storage in canyons of the Colorado Plateau: Geological Society of America Bulletin, v. 99, no. 2, p. 261-271.

Hack, J. T., 1942, The changing physical environment of the Hopi Indians of Arizona, The Museum, v. 1.

Harvey, J. E., and Pederson, J. L., 2011, Reconciling arroyo cycle and paleoflood approaches to late Holocene alluvial records in dryland streams: Quaternary Science Reviews, v. 30, no. 7-8, p. 855-866.

Harvey, J. E., Pederson, J. L., and Rittenour, T. M., 2011, Exploring relations between arroyo cycles and canyon paleoflood records in Buckskin Wash, Utah: Reconciling scientific paradigms: Geological Society of America Bulletin, v. 123, no. 11-12, p. 2266-2276.

Hereford, R., 2002, Valley-fill alluviation during the Little Ice Age (ca. AD 1400-1880), Paria River basin and southern Colorado Plateau, United States: Geological Society of America Bulletin, v. 114, no. 12, p. 1550-1563.

Huff, W., and Rittenour, T., 2014, Holocene alluvial stratigraphy of Kitchen Corral Wash, southern Utah, in MacLean, J. S., Biek, R.F., and Huntoon, J.E., ed., Geology of Utah's Far South: Utah Geological Association Publication 43, p. 77–96.

Kerr, R., 2008, Climate change hot spots mapped across the United States: Science, v. 321, no. 5891, p. 909-909.

Levick, L., J. Fonseca, D. Goodrich, M. Hernandez, D. Semmens, J. Stromberg, R. Leidy, M. Scianni, D. P. Guertin, M. Tluczek, and W. Kepner 2008, The Ecological and Hydrological Significance of Ephemeral and Intermittent Streams in the Arid and Semi-arid American Southwest, in Center, U. S. E. P. A. a. U. A. S. W. R., ed., p. 116 pp.

Nelson, M. S., and Rittenour, T. R., 2014, Middle to late Holocene chronostratigraphy of alluvial fill deposits along Kanab Creek in southern Utah, in MacLean, J. S., Biek, R.F., and Huntoon, J.E., ed., Geology of Utah's Far South, Volume 43, Utah Geological Association Publication p. 97–116.

Riley, K. E., Rittenour, T. M., Pederson, J. L., and Belmont, P., 2019, Erosion rates and patterns in a transient landscape, Grand Staircase, southern Utah, USA: Geology. https://doi.org/10.1130/G45993.1

Webb, R. H., 1985, Late Holocene flooding on the Escalante River, south-central Utah [Ph.D. Dissertation: The University of Arizona., 204 p.

CHAPTER II

LATE HOLOCENE ARROYO DYNAMICS IN SOUTHERN UTAH: A BALANCE BETWEEN CLIMATE FORCING AND GEOMORPHIC THRESHOLDS

Abstract

Ephemeral streams on the Colorado Plateau undergo rapid geomorphic change because of the semi-arid climate, high sediment supply, and flashy hydrology. Arroyos are an end-member channel form characterized by a channel entrenched into fine-grained cohesive valley-fill alluvium. Three periods of aggradation in Johnson Wash are dated to ~2200-1550, 1450-750, and 650-100 ya and constrain two prehistoric entrenchment episodes between 1550-1450 and 750-650 years ago. Quasi-synchronous regional arroyo aggradation and entrenchment over the last 2200 years supports an allogenic control on arroyo cut-fill dynamics. There is a general relation between the timing of arroyo entrenchment and climate transitions from drought to pluvial periods, as well as with an increased frequency of El Nino events. Evidence from cosmogenic ^{10}Be inventories suggest climate change during the mid- to late-Holocene did not influence the rate at which sediment was supplied from hillslopes. Changes in concavity between the aggraded and entrenched longitudinal profile and trends in arroyo wall height support an autogenic control on arroyo entrenchment. Geomorphic analysis suggest reduced concavity in the aggraded state steepens the downstream gradient until a geomorphic threshold is crossed, at which point the channel entrenches. Arroyos appear to be

dynamic threshold-dependent landforms, where aggradation and entrenchment are driven by a combination of allogenic forcing and autogenic processes.

Introduction

Historic stream entrenchment and the formation of arroyo channel forms throughout the southwestern United States at the turn of the 20th century (~1880 ± 30 CE) was one of the most significant historic geomorphic events in the region (e.g., Bryan, 1925; Cooke and Reeves, 1976; Webb, 1985). Historic stream entrenchment destroyed agriculture and rangelands, altered stream hydrology, and transported large volumes of sediment downstream impacting water quality, floodplain and riparian habitat, and reservoir storage capacity. Climate models predict greater temperature extremes and more frequent floods and droughts under elevated greenhouse gas conditions (Diffenbaugh, 2005; Kerr, 2008). Furthermore, increases in natural hazards are expected to have significant socio-economic impacts. This is especially true in the desert southwest were population centers commonly occupy geomorphically active landscapes that are characterized by episodic and sometimes catastrophic movement of sediment and infrequent high magnitude discharge events (Davies and Korup, 2010). The rapid and widespread change in stream dynamics during historic arroyo entrenchment has stimulated questions addressing the forcing mechanisms and necessary geomorphic and climatic conditions that drive episodic channel entrenchment into valley-fill alluvium. Investigating past geomorphic response to Holocene climate change allows the natural

range of variability in fluvial dynamics to be quantified and aides in the prediction of future landscape response to a changing climate.

An arroyo is an end-member channel form characterized by a stream entrenched into fine-grained cohesive valley-fill alluvium, with near vertical channel banks (arroyo walls), and a broad flat channel bottom. Historic arroyo entrenchment exposed tens of meters of Holocene-aged alluvium and revealed several different-aged alluvial packages separated by near-vertical buttressed unconformities (e.g., Hereford, 2002; Harvey et al., 2010; Huff and Rittenour, 2014). These alluvial stratigraphic records archive past hydrologic dynamics and fluvial processes. While many streams in the Southwest US are currently characterized by entrenched arroyo landforms, stratigraphic records indicate these fluvial systems were dominated by aggradation and characterized by shallow channels and floodplain accretion during most of the mid-late Holocene (e.g., Hereford, 2002; Huff and Rittenour, 2014; Nelson and Rittenour, 2014; Townsend et al., 2019). In some arroyo systems, successive periods of aggradation reach similar valley-fill tread heights prior to being entrenched; potentially indicating that entrenchment ensues when a slope-related geomorphic threshold to stability is crossed. This suggests that an autogenic self-regulating dynamic controls the height/thickness of alluvial aggradation and therefore the threshold channel gradient that initiates entrenchment (Townsend et al., 2019). Patton and Schumm (1981) suggested that arroyo cut and fill dynamics are driven by high sediment yields, independent of subtle climate change, and therefore the timing of cutting and filling may not be synchronous in different basins. However, observations of near synchronous regional cut-fill events have led to alternative hypotheses that

climate change is a primary control of arroyo dynamics (e.g., Hack, 1942; Graf, 1987; Hereford, 2002). Deciphering the role of allogenic (i.e., climate) forcing versus autogenic processes (geomorphic thresholds) on arroyo dynamics is needed to understand and predict channel adjustment in these dynamic stream systems.

This research builds off the work of Townsend et al (2019) by adding the alluvial chronostratigraphies of Johnson Wash and Kitchen Corral Wash and information from cosmogenic-nuclide erosion rate data to further test the hypothesis that regional arroyo cut-fill chronologies are synchronous across the Grand Staircase region of the Colorado Plateau. The chronology and stratigraphy of Johnson Wash is compared to arroyo cut-fill chronologies from regional catchments including Kanab Creek (Townsend, 2019), and Kitchen Corral Wash a tributary to the Paria River (Hereford, 2002; Huff and Rittenour, 2014). Furthermore, we evaluate an aggraded versus entrenched longitudinal profile of Johnson Wash to test the hypothesis that a geomorphic threshold is controlling conditions during entrenchment. Primary research questions include 1) What is the timing of aggradation and arroyo entrenchment in Johnson Wash, 2) How does the reconstructed cut-fill chronology compare to other regional catchments, 3) How does the timing of aggradation and entrenchment relate to mid-late Holocene climate, and 4) Is there a systematic trend in aggraded versus entrenched longitudinal profiles in the region.

The 'Arroyo Cycle'

The 'semiarid cycle of erosion' described by Schumm and Hadley (1957) is a

phenomenon where streams oscillate between an entrenched channel constrained between near-vertical channel banks and a shallow aggraded channel that can migrate laterally across a broad valley floor. Early geologic observations recognized that fully loaded (maximum sediment carrying capacity) streams are at a threshold between incision and deposition (Gilbert, 1877). When sediment supply is greater than the capacity of the stream to transport, the stream aggrades. Streams maintain a balance between sediment supply and sediment removal Mackin, (1948). Four categories of hypotheses have been proposed in an effort to determine causative mechanisms of arroyo cut-fill dynamic and include: Human-induced disturbance from intense grazing, farming practices, and water diversion caused changes in vegetation and increases in surface runoff and flood erosion cause arroyo entrenchment, Climate changes led to hydrological and vegetation characteristics conducive to arroyo cut-fill dynamics, Arroyo cut-fill dynamics is an inherent autogenic cycle driven by erosion and deposition, and allogenic forcing coupled with autogenic processes control arroyo cut-fill dynamics.

Historic arroyo entrenchment was observed throughout the Southwest and temporally corresponded to European settlement, the introduction of large numbers of livestock and related grazing, and the associated modification of vegetation on the landscape (Bailey, 1935). Early researchers hypothesized that overgrazing and soil compaction led to accelerated erosion and historic channel entrenchment (Bailey, 1935; Antevs, 1952). Similar correlations have been observed between increased population growth/density of Puebloan people in the Southwest and prehistoric arroyo entrenchment around the 11th-12th century CE (Hall, 1977). Some have hypothesized that

entrenchment at this time could be related to increased agricultural intensity and development of water control features (e.g., Dodge, 1902; Bailey, 1935; Calkins, 1941). Anthropogenic caused mechanism are challenged by evidence that arroyo entrenchment occurred in basins that were isolated from human impacts such as deforestation and livestock grazing. Moreover, some basins did not entrench following the introduction of livestock, and some arroyos were entrenched prior to European settlement (Cooperrider and Hendricks, 1937; Bryan, 1941; Gregory, 1950; Denevan, 1967; Graf, 1985). Furthermore, the alluvial stratigraphic records exposed in arroyo walls suggest that streams have undergone multiple cut-fill events during the mid-late Holocene, prior to European settlement and disturbance (e.g., Waters and Haynes, 2001; Hereford, 2002; Mann and Meltzer, 2007). Pre-historic arroyo entrenchment also occurred prior to the advent of farming and any environmental change caused Puebloan and pre-Puebloan people. These lines of evidence suggest that, while humans influenced vegetation and may have catalyzed erosion; additional driving forces must have contributed to channel entrenchment prior to the 10th-13th century CE (950-550 ya).

Broad-scale, regionally synchronous geomorphic response over the late Holocene, coupled with historic observations of abrupt, widespread arroyo entrenchment is the foundation of climate-related hypotheses. Several studies throughout the Southwest identified quasi-synchronous cut-fill records from multiple catchments. For example, in southern Utah, the timing of arroyo entrenchment during the last 1000 years are strikingly well correlated between Kanab Creek (Smith, 1990; Webb et al., 1991; Summa, 2009), Virgin River (Hereford et al., 1996), Escalante River (Cooley, 1962; Webb, 1985; Webb

and Baker, 1987), and the Paria River (Hereford, 2002). Regionally synchronous phases in arroyo cut-fill dynamics include historic incision at CE ~1880-1920 (Bryan, 1925), aggradation between 800-100 ya, and prehistoric entrenchment 1000-800 ya. The terms "synchronous" and "regional" are somewhat problematic with climate-related hypotheses because precision and accuracy vary based on dating method (Daniels, 2008). As such synchronous should be interpreted within the interval defined by dating error (Webb and Hereford, 2001). Additionally, the stochastic spatial and temporal nature of moisture and hydro-climate throughout the Southwest weakens the assumption that a climate-related geomorphic response of regional watersheds would necessarily be synchronous (Graf, 1983). Climate variability in the Southwest is associated with shifts in mid-latitude and subtropical atmospheric circulation cells (Sheppard et al., 2002). Specifically, the North American Monsoon (NAM) involves the seasonal reversals of wind direction caused by temperature differences between the land and sea and notably cause seasonal changes in rainfall patterns. The Southwest monsoon climate is characterized by increased late summer/fall precipitation; winter precipitation in the Southwest is linked to the El Niño Southern Oscillation (ENSO). The Southwest also encompasses the Basin and Range and Colorado Plateau physiographic provinces giving rise to diverse topography with different climates types. These factors make climate-related hypotheses based on regional synchronicity complicated.

Two general climate-change scenarios have been anecdotally identified as possible drivers initiating arroyo entrenchment (dry-to-wet and wet-to-dry). Dutton (1882) originally proposed that arroyo entrenchment is driven by a shift from dry-to-wet

conditions and this hypothesis is supported by observations of historic arroyo entrenchment, which corresponded to an increase in the frequency of large discharge events between CE ~1862-1942 (Leopold, 1951; Cooke and Reeves, 1976; Graf, 1983; Hereford, 1986; Webb et al., 1991; Webb and Hereford, 2001). Findings in southern Arizona by Waters and Haynes (2001) also concluded that four out of six prehistoric arroyo entrenchment episodes coincided with inferred wetter periods. Mechanistically, increased precipitation and resulting higher streamflow could increase stream power above a critical threshold causing incision and ultimately drive entrenchment. Conversely, during periods of drought, vegetation cover decreases and erosion is expected to increase (Schlesinger et al., 1990), potentially causing sediment supply to be greater than stream capacity, resulting in aggradation (Huntington et al., 1914). Others have argued that a climate change from wet-to-dry conditions could cause arroyo entrenchment based on the idea that increased aridity would decrease vegetation cover and increase surface runoff reaching streams, thus creating increased flashy (peaked) hydrographs and stream power (Bryan, 1925; Hack, 1939, 1942; Leopold and Bull, 1979). Few studies have discussed the role of climate during periods of aggradation. Bryan (1928) proposed that alluviation occurs during overall wetter conditions. Conversely, increased moisture would increase vegetation and result in more channel roughness, less flashy flows, and less erosive streamflow. It has also been hypothesized that cooler, wetter periods would have increased freeze-thaw weathering and increased sediment supply above the transport capacity of the stream, resulting in net aggradation (Hereford, 2002).

Asynchronous timing of cut-fill dynamics within different reaches of a catchment or between basins with similar climate regimes may suggest non-allogenic or complex geomorphic response (Schumm and Hadley, 1957; Schumm and Parker, 1973; Patton and Schumm, 1975; Tucker et al., 2006). Flume experiments and field observations in northwestern Colorado indicate that entrenchment is not necessarily synchronous within a basin and show that erosion/deposition can be coeval within different reaches (e.g., Lewis, 1944; Schumm and Parker, 1973; Patton and Schumm, 1975), as observed in discontinuous ephemeral streams (Bull, 1997; Schumm and Hadley, 1957). Complex response of river systems to perturbation create scenarios where the timing and phase of channel adjustments of a stream to external forces may be temporally transient and spatially variable within a drainage (Schumm, 1973). For example, Schumm and Parker (1973) observed that incision in upstream reaches can lead to excess sediment production and simultaneous aggradation downstream. Observations that aggradation and entrenchment appear to reach the same levels in paleo-arroyo records (Huff, 2013) and that channel slope-profiles of aggraded stream beds are less concave than entrenched channel slope-profiles (Summa, 2009) support the idea that autogenic processes may play an important role in arroyo dynamics.

Allogenic and autogenic forcing mechanisms are not mutually exclusive. Climate-related or human-induced disturbance drivers for arroyo entrenchment may stimulate a complex response within the watershed. Climate may influence the rate of sediment production by enhancing or depressing mechanical and chemical weathering. Stream aggradation is influenced by hydrology and sediment supply. High erosion rates and

sediment yields in semi-arid catchments result in fluvial systems that are dominated by aggradation, which in turn may cause the stream gradient to become locally over-steepened and unstable and subsequent high discharge events can cause the stream to cross a geomorphic threshold for incision. Therefore, we hypothesize arroyo dynamics are controlled by both autogenic dynamics and allogenic forcing that are both stochastic and deterministic.

Physiographic and Climatic Setting

The alluvial valleys on the Skutumpah and Wygaret benches of the Grand Staircase contain extensive valley-fill sediment, which are currently entrenched by continuous arroyos along the axial valleys and connect to mouths of discontinuous gullied tributary basins. Sediment production and erosion rates are high in the region because of easily erodible bedrock and low vegetation density associated with the semi-arid climate. Long-term erosion rates are generally fast and vary spatially from 20 to >1000 m/Myr or mm/kyr (Riley et al., 2019; Ch. III).

Most of the Southwest experiences warm and dry climate conditions during much of the year because of a quasi-permanent subtropical high-pressure ridge that lies over the region (Sheppard et al., 2002). Precipitation is generally bimodal, with peaks in the late summer and winter. The steps in topography and increase in elevation from south to north influences precipitation and vegetation. The precipitation gradient is evident by comparing the total annual precipitation at Lee's ferry, AZ (978 m elevation; 186 mm

precipitation), Kanab Creek, UT (1494 m; 381 mm), and Bryce Canyon, UT (2413 m; 419 mm). The study area is on the northwest boundary of direct influence the North American Monsoon (NAM), which is characterized by increased precipitation in July through September (Adams and Comrie, 1997). Winter precipitation is strongly linked to the phase and intensity of the El Nino Southern Oscillation (ENSO). El Nino conditions in the eastern equatorial Pacific Ocean are related to enhanced winter precipitation in the Southwest, while La Niña conditions (cool eastern Tropical Pacific) produce drier winter conditions (Cayan et al., 1999). Vegetation types are related to elevation and change from subalpine forests to mixed-conifer forests to pinyon/juniper woodlands and to desert scrub ecotones are found at the lowest elevations.

Johnson Wash was settled in 1871 CE and a canal was dug in the center of the alluvial valley to drain saturated meadows and divert surface runoff toward the valley margin for agriculture (Robinson, 1972; Webb et al., 1991) and entrenchment of the alluvial valley in Johnson Wash occurred ~1909-1912 CE (Webb et al., 1991). Initial entrenchment of Kanab Creek was observed in 1872 CE (Dellenbaugh, 1908), and ten years later a 17-meter-deep and 30-meter-wide arroyo formed in response to late summer high discharge events in 1882 and 1883 CE (Carroll, 1960). Further entrenchment occurred in 1884, 1885, and 1886 CE during high spring discharge events (Woolley et al., 1946). Stream dynamics significantly changed from an unconfined, shallow stream channel to a stream entrenched and confined between cohesive, fine-grained, near vertical, arroyo walls. The towns of Johnson and Skutumpah were both abandoned by 1940 CE (Gregory, 1945). Johnson Wash is currently entrenched into the valley-fill

alluvium, the modern stream is aggrading within arroyo walls, and the modern channel has an approximately three-meter-high inset floodplain that thickens downstream.

Methods

This study reconstructs the alluvial chronology of a 15 km reach of Johnson Wash draining the upper ~400 km^2 of the watershed (Figure 2-1). Arroyo walls in Johnson Wash are four to 15 meters high and provide nearly continuous vertical exposures that preserve a record of paleo-arroyo cut-fill sequences. The chronostratigraphy of alluvial fills was characterized using physical descriptions of the sedimentology and stratigraphy and radiocarbon and optically stimulated luminescence (OSL) dating for age control. Crosscutting stratigraphic relationships were described at each outcrop to interpret the relative timing of alluvial units. Fifteen stratigraphic sections, labelled A-O, were described using allostratigraphy, with discrete alluvial packages defined by buttress and other bounding unconformities including paleosols. One stratigraphic section (A) was located in the upper basin amongst the Grey Cliffs, twelve stratigraphic sections (B-M) were located along the trunk stream on the Wygaret Terrace below the White Cliffs, and two sections (N and O) were located along smaller tributary streams. Stratigraphic sections were selected based on the presence of at least one unconformity-bound cut-fill sequence (n=13) or based on their location in the watershed (n=2; stratigraphic sections B and M) to establish a representative suite of valley-fill deposits. Evidence for paleo-arroyo entrenchment was based on the identification of a near vertical buttress unconformity greater than three meters and a colluvial wedge at the base of the paleo-

arroyo wall. These characteristics were used to differentiate arroyo entrenchment from a near-vertical buttressed unconformity produced by lateral channel migration that would be smaller in scale (<3 m) and have shorter persistence (no colluvial wedge at base).

Descriptions of sediment facies were used to interpret depositional environment and followed Miall (1996). Detailed descriptions of individual beds included thickness, geometry, sedimentary structures, grain size, color, sorting, facies association, and inferred depositional setting. In the field, stratigraphic sections were subdivided into descriptive units based on significant changes in depositional characteristics and facies codes (Supplemental Material Table 2-S1) were used to describe and categorize beds in hard to reach arroyo-wall exposures. Depositional environments and facies associations were classified into five broad categories: channel-bottom (CB), channel-margin (CM), channel-margin slackwater (CMs), valley-surface (VS), and colluvial wedge (VSc) similar to previous arroyo work in the area (Harvey et al., 2010; Harvey et al., 2011; Huff and Rittenour, 2014). Soil development was identified in part by massive horizons with darker colors (lower chroma) due to increased organic matter, accumulation of calcium carbonate, and presence of pedogenic structure.

Charcoal samples were collected for radiocarbon dating, specifically targeting burned horizons, needles, twigs, and other annually produced material in order to reduce age over estimations from inbuilt age (Gavin, 2001), however, these materials were rarely observed. Charcoal fragments were pretreated, combusted and converted to graphite, pressed into targets, and measured on an Accelerator Mass Spectrometer (AMS) at the University of California-Irvine Radiocarbon Lab. Radiocarbon ages were corrected for

isotopic fractionation, and the 2-sigma age was calibrated using CALIB 7.0.4 (Reimer et al., 2004) and the IntCal13 calibration curve (Reimer et al., 2013). The weighted mean calibrated ages were rounded to the nearest decade and ages were reported in calibrated years before 2010 CE (cal yr BP_{2010}) in order to use a similar datum to OSL. The primary source of uncertainty associated with radiocarbon dating fluvial deposits is age over-estimation due to the disparity between the timing of death of the plant and the timing of deposition. Multiple samples were dated from each alluvial fill package and in some cases field replicates were analyzed (two charcoal samples collected from the same deposit) to help identify age over estimates. The radiocarbon field replicate analysis results are available as supplemental data.

OSL samples were collected to provide an age estimate of the last time sediment was exposed to light (Huntley et al., 1985). We targeted the upper and lower beds within each unconformity-bound alluvial package. Samples were collected in opaque metal tubes and representative sediment was collected from a 30 cm radius of the sample tube for determination of radio-elemental concentrations for dose rate calculation (Supplemental Material Table 2-S3). The fine-grained quartz sand fraction (150-250 μm) was isolated for single-grain dating at the Utah State University Luminescence Laboratory under safelight, dark room conditions. Ages are rounded to the nearest decade and reported in years ago (ya) with a two-sigma error and has datum of 2010 CE. The most significant source of uncertainty in OSL dating fluvial deposits is partial bleaching due to incomplete solar resetting and incorporation of an inherited luminescence signal, leading to an age over-estimation (Olley et al., 1998; Wallinga, 2002; Jain et al., 2004;

Duller, 2008; Rittenour, 2008). The effects of partial bleaching were minimized by used single-grain dating and a minimum age model (MAM; Galbraith and Roberts, 2012) to identify the population of grains that were most likely zeroed prior to deposition. We sampled facies that were most likely to have been reset by sunlight exposure (bleached) prior to deposition and avoided soils and bioturbation that can mix grains from younger and older deposits. Plane-bedded, low-angle, ripple crossbed sandy lithofacies displayed the best single grain evidence for solar resetting (Summa-Nelson and Rittenour, 2012; Huff and Rittenour, 2014) and were targets for sampling. Sedimentary beds that are massive or contains trough or horizontal crossbeds have been suggested to be the least conducive for OSL dating (Huff, 2013) and were avoided.

The longitude profile of the modern entrenched trunk channel was compared to a reconstructed pre-entrenchment channel on the valley-fill terrace tread in Johnson Wash, Kitchen Corral Wash, and Kanab Creek. The pre-entrenchment channel was reconstructed using 1-meter-resolved National Agriculture Imagery Program (NAIP) imagery and a 10-meter Digital Elevation Model (DEM). A surface was created that capped the entrenched channel using the mapped terrace tread points. The filled channel was added to the modern DEM. Flow pathways and slope-area plots were calculated and analyzed in Topo Toolbox 2 (Schwanghart and Scherler, 2014). The method used thus far in this research needs to be refined. The method for selecting reach endpoints needs to be established because changing these endpoints highly influences the estimated concavity.

Cosmogenic Be-10 derived erosion rate data from modern stream beds and sediment collected from Holocene-aged arroyo walls in complimentary studies (Riley et

al., 2019; Ch III & IV) were used in combination with sedimentology, stratigraphy, radiocarbon, and optically OSL absolute ages from this study to investigate if erosion rates and thus sediment supply varied through the mid-to-late Holocene.

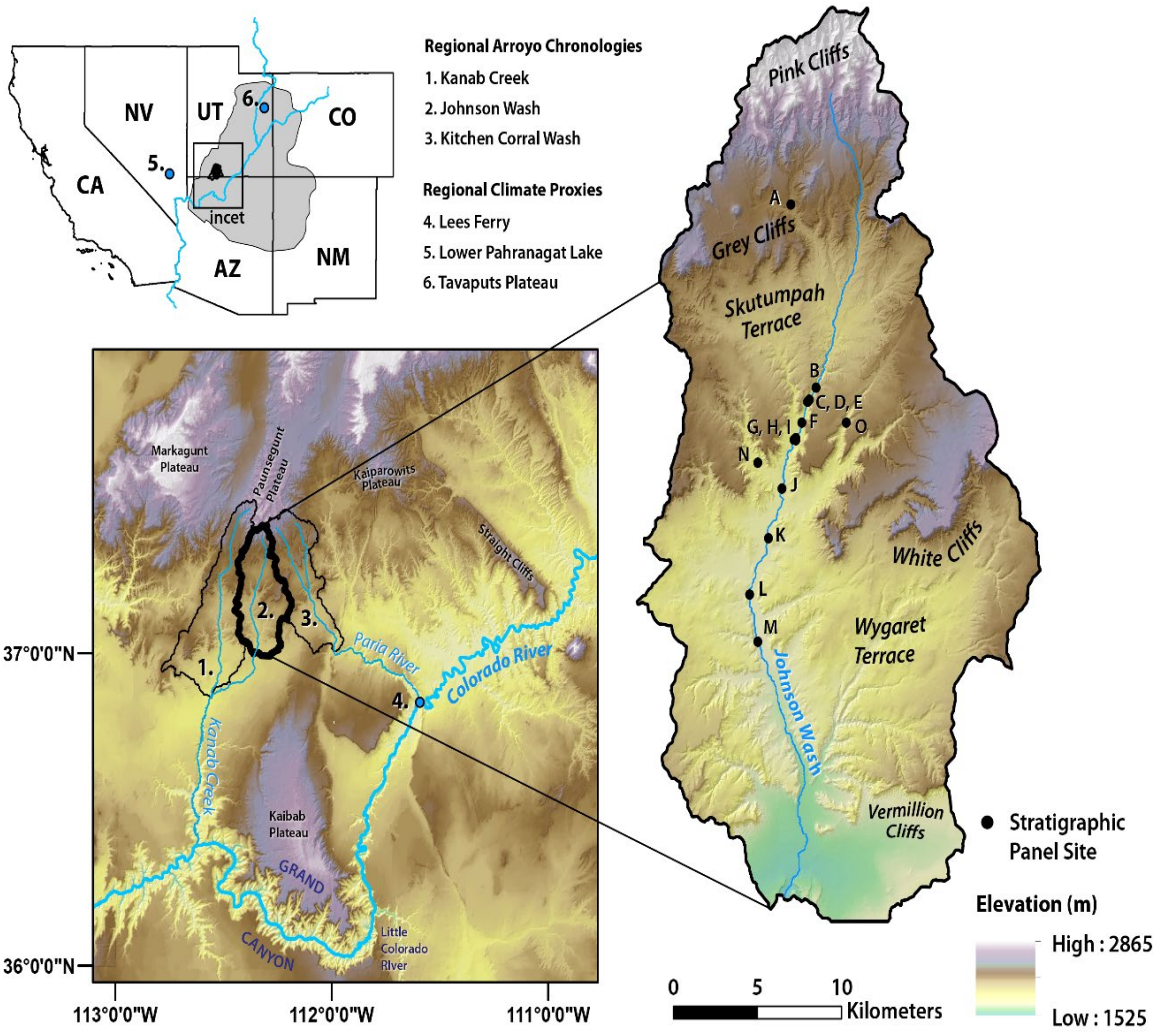

Figure 2-1. Regional map and study area map. The grey polygon represents the Colorado Plateau, the Green and Colorado River are in blue, and the box identifies the inset regional map of watersheds with previous arroyo chronology reconstructions. Upper Johnson Wash is shown with stratigraphic panel locations annotated with capital letters A-O.

Results

Stratigraphy, sedimentology, and age control from fifteen stratigraphic exposures are summarized below with detailed descriptions located in the supplemental material (see footnote[1]). In general, the alluvial fills exposed in Johnson Wash arroyo walls were dominated by sand and fine-grained sedimentary facies with some pebble-gravel lenses. The primary fine-grained facies observed included decimeter- to centimeter-thick beds of variegated and laminated moderate- to well-sorted sand, silt, and clay with centimeter-scale ripples (Fsmv, Fl) and fine-grained massive mud and silt with desiccation cracks (Fm). We interpreted these fine-grained facies as being deposited by the settling of grains in suspension in overbank, abandoned channel, waning flood, or slackwater depositional environments. Sand facies consisted of planar cross-bedded (Sp), trough cross-bedded (St), horizontal laminated (Sh), low angle cross-bedded (Sl), and massive sands (Sm). Sand facies contained sheet, lens, and channel external geometries, centimeter- to meter-scale bed thicknesses that were generally tabular, and laterally continuous with some truncation and onlapping bounding surfaces. Depositional environments of sand facies were interpreted to be channel and channel marginal deposits.

Age control on the alluvial history of aggradation and entrenchment in Johnson Wash consists of 57 radiocarbon-ages (Table 2-1) and 29 OSL ages (Table 2-2) derived from 15 stratigraphic sections. Notably, only twenty-six radiocarbon samples (46%) were

[1] Supplemental material includes stratigraphic descriptions, radiocarbon replicate data, ICP-MS chemistry, dose-rate data, rejection statistics, and equivalent dose (De) distribution statistics for all OSL samples data.

interpreted to accurately represent the depositional age based on stratigraphic relationships and agreement with OSL ages. The remaining 31 radiocarbon ages (54%) were interpreted to not represent depositional ages for three primary reasons. Seven radiocarbon samples resulted in anomalously old ages, ranging from 8,000 to >48,000 radiocarbon-years and were interpreted as being contaminated by or derived from coal deposits. Twenty-two radiocarbon samples resulted in ages interpreted as being too old relative to their stratigraphic position and relationship to OSL and other ^{14}C ages. Two samples resulted in ages that were stratigraphically too young and were interpreted as being an inset deposit or from younger material mixed into the deposit from bioturbation. There was not a clear trend in over-dispersion values for OSL samples and facies classification. The samples with the lowest over-dispersion and skew were inferred to indicate evidence for more complete solar resetting and were associated with trough, horizontal and low-angle crossbed sand facies (Supplemental Material Fig 2-S9). All OSL analysis and results are available as supplemental data.

The oldest period of aggradation identified as Qf1 is constrained to between 2200 and 1550 ya based on eight OSL and one radiocarbon age (Fig 2-4). The alluvial fill package was exposed in eight of the 15 stratigraphic sections and was bounded by unconformities in these stratigraphic sections (Fig 2-5). The thickness of the exposed fill varied between three meters in the downstream profiles (J, K, L and M) to was as thick as 15 meters in the most upstream profile (Profile C). Note the base of alluvial packages is not seen because the current channel is aggrading. Thus, the alluvial fill thicknesses reported here are minimum estimates. The sedimentology of Qf1 was coarser than the

younger fills and units consisted primarily of 10-100 cm thick, ripple and trough cross-bedded and massive sand facies associated with channel bottom and channel margin depositional environments. Finely laminated, variegated, and massive silt and mud facies were more common towards the top of the alluvial package and were generally associated with channel margin slackwater and valley surface depositional environments. The base of the unit and precise initiation of aggradation was not identified; thus, 2200 ya is a minimum age for the start of aggradation of this alluvial package. A buried soil was identified in seven exposures constraining a period of stability between 1800 and 1500 ya prior to entrenchment. Entrenchment into Qf1 is constrained to between 1550 and 1450 ya. Qf1 was capped with younger alluvial-fill package(s) in all exposures, where observed. Based on the observations, the former floodplain surface of Qf1 was likely a few meters lower than the pre-entrenchment floodplain level (Figure 2-4).

The second alluvial-fill package, identified as Qf2, was exposed in 12 of the 15 stratigraphic sections, and five stratigraphic sections contained two bounding unconformities. Eighteen OSL and nine radiocarbon ages constrain the timing of aggradation between 1450 and 750 ya. The thickness of alluvial fills varies between 2-14 meters. The sedimentology of Qf2 consists of alternating sand and fine-grained facies encompassing channel bottom, channel margin, channel margin slackwater, and valley surface depositional environments. Truncation due to paleo-arroyo entrenchment of Qf2 is bracketed between 750-650 ya (e.g., see stratigraphic profile D Figure 2-2). Qf2 is commonly capped by the youngest alluvial-fill (Figure 2 and 3) and aggradation during this time period appears to have been one- to two- meters lower than the most recent

period of aggradation of Qf3 (Figure 2-4).

The stratigraphically youngest alluvial-fill package is Qf3 (Figure 2-2 and 2-3). Two OSL samples and six radiocarbon ages constrain the timing of aggradation of Qf3 to after 650 ya with the culmination of aggradation ~100 years ago based on historical observations of arroyo cutting. Qf3 was exposed and dated in nine stratigraphic sections in the axial trunk stream (Fig 2-5). In some profiles, Qf3 is only observed over topping older alluvial fill packages by ~2.5 m. In other profiles, the exposed thickness of Qf3 varied from 7-10 meters. The sedimentology of Qf3 was dominated by fine-grained facies including variegated and laminated moderate- to well-sorted sand, silt, and clay (Fsmv, Fl). Qf3 overtopped the two older fill packages Qf1 and Qf2. Age control from a stratigraphic exposure in a tributary (site O) suggests correlative aggradation at that location.

Catchment averaged erosion rates from 15 Holocene deposits that represent five discrete alluvial fill packages constrained to 6000-3500, 3200-2500, 2200-1550, 1450-750, and 650-100 years ago ranged from 20 to 420 mm/kyr (Table 2-3; Ch. IV). Twelve spatially similar modern erosion rates were compared to their Holocene analogue (Table 2-3; Riley et. al., 2019; Ch. III). Holocene erosion rates ranged from 20 to 420 mm/kyr integrating over time intervals (T_{ave}) of 1.5 to 28 kyr. The percent of the measured nuclide concentration gained following deposition and burial varied between 0 – 2 % with one outlier of 45 %. Holocene erosion rates were similar to erosion rates measured in modern stream sediment from alluvial reaches, which varied spatially from 20 to >800 mm/kyr.

Concavity was estimated using log-log slope-area plots of the flow pathways of the reconstructed aggraded channel and the modern entrenched channel. Preliminary results comparing modern entrenched longitudinal profile channel concavity with a reconstructed aggraded channel longitudinal profile in Kanab Creek, Johnson Wash, and Kitchen Corral Wash indicate a systematic decrease in channel profile concavity of the aggraded channel form (Figure 2-6). The magnitude of change in concavity between the aggraded and entrenched state varied significantly based on how you delineated the reach (reach endpoints). Thus, these results remain preliminary and more work needs to be done to document the exact boundary conditions and selection criteria followed to complete systematic regional analysis.

Table 2-1. Summary of radiocarbon dates ordered by stratigraphic section (upstream to downstream; then ordered by unit number from youngest to oldest. Bold ages were interpreted as accurately dating the deposit within error of independent age control.

	Lab ID	Strat ID	Depth (cm)	Relative Fill Package # ; Unit #	^{14}C Age (yr BP) (interpretation [1])	Weighted Mean cal yr BP$_{(2010)}$ [2]	+ 2σ	– 2σ
1	UCIAMS-147060	A	850	Qf 2 ; Unit 3	1660 ± 20	**1620**	50	30
2	UCIAMS-151650	A	700	Qf 1 ; Unit 2	2035 ± 20	**2040**	70	50
3	UCIAMS-147061	A	900	Qf 1 ; Unit 1	2400 ± 25	**2480**	260	70
4	UCIAMS-147064	C	1100	Qf 3 ; Unit 19	1135 ± 25 (R)	1100	150	70
5	UCIAMS-137313	C	1200	Qf 2 ; Unit 10	32900 ± 1300 (C)	-	-	-
6	UCIAMS-147062	C	1310	Qf 2 ; Unit 9	1990 ± 20 (R)	2000	50	50
7 [3]	UCIAMS-137312	C	400	Qf 1 ; Unit 6	2475 ± 25 (R)	2630	150	130
8 [3]	UCIAMS-151651	C	400	Qf 1 ; Unit 6	2140 ± 60 (R)	2200	170	150
9	UCIAMS-147063	C	1400	Qf 1 ; Unit 1	3125 ± 35 (R)	3360	140	60
10	UCIAMS-137311	C	1480	Qf 1 ; Unit 1	820 ± 30 (Y)	790	50	40
11 [3]	UCIAMS-137319	D	275	Qf 3 ; Unit 10	115 ± 25 (Y)	190	140	120
12 [3]	UCIAMS-137320	D	275	Qf 3 ; Unit 10	355 ± 35	**460**	90	100
13	UCIAMS-147065	D	450	Qf 3 ; Unit 10	570 ± 25	**660**	70	40
14	UCIAMS-147066	D	300	Qf 2 ; Unit 3	1230 ± 25	**1230**	90	100
15	UCIAMS-147067	D	500	Qf 2 ; Unit 3	1495 ± 20	**1440**	30	50
16	UCIAMS-137314	D	625	Qf 2 ; Unit 2	1495 ± 30	**1440**	140	70
17	UCIAMS-137315	D	1000	Qf 2 ; Unit 1	2195 ± 25	**2290**	80	90
18	UCIAMS-147068	E	925	Qf 2 ; Unit 2	2415 ± 25	**2510**	230	100
19 [3]	UCIAMS-151648	F	280	Qf 2 ; Unit 18	2030 ± 20 (R)	2040	60	60
20 [3]	UCIAMS-147071	F	280	Qf 2 ; Unit 18	> 47200 (C)	-	-	-
21	UCIAMS-147069	F	1115	Qf 2 ; Unit 10	8840 ± 330 (C)	10000	820	910
23	UCIAMS-151647	F	1165	Qf 2 ; Unit 9	1210 ± 45	**1200**	130	140
22	UCIAMS-128113	F	1370	Qf 2 ; Unit 8	2460 ± 15 (R)	2620	140	180
24	UCIAMS-147070	F	1120	Qf 1 ; Unit 1	1785 ± 20	**1760**	**110**	**80**
25	UCIAMS-128112	F	1280	Qf 1 ; Unit 1	1915 ± 15	**1920**	**40**	**40**
26	UCIAMS-128115	G	123	Qf 2 ; Unit 17	350 ± 15	**460**	80	80
27	UCIAMS-128117	G	225	Qf 2 ; Unit 16	440 ± 15	**570**	10	20
28	UCIAMS-128118	G	660	Qf 2 ; Unit 15	1125 ± 15	**1080**	40	40
29	UCIAMS-147076	G	680	Qf 1 ; Unit 3	2280 ± 20	**2360**	50	120
30	UCIAMS-128119	G	830	Qf 1 ; Unit 2	46400 ± 110 (C)	-	-	-
31	UCIAMS-128116	G	1010	Qf 1 ; Unit 1	25600 ± 1500 (C)	-	-	-
32 [3]	UCIAMS-147077	G	1100	Qf 1 ; Unit 1	2950 ± 25 (R)	3170	70	100
33 [3]	UCIAMS-147078	G	1100	Qf 1 ; Unit 1	2985 ± 20 (R)	3220	60	80

[1] Too old because charcoal was reworked/redeposited or old wood (R), coal contamination (C), too young because of bioturbation or inset deposit (Y)

[2] The calibrated weighted mean age was calculated with CALIB 7.1 (Reimer et al., 2004) and the IntCal13 calibration curve (Reimer et al., 2013). Ages reported are in calibrated years before 2010 (cal yr BP$_{2010}$) and 2-sigma error reported.

[3] Replicate sample was analyzed and results are summarized in Table 2-S3 (supplemental material).

Table 2-1. *(Continued)*

Count	Lab ID	Strat ID	Depth (cm)	Relative Fill Package # ; Unit #	^{14}C Age (yr BP) (interpretation [1])	Weighted Mean cal yr BP$_{(2010)}$ [2] + 2σ – 2σ	Count	Lab ID
34 [3]	UCIAMS-147075	H	150	Qf 2 ; Unit 15	1630 ± 20 (R)	1580	70	100
35 [3]	UCIAMS-147074	H	150	Qf 2 ; Unit 15	4480 ± 230 (R/C)	5180	540	660
36	UCIAMS-147073	H	600	Qf 1 ; Unit 3	2825 ± 20 (R)	2980	70	60
37	UCIAMS-137316	H	550	Qf 1 ; Unit 4b	2505 ± 30 (R)	2650	150	100
38	UCIAMS-147072	H	800	Qf 1 ; Unit 4a	2910 ± 20 (R)	3110	90	80
39	UCIAMS-137317	I	125	Qf 3 ; Unit 12	555 ± 30	**620**	80	40
40	UCIAMS-137318	I	700	Qf 2 ; Unit 5	1260 ± 25	**1270**	70	120
41	UCIAMS-147079	I	1100	Qf 1 ; Unit 3	1770 ± 25	**1740**	130	70
42	UCIAMS-147080	J	100	Qf 2 ; Unit 5	1205 ± 20 (R)	1190	90	70
43	UCIAMS-151649	J	350	Qf 1 ; Unit 3	3000 ± 20 (R)	3240	140	100
44 [3]	UCIAMS-147081	J	405	Qf 1 ; Unit 2	2535 ± 20 (R)	2710	50	170
45 [3]	UCIAMS-147082	J	405	Qf 1 ; Unit 2	> 45700	-	-	-
46	UCIAMS-147084	K	200	Qf 3 ; Unit 18	1560 ± 20 (R)	1530	50	70
47 [3]	UCIAMS-136386	K	450	Qf 2 ; Unit 11	1680 ± 15 (R)	**1640**	**40**	**40**
48 [3]	UCIAMS-136387	K	450	Qf 2 ; Unit 11	1675 ± 15 (R)	**1640**	**40**	**30**
49	UCIAMS-147085	K	100	Qf 1 ; Unit 6	> 48500 (C)	-	-	-
50	UCIAMS-147083	K	360	Qf 1 ; Unit 2	2230 ± 25 (R)	2290	100	80
51 [3]	UCIAMS-147088	L	90	Qf 3 ; Unit 10	285 ± 20	**420**	70	70
52 [3]	UCIAMS-147087	L	90	Qf 3 ; Unit 10	1125 ± 20 (R)	1080	50	50
53 [3]	UCIAMS-113994	M	460	Qf 1 ; Unit 1	3185 ± 20 (R)	3470	40	40
54 [3]	UCIAMS-113901	M	460	Qf 1 ; Unit 1	3985 ± 15 (R)	4530	50	50
55	UCIAMS-128114	N	400	Qf 2 ; Unit 2	945 ± 15	**920**	60	60
56	UCIAMS-147086	O	230	Qf 3 ; Unit 2	400 ± 20	**520**	50	130
57	UCIAMS-128120	O	350	Qf 2 ; Unit 1	1485 ± 15	**1430**	40	30

[1] Too old because charcoal was reworked/redeposited or old wood (R), coal contamination (C), too young because of bioturbation or inset deposit (Y)

[2] The calibrated weighted mean age was calculated with CALIB 7.1 (Reimer et al., 2004) and the IntCal13 calibration curve (Reimer et al., 2013). Ages reported are in calibrated years before 2010 (cal yr BP$_{2010}$) and 2-sigma error reported.

Table 2-2. Summary of single-grain OSL ages ordered by stratigraphic section and labelled alphabetically from upstream to downstream with the two tributaries last. Samples were ordered within each stratigraphic profile by alluvial package number (youngest to oldest) and then by unit number (youngest to oldest).

Count	Lab ID	Strat ID - Sample #	Depth (cm)	Relative Fill Package # ; Unit #	Facies Code	Num. of grains [1]	Dose Rate [2] ± 2 σ error (Gy / kyr)	De [3] ± 2 σ error (Gy)	Age ± 2 σ error [4] (ya)
1	USU 1334	B - 4	250	Qf 3 ; Unit 10	Sr	31 (2200)	1.85 ± 0.10	1.21 ± .41	**650 ± 230**
2	USU 1335	B - 5	1040	Qf 2 ; Unit 3	Sm	30 (2700)	1.96 ± 0.10	2.28 ± .63	**1160 ± 340**
3	USU 1682	C - 4	1000	Qf 2 ; Unit 13	Sl	40 (2100)	1.92 ± 0.10	1.20 ± 0.39	**620 ± 210**
4	USU 1680	C - 2	1330	Qf 2 ; Unit 9	Sl	30 (1900)	1.75 ± 0.09	2.48 ± 0.56	**1420 ± 350**
5	USU 1679	C - 1	1480	Qf 1 ; Unit 1	Sh	33 (1700)	1.47 ± 0.08	2.58 ± 0.54	**1750 ± 410**
6	USU 1677	D - 1	375	Qf 2 ; Unit 3	Sh, St	34 (2400)	2.06 ± 0.11	1.74 ± 0.36	**840 ± 200**
7	USU 1678	D - 2	700	Qf 2 ; Unit 1	Sr	31 (3500)	2.86 ± 0.15	4.82 ± 1.51	**1690 ± 550**
8	USU 1676	F - 9	200	Qf 2 ; Unit 8	Sm	57 (2500)	1.90 ± 0.10	1.77 ± 0.41	**930 ± 240**
9	USU 1354	F - 4	1090	Qf 2 ; Unit 4	Sr	36 (2600)	1.48 ± 0.08	1.49 ± 0.58	**1010 ± 410**
10	USU 1355	F - 7	1165	Qf 2 ; Unit 2	Sr	48 (3100)	1.10 ± 0.06	1.52 ± 0.32	**1470 ± 340**
11	USU 1396	G - 4	300	Qf 2 ; Unit 14	Sh	30 (1700)	2.37 ± 0.12	2.22 ± 0.49	**940 ± 230**
12	USU 1395	G - 3	830	Qf 2 ; Unit 7	Sr	32 (2500)	2.55 ± 0.13	3.49 ± 0.79	**1370 ± 340**
13	USU 1392	G - 2	615	Qf 1 ; Unit 3	St	34 (2300)	2.16 ± 0.11	3.97 ± 0.91	**1840 ± 460**
14	USU 1394	G - 1	1125	Qf 1 ; Unit 1	Sh	45 (4200)	1.64 ± 0.09	3.13 ± 0.53	**1910 ± 370**

[1] Age analysis using the single-aliquot regenerative-dose procedure of Murray and Wintle (2000) on single-grains of quartz sand (Duller, 2008). Number of grains used in age calculation and number of grains analyzed in parentheses.

[2] Dose rates are calculated based on water content, sediment chemistry (Table 2) and density (1.9g/cm^3), and using sample depth, elevation (1.7-1.9 km), and latitude/longitude (~37.2/ ~-112.4) following Prescott and Hutton (1994), Aitken and Xie (1990), Aitken (1998).

[3] Equivalent dose (D_E) calculated using the Minimum Age Model (MAM) of Galbraith and Roberts (2012).

[4] Uncertainty associated with OSL age determinations include both random and systematic errors and were calculated in quadrature (Aitken and Alldred, 1972; Aitken, 1976; Aitken, 1985).

Table 2-2. (*Continued*)

Count	Lab ID	Strat ID - Sample #	Depth (cm)	Relative Fill Package # ; Unit #	Facies Code	Num. of grains [1]	Dose Rate [2] ± 2 σ error (Gy / kyr)	De [3] ± 2 σ error (Gy)	Age ± 2 σ error [4] (ya)
15	USU 1684	H - 2	700	Qf 2 ; Unit 15	Sl, Sh	36 (4400)	2.48 ± 0.13	1.78 ± 0.30	**720 ± 140**
16	USU 1685	H - 3	1075	Qf 2 ; Unit 13	Sl	38 (2200)	2.66 ± 0.14	2.19 ± 0.47	**830 ± 190**
17	USU 1683	H - 1	950	Qf 1 ; Unit 2	Sh, Sl	50 (3900)	1.62 ± 0.09	2.45 ± 0.64	**1510 ± 420**
18	USU 1668	I - 7	700	Qf 2 ; Unit 7	Sp	31 (2600)	1.55 ± 0.08	2.04 ± 0.50	**1320 ± 350**
19	USU 1667	I - 5	700	Qf 2 ; Unit 5	Sl	32 (2800)	1.73 ± 0.09	2.49 ± 0.55	**1430 ± 350**
20	USU 1673	I - 1	1130	Qf 2 ; Unit 3	Sh	39 (2800)	1.62 ± 0.09	2.58 ± 0.54	**1600 ± 370**
21	USU 1687	J - 1	500	Qf 1 ; Unit 2	Sp	30 (2100)	1.37 ± 0.08	2.28 ± 0.41	**1660 ± 340**
22	USU 1562	K - 7	175	Qf 3 ; Unit 18	Sp	30 (3100)	1.71 ± 0.09	0.75 ± 0.27	**440 ± 170**
23	USU 1561	K - 3	550	Qf 2 ; Unit 10	Sm	33 (2700)	1.63 ± 0.09	2.31 ± 0.68	**1420 ± 440**
24	USU 1330	K - 6	250	Qf 1 ; Unit 4	Sr	50 (2900)	1.47 ± 0.08	2.25 ± 0.56	**1530 ± 410**
25	USU 1328	K - 1	420	Qf 1 ; Unit 2	Sr	36 (3400)	2.35 ± 0.12	4.14 ± 0.79	**1760 ± 380**
26	USU 1691	L – 1	650	Qf 1 ; Unit 1	Sl	34 (2000)	1.86 ± 0.10	4.06 ± 1.32	**2180 ± 750**
27	USU 1138	M - 2	245	Qf 2 ; Unit 6	Sr	32 (1700)	1.89 ± 0.10	2.53 ± 0.79	**1340 ± 440**
28	USU 1139	M - 1	450	Qf 1 ; Unit 1	Sr	36 (900)	2.89 ± 0.12	6.44 ± 1.71	**2230 ± 630**
29	USU 1352	N-1	485	Qf2 : Unit1	Sh, Sm	30(1500)	1.11 ± 0.06	1.18 ± 0.37	**1060 ± 350**

[1] Age analysis using the single-aliquot regenerative-dose procedure of Murray and Wintle (2000) on single-grains of quartz sand (Duller, 2008). Number of grains used in age calculation and number of grains analyzed in parentheses.

[2] Dose rates are calculated based on water content, sediment chemistry (Table 2) and density (1.9g/cm^3), and using sample depth, elevation (1.7-1.9 km), and latitude/longitude (~37.2/ ~-112.4) following Prescott and Hutton (1994), Aitken and Xie (1990), Aitken (1998).

[3] Equivalent dose (D_E) calculated using the Minimum Age Model (MAM) of Galbraith and Roberts (2012).

[4] Uncertainty associated with OSL age determinations include both random and systematic errors and were calculated in quadrature (Aitken and Alldred, 1972; Aitken, 1976; Aitken, 1985).

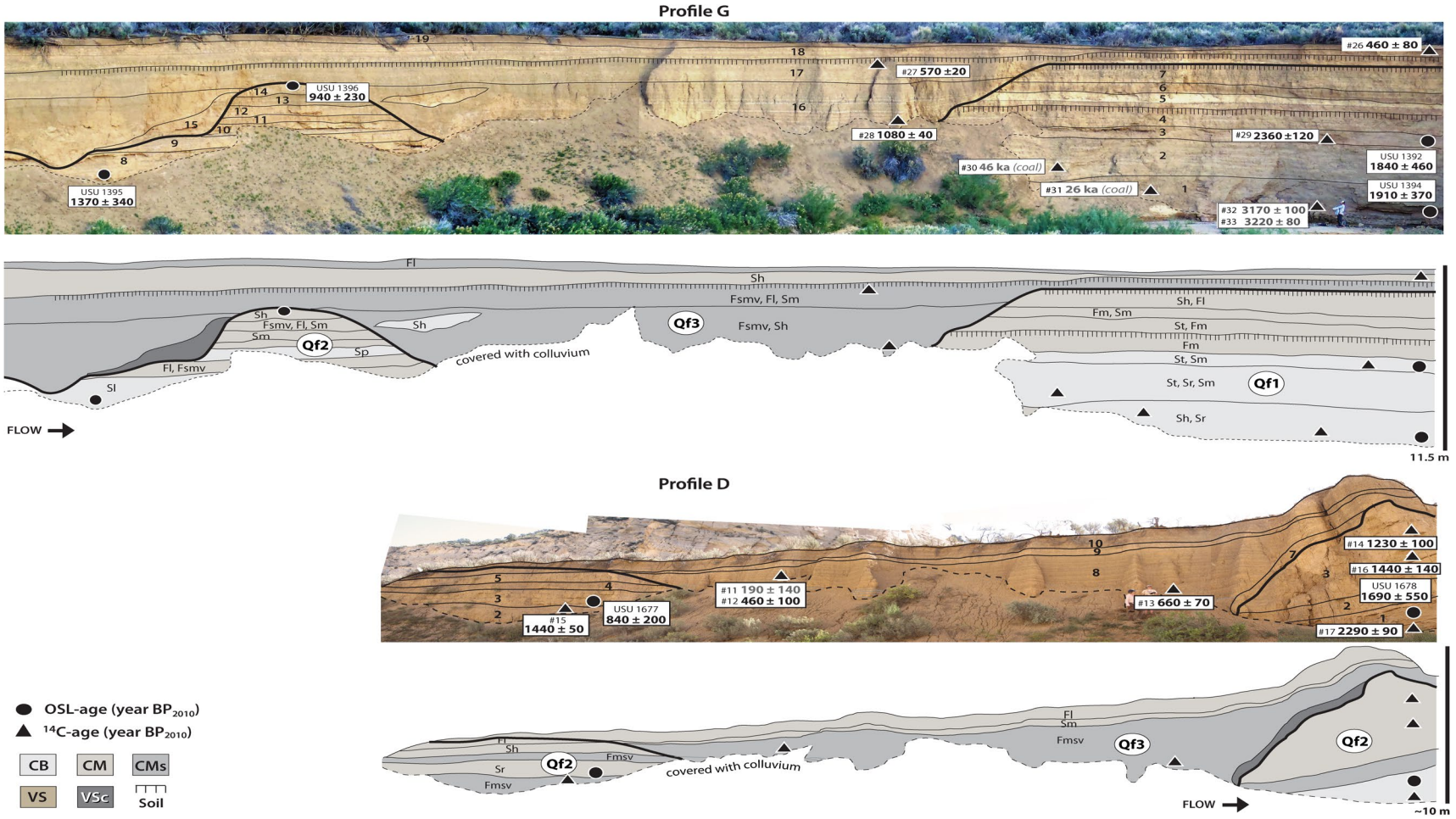

Figure 2-2. Stratigraphic profiles G (top) and D (bottom) show three alluvial packages (Qf1, Qf2, Qf3) separated by buttressed unconformities. OSL and radiocarbon ages are annotated on the photographs and stratigraphic facies and depositional facies associations are annotated on illustration. Refer to text and Table S1 for key to stratigraphic and depositional facies. Radiocarbon ages in grey are problematic based on stratigraphic relations or coal contamination (Table 2-1).

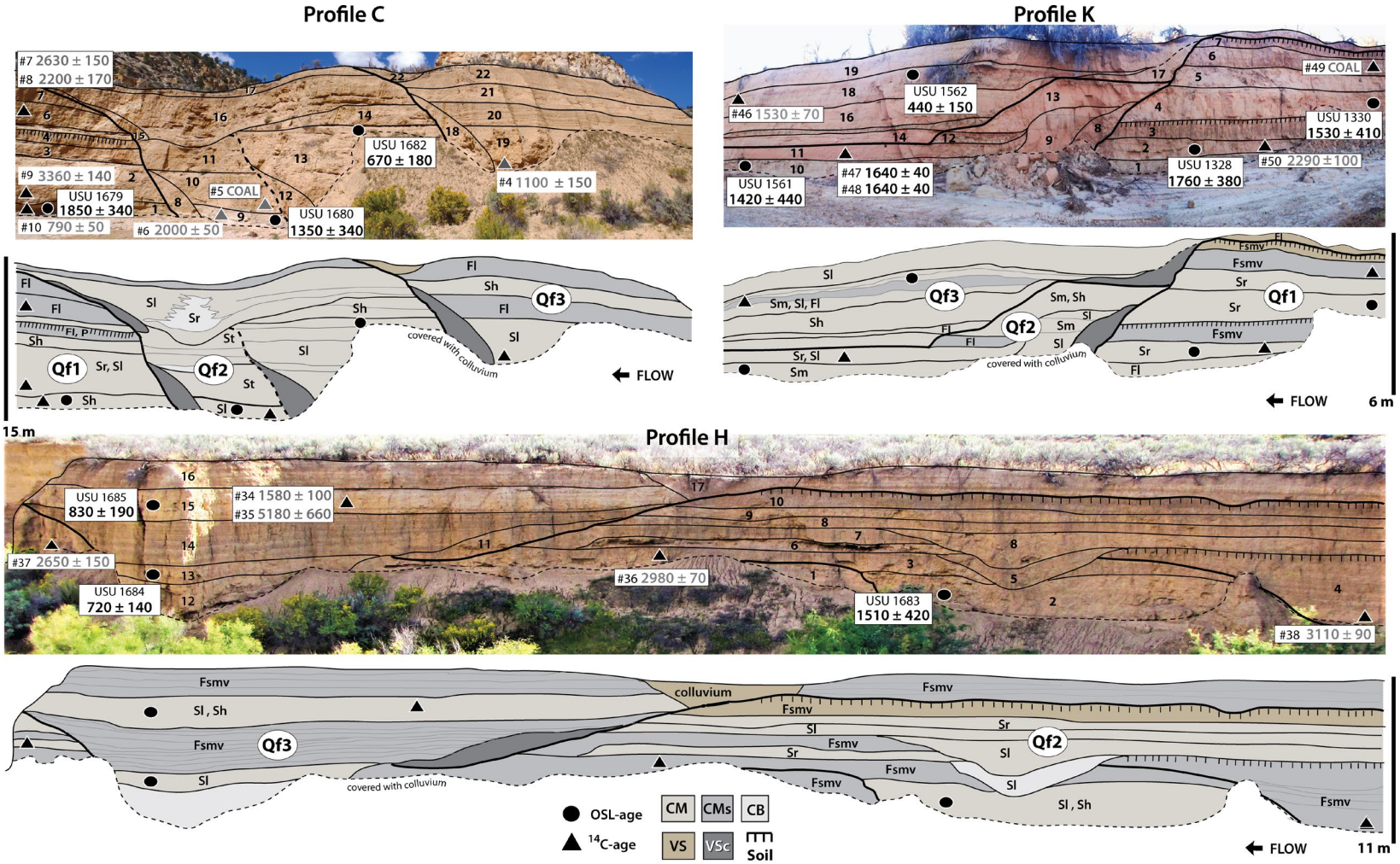

Figure 2-3. Stratigraphic profiles are illustrated in the above figure. OSL and radiocarbon ages are annotated on the photographs and stratigraphic facies and depositional facies associations are annotated on illustration. Radiocarbon ages in grey are problematic based on stratigraphic relations or coal contamination (Table 2-1).

Table 2-3. Post deposition depth-averaged ^{10}Be production, measured ^{10}Be concentrations, depth corrected 10Be concentrations, and inferred erosion rates for modern and Holocene arroyo sample suites.

Sample Suite	PRIME ID	Sample ID	OSL Sample	Age (ka)	Location / Reach Type	Measured ^{10}Be Conc. (at/g)	Analytical Error	Corrected ^{10}Be Conc. (at/g)	Erosion Rate [1] (mm/kyr)	Error [2]	T_{ave} [3] (kyr)
1	201603170	KNB 30	-	0	Vermillion / alluvial	9.09E+04	2.5E+03		120	10	5.00
	201603172	KNB 40	USU 1631	2.9	Vermillion / alluvial	4.71E+05	1.1E+04	4.71E+05	20	10	30.0
2	201600327	KNB 28	-	0	Vermillion / alluvial	8.57E+04	4.6E+03		110	20	5.45
	201603169	KNB 26	USU 356	4.8	Vermillion / alluvial	5.72E+04	1.4E+03	5.68E+04	160	10	3.75
3	201700345	KCW 5	-	0	Vermillion / alluvial	1.89E+05	4.6E+03		60	10	10.00
	201700334	KCW 6	-	0	Vermillion / alluvial	1.73E+05	4.5E+03		65	10	9.25
	201700346	KCW 7		0.2	Vermillion / alluvial	3.60E+05	1.7E+04	3.59E+05	30	5	19.95
	201700347	KCW 8	USU 1192	1.1	Vermillion / alluvial	3.17E+05	1.4E+04	3.17E+05	35	5	17.15
	201700348	KCW 9	USU 1192	1.1	Vermillion / alluvial	1.16E+05	6.1E+03	1.15E+05	100	15	6.00
4	201401587	KNB 19	-	0	Wygaret / alluvial	3.92E+04	1.5E+03		290	40	2.07
	201603168	KNB 17	USU 519	0.8	Wygaret / alluvial	3.47E+04	1.5E+03	3.46E+04	320	50	1.88
	201603167	KNB 16	USU 1030	1.5	Wygaret / alluvial	2.67E+04	2.0E+03	2.66E+04	420	70	1.43
	201401589	KNB 15	USU 363	6.1	Wygaret / alluvial	3.26E+04	1.2E+03	3.25E+04	340	50	1.75
5	201600315	JW 20	-	0	Wygaret / alluvial	4.28E+04	2.1E+03		250	40	2.36
	201700342	JW 23	USU 1139	2.23	Wygaret / alluvial	3.58E+04	2.5E+03	3.58E+04	300	50	2.00
6	201603165	JW 24	-	0	White Cliffs / colluvial	1.22E+04	8.6E+02		710	110	.85
	201501035	JW 1	-	0	White Cliffs / alluvial	3.66E+04	2.0E+03		310	50	1.93
	201501036	JW 2	USU 1394	1.91	White Cliffs / alluvial	5.14E+04	2.4E+03	5.13E+04	220	30	2.73
7	201501044	KNB 9	-	0	Skutumpah / alluvial	3.43E+04	1.5E+03		370	50	1.62
	201501047	KNB 25	USU 1428	3.33	Skutumpah / alluvial	3.41E+04	1.6E+03	3.39E+04	370	50	1.62
	201501046	KNB 24	USU 1763	5.3	Skutumpah / alluvial	4.64E+04	2.0E+03	4.60E+04	270	40	2.22
8	201700336	KNB 7	-	0	Skutumpah / alluvial	1.31E+05	3.9E+03		90	10	6.67
	201700339	KNB 8	USU 1474	1.9	Skutumpah / alluvial	3.94E+05	1.5E+04	3.94E+05	30	5	20.00
9	201501039	JW 13	-	0	Skutumpah / alluvial	3.71E+04	1.7E+03		320	50	1.88
	201700335	JW 26	USU 2241	2.24	Skutumpah / alluvial	7.36E+04	6.0E+03	6.44E+04	190	30	3.16
10	201600325	KCW 4	-	0	Skutumpah / alluvial	7.05E+04	2.4E+03		190	30	3.16
	201700331	KCW 11	USU 2243	1.07	Skutumpah / alluvial	3.61E+05	1.6E+04	3.61E+05	35	5	17.05

[1] Erosion rates are rounded to the nearest 10 for erosion rates >100 and to the nearest 5 for erosion rates <100 mm ky^{-1}.
[2] Uncertainties in erosion rates are propagated from AMS uncertainties and include a 10% 1σ uncertainty in nuclide production rates including scaling factors for altitude, latitude, and topographic shielding and a 5% 1σ uncertainty in density, attenuation coefficients, and half-lives. Errors are rounded to the nearest 10 for erosion rates >100 and to the nearest 5 for erosion rates <100.
[3] T_{ave} is the interval of time that the catchment-averaged erosion rate is averaged.

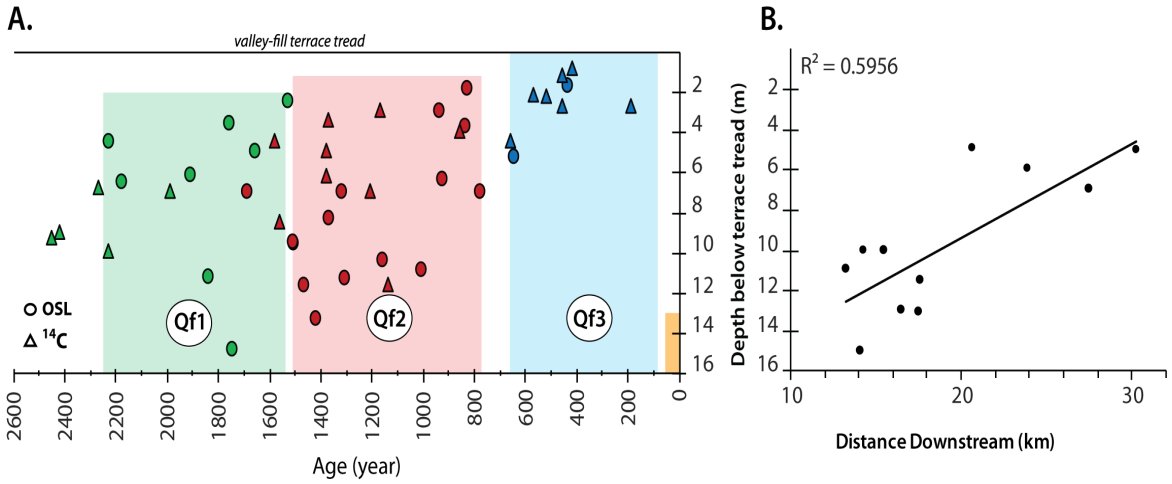

Figure 2-4. A. Scatter plot compares deposit age versus depth below terrace tread. Radiocarbon dates are identified by triangles, OSL ages are identified with circles, and all dates are colored by alluvial-fill package. Note only ages that were interpreted as being accurate were used. B. Scatter plot comparing distance downstream with stratigraphic panel exposure height transformed to depth of channel bottom below terrace tread.

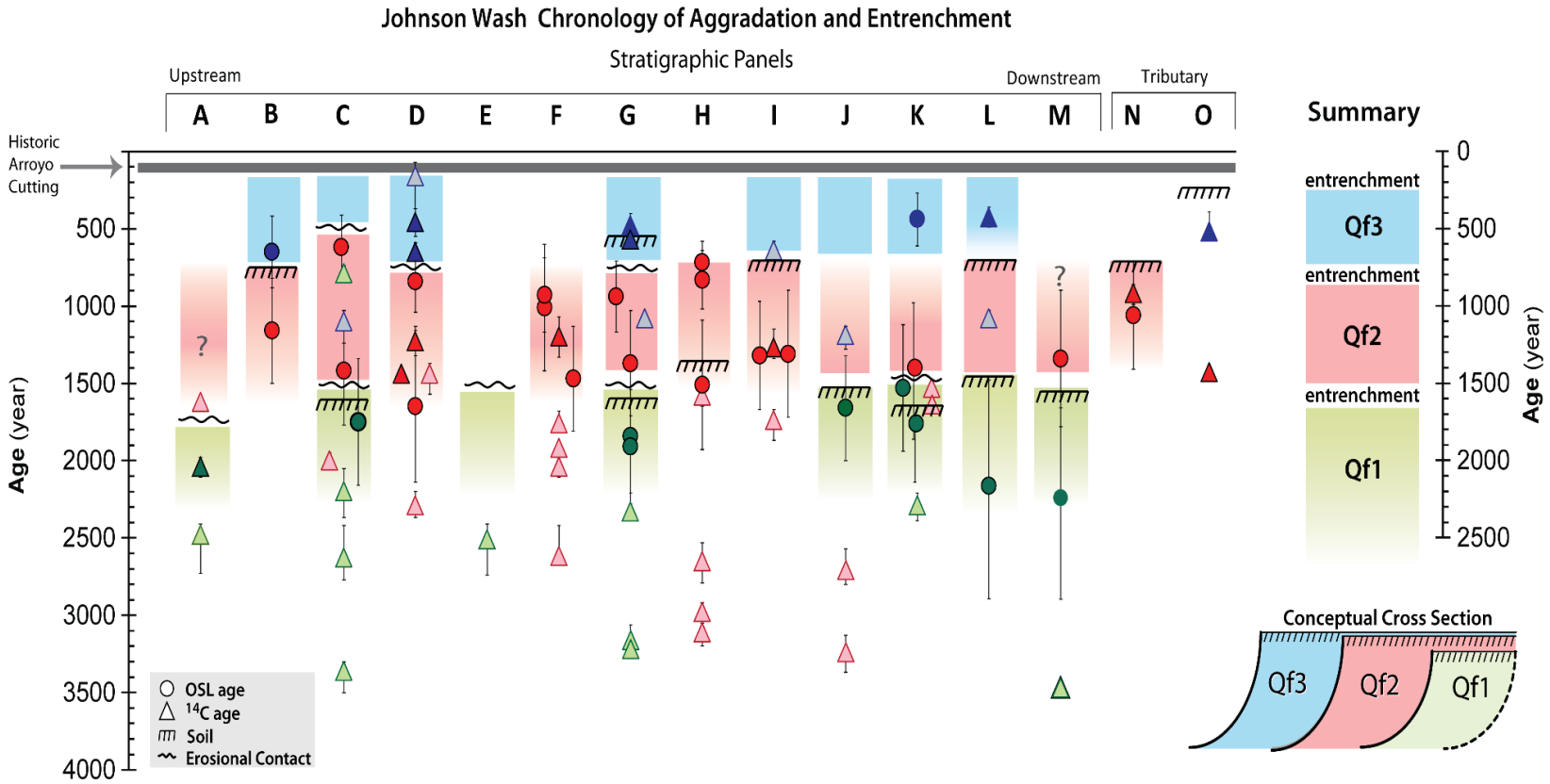

Figure 2-5. Cumulative figure with all OSL and ^{14}C ages plotted with their 2-sigma error for 15 stratigraphic panels. All ages have been converted to years before 2010. Darker, opaque symbols with a black outline represent samples that were interpreted to represent depositional age. Lighter, transparent colored symbols outlined in color are out of stratigraphic order and are interpreted to be the incorrect depositional age of the bed. The color inside each symbol represents the alluvial fill package where the sample was collected.

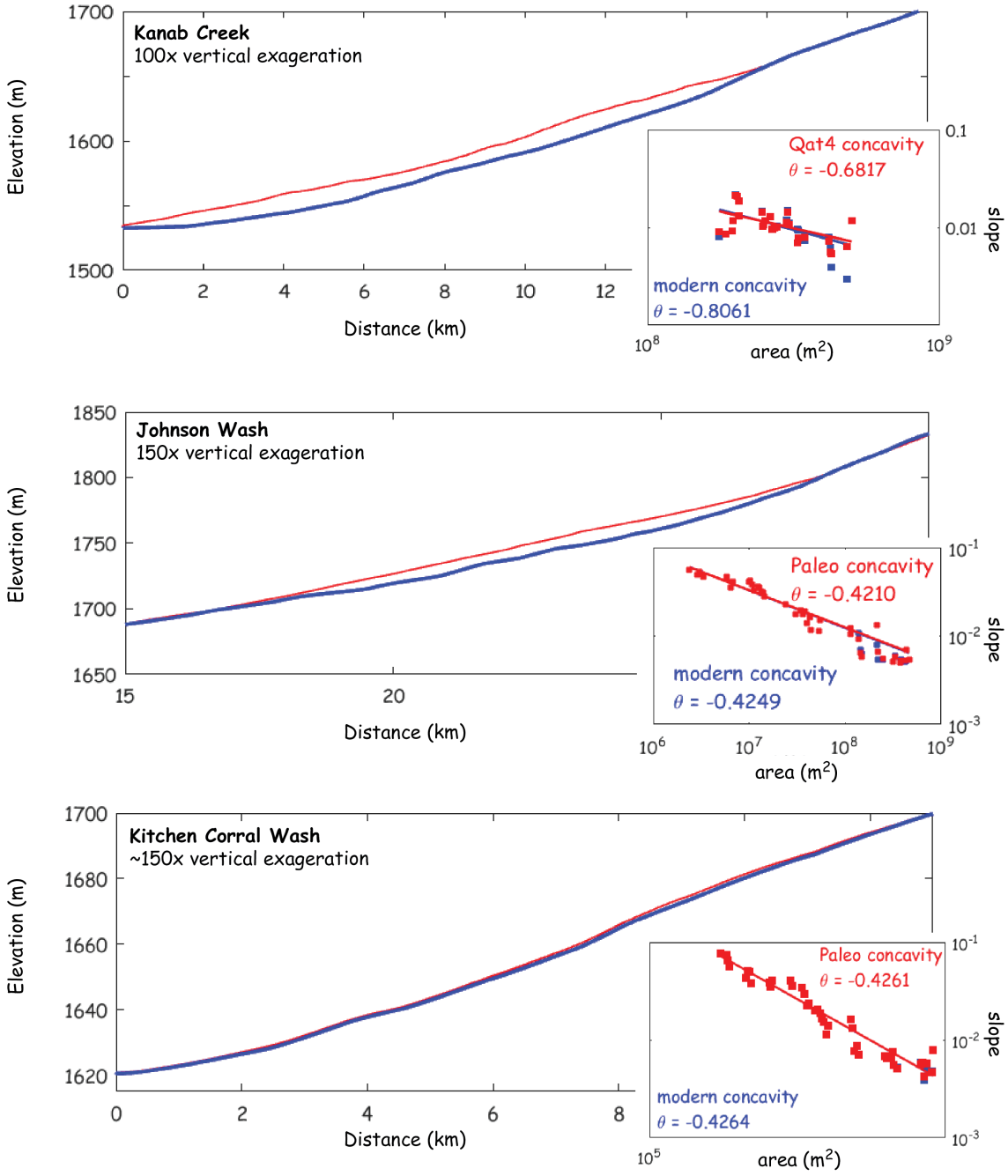

Figure 2-6. Results of the preliminary concavity experiment show a systematic decrease in concavity of the aggraded channel longitude profile.

Discussion

Three periods of aggradation in Johnson Wash are dated to ~2200-1550, 1450-750, and 650-100 ya and constrain two prehistoric entrenchment episodes between 1550-1450 and 750-650 years ago (Figure 2-5). Stream conditions prior to 2200 ya are unknown because older alluvial records were not identified in Johnson Wash. Late Holocene valley aggradation generally took place over 500 to 700 year intervals, while the duration of prehistoric channel entrenchment is constrained to ~100 years; the precision of the timing of entrenchment is limited by the resolution of the dating methods. Sediments preserved in arroyo walls in Johnson Wash and the adjacent watersheds of Kanab Creek and Kitchen Corral Wash record quasi-synchronous (within dating error) fluvial dynamics over the last 2200 years. While three alluvial-fill packages were identified in Johnson Wash and extend to ~2200 years ago, five distinct alluvial fill packages were identified in the two adjacent watersheds of Kanab Creek and Kitchen Corral Wash and extend back in time ~6000 ya (Huff and Rittenour, 2014; Nelson and Rittenour, 2014). The youngest paleo-alluvial-fill package (Qf3; 650-100 yr) in Johnson Wash is synchronous with previously mapped and dated valley-fill alluvium in Kanab Creek, Kitchen Corral Wash, and the main-stem Paria River (Figure 2-6; Hereford, 2002; Huff and Rittenour, 2014; Nelson and Rittenour, 2014; Townsend, 2015). Age control from JW suggests aggradation of the second alluvial-fill package (Qf2) between 1450-750 ya, which is consistent with aggradation in Kanab Creek between1400-800 ya and Kitchen Corral Wash between 1300-800 years ago. The earliest period of aggradation in Johnson Wash (Qf1) was >2200-1550 ya, but the beginning of

aggradation is not well constrained. Kanab Creek aggraded between 2100 and 1450 ya and Kitchen Corral Wash aggraded between 2150 and 1550 ya. Three quaternary-fill-packages dated in Johnson Wash constrain two prehistoric entrenchment periods at 1550-1450 and 750-650 yr and are within 100 years of the timing of entrenchment in the two adjacent basins. Entrenchment events between the two youngest alluvial fills in Kanab Creek are dated to 1450-1400 and 800-750 yr (Summa-Nelson and Rittenour, 2012; Townsend et al., 2019). In Kitchen Corral Wash entrenchment events are similarly dated to 1450–1300 and 800-700 yr (Huff and Rittenour, 2014; Figure 2-6). We consider the alluvial chronologies of Johnson Wash, Kanab Creek, and Kitchen Corral Wash to be quasi-synchronous given the precision of dating techniques and the preservation and exposure of the geologic record.

Hydro-Climate Controls on Entrenchment

A regionally synchronous geomorphic response supports an allogenic (external) forcing of arroyo cut-fill dynamics. Tree-ring derived climate proxies have previously been used to compare the timing of arroyo entrenchment with mean annual precipitation and inferred increased frequency of large floods (Waters and Haynes, 2001; Hereford, 2002). However, the coarse resolution of OSL and radiocarbon dating methods used in alluvial records makes it difficult to compare with the natural variability of annually resolved tree-ring records. Historic channel entrenchment was observed in lower Kanab Creek (1882-1910 CE), upper Kanab Creek (1930-1940 CE), Johnson Wash (~1909-1912

CE), and Kitchen Corral Wash (1880-1920 CE; Webb et al., 1991). Historic arroyo entrenchment corresponded to large floods (Cooke and Reeves, 1976; Webb et al., 1991) and wetter conditions evident in climate proxy records (Figure 2-6). Hydro-climate proxies are paleo-records that can be used to reconstruct water-related climate variables such as stream discharge and precipitation. Discharge is required to entrench an aggraded valley and the timing of quasi-synchronous entrenchment over the last 2200 years generally correspond to reconstructed dry-to-wet hydro-climate variability recorded in hydro-climate proxies. Increased flood frequencies during climate transitions have been previously observed in the mid-west U.S.A. (Knox, 1993). Entrenchment between 800 and 650 ya corresponds to high Colorado River discharge reconstructed using tree rings for Lees Ferry (Meko et al., 2007) and increased ENSO frequency recorded in Laguna Pallcacocha and El Junco Lake (Moy et al., 2002; Conroy et al., 2008) and importantly followed the medieval mega-drought around 900 ya (Meko et al., 2007). The earliest episode of entrenchment (1550-1450 ya) corresponds to a high variability in the average of PDSI gridpoints 87 and 103 values (Cook, 2004; Fig 2-S10) and slightly increased ENSO frequency recorded in El Junco Lake, Galapagos (Conroy et al., 2008). Previous research in New Mexico proposed a causative correlation among ENSO, the strength of the NAM, and cut-fill dynamics in arroyo systems (e.g., Mann and Meltzer, 2007). However, no direct cause and effect relationship has been determined based on paleo climate records due to poor resolution.

Widespread synchronous aggradation between 100-650 and 750-1450 ya are correlative with the Little Ice Age (LIA; ~600-100 yr; Grove, 1988) and the Medieval

Climatic Anomaly (MCA; ~1050-650 cal yr BP; Stine, 1998; Cook et al., 2007). The LIA was a time-period with highly variable hydro-climate in southwest tree-ring records encompassing periods of wet and dry conditions. In contrast, the Medieval Climatic Anomaly was a time characterized by widespread, severe aridity and large decadal to centennial changes in precipitation in the Southwest (Cook et al., 2004; Rasmussen et al., 2006; Jimenez-Moreno et al., 2008). General climate conditions were not consistent between the last two periods of aggradation and suggests aggradation of valley-fills may not be controlled on a first-order by changes in late Holocene climate. While we previously related the timing of entrenchment can be linked to pluvial (wetter) climate conditions that followed drier conditions, entrenchment is not recorded every time hydro-climate transitioned from dry-to-wet. For example, entrenchment did not occur during the extreme climate transitions from drought to pluvial conditions ~480 ya recorded in the Colorado River flow reconstruction (Meko et al., 2007) or ~950 ya recorded in PDSI values (Cook et al., 2004; Figure 2-7). Waters and Haynes (2001) suggest that stratigraphic sequences of arroyo cutting and filling provide excellent paleoclimatic records in desert environments. The alluvial records preserved in arroyo walls suggest that there are complicating factors associated with the lag time required to aggrade the channel to unstable geometries and caution should be applied when using arroyo stratigraphy to infer past climate conditions.

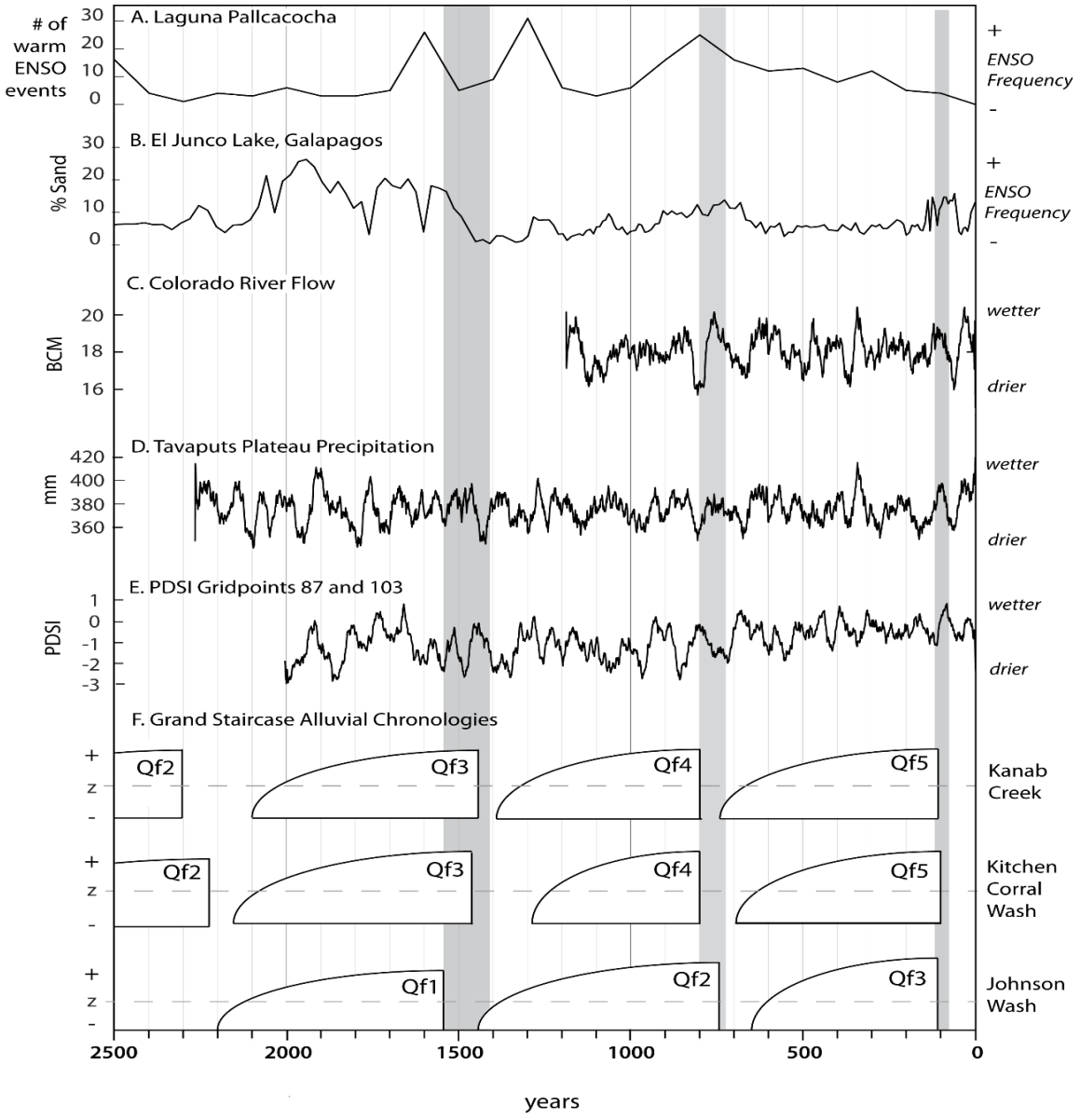

Figure 2-7. Grey bars identify constrained periods of arroyo cutting in adjacent study area catchments. **A)** Laguna Pallcacocha Sediment Color Intensity Data (Moy et al., 2002). **B)** El Junco Lake, Galápagos grain size data (Conroy et al., 2008). **C)** Reconstructed annual flows (BCM = Billion Cubic Meters) of the Colorado River at Lee Ferry with a 30-year moving average (Meko et al., 2007). **D**) Reconstruction of precipitation for the Tavaputs Plateau with a 30-year moving average (Knight et al., 2010). **E)** Average of gridpoints 87 and 103 (Figure 2-S10) PDSI reconstruction with a 30-year moving average (Cook et al., 2004). **F)** Arroyo chronologies for Kanab Creek (Nelson and Rittenour, 2014; Townsend, 2015), Kitchen Corral Wash (Huff and Rittenour, 2014) and Johnson Wash (this study).

Sediment Supply Driven Aggradation

Catchment averaged erosion rates derived from cosmogenic nuclide Beryllium-10 were previously quantified for Holocene-aged sediment samples (n=15) collected from alluvial fill packages in Kanab Creek, Johnson Wash, and Kitchen Corral Wash and from modern stream analogues (n=12) associated with the Holocene deposits and are used here to evaluate temporal changes in sediment supply during the mid- to late-Holocene (Riley et al., 2019; Ch. IV; Table 2-3). Patton and Schumm (1981) suggested channel modification and arroyo cut-fill dynamics are dependent on sediment yields and independent of subtle climate shifts. There was no systematic difference between late Holocene and modern erosion rates (Figure 2-7A). This suggests climate change during the Holocene did not influence the rate sediment was being supplied from hillslopes. However, temporal changes in erosion rates could be deciphered if topographic position within the landscape was considered. In the Vermillion Cliffs, Holocene erosion rates were inconsistent (greater and less than) with modern erosion rates (Figure 2-7B; sample suites 1-3). In the middle of the Wygaret Terrace, Holocene erosion rates were faster than modern erosion rates. At the base of the White Cliffs and on the Skutumpah Terrace, Holocene erosion rates were slower than modern erosion rates.

The source and amount of sediment supply in arroyo systems could vary as a function of channel-bed elevation relative to channel-bank height. The near-channel environment plays a critical role on the sediment supply of streams (Walter and Merritts, 2008; Vaughan et al., 2017). One hypothesis to explain differences between the

cosmogenic signature and inferred ^{10}Be erosion rates in Holocene alluvium and modern channels relates to the contribution of sediment sourced from the nearby arroyo walls versus sediment sourced from distal sources such as exposed bedrock. While modern sediment yields include sediment sourced from throughout the watershed, some proportion of sediment is supplied by collapsing arroyo walls. In this manner, valley-fills are well mixed over the timescale of sediment storage evident in the similar long-term (1000's of years) erosion rates between the modern channel and in different Holocene-aged stored alluvium. As the channel aggrades, the supply of sediment from the bed and banks decrease and sediment supply likely increases from hillslopes and bedrock outcrops. Radiocarbon dated organic material from alluvial sediment found in arroyo walls was highly susceptible to age over-estimation caused by the reworking of charcoal from previously stored sediment and collapsing channel banks. Arroyo walls in Johnson Wash store alluvium for centuries to millennium and channels episodically entrench 10's of meters. While Hereford (2002) suggested hillslope processes were the primary source of alluvium and not the reworking of axial sediments, this study suggests that there is a high degree of reworking and mixing of past alluvial fill sediment. Sediment mixing is evident in the charcoal record, where consistently charcoal in the younger fill package would contain ages that were correlative with the older unconformity bound packages (Figure 2-5). Furthermore, colluvium was observed along the base of modern arroyo walls and at the bases of prehistoric buttress unconformities records collapsing arroyo walls and reworking of previously stored valley-fill alluvium. However, sediment from bank collapse cannot geometrically cause significant channel aggradation. While sediment supplied from bank

collapse does contribute some, it cannot be much in relation to the full arroyo fill package. Sediment supply has been greater than the capacity of the stream during the late Holocene evident in Holocene-aged filled alluvial valleys and arroyo channel forms.

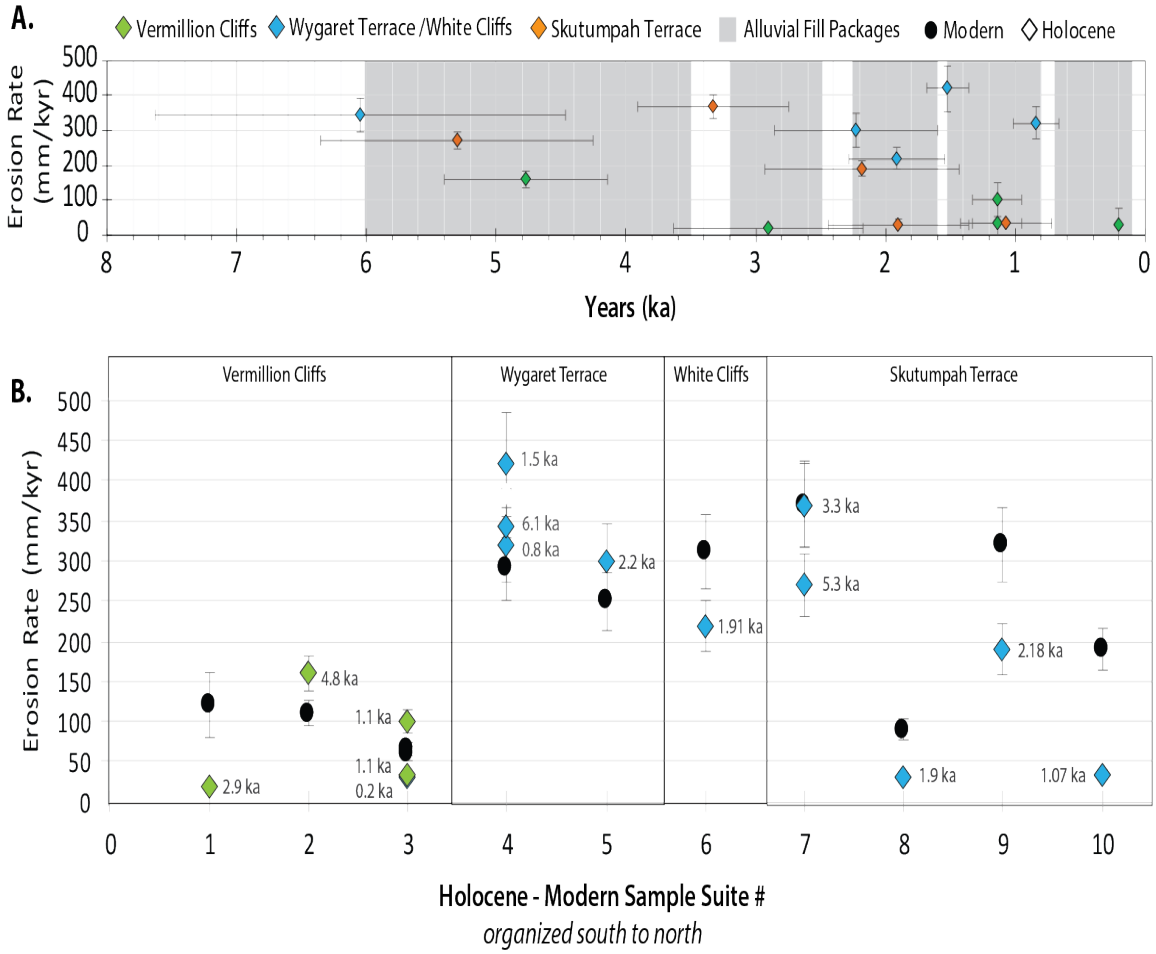

Figure 2-8. A. Erosion rate versus time plot with erosion rates classified by topographic position in the landscape. **B.** Comparison of Holocene and modern samples collected from the same stream reach.

Arroyos and Geomorphic Thresholds

While quasi-synchronous regional arroyo aggradation and entrenchment supports an allogenic driver and a weak relation between climate conditions and the timing of arroyo entrenchment is apparent, there is evidence in support of autogenic controls on arroyo cut-fill dynamics. The modern concavities of the entrenched longitudinal profile of Johnson Wash, Kanab Creek, and Kitchen Corral Wash were greater than the reconstructed concavities of the aggraded channels. Another analysis of the longitudinal profile in Kanab Creek found similar reduction in the concavity for aggraded alluvial fills (Townsend et al., 2019). The height of arroyo walls along the study reach generally decreased downstream, which is related to differences in modern versus pre-entrenchment fill surface concavity. It has been hypothesized that arroyo cut-fill dynamics would occur in semi-arid watersheds that have high sediment supply to discharge ratios without any allogenic forcing such as climate change, due to an inherent instability of aggraded valleys and arroyo landforms (Schumm, 1973; Patton and Schumm, 1975).

The characteristic timing of aggradation (~500 to 700 years; Figure 2-6) observed in regional alluvial records is partially controlled by the sediment yield of the stream. The distribution of slope and different rock types are similar among the three watersheds, which are two dominant controls on erosion rate, sediment supply, and likely aggradation rate. Modern erosion rates were similar for reaches with similar catchment areas and topographic positions among Kanab Creek, Johnson Wash, and Kitchen Corral. Thus, valley fills are reaching critical instability thresholds at similar times recording a quasi-

synchronous geomorphic response.

Autogenic fluctuations in sediment transport and channel form have been observed in other depositional systems such as experimental deltas (e.g., Whipple et al., 1998) and alluvial fans (Bull, 1977). Kim and Jerolmack (2008) describe the autogenic processes of avulsion in an experimental delta and compare these observations to alluvial fans, arroyos, and hillslope channel initiation. Historic observations indicate that the most recent arroyo entrenchment (~1880 ± 30 CE) occurred in response to large floods (Leopold, 1951; Cooke and Reeves, 1976; Graf, 1983; Hereford, 1986; Webb et al., 1991; Webb and Hereford, 2001). While sufficient discharge is required to incise a channel, the timing of arroyo entrenchment may also be closely tied to preconditions of channel slope, rather than solely on the frequency, magnitude, and duration of discharge events. In order for an arroyo to become entrenched, aggraded arroyo systems require threshold slopes in addition to stream power to transport sediment and incise the streambed.

Greater sediment deposition and aggradation at the bottom of the stream reach may be related to the effects of downstream attenuation of discharge due to infiltration into the channel bed reducing stream power. Schumm and Hadley (1957) proposed a model where the loss of discharge through channel-bed infiltration promoted aggradation, which steepened the gradient, and caused incision. Aggradation decreases channel concavity (Figure 2-4C) and increases slope to a geomorphic threshold; when approached or crossed the channel becomes unstable and results in entrenchment when adequate discharge is applied. In this sense, the absolute magnitude of discharge events that drive arroyo entrenchment is less important than the preceding conditions of stream grade.

Conclusions

The alluvial chronology preserved in Johnson Wash records three periods of aggradation (~2200-1550, 1450-750, and 650-100 ya) and constrain two prehistoric entrenchment episodes (1550-1450 and 750-650 ya). Stratigraphic records from three adjacent drainages (Kanab Creek, Johnson Wash, and Kitchen Corral Wash) all show primarily aggradational conditions during the last 2200 years. Consistent high sediment supply produced by high erosion rates of retreating bedrock escarpments throughout the Holocene combined with limited transport capacity (low discharge) of seasonally flashy watersheds results in a channel landform that undergoes episodic instability over 10^2-10^3 year timescales. Discharge is required to entrench aggraded valley-fills and the timing of regional entrenchment over the last 2200 roughly corresponds to dry-to-wet hydro-climate variability. This study also highlights a potential role of a threshold slope that is approached with a decrease in the concavity of the longitudinal profile as the channel bed aggrades.

Acknowledgments

I would like to thank John Southon for expertise, access, and measurements from the W. M. Keck Carbon Cycle Accelerator Mass Spectrometry Laboratory at the University of California, Irvine. I would also like to than Michelle Nelson and Carlie Idecker for expertise, access, and measurements from the Optically Luminescence

Laboratory at Utah State University. This research was primarily supported by the NSF Career Grant EAR-1057192 awarded to Tammy Rittenour. Additional funding was provided by the Utah State Ecology Center, Geologic Society of America, and Utah State Optically Stimulated Luminescence Lab awarded to Kerry Riley.

References Cited

Adams, D. K., and Comrie, A. C., 1997, The North American monsoon: Bulletin of the American Meteorological Society, v. 78, no. 10, p. 2197-2213.

Aitken, M.J., 1998. Introduction to optical dating: the dating of Quaternary sediments by the use of photon-stimulated luminescence. Clarendon Press.

Aitken, M.J. and Xie, J., 1992. Optical dating using infrared diodes: young samples. Quaternary Science Reviews, 11(1-2), p.147-152.

Antevs, E. V., 1952, Arroyo-cutting and filling: Journal of Geology, v. 60, no. 4, p. 375-385.

Bailey, R. W., 1935, Epicycles of Erosion in the Valleys of the Colorado Plateau Province: The Journal of Geology, v. 43, no. 4, p. 337-355.

Bryan, K., 1925, Date of Channel Trenching (Arroyo Cutting) in the Arid Southwest: Science, v. 62, no. 1607, p. 338-344.

Bryan, K. 1928. Change in plant association by change in ground water level. Ecology 9:474-478.

Bryan, K, 1941, Correlation of the deposits of Sandia Cave, New Mexico, with the glacial chronology, Smithsonian Institution.

Bull, W. B., 1997, Discontinuous ephemeral streams: Geomorphology, v. 19, no. 3–4, p. 227-276.

Calkins, H. G., 1941, Man and gullies: New Mexico Quarterly, v. 11, no. 1, p. 8.

Carroll, E. C., 1960, History of Kane County, Kane County Daughters of Utah Pioneers.

Cayan, D. R., Redmond, K. T., and Riddle, L. G., 1999, ENSO and hydrologic extremes in the western United States: Journal of Climate, v. 12, no. 9, p. 2881-2893.

Conroy, J. L., Overpeck, J. T., Cole, J. E., Shanahan, T. M., and Steinitz-Kannan, M., 2008, Holocene changes in eastern tropical Pacific climate inferred from a Galápagos lake sediment record: Quaternary Science Reviews, v. 27, no. 11–12, p. 1166-1180.

Cook, E. R., Seager, R., Cane, M. A., and Stahle, D. W., 2007, North American drought: Reconstructions, causes, and consequences: Earth-Science Reviews, v. 81, no. 1, p. 93-134.

Cook, E. R., Woodhouse, C. A., Eakin, C. M., Meko, D. M., and Stahle, D. W., 2004, Long-term aridity changes in the western United States: Science, v. 306, no. 5698, p. 1015-1018.

Cooke, R. U., and Reeves, R. W., 1976, Arroyos and environmental change: Clarendon, Oxford.

Cooley, M. E., 1962, Late Pleistocene and recent erosion and alluviation in parts of the Colorado River system, Arizona and Utah: US Geological Survey Professional Paper, p. B48-B50.

Cooperrider, C. K., and Hendricks, B. A., 1937, Soil erosion and stream flow on range and forest lands of the upper Rio Grande watershed in relation to land resources and human welfare: United States Department of Agriculture, Economic Research Service.

Daniels, J. M., 2008, Distinguishing allogenic from autogenic causes of bed elevation change in late Quaternary alluvial stratigraphic records: Geomorphology, v. 101, no. 1–2, p. 159-171.

Davies, T. R., and Korup, O., 2010, Sediment cascades in active landscapes: Sediment Cascades: An Integrated Approach, p. 89-115.

Dellenbaugh, F. S., 1908, A canyon voyage: The narrative of the second Powell expedition down the Green-Colorado River from Wyoming, and the explorations on land, in the years 1871 and 1872, University of Arizona Press.

Denevan, W. M., 1967, Livestock numbers in nineteenth-century New Mexico, and the problem of gullying in the Southwest: Annals of the Association of American Geographers, v. 57, no. 4, p. 691-703.

Diffenbaugh, N. S., 2005, Sensitivity of extreme climate events to CO2-induced biophysical atmosphere-vegetation feedbacks in the western United States: Geophysical Research Letters, v. 32, no. 7.

Dodge, R. E., 1902, Arroyo formation: Science, v. 15, p. 746.

Duller, G. A., 2008, Single-grain optical dating of Quaternary sediments: why aliquot size matters in luminescence dating: Boreas, v. 37, no. 4, p. 589-612.

Dutton, C. E., 1882. Tertiary history of the Grand Canyon district. American Journal of Science, (140), 81-89.

Galbraith, R., and Roberts, R. G., 2012, Statistical aspects of equivalent dose and error calculation and display in OSL dating: an overview and some recommendations: Quaternary Geochronology, v. 11, p. 1-27.

Gavin, D. G., 2001, Estimation of inbuilt age in radiocarbon ages of soil charcoal for fire history studies: Radiocarbon, v. 43, no. 1, p. 27-44.

Gilbert, G. K., 1877. Geology of the Henry mountains (pp. i-160). Government Printing Office.

Graf, W. L., 1983. The arroyo problem—palaeohydrology and palaeohydraulics in the short term. In *Background to palaeohydrology. A perspective* (pp. 279-302).

Graf, W. L., 1985, The Colorado River: Instability and basin management: Association of American geographers, Washington, DC (USA).

Graf, W. L., 1987, Late Holocene sediment storage in canyons of the Colorado Plateau: Geological Society of America Bulletin, v. 99, no. 2, p. 261-271.

Gregory, H. E., 1945, Population of Southern Utah: Economic Geography, v. 21, no. 1, p. 29-57.

Gregory, H. E., 1950, Geology and Geography of the Zion Park Region, Utah and Arizona... a Comprehensive Report on a Scenic and Historic Region of the Southwest, US Government Printing Office.

Grove, J. M., 1988, The Little Ice Age: New York, Methuen.

Hack, J. T., 1939, The Late Quaternary History of Several Valleys of Northern Arizona: A Preliminary Announcement, Museum of Northern Arizona.

Hack, J. T., 1942, The changing physical environment of the Hopi Indians of Arizona, The Museum, v. 1.

Hall, S. A., 1977, Late quaternary sedimentation and paleoecologic history of Chaco Canyon, New Mexico: Geological Society of America Bulletin, v. 88, no. 11, p. 1593-1618.

Harvey, J. E., Pederson, J. L., and Rittenour, T. M., 2010, The alluvial records of Buckskin Wash, Utah, *in* Carney, S. M., Tabet, D.E. and Johnson, C.L., ed., Utah Geological Association Publication, Volume 39, Utah Geological Association, p. 19-37.

Harvey, J. E., Pederson, J. L., and Rittenour, T. M., 2011, Exploring relations between arroyo cycles and canyon paleoflood records in Buckskin Wash, Utah: Reconciling scientific paradigms: Geological Society of America Bulletin, v. 123, no. 11-12, p. 2266-2276.

Hereford, R., 1986, Modern alluvial history of the Paria Rver drainage basin, southern Utah: Quaternary Research, v. 25, no. 3, p. 293-311.

Hereford, R., 2002, Valley-fill alluviation during the Little Ice Age (ca. AD 1400-1880), Paria River basin and southern Colorado Plateau, United States: Geological Society of America Bulletin, v. 114, no. 12, p. 1550-1563.

Hereford, R., Jacoby, G. C., and McCord, V. A. S., 1996, Late Holocene Alluvial Geomorphology of the Virgin River in the Zion National Park Area, Southwest Utah: Geological Society of America Special Papers, v. 310, p. 1-41.

Huff, W., and Rittenour, T., 2014, Holocene alluvial stratigraphy of Kitchen Corral Wash, southern Utah, *in* MacLean, J. S., Biek, R.F., and Huntoon, J.E., ed., Geology of Utah's Far South: Utah Geological Association Publication 43, p. 77–96.

Huff, W. M., 2013, A middle to late Holocene record of arroyo cut-fill events in Kitchen Corral Wash, southern Utah [M.S.: Utah State University, 194 p.

Huntington, E., Schuchert, C., Douglass, A. E., and Kullmer, C. J., 1914, The climatic factor as illustrated in arid America, Carnegie institution of Washington, v. 192.

Huntley, D. J., Godfreysmith, D. I., and Thewalt, M. L. W., 1985, Optical dating of sediments: Nature, v. 313, no. 5998, p. 105-107.

Jain, M., Thomsen, K. J., Bøtter-Jensen, L., and Murray, A. S., 2004, Thermal transfer and apparent-dose distributions in poorly bleached mortar samples: results from single grains and small aliquots of quartz: Radiation Measurements, v. 38, no. 1, p. 101-109.

Jimenez-Moreno, G., Fawcett, P. J., and Anderson, R. S., 2008, Millennial- and centennial-scale vegetation and climate changes during the late Pleistocene and Holocene from northern New Mexico (USA): Quaternary Science Reviews, v. 27, no. 13-14, p. 1442-1452.

Kerr, R., 2008, Climate change hot spots mapped across the United States: Science, v. 321, no. 5891, p. 909-909.

Kim, W., and Jerolmack, D. J., 2008, The Pulse of Calm Fan Deltas: The Journal of Geology, v. 116, no. 4, p. 315-330.

Knight, T. A., Meko, D. M., and Baisan, C. H., 2010, A bimillennial-length tree-ring reconstruction of precipitation for the Tavaputs Plateau, Northeastern Utah: Quaternary Research, v. 73, no. 1, p. 107-117.

Knox, J. C., 1993, Large increases in flood magnitude in response to modest changes in climate: Nature, v. 361, no. 6411, p. 430-432.

Leopold, L. B., 1951, Rainfall frequency: an aspect of climatic variation, American Geophysical Union.

Leopold, L. B., and Bull, W. B., 1979, Base level, aggradation, and grade: Proceedings of the American Philosophical Society, p. 168-202.

Lewis, W., 1944, Stream trough experiments and terrace formation: Geological Magazine, v. 81, no. 06, p. 241-253.

Mackin, J. Hoover (1948). Concept of the graded river. Geological Society of America Bulletin, 59(5), 463-512.

Mann, D. H., and Meltzer, D. J., 2007, Millennial-scale dynamics of valley fills over the past 12,000 14C yr in northeastern New Mexico, USA: Geological Society of America Bulletin, v. 119, no. 11-12, p. 1433-1448.

Meko, D. M., Woodhouse, C. A., Baisan, C. A., Knight, T., Lukas, J. J., Hughes, M. K., and Salzer, M. W., 2007, Medieval drought in the upper Colorado River Basin: Geophysical Research Letters, v. 34, no. 10, p. L10705.

Miall, M. 1996. The geology of fluvial deposits. p. 582.

Moy, C. M., Seltzer, G. O., Rodbell, D. T., and Anderson, D. M., 2002, Variability of El Niño/Southern Oscillation activity at millennial timescales during the Holocene epoch: Nature, v. 420, no. 6912, p. 162-165.

Murray, A.S. and Wintle, A.G., 2000. Luminescence dating of quartz using an improved single-aliquot regenerative-dose protocol. Radiation measurements, 32(1), pp.57-73.

Nelson, M. S., and Rittenour, T., 2014, Middle to late Holocene chronostratigraphy of alluvial fill deposits along Kanab Creek in southern Utah: Geology of Utah's Far South: Utah Geological Association, Publication, v. 43, p. 97-116.

Olley, J., Caitcheon, G., and Murray, A., 1998, The distribution of apparent dose as determined by optically stimulated luminescence in small aliquots of fluvial quartz: Implications for dating young sediments: Quaternary Science Reviews, v. 17, no. 11, p. 1033-1040.

Patton, P. C., and Schumm, S. A., 1975, Gully erosion, Northwestern Colorado - threshold phenomenon Geology, v. 3, no. 2, p. 88-90.

Patton, P. C., & Schumm, S. A. (1981). Ephemeral-stream processes: Implications for studies of Quaternary valley fills. Quaternary Research, 15(1), p. 24-43.

Prescott, J.R. and Hutton, J.T., 1994. Cosmic ray contributions to dose rates for luminescence and ESR dating: large depths and long-term time variations. Radiation measurements, 23(2-3), p. 497-500.

Rasmussen, J. B., Polyak, V. J., and Asmerom, Y., 2006, Evidence for Pacific-modulated precipitation variability during the late Holocene from the southwestern USA: Geophysical Research Letters, v. 33, no. 8.

Reimer, P. J., Baillie, M. G. L., Bard, E., Bayliss, A., Beck, J. W., Bertrand, C. J. H., Blackwell, P. G., Buck, C. E., Burr, G. S., Cutler, K. B., Damon, P. E., Edwards, R. L., Fairbanks, R. G., Friedrich, M., Guilderson, T. P., Hogg, A. G., Hughen, K. A., Kromer, B., McCormac, G., Manning, S., Ramsey, C. B., Reimer, R. W., Remmele, S., Southon, J. R., Stuiver, M., Talamo, S., Taylor, F. W., van der Plicht, J., and Weyhenmeyer, C. E., 2004, IntCal04 terrestrial radiocarbon age calibration, 0-26 cal kyr BP: Radiocarbon, v. 46, no. 3, p. 1029-1058.

Reimer, P. J., Bard, E., Bayliss, A., Beck, J. W., Blackwell, P. G., Ramsey, C. B., Buck, C. E., Cheng, H., Edwards, R. L., and Friedrich, M., 2013, IntCal13 and Marine13 radiocarbon age calibration curves 0–50,000 years cal BP: Radiocarbon, v. 55, no. 4, p. 1869-1887.

Riley, K. E., Rittenour, T. M., Pederson, J. L., and Belmont, P., 2019, Erosion rates and patterns in a transient landscape, Grand Staircase, southern Utah, USA: Geology.

Rittenour, T. M., 2008, Luminescence dating of fluvial deposits: applications to geomorphic, palaeoseismic and archaeological research: Boreas, v. 37, no. 4, p. 613-635.

Robinson, A., 1972, Romance of a church farmhouse: Kane County, Utah: Salt Lake City, The Utah Printing Company, p. 48.

Schlesinger, W. H., Reynolds, J. F., Cunningham, G. L., Huenneke, L. F., Jarrell, W. M., Virginia, R. A., and Whitford, W. G., 1990, Biological feedbacks in global desertification: Science, v. 247, no. 4946, p. 1043-1048.

Schumm, S., 1973, Geomorphic thresholds and complex response of drainage systems: Fluvial geomorphology, v. 6, p. 69-85.

Schumm, S. A., and Hadley, R. F., 1957, Arroyos and the semiarid cycle of erosion [Wyoming and New Mexico]: American Journal of Science, v. 255, no. 3, p. 161-174.

Schumm, S. A., and Parker, R. S., 1973, Implications of Complex Response of Drainage Systems for Quaternary Alluvial Stratigraphy: Nature physical science, v. 253, no. 128, p. 99-100.

Schwanghart, W., and Scherler, D., 2014, Short Communication: TopoToolbox 2–MATLAB-based software for topographic analysis and modeling in Earth surface sciences: Earth Surface Dynamics, v. 2, no. 1, p. 1-7.

Sheppard, P. R., Comrie, A. C., Packin, G. D., Angersbach, K., and Hughes, M. K., 2002, The climate of the US Southwest: Climate Research, v. 21, no. 3, p. 219-238.

Smith, S., 1990, Large floods and rapid entrenchment Kanab Creek, southern Utah [MS Thesis]: University of Arizona, 82 p. p.

Stine, S., 1998. Medieval climatic anomaly in the Americas. In Water, Environment and Society in Times of Climatic Change, p. 43-67.

Summa-Nelson, M. C., and Rittenour, T. M., 2012, Application of OSL dating to middle to late Holocene arroyo sediments in Kanab Creek, southern Utah, USA: Quaternary Geochronology, v. 10, p. 167-174.

Summa, M., 2009, Geologic mapping, alluvial stratigraphy, and Optically Stimulated Luminescence dating of the Kanab Creek area, southern Utah [MS: Utah State University, 184 p.

Townsend, K. F., 2015, A Chronostratigraphic Record of Arroyo Entrenchment and Aggradation in Kanab Creek, Southern Utah.

Townsend, K. F., Nelson, M. S., Rittenour, T. M., and Pederson, J. L., 2019, Anatomy and evolution of a dynamic arroyo system, Kanab Creek, southern Utah, USA: Geological Society of America Bulletin.

Tucker, G. E., Arnold, L., Bras, R. L., Flores, H., Istanbulluoglu, E., and Sólyom, P., 2006, Headwater channel dynamics in semiarid rangelands, Colorado high plains, USA: Geological Society of America Bulletin, v. 118, no. 7-8, p. 959-974.

Vaughan, A. A., Belmont, P., Hawkins, C. P., and Wilcock, P., 2017, Near-Channel Versus Watershed Controls on Sediment Rating Curves: Journal of Geophysical Research: Earth Surface.

Wallinga, J., 2002, Optically stimulated luminescence dating of fluvial deposits: a review: Boreas, v. 31, no. 4, p. 303-322.

Walter, R. C., and Merritts, D. J., 2008, Natural Streams and the Legacy of Water-Powered Mills: Science, v. 319, no. 5861, p. 299-304.

Waters, M. R., and Haynes, C. V., 2001, Late Quaternary arroyo formation and climate change in the American Southwest: Geology, v. 29, no. 5, p. 399-402.

Webb, R., and Hereford, R., 2001. Floods and geomorphic change in the southwestern United States: an historical perspective, *in* Proceedings Proceedings of the seventh federal interagency sedimentation conference, p. 25-29.

Webb, R. H., 1985, Late Holocene flooding on the Escalante River, south-central Utah [Ph.D. Dissertation: The University of Arizona., 204 p.

Webb, R. H., and Baker, V. R., 1987. Changes hydrologic conditions related to large floods on the Escalante River, south-central Utah, *in* Proceedings International symposium on flood frequency and risk analyses, p. 309-323.

Webb, R. H., Smith, S. S., and McCord, V. A., 1991, Historic channel change of Kanab Creek, Southern Utah and Northern Arizona: Grand Canyon, Natural History Association Monograph.

Whipple, K. X., Parker, G., Paola, C., and Mohrig, D., 1998, Channel dynamics, sediment transport, and the slope of alluvial fans: experimental study: The Journal of Geology, v. 106, no. 6, p. 677-694.

Woolley, R. R., Marsell, R. E., and Grover, N. C., 1946, Cloudburst floods in Utah, 1850-1938, US Government Printing Office.

Supplemental Material

Table 2-S1. Locations for the 15 stratigraphic panels described and dated in this study.

ID	Stratigraphic Panel Name	Latitude	Longitude	Elevation (m ASL)	Exposure Height (m)
A	Thompson Creek (tributary)	37.33053	-112.37371	1950	10.5
B	Upper Skutumpah	37.24728	-112.35521	1770	11
C	Middle Skutumpah	37.24154	-112.35978	1760	15
D	Lower Skutumpah	37.24049	-112.36064	1755	10
E	Half-Cut Skutumpah	37.24049	-112.36064	1750	10
F	Basalt Junction	37.23106	-112.36467	1745	13
G	Where the Basalt Ends (WTBE)	37.22302	-112.36850	1735	11.5
H	Upper Right WTBE	37.22396	-112.36855	1730	13.1
I	Lower Right WTBE	37.22312	-112.36949	1730	11.5
J	Above Dam	37.20069	-112.37725	1705	5
K	Below Dam	37.17746	-112.38585	1685	6
L	Bedrock	37.15202	-112.39815	1660	7
M	Holland Ranch	37.13059	-112.39248	1645	5.1
N	Swapp Creek (tributary)	37.21234	-112.39381	1795	5
O	Cottonwood Creek (tributary)	37.23130	-112.33472	1740	4

Facies Code	Facies and Sedimentary Structures	Interpretation	Examples
Gmm	matrix-supported, massive gravel	plastic debris flow (high strength, viscous)	
St	trough cross-bedded sand (may be pebbly)	sinuously crested and linguid (3D dunes)	
Sp	planar cross-bedded sand (may be pebbly)	transverse and linguid bedforms (2D dunes)	
Sr	ripple cross-laminated sand	ripples (lower flow regime)	
Sh	horizontal laminated sand (may be pebbly)	plane bed flow (critical flow)	
Sl	low-angle (< 15 deg) cross-bedded sand (may be pebbly)	scour fills, humpback or washed-out dunes, antidunes	
Sm	massive or faintly laminated sand	sediment gravity flow deposits	
Fl	finely laminated, very small rippled sand, silt, and mud	overbank, abandoned channel, or waning flood deposits	
Fsmv	variegated silt and mud	back swamp or abandoned channel deposits	
Fm	massive mud and silt with desiccation cracks	overbank, abandoned channel, or drape deposits	
C	colluvial wedge with upturned blocks of alluvium	collapse of channel banks (arroyo walls)	
P	paleosol with pedogenic features or massive	soil	

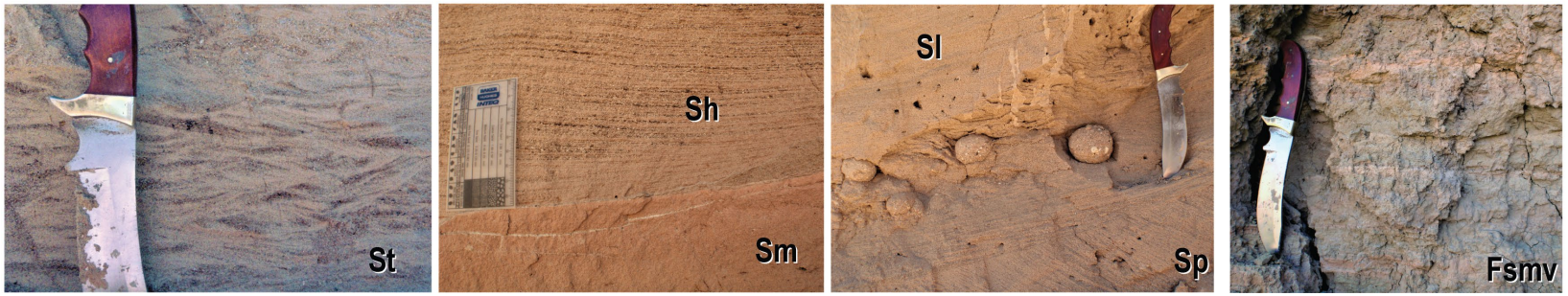

Figure 2-S1. Facies classification for fluvial deposits (modified from Miall, 1996).

Stratigraphic Descriptions

Johnson Wash is the largest tributary to Kanab Creek. The confluence is located in northern Arizona south of Fredonia. This study takes place in the headwaters of Johnson Wash north of US Highway (HW) 89 (Figure 2-1 in the main text). Most of the stratigraphic panels described and dated in this study are located on the Wygaret Terrace located between the White Cliffs and HW 89. One stratigraphic panel is located above the White Cliffs and Grey Cliffs on the Podunk Terrace. The following stratigraphic descriptions are listed from upstream to downstream and the two tributary panels are described last.

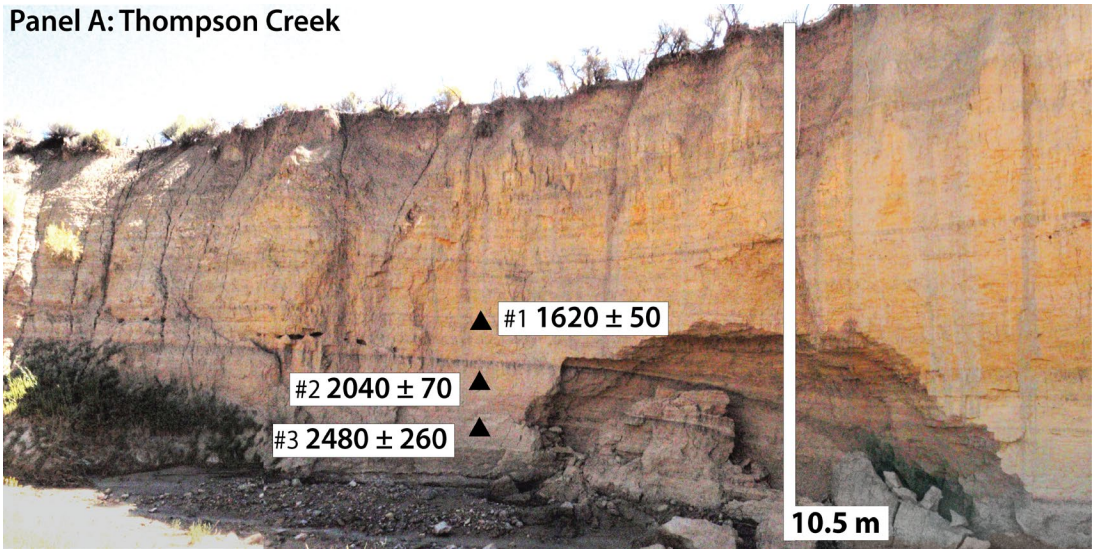

Figure 2-S2 – Photograph of stratigraphic panel A in Thompson Creek. Black triangles are dated radiocarbon samples in calibrated years BP with the present being 2010.

Panel A: Thompson Creek

Stratigraphic panel A (Figure 2-S2) was located on Thompson Creek on the Podunk Terrace (referring to the topographic bench of the Grand Staircase) between the Pink Cliffs and the Grey Cliffs (Figure 2-1 in the main text). Thompson Creek is a headwater tributary of Johnson Wash and is the location of the farthest upstream stratigraphic panel in this study. The exposure is approximately 10.5 meters high and contains two alluvial packages separated by a ~3.5 m-tall buttress unconformity shown in the bottom of the panel. This panel was sampled to provide a preliminary age of fill on the Skutumpah Terrace and was not revisited to complete full description. Charcoal (#1, #2, and #3) was collected at the base of the profile above and below the unconformity. Radiocarbon results produce two ages associated with the older alluvial-fill package (Qf1) of 2480 and 2040 cal ya BP_{2010} and the younger alluvial-fill (Qf2) was 1620 cal ya BP_{2010}. These data bracket the timing of the unconformity to between 1650 and 2000 cal ya BP_{2010}. The interpretation of the alluvial chronology of this panel is limited because only one dating method was applied.

Skutumpah Canyon

Thompson Creek, Skutumpah Creek, and Red Wash come together above the White Cliffs and descend through the White Cliffs through Skutumpah Canyon. The canyon walls are formed by the White Cliffs, where vertical cliffs of Navajo Sandstone constrict the width of valley-fill alluvium to 100-300 m wide (Figure 2-S3). One continuous alluvial-fill terrace is observed in this valley and the modern stream is entrenched 10-15 meters. Four stratigraphic panels (B, C, D, and E) were described and dated in this reach.

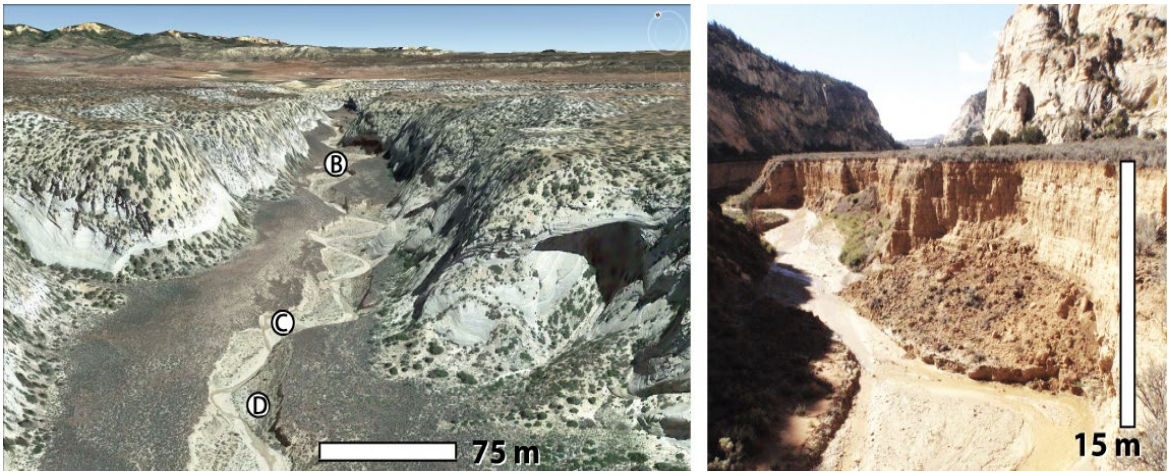

Figure 2-S3. (Left) Google Earth image looking upstream of Skutumpah Canyon. The locations of three stratigraphic profiles identified. The Pink Cliffs can be seen on the distant horizon. (Right) Photograph illustrating the depth of alluvium that fills Skutumpah Canyon

Panel B: Upper Skutumpah Canyon

Stratigraphic panel B (Figure 2-S4) was the farthest upstream panel in the Skutumpah Canyon reach of Johnson Wash (Figure 2-S3). The 10.4 m high profile was composed of horizontally bedded units and contained two weakly developed buried soils around 6 m and 8.3 m below the terrace tread. The buried soils were identified by weak pedogenic structure, calcium carbonate precipitation, and oxidation. Sedimentary faces included variegated silt and mud, finely laminated rippled sand, silt and clay, trough cross-bedded sands with pebbles, and ripple cross-bedded sands. Two OSL samples (USU 1334 and USU 1335) date the timing of aggradation below and above the buried soils. The OSL sample from below the unconformity produced an age of 1160 ± 340 ya and the overlying sample was 650 ± 230 ya. The base of the arroyo walls were covered with colluvium.

Stratigraphic panel C (Figure 2-3 in the main text) was located on the west side of the stream in the constricted Skutumpah Canyon reach of Johnson Wash (Figure 2-S3). The 15-meter-high profile contained three unconformity-bound packages of alluvium identified as Qf1, Qf2, and Qf3 from oldest to youngest. The oldest exposed and dated package (Qf1) was located in the downstream section of the exposure. One OSL sample (USU 1679) was collected from 14.8 m below the terrace tread and was 1750 ± 410 ya. One radiocarbon sample (#10) also collected from the base around 14.8 meters was anomalously young at 790 ± 50 cal ya BP_{2010}. The age inversion was interpreted to be a result of deposition in an undercut bank. Two replicate radiocarbon samples (#7 and #8) were collected from the top of the profile above the soil horizon in the oldest package. The

charcoal ages were 2630 ± 150 and 2200 ± 170 cal yr BP_{2010} and were interpreted as being redeposited from previously stored alluvium.

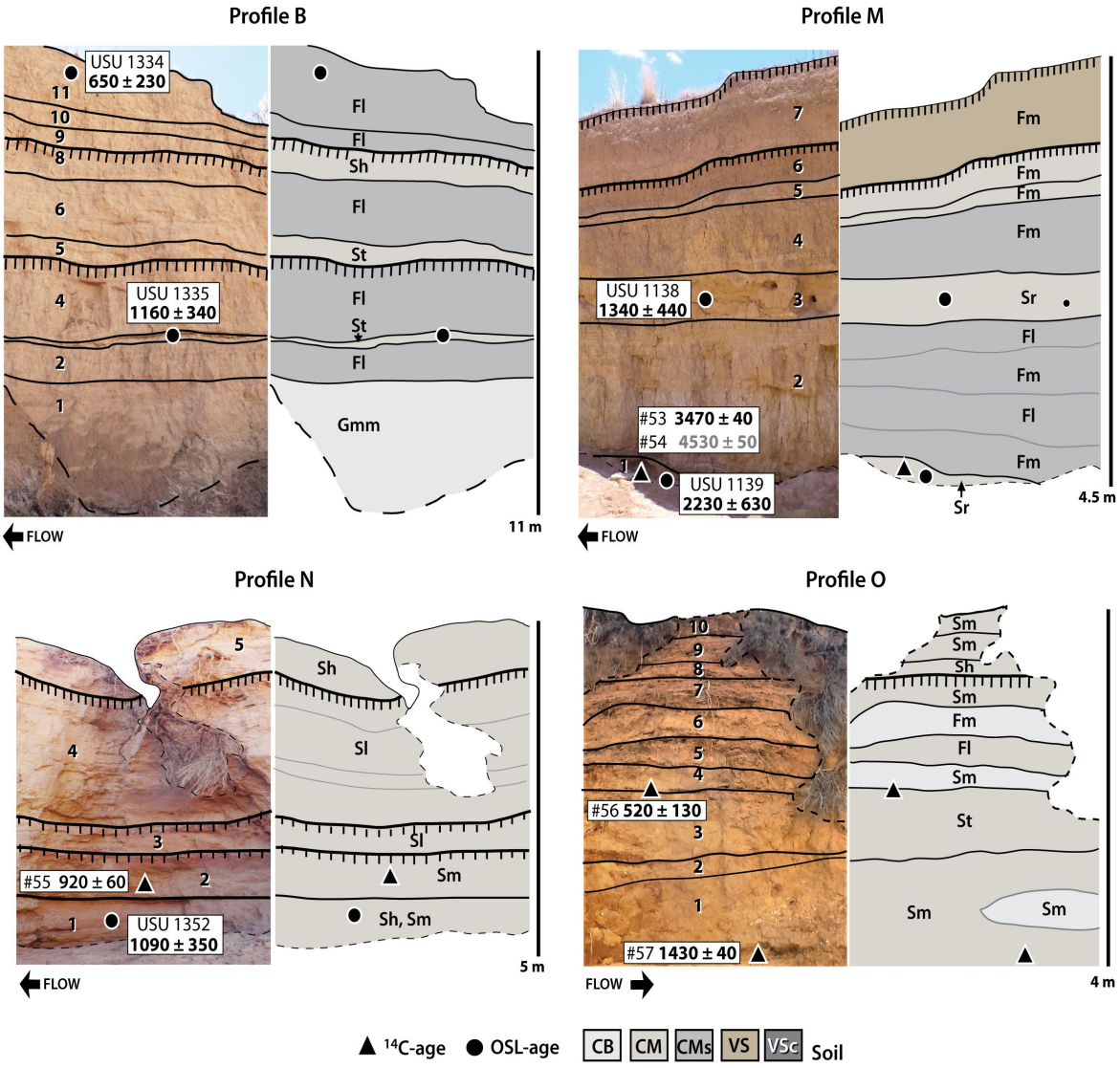

Figure 2-S4. Stratigraphic profiles B, M, N, and O show generally tabular bedding, horizontally bedded, sand and fine-grained facies with weak buried soils.

Panel C: Middle Skutumpah Canyon

An unconformity abuts the oldest package upstream and appears to extend from a few meters below the terrace tread to the base of the exposure (15-m-depth) where the arroyo wall is covered with colluvium. A paleo colluvial wedge also abuts the unconformity (unit 8). The alluvial package upstream of the unconformity consists primarily of channel deposits and contains both lenticular and horizontally bedded low-angle and tough cross-bedded sands. One OSL-age (USU 1680) at the base of the package produced an age of 1420 ± 350 ya. Two radiocarbon ages were analyzed from the base of the package; one resulted in an age of 32,900 C_{14} ya and was interpreted to be contaminated with coal (#5) and the other resulted in an age of 2000 ± 50 cal ya BP_{2010} (#6). The 2000-year radiocarbon age was interpreted as being a redeposited piece of charcoal and the OSL age was interpreted as being accurate. The timing of incision between the deposition of Qf3 and Qf2 is constrained to between 1850 and 1350 ya in this stratigraphic panel.

A potential unconformity upstream of this package was identified by the presence of up-turned colluvial blocks at the base of the exposure. Weathering, clay drapes over the face of the exposure, and inaccessibility make this section difficult to interpret. One OSL age (USU 1682) was collected 10 m below the terrace tread and was 620 ± 210 ya. A final distinct unconformity is located on the farthest upstream extent of this stratigraphic panel and extends from the terrace tread to the colluvial apron at the base of the modern arroyo wall. One radiocarbon age (#4) was collected and dated from the base of this package to

1100 ± 150 cal ya BP_{2010}. The sample location was located close to a paleo-colluvial wedge, which is not ideal. Variegated sand, silt, and clay dominate the youngest alluvial package. The timing of incision between the deposition of Qf2 and Qf1 is not well constrained here.

Panel D: Lower Skutumpah Canyon

Stratigraphic panel D (Figure 2-2 in the main text) was located on the east side of the stream in the constricted reach of Skutumpah Canyon (Figure 2-S3). Two distinct unconformities bound two alluvial fill packages identified as Qf2, and Qf3. The oldest package was exposed upstream and downstream sections of the stratigraphic panel and was dominated by channel-margin deposits that contained alternating fine-grained and sand beds. Dominate sand facies included ripple, low angle, planar, and trough cross-bedded sand units. Dominant fine-grained facies included variegated, finely laminated, and massive sand, silt, and clay. Two OSL ages (USU 1677 and USU 1678) constrain the timing of deposition of the older alluvial package to 1690 ± 550 and 840 ± 200 ya. These ages are supported by three radiocarbon ages (#14, #15, #16) that resulted in ages of 1230 ± 100, 1440 ± 50, and 1440 ± 140 cal ya BP_{2010}; the latter two ages where field replicates (i.e., two discrete pieces of charcoal dated from the same depositional bed). One radiocarbon sample (#17) resulted in an older age of 2290 ± 90 cal ya BP_{2010} that was interpreted as being redeposited charcoal.

The younger package, Qf3, was bounded on both sides by an unconformity. This

package likely represents a side channel of the paleo arroyo because two channel banks (arroyo walls) are filled with channel margin slackwater deposits of variegated sand, silt, and clay. Three radiocarbons samples constrain the timing of deposition of this alluvial-fill package because there were no suitable sand beds to sample for OSL. Two replicate samples (#11 and # 12) from 2.75 meters below the terrace tread resulted in statistically different ages of 190 ± 140 and 460 ± 100 cal ya BP_{2010}. The younger age was interpreted to be too young and was probably caused by bioturbation. The third radiocarbon age was collected from 4.5 m, the base of the exposed package and was 660 ± 70 cal ya BP_{2010}. The timing of incision between the deposition of Qf2 and Qf3 is tightly constrained to 840-660 ya.

Panel E: Half-Cut Skutumpah Canyon

Stratigraphic panel E was located on the left side of the stream looking downstream in the constricted reach of Skutumpah Canyon (Figure 2-S3) just downstream of panel D. This exposure contained one shallow unconformity that cut 5-6 m of the 11 m exposure (Figure 2-S5). One charcoal sample (#18) was collected from below the unconformity and resulted in an age of 2510 ± 230 cal ya BP_{2010}. No further work was done on this stratigraphic section.

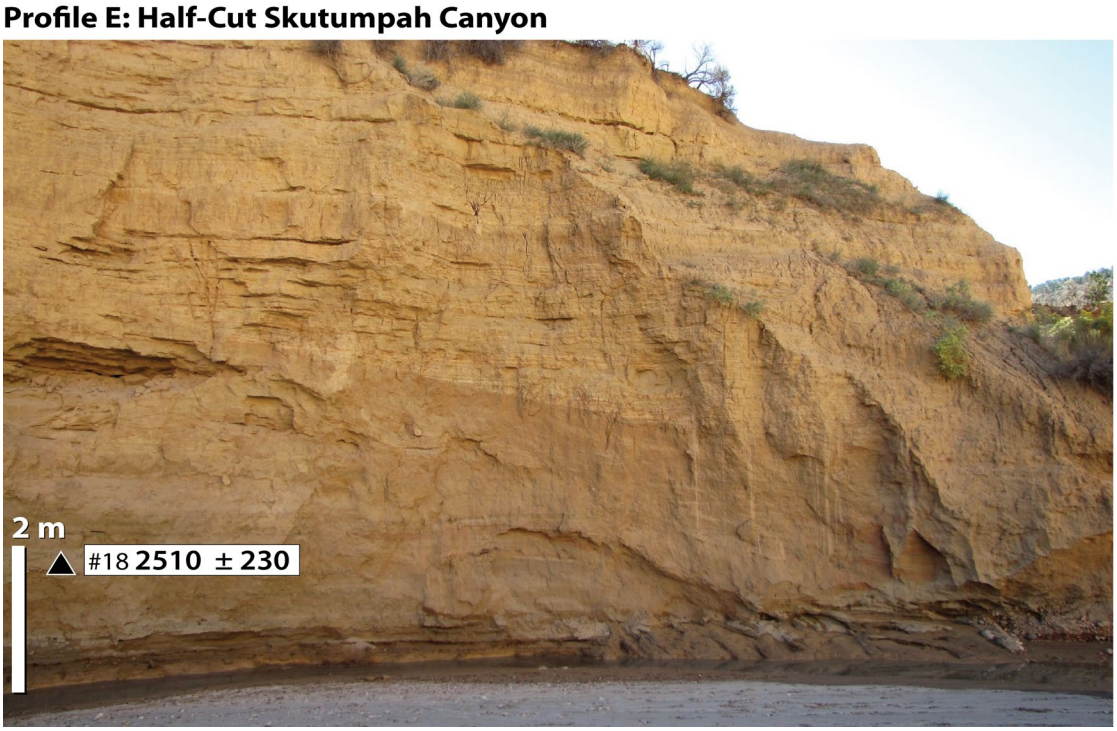

Figure 2-S5 – Photograph of stratigraphic panel E from Skutumpah Canyon. The black triangle is a dated radiocarbon sample in calibrated years BP.

Panel F: Basalt Junction

Stratigraphic panel F was located below the confluence of Johnson Canyon to the west and Skutumpah Canyon to the north. The 13-meter-high exposure contained two alluvial-fill packages, but the chronology of this exposure is easiest to interpret based on one fill package (Figure 2-S6). A shallow 2-meter-high unconformity with a colluvial wedge is located at the base of the exposure; a continuous, near vertical unconformity is not clearly observed. The stratigraphic section contains horizontally bedded fine-grained and sand dominated facies. Two samples were collected and analyzed to constrain the

timing of deposition of the package upstream of the potential unconformity. One OSL sample (USU 1354) was collected from 10.9 meters below the terrace tread and resulted in ages of 1010 ± 410 ya. Two radiocarbon samples (#24 and #25) were collected from 11.2 and 12.8 m depth and resulted in ages of 1760 ± 110 and 1920 ± 40 cal ya BP_{2010}. These charcoal sample ages were interpreted as being redeposited from older stored deposits. The younger alluvial package onlaps the older package at the base of the exposure, but this relation becomes unclear toward the terrace tread. Three radiocarbon samples (#21, #22, and #23) from the base of the younger package yielded ages of 10,000 ± 910, 1200 ± 140, and 2620 ± 180 cal ya BP_{2010} and one OSL age (USU 1355) was 1470 ± 340 ya. One OSL age (USU 1676) constrains the top of the package below a soil horizon to 930 ± 240 ya. One radiocarbon sample (#19) was collected and dated above the soil horizon to 2040 ± 60 cal ya BP_{2010} and was interpreted as being redeposited charcoal. It is possible that this stratigraphic section represents one aggradation period and the small observed unconformities represent lateral channel migration and not a significant entrenchment episode. The three OSL ages are stratigraphically coherent relative to depth below terrace tread.

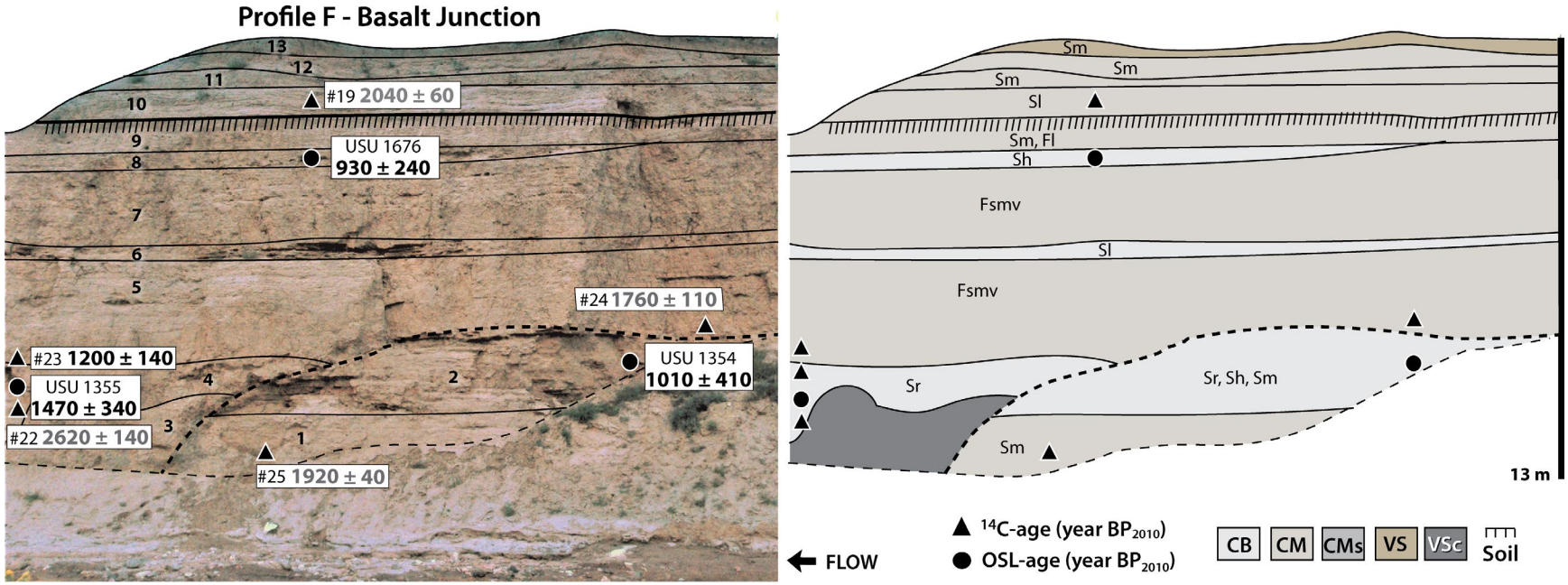

Figure 2-S6. Stratigraphic panel F. Black triangles are radiocarbon samples. Black circles are OSL samples. The numbers on the photograph refer to discrete depositional units and the codes in the drawing refer to facies abbreviations described in Table S1. OSL ages are in yr BP and referenced to 2010 AD as present and radiocarbon ages are in cal yr BP and referenced to 2010 AD. Qf1, Qf2, and Qf3 refer to the different three periods of aggradation identified in the Johnson Wash stratigraphic record. Radiocarbon samples that resulted in coal are not included in figure.

Panel G: Where the Basalt Ends (WTBE)

Stratigraphic panel G was located on a meander bend on the left side of Johnson Wash (Figure 2-S7). The exposure height was 11.5 meters along this 170-meter-long exposure. This panel records all three alluvial-fill packages described and dated in Johnson Wash for this study. Two distinct unconformities bound the three alluvial-fill-packages identified as Qf1, Qf2, and Qf3 from oldest to youngest (Figure 2-2 in the main text). The oldest alluvial package (Qf1) is exposed in the downstream section of the panel, bounded by an unconformity upstream, and is capped with a buried soil. The alluvial-fill package is tabular and horizontally bedded. The bottom three units were composed of massive, planar, horizontal, ripple, and trough cross-bedded sand facies. Laminated and massive fine-grained facies were observed higher in the profile. A second buried soil was observed 5 meters below the terrace tread. Two OSL samples (USU 1392 and USU 1394) from the middle (6.15 m) and bottom (11.25 m) of Qf1 resulting in depositional ages of 1840 ± 460 and 1910 ± 370 ya. Five additional radiocarbon samples were dated (#29-33); all of which were stratigraphically too old. Two ^{14}C-ages were identified as coal and three ages, 2360 ± 120, 3170 ± 100, and 3220 ± 80 cal ya BP_{2010}, were interpreted as being redeposited charcoal. Upstream, Qf3 onlaps and over-tops Qf1. Two small windows of Qf2 were exposed within Qf3 (note – only one Qf2 window shown in Figure 2-2 in the main text). Two OSL ages were used to constrain the timing of deposition of Qf2. USU 1395 was collected at 8.3-meter-depth and resulted in an age of 1370 ± 340 ya and USU 1396 was collected at 3-meter-depth and was 940 ± 230 ya. Thus, the timing of

entrenchment between Qf1 and Qf2 is constrained here to have taken place approximately between 1840 and 1370 ya. Deposits in Qf2 are tabular, horizontal-bedded, alternating sand and fine-grained facies. The youngest alluvial package in this stratigraphic panel is Qf3 and is dominated with fine-grained facies including variegated and laminated sand, silt, and clay. Three radiocarbon samples (#26, #27, and #28) date the timing of deposition from bottom to top of the package. The bottom sample was 1080 ± 40 cal ya BP_{2010} and was interpreted as being redeposited. The middle sample was collected from 2.25 m and was 570 ± 20 cal ya BP_{2010} and the top sample was collected from 1.23 m depth below terrace tread and was 460 ± 80 cal ya BP_{2010}. A weak buried soil was identified between the top two ^{14}C-samples in Qf3. The buried soil unit was massive and fine-grained with prismatic pedogenic structure, abundant roots, and discoloration and mottling from the translocation of ions, and contained abundant carbonate filaments and nodules. The episode of entrenchment that followed aggradation of Qf2 and preceded Qf3 is constrained in this profile to between 570 and 940 ya.

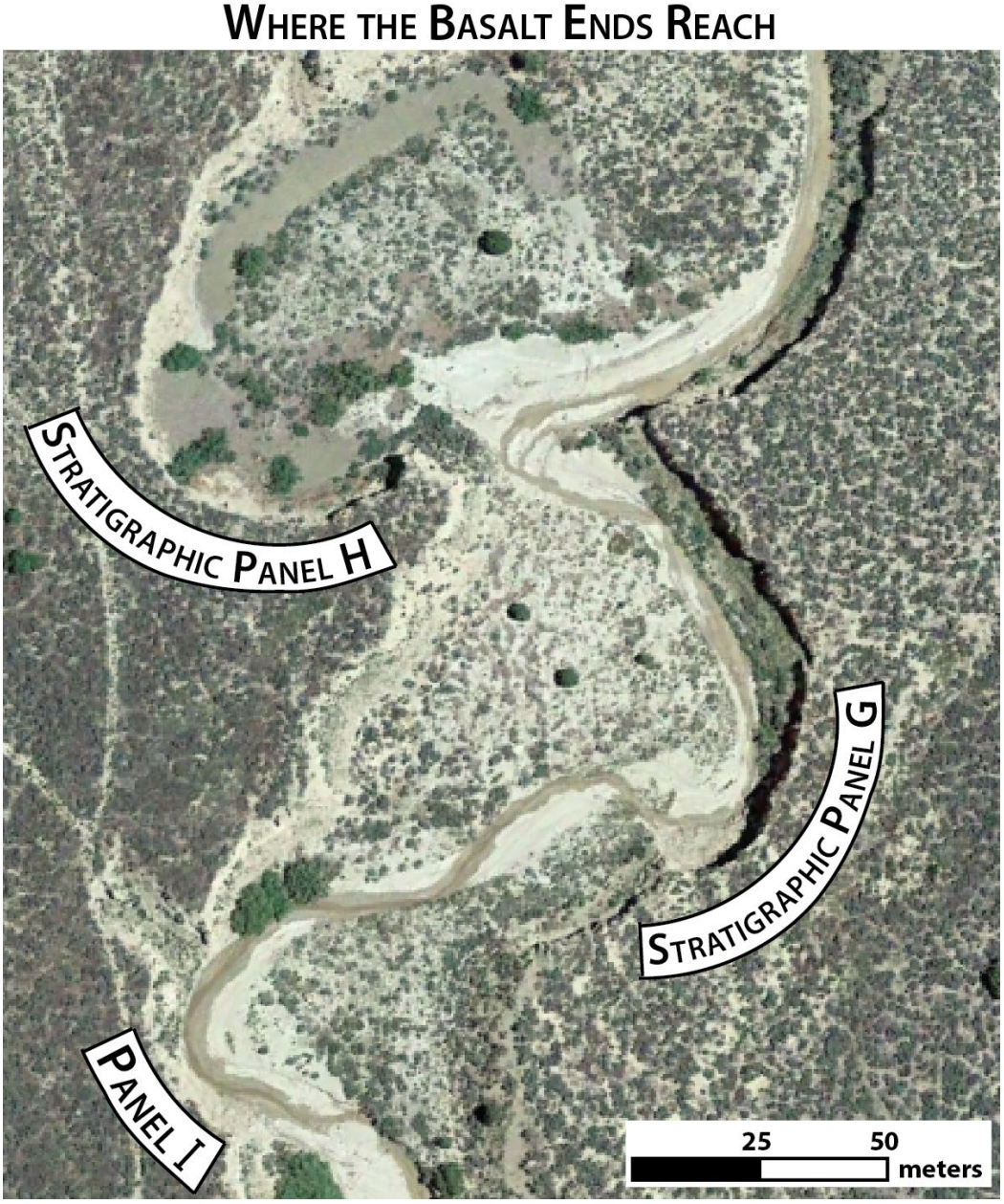

Figure 2-S7. Overhead view of the location of the three stratigraphic sections labeled

Panel H: Where the Basalt Ends Upper Right

Stratigraphic panel H was located just upstream of panel G on the west side of the Johnson Wash in a meander bend (Figure 2-S5)**.** The 11-meter-high and 180-meter-long exposure contained at least two alluvial-fill packages that correspond to Qf2 and Qf3 (Figure 2-3 in main text).

The older alluvial-fill package (Qf2) contained two shallow unconformities and a channel feature. Deposits were generally tabular, horizontal-bedded, and contained alternating sand and fine-grained facies including low angle, horizontal, and ripple cross-bedded sands and variegated sand, silt, and clay facies. A buried soil tops the alluvial-fill package at 2-meter-depth and another buried soil is observed at 5-meter-depth. One OSL age (USU 1683) located at the base of the package (9.5-meter-depth) was used to characterize the timing of aggradation to around 1510 ± 420 ya. Two additional radiocarbon samples were dated to 2980 ± 70 and 3110 ± 90 cal ya BP_{2010} (#36 and #38), but these samples were interpreted as being redeposited because they were significantly older than the OSL deposit stratigraphically below them. This alluvial package was truncated downstream and an 8-meter-high unconformity was observed with a colluvial wedge at the base.

The youngest alluvial package (Qf3) contained a channel deposit at the base and on-lapped and over-topped Qf2 higher up. The package contained alternating sand and fine-grain facies. Two OSL ages (USU 1685 and USU 1684) provide age control for the timing of deposition resulting in ages of 830 ± 190 and 720 ± 140 ya. One pair of replicate

radiocarbon samples (#34 and #35) were dated to 1580 ± 100 and 5180 ± 660 cal ya BP_{2010}, but these samples were interpreted as being redeposited.

Panel I: Where the Basalt Ends Lower Right

Stratigraphic panel I was located just downstream of panel H on the right side of the Johnson Wash in a meander bend (Figure 2-S8; 2-S7)**.** The 11.5-meter-high exposure contains one shallow unconformity and one additional unconformity that likely represent channel scrolling caused by lateral migration of the channel within arroyo walls. I am not confident that this exposure represents multiple cut-fill packages because of age control results and clarity of unconformities.

The base of the oldest package was dated with one OSL sample (USU 1673) to 1600 ± 370 ya and with one radiocarbon sample (#41) to 1740 ± 130 cal yr BP_{2010}. The package was capped with a younger alluvial-fill and contains a buried soil 1-meter below the terrace tread. A radiocarbon sample (#39) was collected 1.25-meter-depth from the buried soil horizon and dated to 620 ± 80 cal yr BP_{2010}. A second OSL sample (USU 1667) was collected at the base of the second potential alluvial package to 1430 ± 350 ya and a radiocarbon was also sampled (#40) and resulted in an age of 1270 ± 120 cal yr BP_{2010}. A third OSL sample (USU 1668) was dated across the potential second unconformity and resulted in 1320 ± 350 ya. All three OSL samples within this exposure were correlated with the timing of Qf2.

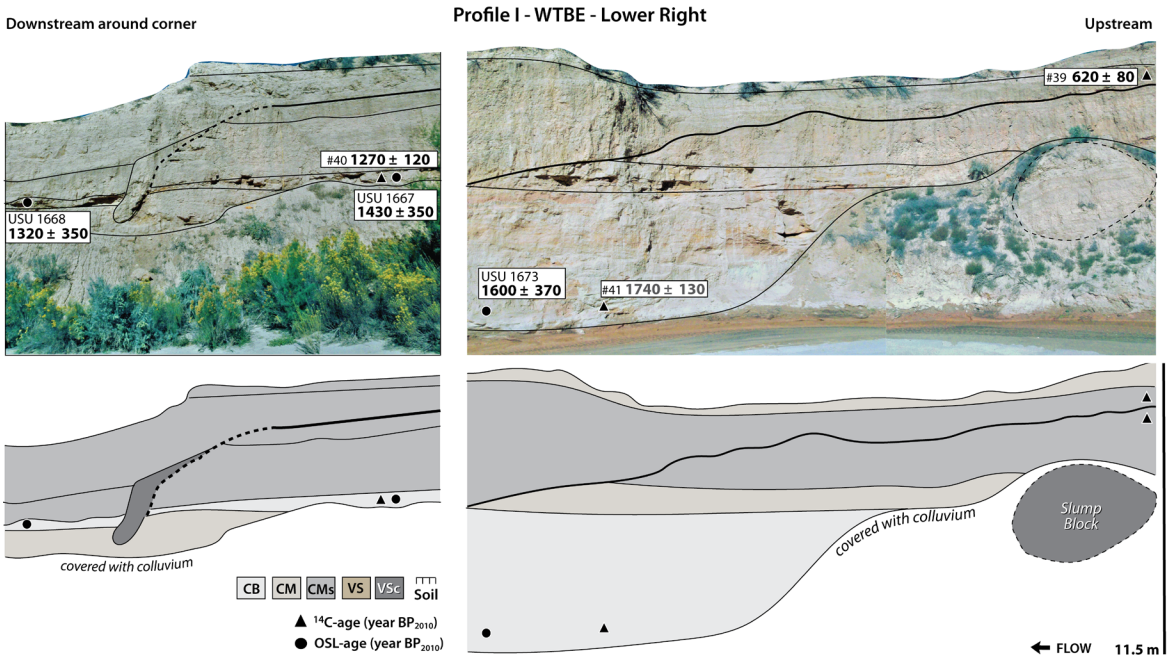

Figure 2-S8. Stratigraphic panel I. Black triangles are radiocarbon samples. Black circles are OSL samples. OSL ages are in yr BP and referenced to 2010 AD as present and radiocarbon ages are in cal yr BP and referenced to 2010 AD. A thicker black line annotates unconformities and a dashed line identifies uncertainty in interpretation. Individual units are not identified in this illustration.

Panel J: Above Dam

Stratigraphic panel J was located upstream of where Johnson Wash road crosses the arroyo above the diversion dam structure. In general, stratigraphic profile height decreased in the four downstream exposures (Table 2-S1). The 5-meter-high exposure is on the west channel bank and contains potentially three alluvial-fill packages. One OSL and four radiocarbon samples constrain the age of the alluvium.

The oldest alluvial package was the focus of age control because Qf2 and Qf3

alluvial-fill packages were well constrained in other stratigraphic panels. Sediments were dominated with channel margin deposits and one inset channel bottom deposit was observed at the top of the package at 0.5-meter-depth below the terrace tread. Channel margin deposits contained alternating sand and fine-grained and consisted of low-angle and planar cross-bedded sands, massive sands, and finely laminated silts and clays. The oldest package was dated with two field replicate radiocarbon samples (#44 and #45) at 4.5-meter-depth and resulted in statistically different ages; one being coal and the other was 2710 ± 170 cal yr BP_{2010} and was interpreted as being redeposited charcoal. One OSL sample (USU 1687) was collected at 3-meters-depth directly below a buried soil horizon to 1660 ± 340 ya. The OSL sample was collected from a 1-meter-thick, planar-cross-bedded, medium to very fine sand bed and contained charcoal. The buried soil characterized by a darker Munsell color (7.5 YR 4/4), calcium carbonate nodules, lack of sedimentary structures, and the presence of roots. One radiocarbon age (#43) was also dated from this bed and resulted in an age of 3240 ± 140 cal ya BP_{2010}, which was interpreted as being too old relative to the OSL sample. The buried soil relative the OSL age corresponds to the timing of arroyo cutting between Qf3 and Qf2 recoded in other stratigraphic panels in Johnson Wash.

A potential colluvial wedge was found abutting the older alluvial package along an unconformity, but the exposure was difficult to interpret because of weathering and erosion. The younger alluvial package contained steeply dipping beds that onlapped the colluvial wedge. The sedimentology of this package consisted primarily of cm-scale, very fine to fine-grained, ripple cross-bedded sands and finely laminated sands, silts, and clays

with some pebble lenses. A 1.5-meter-thick massive sand bed was also observed. An inset channel was observed within the younger alluvial package that contained ripple cross-bedded sands. One radiocarbon sample (#42) was dated from this package above the inset channel at 1-meter-depth below the terrace tread and resulted in an age of 1190 ± 90 cal ya BP_{2010}. While this charcoal sample is in the stratigraphic correct order, the location of the sample relative to the terrace tread makes the age appear to be too old and was interpreted as being reworked charcoal from an older deposit.

Panel K: Below Dam

Stratigraphic panel K was located downstream of where Johnson Wash road crosses the arroyo above the diversion structure. The 6-meter-high exposure is on the right side of Johnson Wash and contains at three alluvial-fill packages separated by two buttress unconformities (Figure 2-3 in main text).

The oldest alluvial-fill package is correlated with Qf1. Two OSL samples (USU 1328 and USU 1330) were collected from 4.2- and 2.5-meter-depths and resulted in depositional ages of 1760 ± 380 and 1530 ± 410 ya respectively. Two charcoal samples collected from this site did not provide reliable age estimates for the timing of deposition of Qf1. One radiocarbon sample (#50) yielded an age that was stratigraphically too old (2290 ± 100 cal ya BP_{2010}) indicating that the charcoal had been redeposited and a second radiocarbon sample (#49) resulted in an age that was older than radiocarbon dating can date indicating the sample was coal. A buried soil caps this alluvial package and was

formed in the the last deposit prior to entrenchment. A colluvial wedge onlaps the unconformity that truncates the oldest alluvial-fill package.

The next alluvial fill package is identified as Qf2 based on one OSL age (USU 1561) from the bottom of the exposure (5.5-meter-depth) date the timing of deposition to 1420 ± 440 ya. Two radiocarbon dated field replicates (#47 and #49) produced ages of 1640 ± 40 and 1640 ± 40 cal ya BP_{2010}. The first unit in this fill-package is comprised of three meter-scale sand beds that onlap the colluvial wedge at one bounding contact and are truncated on the other. This unit was interpreted as a scrolling sequence formed by lateral channel migration. Sediment aggraded about 4-meters and then the stream entrenched 3 meters. The youngest alluvial-fill package onlaps Qf2 and one OSL (USU 1562) sample yields a depositional age of 440 ± 170 ya.

Panel L: Bedrock

Stratigraphic panel L was located on the western edge of the alluvial valley abutting the underlying bedrock. Only one alluvial-fill package was identified in this 7-meter exposure. One OSL and two radiocarbon samples constrain the age of the alluvium. OSL sample USU 1691 was collected from 6.5-meters below the terrace tread and dated to 2180 ± 750 ya. This sample was one of the oldest OSL samples dated in Johnson Wash. Radiocarbon field replicates (#51 and #52) were sampled from the top of the exposure above a buried soil and resulted in statistically different ages 420 ± 70 and 1080 ± 50 cal yr BP_{2010}. The base of this exposure correlates to the earliest alluvial-fill package in the

stratigraphic record in Johnson Wash and the buried soil potentially delineates the youngest alluvial-fill package Qf3. (No good picture was obtained at this site.)

Panel M: Holland Ranch

Stratigraphic panel M was the farthest downstream panel in Johnson Wash (Table 2-S1; Figure 2-S4). The profile is 4.6 meters high and contains one buried soil. Units were generally tabular and massive with dry colors of 10 YR 7/4, 10 YR 7/3, and 10 YR 7/2. Two OSL and one radiocarbon sample constrain the age of the alluvium. The oldest deposit (unit 1) was located 4.5 m below the terrace tread with an OSL age of 2230 ± 630 ya (USU 1139). Radiocarbon field replicates #53 and #54 were sampled 4.6 m and resulted in statistically different ages of 3470 ± 40 and 4530 ± 50 cal yr BP_{2010} and were interpreted as too old from the reworking of previously deposited charcoal. OSL sample USU 1138 was collected from 2.45-meters below the terrace tread and dated to 1340 ± 440 ya. There were calcium carbonate accumulations through the entirety of the profile. The primary facies observed were fine-grained massive deposits (Fm) and few units with weak sedimentary structures including ripple cross-laminated sands (Sr) and finely laminated, rippled sand, silt, and clay (Fl).

Panel N: Swapp Creek

Stratigraphic panel N is located on the tributary Swapp Creek and drains the White Cliffs on the northwest corner of the Wygaret Terrace in Johnson Wash (Figure 2-S4). The tributary was graded to the terrace tread of the Wygaret Terrace. There is a head cut near the modern arroyo landform that is eroding headward up Swapp Creek. The 5-meter-high profile was dominated by sand facies including horizontally bedded sands (Sh), low angle cross-bedded sands (Sl), and massive sands (Sm). The profile had very little fine-grained facies. One coarser deposit was located 50 cm below terrace tread and contained pebbles with b-axis' of up to 6 cm. The sediment was generally 10 YR 8/6 that transitioned to 7.5 6/6 toward top of the beds. The modern channel contained pebbles to boulder size clasts. Three weakly developed buried soils were identified. Soil formation characteristics identified included bioturbation, roots, blocky pedogenic structure, carbonate filaments, and gradation in color within beds indicating translocation of ions. One radiocarbon sample (#55) was collected from 4 m below the terrace tread and resulted in an age of 920 ± 60 cal yr BP_{2010}. OSL sample USU 1352 was collected from 4.85 meters below the terrace tread and dated to 1060 ± 350 ya.

Panel O: Left Fork Cottonwood Creek

Stratigraphic profile O (Figure 2-S4) is located on the left fork of Cottonwood Creek tributary around 1800 m elevation. The tributary drains the White Cliffs on the east

side of Johnson Wash. The valley width of the tributary was narrow (~100 m wide) confined by Navajo Sandstone of the White Cliffs. The talus aprons at the base of the cliffs appears to me the primary source of sediment. The valley-fill alluvium ends just upstream of the profile site and the channel then cuts through bedrock. Valley-fill alluvium continues downstream to the confluence with the trunk stream Johnson Wash. However, incision into the valley-fill ends before the confluence with the right fork of Cottonwood Creek. The valley-fill terrace was covered with juniper, pinyon pine, and sagebrush. The 4-meter-high profile was dominated by sand facies including one unit with horizontally bedded sands (Sh) and one unit with trough cross-bedded sands (St). The dominant facies were massive sands (Sm) with some pebbly channel bottom lenses. The profile contained one unit with laminated rippled sand, silt, and clay (Fl). The junipers appeared to germinate in the upper most unit (top 60 cm). There was charcoal present throughout the profile and two radiocarbon samples (#56 and #57) resulted in ages of 520 ± 130 and 1430 ± 40 cal yr BP_{2010}. It is not clear if these ages accurately date the timing of deposition of the two deposits because no other independent age control was obtained at this site.

Radiocarbon Field Replicate Analysis

Seven radiocarbon field replicates were sampled and dated to test if samples from the same discrete deposit recorded the same radiocarbon age (Table 2-S2)**.** Two pairs of sample replicates resulted in statistically similar age distributions, one replicate was coal, and four field replicates resulted in statistically different ages and the disparity between field replicate ages ranged from 0 to 1070 years.

Table 2-S2. Summary table of radiocarbon replicates that were sampled and dated from the same discrete depositional bed to identify errors associated with ^{14}C-dating arroyo walls in southern Utah.

Sample #	Profile #	Depth (cm)	^{14}C Age	Weighted Mean	Error + 2 σ	Error - 2 σ	Disparity	Interpretation of error
7	C	400	2475 ± 25	2630	150	130	430	*Older sample was reworked from older deposit*
8	C	400	2140 ± 60	2200	170	150		
11	D	275	115 ± 25	190	140	120	270	*Younger sample was bioturbated*
12	D	275	355 ± 35	460	90	100		
32	G	1100	2950 ± 25	3170	70	100	50	*Statistically similar age distributions*
33	G	1100	2985 ± 20	3220	60	80		
44	J	405	2535 ± 20	2710	50	170	-	*Older sample was coal*
45	J	405	> 45,700	-	-	-		
47	K	450	1680 ± 15	1640	40	40	0	*Statistically similar age distributions*
48	K	450	1675 ± 15	1640	40	30		
51	L	90	285 ± 20	420	70	70	660	*Older sample was reworked from older deposit*
52	L	90	1125 ± 20	1080	50	50		
53	M	460	3185 ± 20	3470	50	50	1070	*Older sample was reworked from older deposit*
54	M	460	3985 ± 15	4530	40	30		

Table 2-S3. ICP-MS chemistry and dose-rate data and equivalent dose (De) distribution statistics for all OSL samples.

Sample #	USU ID	In-situ H2O [1] (%)	Grainsize (microns)	K (%) [2]	U (ppm) [9]	Th (ppm) [9]	Rb (ppm) [9]	Cosmic (Gy/ka)	OD [3] (%)	SKEW (%)	Grains within 2 σ of MAM
1	1334	1.3	180 - 212	1.19 ± 0.03	1.0 ± 0.1	4.5 ± 0.4	43.0 ± 1.7	0.21 ± 0.02	54	1.43	19 %
2	1335	1.1	180 - 212	1.46 ± 0.04	1.0 ± 0.1	3.6 ± 0.3	63.7 ± 2.5	0.09 ± 0.01	35.3	1.09	27 %
3	1682	-	150 - 180	1.30 ± 0.03	1.3 ± 0.1	4.0 ± 0.4	52.2 ± 2.1	0.09 ± 0.01	66.3	2.23	13 %
4	1680	-	150 - 180	1.24 ± 0.03	0.9 ± 0.1	4.1 ± 0.4	45.7 ± 1.8	0.07 ± 0.01	27.3	0.46	37 %
5	1679	0.5	125 - 180	1.01 ± 0.03	0.8 ±0.1	3.6 ± 0.3	38.0 ± 1.5	0.06 ± 0.01	37.1	1.52	27 %
6	1677	-	180 - 212	1.33 ± 0.03	1.3 ± 0.1	4.6 ± 0.4	53.6 ± 2.1	0.18 ± 0.02	33.0	1.43	38 %
7	1678	-	180 - 212	1.98 ± 0.05	1.7 ± 0.1	6.7 ± 0.6	71.6 ± 2.9	0.13 ± 0.01	31.3	1.60	41 %
8	1676	0.3	125 - 180	1.28 ± 0.03 1.27 ± 0.03 1.27 ± 0.03	51.5 ± 2.1 54.3 ± 2.1 50.3 ± 2.1	3.8 ± 0.3 4.1 ± 0.3 3.2 ± 0.3	1.2 ± 0.1 1.3 ± 0.1 1.1 ± 0.1	0.13 ± 0.01	33.6	0.92	30 %
9	1354	0.5	180 - 212	0.89 ± 0.02	1.0 ± 0.1	4.7 ± 0.4	36.1 ± 1.4	0.09 ± 0.01	62.4	1.84	22 %
10	1355	0.3	180 - 212	0.73 ± 0.02 0.69 ± 0.02 0.70 ± 0.02	0.7 ± 0.1 0.5 ± 0.1 0.5 ± 0.1	2.4 ± 0.2 1.8 ± 0.2 1.8 ± 0.2	29.9 ± 1.1 26.1 ± 1.1 27.2 ± 1.1	0.08 ± 0.01	39.5	0.87	19 %
11	1396	4.5	180 - 212	1.59 ± 0.04	1.6 ± 0.1	4.8 ± 0.4	63.2 ± 2.5	0.20 ± 0.02	35.7	0.85	23 %
12	1395	0.9	180 - 212	1.74 ± 0.04	1.7 ± 0.1	5.7 ± 0.5	66.7 ± 2.7	0.11 ± 0.01	42.5	0.27	16 %
13	1392	1.7	180 - 212	1.46 ± 0.04	1.4 ± 0.1	4.5 ± 0.4	55.9 ± 2.2	0.14 ± 0.01	28.3	0.60	41 %
14	1394	2.6	180 - 212	1.09 ± 0.03 1.05 ± 0.03	1.2 ± 0.1 1.2 ± 0.1	4.2 ± 0.4 3.9 ± 0.4	40.1 ± 1.5 36.4 ± 1.5	0.08 ± 0.01	33.4	0.79	18 %
15	1684	-	180 - 212	1.46 ± 0.04	2.0 ± 0.1	7.4 ± 0.7	71.8 ± 2.9	0.13 ± 0.01	38.7	0.32	19 %
16	1685	-	150 - 212	1.57 ± 0.04	2.0 ± 0.1	6.6 ± 0.6	68.8 ± 2.8	0.23 ± 0.02	39.4	1.97	23 %
17	1683	0.3	150 - 180	1.11 ± 0.03	1.0 ± 0.1	3.3 ± 0.3	37.9 ± 1.5	0.10 ± 0.01	51.3	2.23	31%
18	1668	0.3	180 - 212	1.03 ± 0.03	0.9 ± 0.1	3.4 ± 0.3	42.0 ± 1.7	0.13 ± 0.01	56.6	1.51	32 %
19	1667	0.4	180 - 212	1.19 ± 0.03	1.0 ± 0.1	3.6 ± 0.3	48.6 ± 1.9	0.13 ± 0.01	29.3	0.41	44 %
20	1673	2.3	150 - 180	1.18 ± 0.03	0.8 ± 0.1	3.1 ± 0.3	42.9 ± 1.7	0.08 ± 0.01	30.5	2.63	46 %
21	1687	-	180 - 212	0.90 ± 0.02	0.8 ± 0.1	2.6 ± 0.2	34.8 ± 1.4	0.16 ± 0.02	35.0	1.34	17 %
22	1562	-	180 - 212	1.15 ± 0.03	0.8 ± 0.1	2.9 ± 0.3	44.2 ± 1.8	0.23 ± 0.02	77.8	2.93	17 %
23	1561	3.9	180 - 212	1.05 ± 0.03	1.0 ± 0.1	3.9 ± 0.4	42.1 ± 1.7	0.15 ± 0.01	60.9	1.47	20 %
24	1330	0.5	180 - 212	0.91 ± 0.02	0.8 ± 0.1	3.1 ± 0.3	34.8 ± 1.4	0.21 ± 0.02	44.6	1.22	20 %
25	1328	2.3	180 - 212	1.54 ± 0.04	1.8 ± 0.1	5.3 ± 0.5	63.3 ± 2.5	0.11 ± 0.01	34.8	1.18	17 %
26	1691	-	150 - 180	1.34 ± 0.03	0.9 ± 0.1	3.6 ± 0.3	48.9 ± 2.0	0.13 ± 0.01	62.6	2.87	35 %
27	1138	1.6	90 - 150	1.16 ± 0.03	1.0 ± 0.1	4.5 ± 0.4	43.0 ± 1.7	0.21 ± 0.02	51.6	2.16	16 %
28	1139	9.8	75 - 125	1.72 ± 0.04	2.2 ± 0.2	7.4 ± 0.7	65.8 ± 2.6	0.16 ± 0.02	28.3	1.33	47 %
29	1352	2.2	180 - 212	0.78 ± 0.02	0.5 ± 0.1	1.3 ± 0.2	32.2 ± 1.3	0.16 ± 0.02	61.7	1.22	20 %

[1] Assumed 3 ± 3% for moisture content over burial history for in-situ values <3%.
[2] Radio-elemental concentrations determined by ALS Chemex using ICP-MS and ICP-AES techniques; dose rate is derived from concentrations by conversion factors from Guérin et al. (2011).
[3] Overdispersion (OD) represents variance in D_E data beyond measurement uncertainties, OD >30% may indicate significant scatter due to depositional or post-depositional processes.

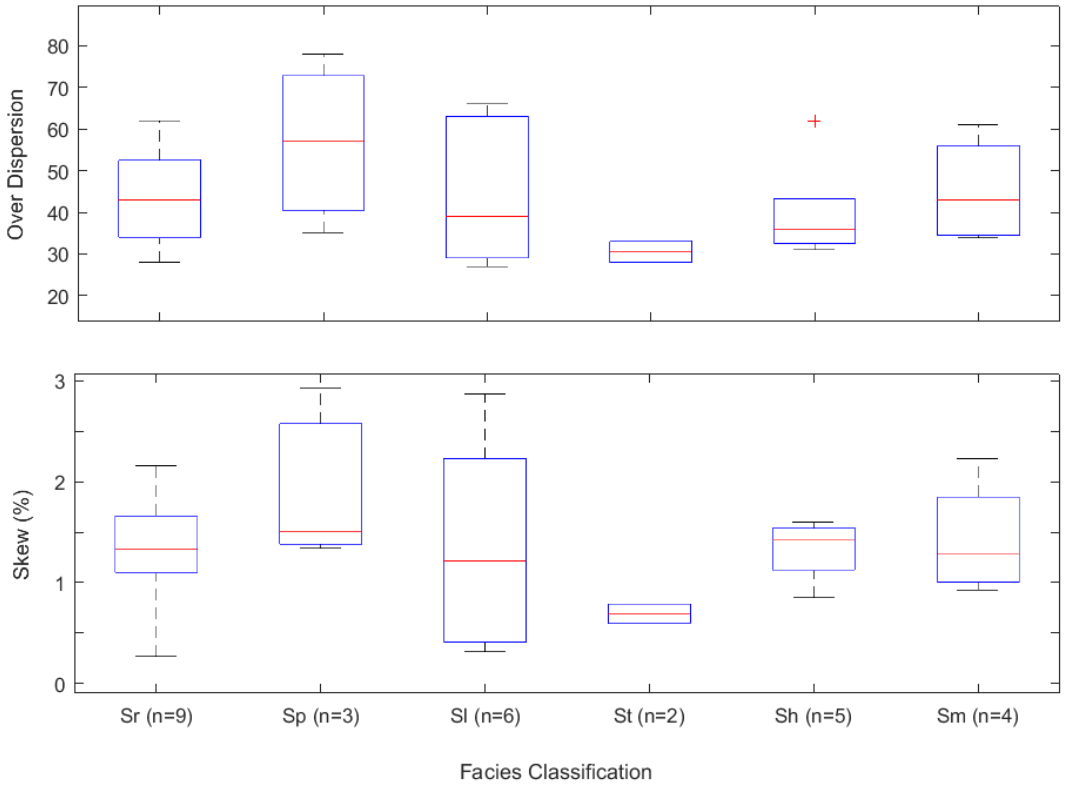

Figure 2-S9. Boxplot compares over-dispersion values and skew percentages for OSL samples grouped by facies classification.

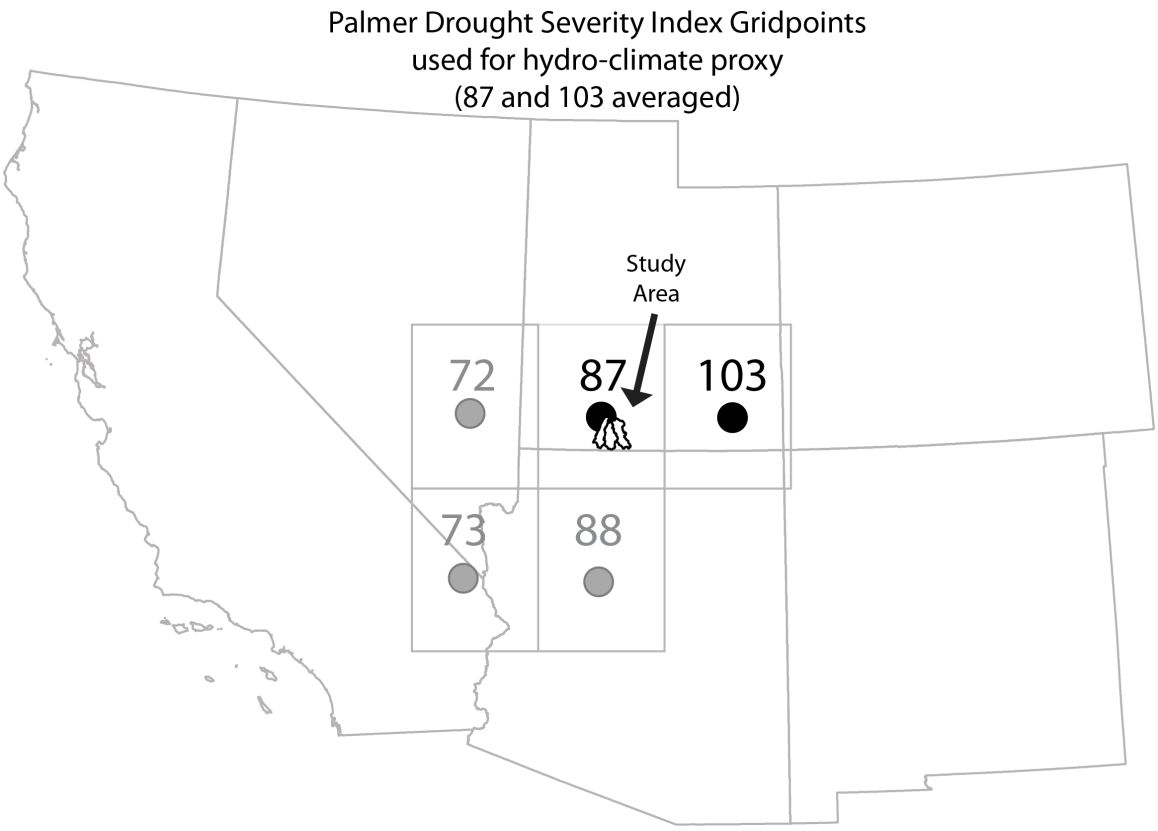

Figure 2-S10. Location of nearby PDSI gridpoints (Cook et al., 2004) used in climate analysis.

Table 2-S4. Rejection statistics for all OSL samples. A large number of single grains (73,400) were analyzed to acquire at least 30 accepted grains for each sample dated with single-grain OSL. 1.8% of total grains analyzed were accepted; 98.2% grains were. Grains were rejected because of low luminescence signals (89.1%), feldspar contamination indicated by a high IR depletion ratio (1.2%), poor recycling ratio (6.4%), high recuperation (0.6%), natural equivalent dose that was greater than the highest regenerative dose (0.5%), or poor dose-response growth-curve fit due to high De error (0.5%).

USU ID	Grainsize (microns)	Number of grains run	Nested criteria (left to right) for grain rejection						Number of grains rejected	Number of grains accepted	Percent Accepted (%)
			low signal	IR Depletion > 2	R1/R1' > 20%	Recuperation > 1 Gy	De > Highest Regen (> 1.1)	poor DR curve fit (very hi error)			
1334	180 - 212	2200	1926	0	177	30	15	21	2169	31	1.4
1335	180 - 212	2700	2448	60	138	7	6	11	2670	30	1.1
1682	150 - 180	2100	1825	42	164	20	1	8	2060	40	1.9
1680	150 - 180	1900	1693	0	146	13	17	1	1870	30	1.6
1679	125 - 180	1700	1466	36	132	14	4	15	1667	33	1.9
1677	180 - 212	2400	2159	31	111	12	20	33	2366	34	1.4
1678	180 - 212	3500	3224	0	196	21	7	21	3469	31	0.9
1676	125 - 180	2500	2142	0	261	17	11	12	2443	57	2.3
1354	180 - 212	2600	2360	31	148	11	6	8	2564	36	1.4
1355	180 - 212	3100	2811	0	188	29	16	8	3052	48	1.5
1396	180 - 212	1700	1501	0	139	15	6	9	1670	30	1.8
1395	180 - 212	2500	2171	68	147	17	45	20	2468	32	1.3
1392	180 - 212	2300	2067	48	107	8	10	26	2266	34	1.5
1394	180 - 212	4200	3843	87	160	25	26	14	4155	45	1.1
1684	180 - 212	4400	4104	0	220	16	15	9	4364	36	0.8
1685	150 - 212	1200	980	36	109	8	8	21	1162	38	3.2
1683	150 - 180	3900	3542	59	156	11	24	58	3850	50	1.3
1668	180 - 212	2600	2340	0	182	10	8	29	2569	31	1.2
1667	180 - 212	2800	2536	0	187	12	6	27	2768	32	1.1
1673	150 - 180	2800	2473	58	190	11	11	18	2761	39	1.4
1687	180 - 212	2100	1903	0	128	17	9	13	2070	30	1.4
1562	180 - 212	3100	2782	59	176	7	13	33	3070	30	1.0
1561	180 - 212	2700	2379	76	161	20	14	17	2667	33	1.2
1330	180 - 212	2900	2576	81	153	10	13	17	2850	50	1.7
1328	180 - 212	3400	2972	100	251	21	14	6	3364	36	1.1
1691	150 - 180	2000	1808	0	128	15	11	4	1966	34	1.7
1138	90 - 150	1700	1450	0	180	20	10	8	1668	32	1.9
1139	75 - 125	900	642	40	144	10	15	13	864	36	4.0
1352	180 - 212	1500	1279	0	141	10	14	26	1470	30	2.0

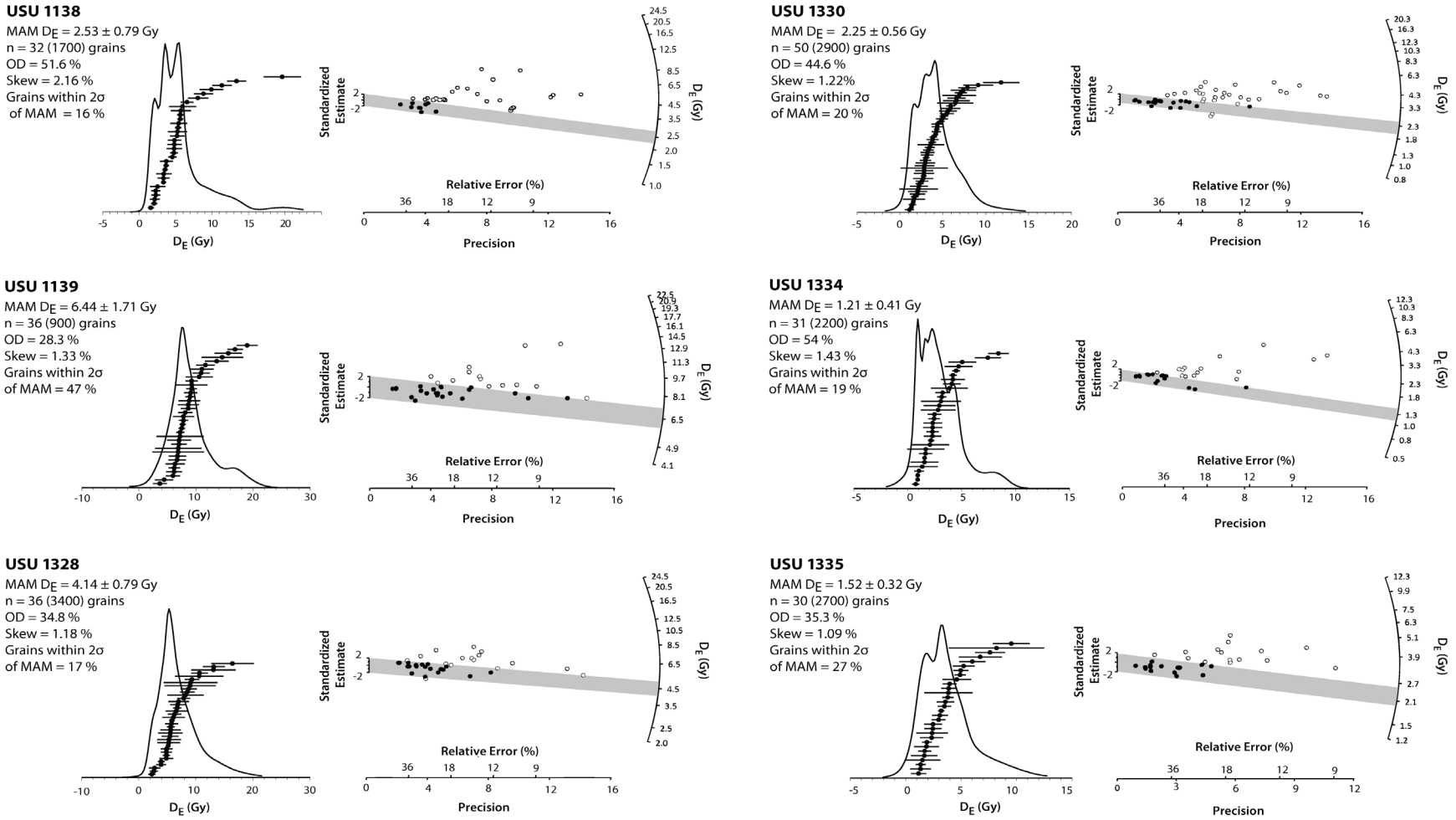

Figure 2-S11. De distributions for OSL samples plotted as probability distribution functions (PDF's) on the left and radial plots on the right. The circles on both plots represent the equivalent dose (D_E) estimate for all accepted grains. In the radial plots, the black circles and grey highlighted area represent accepted grains that were within 2-sigma error of the Minimum Age Model (MAM) estimate.

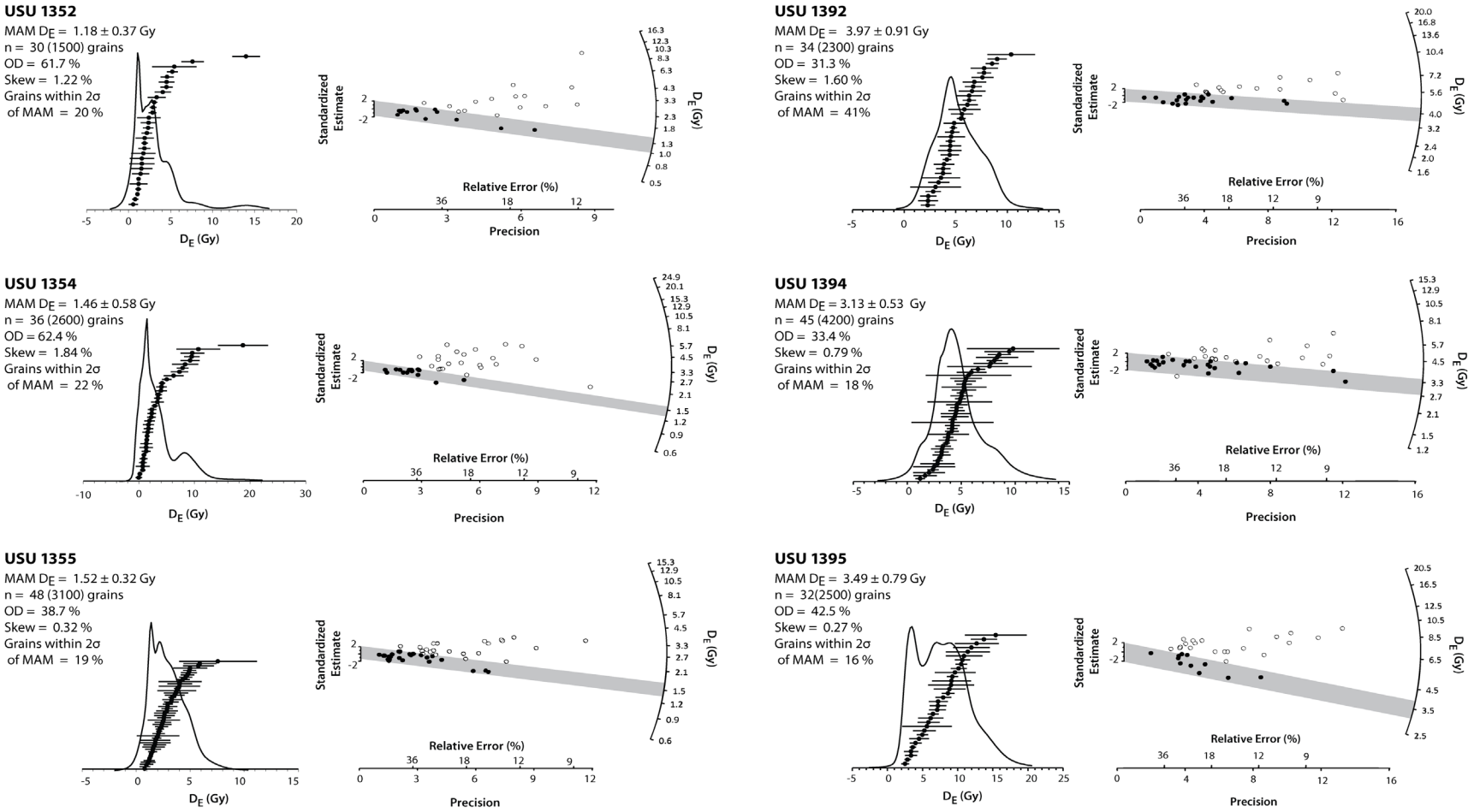

Figure 2-S12. De distributions for OSL samples plotted as probability distribution functions (PDF's) on the left and radial plots on the right. The circles on both plots represent the equivalent dose (D_E) estimate for all accepted grains. In the radial plots, the black circles and grey highlighted area represent accepted grains that were within 2-sigma error of the Minimum Age Model (MAM) estimate.

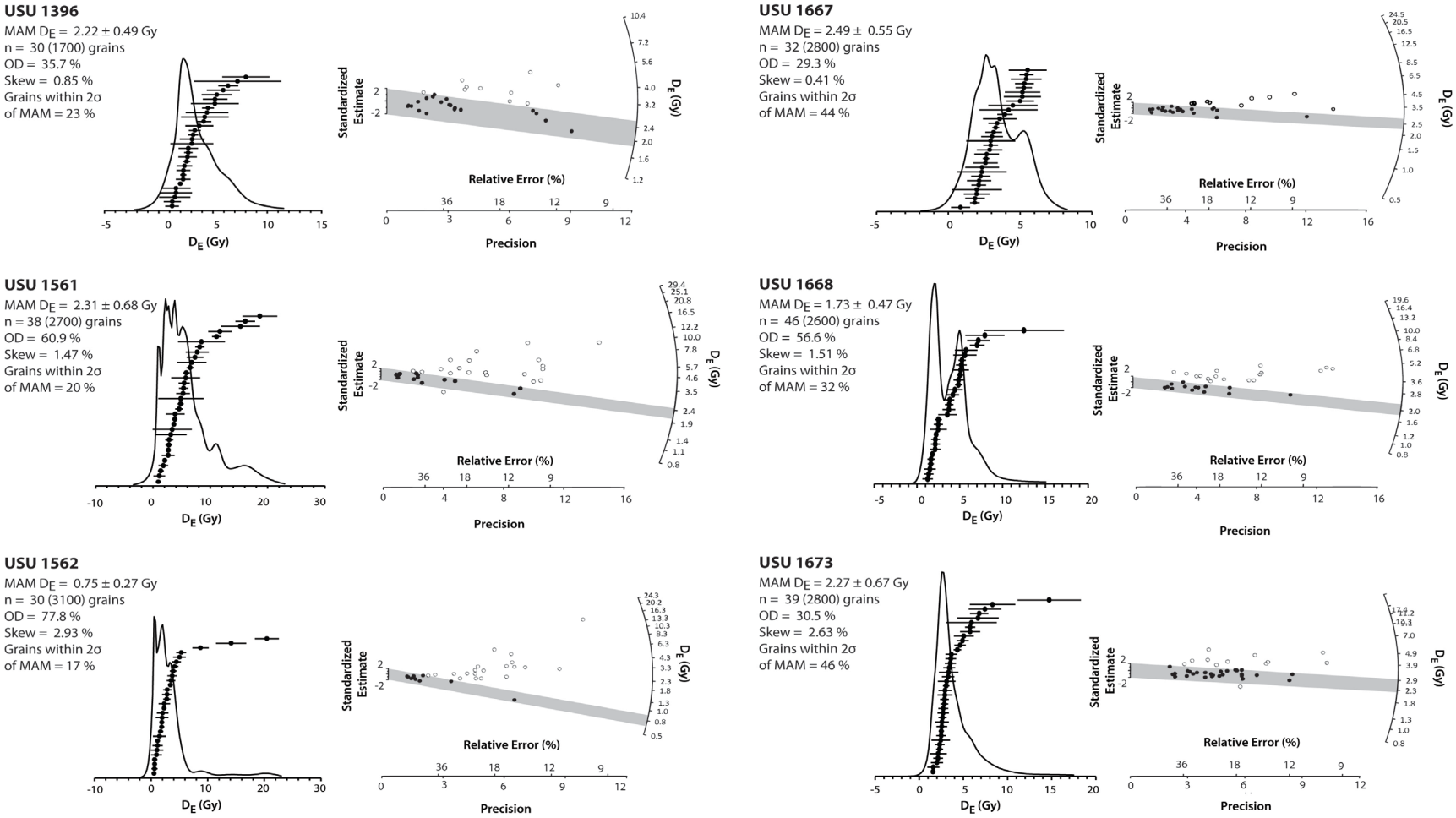

Figure 2-S13. De distributions for OSL samples plotted as probability distribution functions (PDF's) on the left and radial plots on the right. The circles on both plots represent the equivalent dose (D_E) estimate for all accepted grains. In the radial plots, the black circles and grey highlighted area represent accepted grains that were within 2-sigma error of the Minimum Age Model (MAM) estimate.

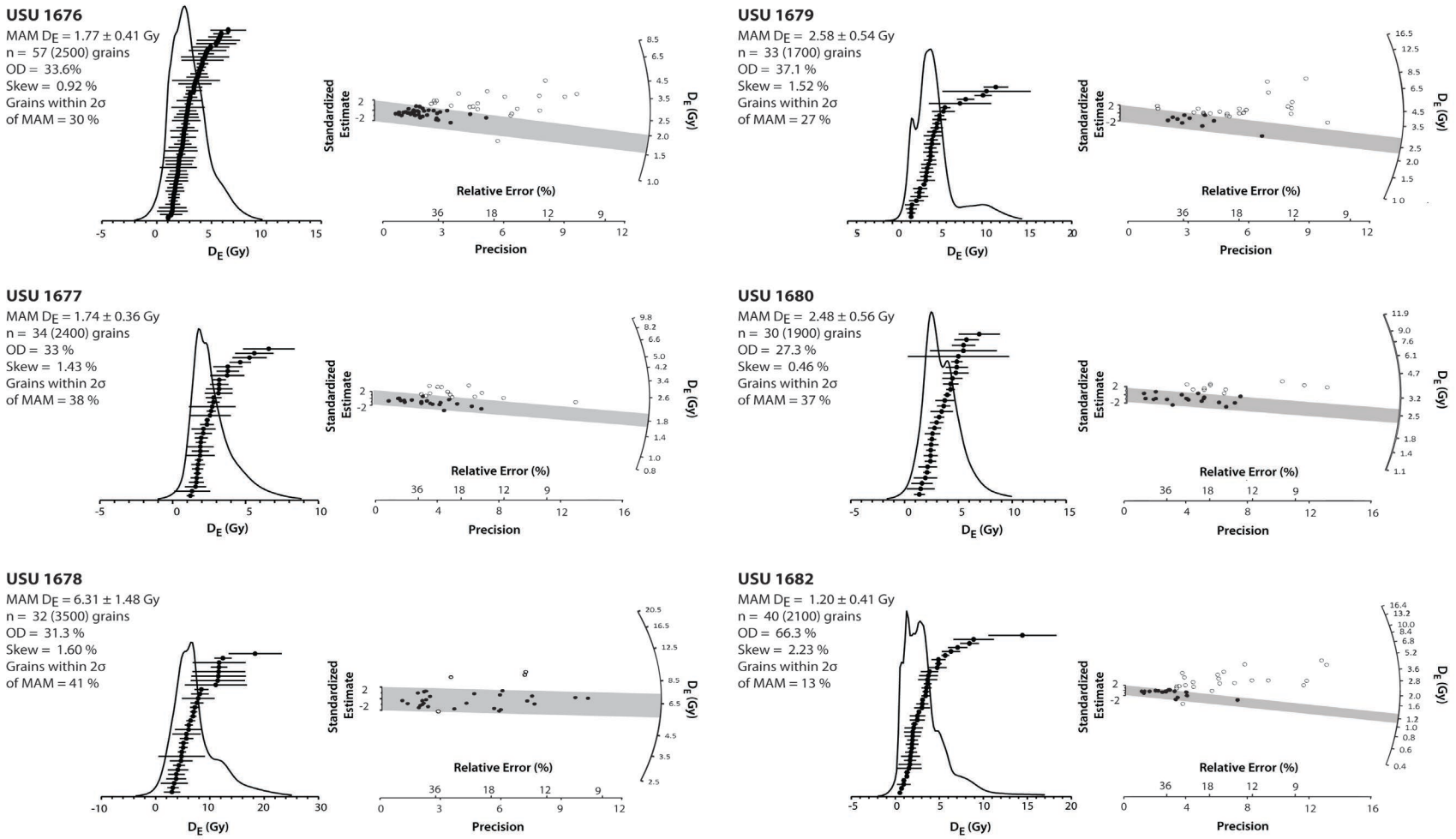

Figure 2-S14. De distributions for OSL samples plotted as probability distribution functions (PDF's) on the left and radial plots on the right. The circles on both plots represent the equivalent dose (D_E) estimate for all accepted grains. In the radial plots, the black circles and grey highlighted area represent accepted grains that were within 2-sigma error of the Minimum Age Model (MAM) estimate.

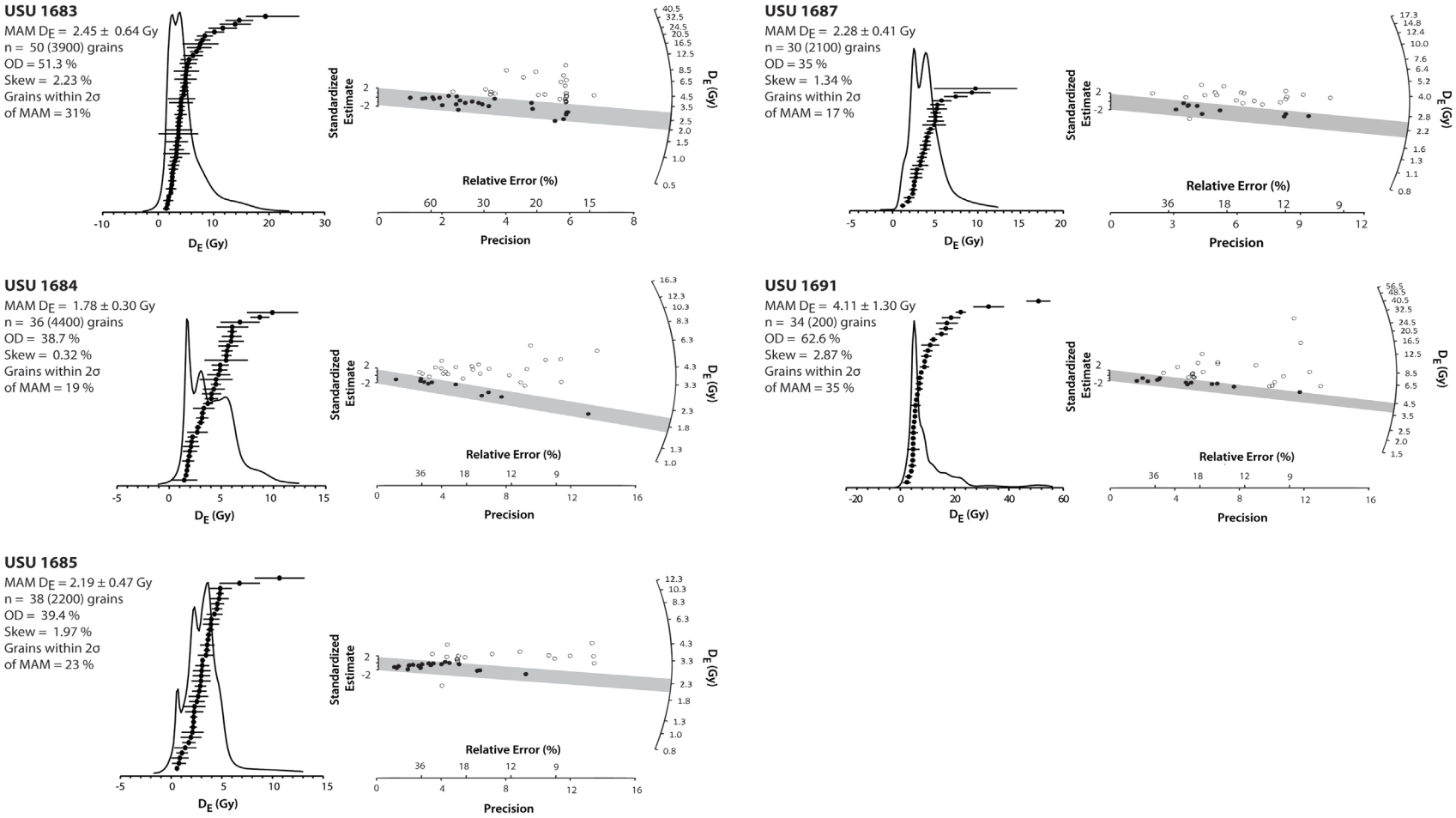

Figure 2-S15. De distributions for OSL samples plotted as probability distribution functions (PDF's) on the left and radial plots on the right. The circles on both plots represent the equivalent dose (D_E) estimate for all accepted grains. In the radial plots, the black circles and grey highlighted area represent accepted grains that were within 2-sigma error of the Minimum Age Model (MAM) estimate.

References Cited

Cook, E. R., Woodhouse, C. A., Eakin, C. M., Meko, D. M., and Stahle, D. W., 2004, Long-term aridity changes in the western United States: Science, v. 306, no. 5698, p. 1015-1018.

Guérin, G., Mercier, N. and Adamiec, G., 2011. Dose-rate conversion factors: update. Ancient TL, 29(1), pp.5-8.

Miall, M. 1996. The geology of fluvial deposits. p. 582.

CHAPTER III

EROSION RATES AND PATTERNS IN A TRANSIENT LANDSCAPE, GRAND STAIRCASE, SOUTHERN UTAH, USA

Citation: Riley, K. E., Rittenour, T. M., Pederson, J. L., and Belmont, P., 2019, Erosion rates and patterns in a transient landscape, Grand Staircase, southern Utah, USA: Geology. https://doi.org/10.1130/G45993.1

Abstract

Cosmogenic ^{10}Be concentrations in alluvial sediment are widely used to infer long-term, catchment-averaged erosion rates based on the assumption the landscape is in mass-flux steady state. However, many landscapes are out of equilibrium over millennial timescales due to tectonic and climatic forcing. The Grand Staircase of the Colorado Plateau (North America) is a transient landscape, adjusting to base level fall from the carving of Grand Canyon and is characterized by cliff-bench topography caused by differential erosion of lithologic units. ^{10}Be concentrations from 52 alluvial and colluvial samples, collected in nested fashion from five catchments, produced inferred erosion rates ranging from 20 to >3500 m/m.y. (or mm/k.y.). We attribute this high variance in part to lithologic-controlled steepness and hotspots of erosion related to cliff retreat along the White Cliffs (escarpment near Mt. Carmel Junction, Utah), as well as headward drainage expansion along the uppermost Pink Cliffs (escarpment within Bryce Canyon National Park). Initial results from the downslope Vermillion Cliffs (near Kanab) indicate lower erosion rates and overall slope despite similar rock types, suggesting knickzone migration has passed that lower region of our study area. ^{10}Be concentrations measured

along trunk streams systematically match local-subcatchment erosion rates, with muted influence from upstream sediment sources. This is consistent with intermittent sediment conveyance between cliff and bench terrain with sediment storage and then localized release associated with the well-studied, ephemeral arroyo systems in the region. Therefore, detrital cosmogenic nuclide records in transient landscapes may not individually reflect upstream catchment-averaged erosion rates. Yet, they can provide insight into unsteady upslope-directed erosion and downslope-directed sediment conveyance in these dynamic landscapes.

Introduction

Long-term erosion rates are valuable for quantifying the pace of landscape evolution, amount of sediment flux, and rates of geomorphic processes. Cosmogenic-nuclide concentrations in quartz from river sediment are a widespread approach to estimate long-term (10^3-10^6 yr) erosion rates of the upstream contributing area (Granger et al., 1996). This assumes steady state conditions, where the time-averaged sediment and ^{10}Be produced throughout the catchment are in equilibrium with ^{10}Be concentrations and sediment yield leaving the basin. However, many landscapes are not in topographic or erosional steady state and instead are adjusting to changing boundary conditions imposed by tectonic and climatic perturbations. Furthermore, sediment storage and release within catchments impose unsteadiness over centennial to millennial timescales. Under such transient conditions, ^{10}Be concentrations in stream sediment may reflect spatial variability in processes and non-proportional contributions from different source areas

(e.g., Belmont et al., 2007; Willenbring et al., 2013).

In landscapes with steady tectonic and climate forcing and uniform substrate, rivers evolve toward smooth, concave channel longitudinal profiles to match transport capacity with sediment supply throughout the drainage network (Gilbert, 1877; Whipple et al., 1999; Whipple and Tucker, 2002). In contrast, transient landscapes are characterized by channel long-profile convexities and hillslope escarpments, representing spatial disequilibrium in the erosion and sediment routing system. Knickzones can be generated by spatial and temporal variability in tectonic uplift or base level fall (e.g., Whipple and Tucker, 1999; Wobus et al., 2006) or changes in bedrock erodibility (Bursztyn et al., 2015). Specifically, differences in rock erodibility in cliff-bench landscapes complicate sediment yield patterns and inferred mean erosion rates (e.g., Von Blanckenburg, 2006), with cliffs having higher erosion rates partly due to their geometry alone (Forte et al., 2016).

Temporal variations in catchment-scale processes can also influence erosion rates. Watersheds are commonly marked by sediment cascades, where sediment is produced from bedrock, transported downslope, and deposited over variable spatial and temporal scales. In the semi-arid catchments of the Grand Staircase, well-studied arroyo systems produce unsteady sediment cascades exhibiting a complex response to allogenic forcing or autogenic processes (Schumm, 1973; Harvey and Pederson, 2011) Factors and processes related to unsteady sediment cascades can influence ^{10}Be concentrations in alluvium (Viparelli et al., 2013).

In this study, we investigated how inferred erosion rates vary spatially in the topographically and lithologically diverse Grand Staircase region of southern Utah. We

analyzed detrital ^{10}Be concentrations from quartz in 52 samples of modern channel alluvium/colluvium from catchments ranging from 0.01 to 1200 km^2, using standard methods for ^{10}Be isolation and erosion rate calculation (Gosse and Phillips, 2001) as detailed in the Data Repository (see footnote[1]). We address the following questions: What do cosmogenic-nuclide estimates of erosion rate tell us about processes in this transient landscape? Do ^{10}Be concentrations from channel sediment represent upstream catchment-averaged erosion rates? How do apparent erosion rates vary across catchments as rock type and cliff-and-bench topography vary?

Physiographic Setting

This study takes place in the colorful cliff-bench topography of the Grand Staircase in the Colorado Plateau physiographic province, southern Utah. Integration of the Colorado River to the Gulf of California caused dramatic base level fall, resulting in the incision of much of Grand Canyon over the past 6 m.y. (e.g., Longwell, 1946; Spencer et al., 2001; Pederson et al., 2002) and headward migrating incision in the Colorado Plateau (e.g., Cook et al., 2009; Darling and Whipple, 2015; Jochems and Pederson, 2015). It has long been recognized that the topography of the Grand Staircase was developed by recession of escarpments (Dutton and Powell, 1880; Gregory, 1951), but the rates of recession have yet to be quantified. This study focuses on the headwaters

[1] GSA Data Repository item 2019293, Detailed methods, study catchment morphology, and cosmogenic nuclide data are available online at https://www.geosociety.org/datarepository/2019/2019293.pdf, or on request from editing@geosociety.org or Documents Secretary, GSA, P.O. Box 9140, Boulder, CO 80301, USA.

of Kanab Creek, Johnson Wash, Kitchen Corral Wash, and the Paria River, four tributaries draining south to the Colorado River in Grand Canyon and incising through gently north-dipping Mesozoic and Cenozoic sedimentary rocks (Fig. 3-1A). The northward draining East Fork of the Sevier River on the low-relief Paunsaugunt Plateau shares a watershed boundary with all four tributaries and is used for comparison of a watershed with similar lithology, but much gentler gradient toward the Great Basin. The Grand Staircase contains stair-stepped topography with topographic escarpments composed of more resistant sedimentary rocks (Fig. 3-1B); listed in order of ascending elevation the escarpments include the Vermillion, White, Gray, and Pink Cliffs. Benches between the cliffs include the Wygaret, Skutumpah, Podunk, and Paria Terraces.

The long-profile morphology of the N-S oriented stream channels reflects the stratigraphic sequence of rock types that they bisect. For example, the profile of Kanab Creek has a significant knickzone where it crosses the White Cliffs (to the east of Mt. Carmel Junction, Utah; Fig. 3-2A). Streams flowing across the benches between cliffs have lower gradient alluvial reaches with arroyo channels entrenched into Holocene-aged, fine-grained valley-fill alluvium. These semi-arid streams have transitioned between an entrenched arroyo and an aggraded state with an unconfined channel on a broad floodplain multiple times over the last 6 ka. While arroyo aggradation occurs over centuries, entrenchment is quite rapid, observed historically over a few decades (Webb et al., 1991).

Spatial Patterns of Erosion

Detrital ^{10}Be-inferred erosion rates vary spatially in the study area from 20 to >3500 m/Myr (or mm/kyr) reflecting lithologic and geomorphic influences on steepness and erosion rates (Fig. 3-1C and Tables 3-S1 and 3-S2; see footnote[1]). Broadly, the expected correlation between slope and erosion rate is found in this study area (Fig. 3-2A), with small, steep headwater basins (17-25˚ mean slope) draining the Pink Cliffs (Tertiary Claron Formation; such as at Bryce Canyon National Park) recording some of the fastest erosion rates (420-830 mm/kyr; n=6). Less steep (8-12˚ mean slope) headwater basins draining the Skutumpah Terrace (below Bryce Canyon National Park) record lower erosion rates (90-180 mm/kyr; n=3). The highest erosion rates were calculated from steep catchments (9-38˚ mean slope) draining the Navajo sandstone of the White Cliffs (220 to >3500 mm/kyr; n=5), the mid-escarpment of the study area. Interestingly, similarly steep (8-32˚ mean slope) catchments draining the downslope Vermillion Cliffs (near Kanab, Utah) record some of the lowest erosion rates (20-150 mm/kyr; n = 5), though we recognize this includes one notable outlier (Fig 2C). Regardless, low erosion rates in the Vermillion Cliffs are unexpected, as logic and modeling suggest cliff geometry alone should result in consistently high erosion rates (Forte et al., 2016).

Another unexpected observation is that erosion rates are similar in local-sourced tributaries and adjacent trunk streams of the same reach despite differences in the upstream source area (Fig. 2B). We suggest this pattern is due to trunk stream sediment being dominated by local sources and lacking delivery of sediment from upstream. For example, erosion rates calculated from trunk streams drop significantly from 315 ± 30 mm/kyr (n=7) to 130 ± 50 mm/kyr (n=8) after streams cross the slowly eroding

Vermillion Cliffs (90 ± 50 mm/kyr, n=5), suggesting storage or a lack of sediment conveyance from the rapidly eroding escarpments farther upstream (Fig. 1C).

As a test for the influence of proximal versus distal source areas on calculated erosion rates, we discriminated alluvial samples in the field by color and grain-size and compared erosion rates from different subsamples at three locations (Fig. 1C). We interpret red colored, alluvial sand beds as dominantly sourced from Kayenta and Moenave sandstones forming the Vermillion Cliffs, while better sorted alluvial beds of white-colored sand are interpreted as derived from tributaries draining the Navajo Sandstone of the White Cliffs. Results indicate that samples from red-colored beds exhibit erosion rates (60-120 mm/kyr; n=3) similar to the average erosion rate of tributaries draining the Vermillion Cliffs (90 ± 50 mm/kyr; n=5), while white sediments from the same reach produce higher erosion rates (70-200 mm/kyr; n=3), which approach the high erosion rates of the White Cliffs (220 to >3500 mm/kyr). These results further support the interpretation that each reach and bedrock escarpment has distinct erosion rates that are not well mixed in these ephemeral drainages.

Influence of Upslope Knickzone Migration and Unsteady Downslope Sediment Cascades

Apparent erosion rates in the Grand Staircase are characterized by spatial variability and non-proportional contributions from upstream areas, reflecting a transient landscape with variable sediment production, storage, and release. Detrital ^{10}Be concentrations indicate that the White and Pink Cliffs are hotspots for erosion, whereas the Vermillion Cliffs are not. This spatial pattern in erosion rates may reflect upstream-

migrating incision signals from Colorado River baselevel fall. In this scenario, the wave of incision currently reflected in the White and Pink Cliffs has passed the Vermillion Cliffs, although they remain in topographic equilibrium with rock strength as a steep escarpment. Consistent with this, stream long profiles in the study area record a knickzone through the White Cliffs but not through the Vermillion Cliffs downstream (Fig. 3-2A). Also, low erosion rates around the Vermillion Cliffs are consistent with buffering of the entire study area from continued, rapid erosion by the present knickzone downslope below the Kaibab Formation at the Grand Canyon rim (Darling and Whipple, 2015). In contrast, the headwaters of the north-draining E. Fork of the Sevier River erodes the same rock unit as the Pink Cliffs, but it has erosion rates a full magnitude slower (130-50 mm/kyr; n=2) than on the south side of the divide. Differences in gradient across this divide are further testament for disequilibrium and active divide migration to the north along the Pink Cliffs (Fig. 3-1B).

Field observations of Holocene sediment storage in alluvial terraces, colluvial aprons, and aggraded valley-fills suggest the landscape is eroding faster than dryland streams can transport sediment out of the system over Holocene timescales. High erosion rates from the Pink and White Cliffs result in high sediment supply to these mostly ephemeral streams flowing across low-relief benches, leading to stream aggradation and episodic evacuation during arroyo entrenchment. Stratigraphic evidence exposed in arroyo walls indicates streams across the region have oscillated between aggraded fills and entrenched arroyos during the last 3-6 kyr with cycle lengths of 0.3-0.9 kyr (Townsend et al., 2019). While individual arroyo cycles are too short in duration to be explained by changes in sediment production, linkages between the mid Holocene

initiation of arroyo dynamics and enhanced erosion rates are possible, as ^{10}Be concentrations and production rates indicate that our erosion-rate values from alluvial samples are integrated over 3.8 kyr timescales (0.2-18 kyr range). Alluvial sediment yields calculated from cosmogenic-derived erosion rates range from 90 to >2200 Mg/km^2/yr (mean 930 Mg/km^2/yr, ρ= 2.6 g cm^{-3}, Table 3-S2, see footnote[1]). These estimates are consistent with sediment gauge data, for example, in Kanab Creek mean annual (CE 1968-1973) sediment yield of 290 Mg/km^2/yr (Webb and Griffiths, 2001) matches well the long-term cosmogenic derived sediment yield of 300 Mg/km^2/yr from the same reach (sample 20, Table 3-S2, see footnote[1]). This consistency suggests that modern sediment transport operates at similar rates as long-term erosion rates averaging over centuries to millennia, which is surprising, considering spatial and temporal variability in erosion in the study area. However, there have been times in the past 200 years when sediment yields were much higher or lower than the long-term rate, and that historic sediment yields may average out to the long-term rate by coincidence.

Conclusion and Implications

It is commonly assumed that detrital ^{10}Be concentrations in alluvial sediment from steady-state landscapes reflect catchment-averaged erosion rates. However, interpretations are more complex in disequillibrium landscapes with upslope-directed transient erosion and downslope-directed unsteady sediment cascades. In such cases, ^{10}Be concentrations likely reflect disproportional contributions from upstream areas due to lithologic and topographic variations and intermittent sediment storage and transport.

In the stair-stepped landscape of the Grand Staircase, cosmogenic ^{10}Be erosion rates exhibit high spatial variability from 20 to >3500 m/Myr, which nevertheless follow an expected correlation between slope and erosion rate. An exception to this rule is that the lowest erosion rates are observed in the Vermillion Cliffs, the first major escarpment upslope of the Grand Canyon rim, counter to model expectations (e.g. Forte et al. 2016). Additional data and further testing will be needed to confirm this result and determine its explanation. Hotspots of erosion are focused in the upper escarpments of the White and Pink Cliffs, interpreted as the locations of migrating knickzones and basin expansion. These hotspots of erosion produce high, local sediment yields (500 to >2000 Mg/km^2/yr) by cliff retreat, leading to episodic sediment storage on low-relief benches and alluvial-valley fills downstream. Cosmogenic ^{10}Be concentrations measured along trunk streams match local-catchment erosion rates more so than up-catchment averages, which we suggest reflects the intermittent sediment conveyance between cliff and bench topographies and episodic, local sediment supply characteristic of arroyo systems. Although individual ^{10}Be values within a transient landscape may not provide accurate erosion rate averages, such data can provide valuable insights related to both upslope and downslope-directed, unsteady geomorphic processes.

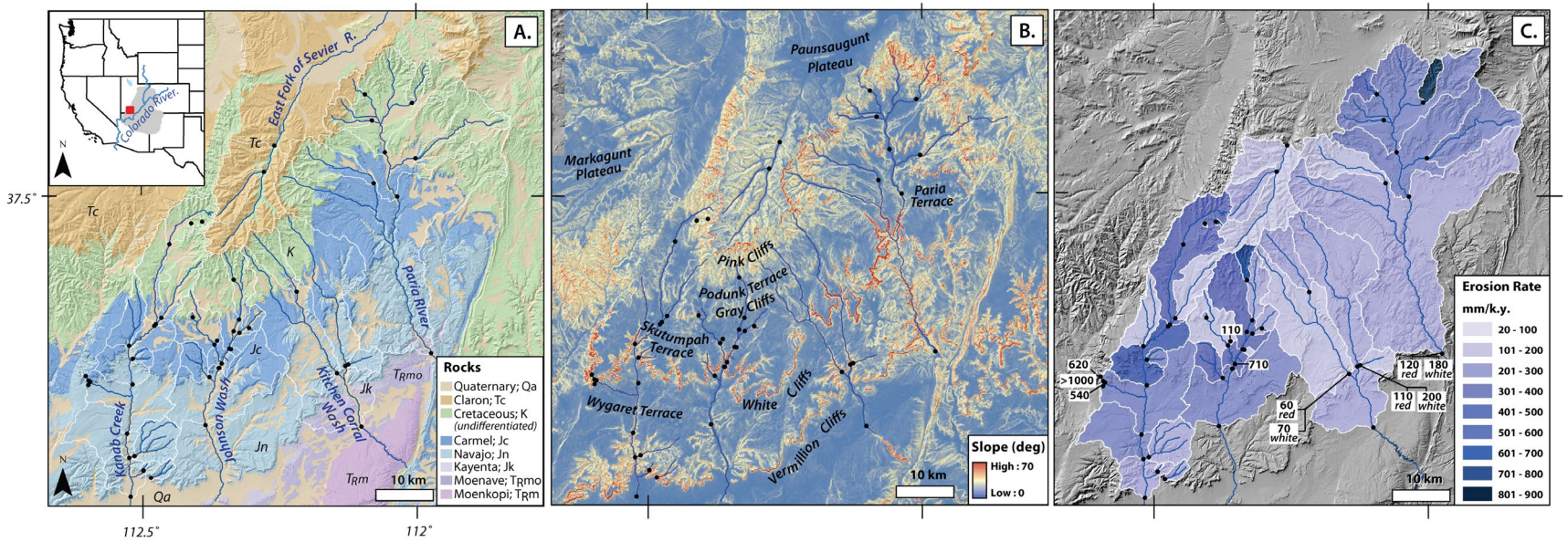

Figure 3-1 – **A)** Geologic map of the study area; black dots indicate sample locations for detrital ^{10}Be. Inset map shows location of the study area in southern Utah, the Colorado Plateau and Colorado River in the western US. **B)** Slope map shows the prominent escarpments in red tones and low relief slopes in blue tones. Names of escarpments (cliffs) and benches (terraces) indicated. Note steep headwater escarpment of southward draining streams forming the Pink Cliffs and low relief of the Paunsaugunt Plateau. These geomorphic relationships indicate headward drainage migration. **C)** Mean erosion rates for the upstream contributing area inferred from detrital ^{10}Be concentrations. Erosion rate values are annotated for catchments too small to see at this scale. Cosmogenic nuclide and erosion rate data are available as supplemental data (see footnote[1]).

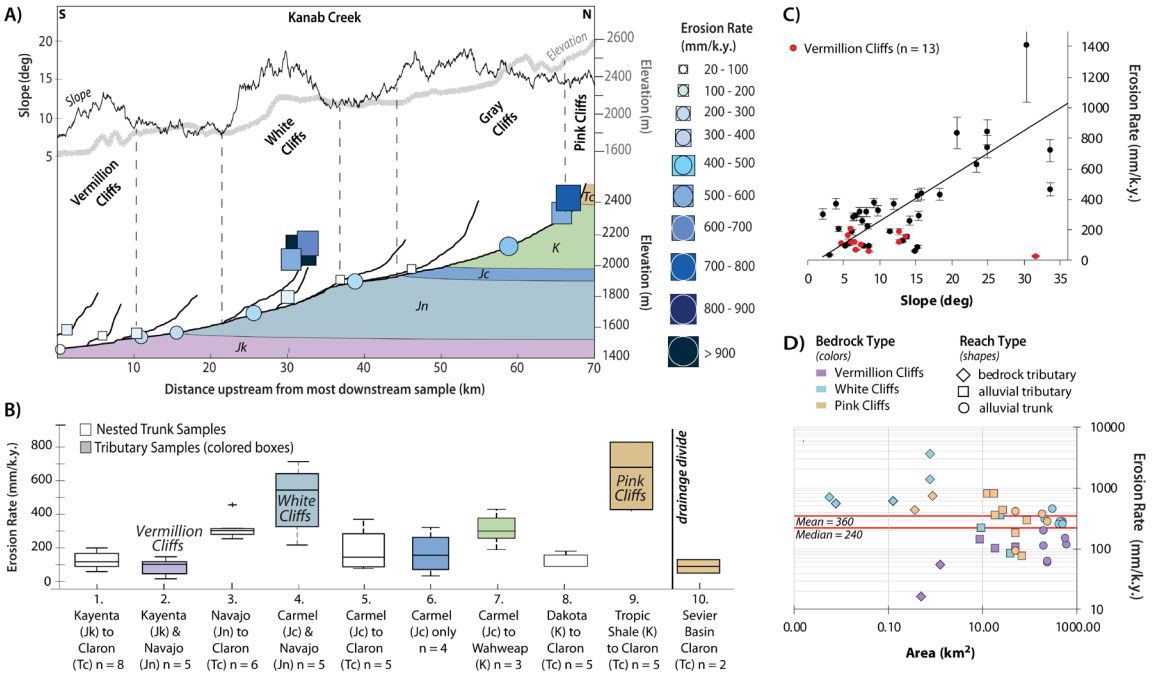

Figure 3-2 – A) The longitudinal profile of Kanab Creek, Utah, and its tributaries are plotted on the bottom with lithologic unit identified (for rock units, see Fig. 1 and Table DR 3 [footnote[1]]). Erosion rate samples collected along the trunk stream in Kanab Creek are indicated with circles and tributary samples with squares. The size and color of the symbol (circle or square) represents the magnitude of erosion rate. The mean terrain slope and elevation calculated along a swath-transect from the northern divide of the watershed to the southern outlet are plotted at the top. **B)** Box-and-whisker plot showing how erosion rates vary when grouped by lithology of the upstream contributing area, plotted and numbered in order of downstream to upstream sample locations. Note higher erosion rates are measured in basins draining the White and Pink Cliffs (Grand Staircase, southern Utah) and lower erosion rates are measured in the Vermillion Cliffs. White boxes represent nested samples from the trunk stream and colored boxes represent samples from local tributary catchments draining rock units as color-coded in panel A. **C)** Median catchment slope corresponds with erosion rate. Data highlighted in red are from the Vermillion Cliffs, where no erosion rates above 200 mm/k.y. were found, and an outlier sample exists. Vermillion Cliffs samples include trunk and tributary rock type groups #1 and #2 (see Table DR3). **D)** Log-log plot of erosion rates versus catchment area. Data are classified by lithology and stream reach morphology. Mean erosion rate for the entire study area is 360 mm/kyr and the median is 240 mm/kyr.

Acknowledgments

We would like to than Cliff Riebe and Claire Lukens for expertise and access to the cosmogenic nuclide lab at the University of Wyoming (Laramie, Wyoming, USA) and the PRIME Lab (Purdue Rare Isotope Measurement Laboratory) at Purdue University (West Lafayette, Indiana) for quartz processing, nuclide extraction, and measurements. We would also like to thank the National Science Foundation for funding this research (EAR-1057192 and EAR -1536296) awarded to Rittenour and Riley.

References Cited

Belmont, P., Pazzaglia, F. J., and Gosse, J. C., 2007, Cosmogenic Be-10 as a tracer for hillslope and channel sediment dynamics in the Clearwater River, western Washington State: Earth and Planetary Science Letters, v. 264, no. 1-2, p. 123-135.

Bursztyn, N., Pederson, J., Tressler, C., Mackley, R., and Mitchell, K., 2015, Rock strength along a fluvial transect of the Colorado Plateau–quantifying a fundamental control on geomorphology: Earth and Planetary Science Letters, v. 429, p. 90-100.

Cook, K. L., Whipple, K. X., Heimsath, A. M., and Hanks, T. C., 2009, Rapid incision of the Colorado River in Glen Canyon–insights from channel profiles, local incision rates, and modeling of lithologic controls: Earth Surface Processes and Landforms, v. 34, no. 7, p. 994-1010.

Darling, A., and Whipple, K., 2015, Geomorphic constraints on the age of the western Grand Canyon: Geosphere, v. 11, no. 4, p. 958-976.

Dutton, C. E., and Powell, J. W., 1880, Report on the Geology of the High Plateaus of Utah: Government Printing Office.

Forte, A. M., Yanites, B. J., and Whipple, K. X., 2016, Complexities of landscape evolution during incision through layered stratigraphy with contrasts in rock strength: Earth Surface Processes and Landforms, v. 41, no. 12, p. 1736-1757.

Gilbert, G., 1877, Geology of the Henry Mountains: US geographical and geological survey of the Rocky Mountain region: US Government Printing Office: Washington, DC.

Gosse, J. C., and Phillips, F. M., 2001, Terrestrial in situ cosmogenic nuclides: theory and application: Quaternary Science Reviews, v. 20, no. 14, p. 1475-1560.

Granger, D. E., Kirchner, J. W., and Finkel, R., 1996, Spatially Averaged Long-Term Erosion Rates Measured from in Situ-Produced Cosmogenic Nuclides in Alluvial Sediment: The Journal of Geology, v. 104, no. 3, p. 249-257.

Gregory, H. E., 1951, The geology and geography of the Paunsaugunt region, Utah, 2330-7102.

Harvey, J. E., and Pederson, J. L., 2011, Reconciling arroyo cycle and paleoflood approaches to late Holocene alluvial records in dryland streams: Quaternary Science Reviews, v. 30, no. 7-8, p. 855-866.

Jochems, A. P., and Pederson, J. L., 2015, Active salt deformation and rapid, transient incision along the Colorado River near Moab, Utah: Journal of Geophysical Research: Earth Surface, v. 120, no. 4, p. 730-744.

Longwell, C. R., 1946, How old is the Colorado River?: American Journal of Science, v. 244, no. 12, p. 817-835.

Pederson, J. L., Mackley, R. D., and Eddleman, J. L., 2002, Colorado Plateau uplift and erosion evaluated using GIS: GSA TODAY, v. 12, no. 8, p. 4-10.

Schumm, S., 1973, Geomorphic thresholds and complex response of drainage systems: Fluvial geomorphology, v. 6, p. 69-85.

Spencer, J., Peters, L., McIntosh, W., Patchett, P., Young, R., and Spamer, E., 2001, 40Ar/39Ar geochronology of the Hualapai Limestone and Bouse Formation and implications for the age of the lower Colorado River: Colorado River: Origin and evolution: Grand Canyon, Arizona, Grand Canyon Association, p. 89-91.

Townsend, K. F., Nelson, M. S., Rittenour, T. M., and Pederson, J. L., 2019, Anatomy and evolution of a dynamic arroyo system, Kanab Creek, southern Utah, USA: Geological Society of America Bulletin.

Viparelli, E., Lauer, J. W., Belmont, P., and Parker, G., 2013, A numerical model to develop long-term sediment budgets using isotopic sediment fingerprints: Computers & geosciences, v. 53, p. 114-122.

Von Blanckenburg, F., 2006, The control mechanisms of erosion and weathering at basin scale from cosmogenic nuclides in river sediment: Earth and Planetary Science Letters, v. 242, no. 3-4, p. 224-239.

Webb, R. H., and Griffiths, P. G., Techniques for Estimating Sediment Yield of Ungaged Tributaries on the Southern Colorado Plateau, *in* Proceedings Proceedings of the Seventh Federal Interagency Sedimentation Conference, Reno, Nevada, 2001.

Webb, R. H., Smith, S. S., and McCord, V. A., 1991, Historic channel change of Kanab Creek, Southern Utah and Northern Arizona: Grand Canyon, Natural History Association Monograph.

Whipple, K. X., Kirby, E., and Brocklehurst, S. H., 1999, Geomorphic limits to climate-induced increases in topographic relief: Nature, v. 401, no. 6748, p. 39-43.

Whipple, K. X., and Tucker, G. E., 1999, Dynamics of the stream-power river incision model: Implications for height limits of mountain ranges, landscape response timescales, and research needs: Journal of Geophysical Research: Solid Earth, v. 104, no. B8, p. 17661-17674.

Whipple, K. X., and Tucker, G. E., 2002, Implications of sediment-flux-dependent river incision models for landscape evolution: Journal of Geophysical Research: Solid Earth, v. 107, no. B2, p. ETG 3-1-ETG 3-20.

Willenbring, J. K., Gasparini, N. M., Crosby, B. T., and Brocard, G., 2013, What does a mean mean? The temporal evolution of detrital cosmogenic denudation rates in a transient landscape: Geology, v. 41, no. 12, p. 1215-1218.

Wobus, C., Whipple, K. X., Kirby, E., Snyder, N., Johnson, J., Spyropolou, K., Crosby, B., and Sheehan, D., 2006, Tectonics from topography: Procedures, promise, and pitfalls: Special Papers-Geological Society of America, v. 398, p. 55.

GSA Data Repository item 2019293 (Supplemental Material)

Erosion Rates from Cosmogenic Nuclides Methods

The production of cosmogenic ^{10}Be in quartz dominantly occurs in the upper 1-2 m of Earth's surface through neutron spallation and muon capture at a predictable rate (Lal, 1991) allowing the accumulated ^{10}Be concentration to be a proxy for denudation rates. In our study, denudation is largely driven by physical erosion, as chemical weathering is minimal due to semi-arid conditions (Riebe and Granger, 2013). The accumulation of ^{10}Be is proportional to the average production rate and inversely proportional to the average erosion rate over the contributing area (Granger et al., 1996). We analyzed 49 samples of modern channel alluvium and 3 samples of colluvium from catchment areas ranging from 0.01 to 1200 km^2. Duplicate samples from different channel barforms within the same reach were collected at three locations to compare how erosion rates vary based on source lithology, which was differentiated based on sediment color. We also tested the heterogeneity of ^{10}Be within individual samples by analyzing three pairs of replicates. We isolated ^{10}Be from quartz extracts using standard practices (Kohl and Nishiizumi, 1992), spiked the ^{10}Be isolate with ^{9}Be, measured ^{10}Be concentrations using accelerator mass spectrometry, and calculated erosion rates using the CRONUS online calculator Version 2.3 (Balco et al., 2008).

Quartz was isolated from 250-500 micron grain size fraction of alluvial and colluvial samples at Utah State University and the University of Wyoming by physical and chemical methods (Kohl and Nishiizumi, 1992; Granger et al., 1996). The quartz was

then spiked with a ^{9}Be carrier (~0.8 g of carrier for each sample). Each batch of samples processed contained at least one process blank. We first digested the quartz and then a series of acid fuming treatments were performed to remove Flouro-Silica compounds. Iron and Titanium were removed through a series of precipitation reactions. Beryllium was then separated by ion exchange chromatography, precipitated, dried, and converted to Beryllium Oxide. The Beryllium Oxide was mixed with a Niobium binder and then packed into cathodes. BeO targets were prepared for Accelerator Mass Spectrometry, which yielded measurements of ^{10}Be/^{9}Be. Be-10 concentrations were calculated using the ratio of ^{10}Be/^{9}Be and concentrations of Be in the quartz determined from the measurements of quartz masses and Be carrier masses. The Be concentration is a function of production rate and the average erosion rate over a timescale of the order attenuation depth (Λ)/ erosion rate (E) (Granger et al., 1996) assuming that the constant radionuclide meanlife of 2.2 My is greater than Λ/E. Erosion must be rapid enough to make radioactive decay insignificant. The production rate of ^{10}Be is a function of altitude, latitude, longitude, irradiation geometry, and cosmic shielding. Shielding correction factors applied to production rates were based on original work by Dunne et al. (1999) and calculated in Matlab using the code in Topo Toolbox v2 (Schwanghart and Scherler, 2014). Differences between topographic shielding factors calculated using a 10 m USGS NED 1/3 arc second versus 30 m digital elevation models were minimal (< 5%) for the first 25 basins analyzed. Topographic shielding factors were calculated only using 30m DEM for the remaining basins. The hypsometric-weighted-average elevation and latitude for each basin were calculated and input into the CRONUS calculator. The CRONUS-Earth Project ^{10}Be–^{26}Al calculator was used to calculate surface erosion rates. Production

rates were calculated for the contributing area of each sample based on inputs (Table 3-S2) to the calculator including: sample name, latitude (dd), longitude (dd), elevation (m), elv/pressure (flag), thickness (cm), density (gcm^{-2}), shielding, [Be-10] ($atomsg^{-1}$), error ($atomsg^{-1}$), and name of Be-10 standardization ($atomsg^{-1}$).

Table 3-S1 –– Sample location and cosmogenic nuclide data for study catchments.

Sample # [1]	PRIME ID	Rock Type Group [2]	Basin Scale	Location Name	Sample Elev. (m)	Sample Latitude (dd)	Sample Longitude (dd)	Area (km^2)	$^{10}Be/^{9}Be$ (10^{-15})	^{10}Be Concentration (10^4 atoms g^{-1}) [4]	Analytical Error % [4]
1	201401583	4	colluvium	White Cliffs Apron	2016	37.19350	-112.622434	0.01	74.480	1.96 ± 0.11	6
2	201603171	4	tributary	Red Canyon	2011	37.20744	-112.626880	0.1	95.736	1.89 ± 0.05	3
3	201501042	9	tributary	Rush Canyon	2334	37.44780	-112.425630	0.4	131.111	3.30 ± 0.13	4
4	201600330	2	colluvium	Vermillion Cliffs Apron	1557	37.05946	-112.511611	0.5	21.784	43.88 ± 3.98	9
5 [3]	201501045	4	tributary	Red Canyon	1886	37.20445	-112.623770	0.8	13.611	0.31 ± 0.07	23
6 [3]	201700337	4	tributary	Red Canyon	1886	37.20445	-112.623770	0.8	13.150	0.78 ± 0.18	24
7	201401582	9	tributary	Rush Canyon	2381	37.45369	-112.405110	0.9	76.7224	1.96 ± 0.11	5
8	201600329	2	tributary	Toms Canyon Trib.	1547	37.06022	-112.512130	1.3	782.593	16.09 ± 0.28	2
9	201600320	2	tributary	Pugh Canyon	1547	37.04907	-112.496023	9	336.279	6.24 ± 0.16	3
10	201401585	4	tributary	Basalt Gates	1732	37.23610	-112.536628	9	182.117	4.85 ± 0.19	4
11	201401584	7	tributary	Fourmile Hollow	1765	37.25740	-112.543931	40	461.607	12.72 ± 0.40	3
12	201700336	5	tributary	Sink Valley Wash	1910	37.30262	-112.484102	50	176.315	13.10 ± 0.39	3
13	201600327	2	tributary	Hog Canyon	1539	37.08308	-112.526285	51	318.908	8.57 ± 0.46	5
14	201501043	9	trunk	40.5 km upstream	2073	37.46326	-112.428570	51	116.566	3.30 ± 0.13	4
15	201501044	5	trunk	39 km upstream	1894	37.39920	-112.455670	190	113.127	3.43 ± 0.15	4
16 [3]	201401586	3	trunk	24 km upstream	1668	37.19471	-112.536020	315	93.762	2.38 ± 0.12	5
17 [3]	201600326	3	trunk	24 km upstream	1668	37.19471	-112.536020	315	86.923	3.58 ± 0.25	7
18	201401587	3	trunk	12.7 km upstream	1549	37.11864	-112.543931	440	161.275	3.92 ± 0.15	4
19	201401588	3	trunk	8 km upstream	1532	37.08091	-112.540279	517	148.789	3.90 ± 0.16	4
20	201603170	1	trunk	0 km upstream	1476	37.01855	-112.537484	616	265.839	9.09 ± 0.25	3
21	201603165	4	colluvium	White Cliffs Apron	1764	37.22949	-112.364448	0.01	48.326	1.22 ± 0.09	7
22	201600316	6	tributary	Little Carmel	1847	37.26362	-112.368414	0.2	302.319	9.16 ± 0.33	4
23	201401590	6	tributary	Red Creek	1878	37.28843	-112.311463	0.5	127.882	3.26 ± 0.20	6
24	201501037	7	tributary	Bald Knoll West	1977	37.30302	-112.418589	1	161.451	6.16 ± 0.27	4
25	201401592	5	tributary	Skutumpah	1820	37.25374	-112.345542	2	1798.130	29.99 ± 0.78	3
26 [3]	201501038	9	tributary	Mill Creek	2085	37.36506	-112.342016	13	57.558	1.67 ± 0.15	9
27 [3]	201600314	9	tributary	Mill Creek	2085	37.36506	-112.342016	13	114.156	2.22 ± 0.09	4
28	201401591	6	tributary	Red Creek	1828	37.28052	-112.328502	14	193.803	5.24 ± 0.20	4
29	201501040	4	tributary	Swapp Creek	1730	37.20900	-112.386603	25	77.918	2.87 ± 0.17	6

Table 3-S1 (*continued*)

Sample # [1]	PRIME ID	Rock Type Group [2]	Basin Scale	Location Name	Sample Elev. (m)	Sample Latitude (dd)	Sample Longitude (dd)	Area (km^2)	$^{10}Be/^{9}Be$ (10^{-15})	^{10}Be Concentration (10^4 atoms g^{-1}) [4]	Analytical Error % [4]
30	201700343	5	trunk	26 km upstream	1856	37.30031	-112.330183	44	128.088	8.49 ± 0.32	4
31	201501041	7	trunk	23 km upstream	1807	37.26038	-112.377879	55	310.719	11.59 ± 0.34	3
32	201501039	3	trunk	21 km upstream	1775	37.25418	-112.349316	141	99.282	3.71 ± 0.17	5
33	201501035	3	trunk	11.5 km upstream	1513	37.22313	-112.369419	213	91.192	3.66 ± 0.20	5
34	201600315	3	trunk	0 km upstream	1664	37.13210	-112.390823	412	140.082	4.28 ± 0.21	5
35	201600324	2	tributary	Box Elder Canyon	1703	37.23109	-112.117414	19	459.843	9.97 ± 0.22	2
36	201600325	8	tributary	Meadow Creek	1894	37.34464	-112.216949	50	251.474	7.05 ± 0.24	3
37	201600318	1	trunk	Park Wash (red)	1698	37.22902	-112.123033	200	367.026	9.79 ± 0.23	2
38	201600319	1	trunk	Park Wash (white)	1698	37.22902	-112.123033	200	289.140	5.51 ± 0.21	4
39	201700345	1	trunk	Park Wash Site E (red)	1691	37.21693	-112.140588	238	220.126	18.93 ± 0.46	2
40	201700334	1	trunk	Park Wash Site E (white)	1691	37.21693	-112.140588	238	247.507	17.31 ± 0.45	3
41	201600332	1	trunk	0 km upstream	1616	37.13218	-112.091533	559	259.012	7.09 ± 0.20	3
42	201603166	9	tributary	Henderson Creek	1990	37.64638	-112.002389	18	75.972	1.49 ± 0.08	5
43	201600321	8	tributary	Upper Paria	1991	37.65741	-112.091018	19	121.177	3.54 ± 0.13	4
44	201600331	8	tributary	Bryce Creek	1902	37.61719	-112.077119	28	138.656	2.92 ± 0.15	5
45	201700344	5	tributary	Sheep Creek	1836	37.51960	-112.074344	69	207.224	15.60 ± 0.39	3
46	201700328	8	tributary	Henryville Creek	1817	37.56056	-111.98877	87	82.854	4.09 ± 0.34	8
47	201700329	8	trunk	43 km upstream	1786	37.56193	-112.051099	246	98.257	4.39 ± 0.26	6
48	201700351	5	trunk	35 km upstream	1697	37.49790	-112.024089	495	79.949	4.64 ± 0.34	7
49	201700349	1	trunk	0 km upstream (white)	1443	37.25348	-111.957845	1170	98.904	6.18 ± 0.58	9
50	201700350	1	trunk	0 km upstream (red)	1443	37.25348	-111.957845	1170	75.986	9.48 ± 0.48	5
51	201600322	10	tributary	Upper Kanab Creek	2425	37.53012	-112.285115	40	731.269	13.17 ± 0.22	2
52	201700333	10	trunk	Upper Sevier Creek	2047	37.57671	-112.265081	185	278.926	31.21 ± 0.97	3

[1] Sample locations are shown on Figure DR 1, ordered based on catchment area

[2] Rock type group based on upstream contributing area and are identified in Figure 2B and described in Tables DR 3 and DR 4

[3] Replicate analysis of the same samples (numbers 5 & 6, 16 & 17 and 26 & 27). Result with the lowest analytical error was used for apparent erosion rate calculation.

[4] Input to the CRONUS-Earth Project ^{10}Be–^{26}Al calculator.

Table 3-S2 - CRONUS inputs, Be-10 production rates, erosion rates and sediment yields, and topographic metrics.

Sample	Type/ Scale	Rock Type Group[2]	Basin Area (km^2)	Basin Mean Ksn[3]	Basin Mean Slope (deg)	Basin Total Relief (km)	Basin Mean Lat. (dd) [4]	Basin Mean Long. (dd) [4]	Eff. Elev. (m) [4]	Topo. Shield Factor [4]	Basin Mean Production Rate (at/g/yr)	Sample Site Production Rate (at/g/yr)	% Diff.	Erosion Rate [5] (mm/kyr)	Sediment Yield [6] (Mg km^{-2}yr^{-1})	T_{ave} (kyr) [7]
1	colluvium	4	0.01	-	38	0.1	37.1931	-112.6221	2056	0.921	16.647	15.874	5	540 ± 80	1420	1.1
2	tributary	4	0.1	5.29	21	0.2	37.2095	-112.6300	2133	0.962	18.310	16.503	10	620 ± 90	1610	1.0
3	tributary	9	0.4	4.67	19	0.3	37.4478	-112.4257	2405	0.983	22.493	20.958	7	430 ± 60	1110	1.4
4	colluvium	2	0.5	-	32	0.1	37.0598	-112.5100	1606	0.872	11.457	10.905	5	15 ± 5	40	36.7
5	tributary	4	0.8	-	30	0.3	37.1931	-112.6221	2057	0.943	17.017	14.848	13	3560 ± 990	9260	.2
6	tributary	4	0.8	-	30	0.3	37.1931	-112.6221	2057	0.943	17.017	14.848	13	1400 ± 400	3640	.4
7	tributary	9	0.9	4.64	25	0.4	37.4522	-112.3994	2504	0.940	23.008	20.730	10	740 ± 110	1920	.8
8	tributary	2	1.3	7.07	12	0.2	37.0673	-112.5100	1735	0.983	14.133	12.184	14	55 ± 10	150	10.7
9	tributary	2	9	5.83	16	0.4	37.0607	-112.4700	1760	0.973	14.244	12.054	15	150 ± 20	380	4.1
10	tributary	4	9	7.01	15	0.3	37.2400	-112.5148	1948	0.984	16.472	13.922	15	220 ± 30	570	2.8
11	tributary	7	40	3.88	12	0.6	37.3011	-112.5426	1995	0.992	17.214	14.403	16	85 ± 10	220	7.0
12	trunk	5	50	3.18	11	0.9	37.3579	-112.4461	2137	0.991	18.980	15.919	16	90 ± 10	240	6.6
13	tributary	2	51	3.30	8	0.4	37.1068	-112.4900	1751	0.992	14.453	12.244	15	110 ± 20	280	5.5
14	trunk	9	51	4.07	17	0.8	37.4631	-112.4284	2382	0.972	21.942	17.476	20	420 ± 60	1090	1.4
15	trunk	5	190	3.67	13	0.9	37.3991	-112.4553	2217	0.985	20.044	15.778	21	370 ± 50	960	1.6
16	trunk	3	315	3.89	37	1.1	37.2583	-112.5090	1976	0.985	16.973	13.439	21	460 ± 70	1190	1.3
17	trunk	3	315	3.89	37	1.1	37.2583	-112.5090	1976	0.985	16.973	13.439	21	300 ± 50	790	2.0
18	trunk	3	440	3.83	12	1.3	37.2999	-112.4968	2038	0.986	17.726	12.344	30	290 ± 40	750	2.1
19	trunk	3	517	3.76	11	1.3	37.2583	-112.5090	1976	0.987	16.973	12.184	28	280 ± 40	720	2.2
20	trunk	1	616	3.76	11	1.4	37.2441	-112.5100	1957	0.986	16.742	11.692	30	120 ± 20	300	5.1
21	colluvium	4	0.01	-	33	0.2	37.2300	-112.3620	1860	0.843	13.298	12.223	8	710 ± 110	1860	.8
22	tributary	6	0.2	1.49	6	0.1	37.2669	-112.3700	1863	0.999	15.848	15.386	3	110 ± 20	290	5.4
23	tributary	6	0.5	2.87	13	0.1	37.2851	-112.3100	1926	0.994	16.401	15.568	5	320 ± 50	840	1.9
24	tributary	7	1	2.51	9	0.1	37.3079	-112.4200	2038	0.993	17.726	16.662	6	180 ± 30	480	3.3
25	tributary	5	2	5.22	5	0.1	37.2513	-112.3400	1896	0.977	15.890	14.805	7	35 ± 5	90	18.1
26	tributary	9	13	5.01	22	0.8	37.3962	-112.3500	2399	0.957	21.923	17.397	21	830 ± 140	2160	.7
27	tributary	9	13	5.01	22	0.8	37.3962	-112.3500	2399	0.957	21.923	17.397	21	620 ± 90	1620	1.0
28	tributary	6	14	2.10	7	0.3	37.3003	-112.3000	1926	0.995	16.571	15.196	8	200 ± 30	530	3.0
29	tributary	4	25	3.99	9	0.3	37.2354	-112.4200	1928	0.982	16.241	13.892	14	360 ± 50	940	1.7
30	trunk	5	44	3.85	16	1.0	37.3661	-112.3292	2194	0.977	19.523	15.187	22	150 ± 20	380	4.1
31	trunk	7	55	2.19	8	0.4	37.2933	-112.4100	1968	0.995	17.053	14.965	12	95 ± 15	240	6.4
32	trunk	3	141	3.33	11	1.1	37.3376	-112.3500	2096	0.986	18.448	14.493	21	320 ± 50	820	1.9
33	trunk	3	213	3.26	12	1.1	37.3185	-112.3700	2050	0.987	17.876	12.053	33	310 ± 50	810	1.9
34	trunk	3	412	3.26	13	0.3	37.2625	-112.3600	1982	0.985	17.043	13.379	21	250 ± 40	660	2.4

Table 3-S2 (*continued*)

Sample # [1]	Type/ Scale	Rock Type Group[2]	Basin Area (km^2)	Basin Mean Ksn[3]	Basin Mean Slope (deg)	Basin Total Relief (km)	Basin Mean Lat. (dd) [4]	Basin Mean Long. (dd) [4]	Eff. Elev. (m) [4]	Topo. Shield Factor [4]	Basin Mean Production Rate (at/g/yr)	Sample Site Production Rate (at/g/yr)	% Diff.	Erosion Rate [5] (mm/kyr)	Sediment Yield [6] ($Mg\ km^{-2}yr^{-1}$)	T_{ave} (kyr) [7]
35	tributary	2	19	3.04	9	0.3	37.2399	-112.0797	1884	0.993	15.909	13.780	13	100 ± 10	260	5.9
36	tributary	8	50	5.18	13	0.9	37.4022	-112.2669	2302	0.984	20.998	15.598	26	190 ± 30	490	3.2
37	trunk	1	200	4.16	10	1.1	37.3702	-112.1635	2049	0.982	17.696	13.590	23	110 ± 20	300	5.2
38	trunk	1	200	4.16	10	1.1	37.3702	-112.1635	2049	0.982	17.696	13.590	23	200 ± 30	530	2.9
39	trunk	1	238	3.59	11	1.2	37.3118	-112.2333	2050	0.987	17.866	13.660	24	60 ± 10	150	10.1
40	trunk	1	238	3.59	11	1.2	37.3118	-112.2333	2050	0.987	17.866	13.660	24	65 ± 10	170	9.3
41	trunk	1	559	3.59	9	1.2	37.3051	-112.1848	1996	0.985	17.214	12.937	25	150 ± 20	400	3.9
42	tributary	9	18	3.41	24	0.6	37.6795	-111.9852	2228	0.951	19.495	16.252	17	830 ± 120	2170	.7
43	tributary	8	19	4.78	13	0.5	37.6704	-112.1201	2236	0.986	20.425	16.952	17	360 ± 50	950	1.7
44	tributary	8	28	4.39	17	0.6	37.6264	-112.1355	2225	0.974	19.844	15.619	21	430 ± 60	1120	1.4
45	tributary	5	69	3.60	15	0.8	37.5538	-112.1706	2185	0.976	19.483	15.046	23	80 ± 10	200	7.7
46	tributary	8	87	3.70	2	1.0	37.6040	-111.8956	2160	0.975	19.171	14.865	22	300 ± 50	770	2.0
47	trunk	8	246	4.37	18	1.3	37.6614	-112.0396	2213	0.972	19.704	14.404	27	280 ± 40	740	2.1
48	trunk	5	495	4.02	17	1.4	37.6268	-112.0068	2142	0.974	18.761	13.520	28	260 ± 40	670	2.3
49	trunk	1	1170	4.11	16	1.7	37.5240	-112.0316	2045	0.974	17.526	11.230	36	180 ± 30	470	3.3
50	trunk	1	1170	4.11	16	1.7	37.5240	-112.0316	2045	0.974	17.526	11.230	36	120 ± 20	310	5.1
51	tributary	10	40	4.09	14	0.4	37.4971	-112.34	2665	0.986	26.866	22.482	16	126 ± 18	330	4.8
52	trunk	10	185	3.87	15	0.5	37.5004	-112.32	2639	0.987	26.425	17.575	33	52 ± 7	140	11.5

[1] Sample locations are shown on Figure DR 1, ordered based on catchment area

[2] Rock type groups are described in Table DR 3 and Table DR 4.

[3] Channel steepness (K_{sn}) was calculated using a reference concavity (-0.0350) defined by the regional slope/area plot.

[4] Input to the CRONUS-Earth Project ^{10}Be–^{26}Al calculator.

[5] Uncertainties in erosion rates are propagated from AMS uncertainties and include a 10% 1σ uncertainty in nuclide production rates including scaling factors for altitude, latitude, and topographic shielding and a 5% 1σ uncertainty in density, attenuation coefficients, and half-lives.

[6] Sediment yields were calculated using erosion rates and a density of 2.6 g cm^{-3} and rounded to the nearest 10 Mg $km^{-2}yr^{-1}$.

[7] The interval of time that the catchment-averaged erosion rates are averaged over (T_{ave})

Table 3-S3 - Description of rock type groups (Doelling et al., 2000).

Rock Type Group #	Description
1	Kayenta to Claron: Basins that contain all lithologies described below including Tc, Kk, Kw, Ks, Kt, Kd, Jcl, Jn, and Jk.
2	Kayenta and Navajo: Basins contain lower Jurassic rocks including the Kayenta Formation (Jk) and Navajo Sandstone (Jn). Kayenta forms the upper part of the Vermillion Cliffs and is the surface of the Wygaret Terrace, is 190-350 feet thick, and is a succession of lenticular, primarily medium-grained, fluvial cross-bedded, thick-bedded sandstone with thinner red inter-beds of siltstone and mudstone that forms thick ledges. Navajo Sandstone is a massive 1300-1500 feet thick cliff-forming rock, whose upper part forms the White Cliffs of the Grand Staircase. Navajo Sandstone is light-colored, sub-rounded to well rounded, well sorted, fine- to medium-grained, frosted, and quartz-rich with high angle cross-beds. The Navajo Sandstone is characterized by smooth vertical or rounded cliffs.
3	Navajo to Claron: Basins contain Navajo Sandstone described above and all lithologies described below including Tc, Kk, Kw, Ks, Kt, Kd, Jcl, and Jn.
4	Carmel and Navajo: Basins contain Navajo Sandstone described above and is overlain by Jurassic rocks of the lower and upper Carmel Formation (Jc). The lower Carmel Formation grades into Page Sandstone from west to east in the Paria River. In the Grand Staircase region, the lower Carmel Formation consists of sandstones, siltstones, calcareous shale, and some limestone.
5	Carmel to Claron: Basins contain the Carmel Formation described above and all lithologies described below including Tc, Kk, Kw, Ks, Kt, Kd, and Jcl.
6	Carmel: Basins only contain members of the Carmel Formation described above.
7	Carmel to Wahweap: Basins contain the lower Carmel Formation described above as well as Jurassic rocks from the Entrada Sandstone (Je) and Cretaceous rocks including the Dakota Formation (Kd), Tropic Shale (Kt), Straight Cliffs Formation (Ks), and the Wahweap Formation (Kw). On the Skutumpah Terrace Entrada Sandstone is overlain by the Dakota Formation and forms the base of the Grey Cliffs in the Grand Staircase. The Dakota Formation contains interbedded mudstone, sandstone, coal, and conglomerate. Tropic Shale is a mudstone and shale unit with some sandstone, siltstone, and limestone and forms gray slopes susceptible to mass movements. The Straight Cliffs Formation is thin throughout the study area and while the Formation is composed of four members, no specific member has been identified in the study area. The four members include a resistant, cliff-forming sandstone; ledge- and cliff-forming shales and sandstones; a slope- and ledge-former of shales, coals, and sandstones; and the upper, prominent cliff forming coarse-grained sandstones. Overlying the Straight Cliffs Formation are slope forming, fine-grained sediments of the Wahweap Formation. Wahweap is composed of interbedded, less-resistant mudstones and siltstones and resistant and non-resistant sandstones and conglomerates. More resistant, cliff-forming sandstones are present in the upper part of the Wahweap.
8	Dakota to Claron: Basins contain the rock types described above including Kw, Ks, Kt, Kd and below including the Tc and Kk.
9	Tropic Shale to Claron: Basins contain the rock types described above including Tc, Kk, Kw, Ks, and Kt. The Cretaceous Kaiparowits Formation (Kk) overlies the Wahweap Formation. The Kaiparowits Formation is mostly a slope-forming fine-grained sandstone and is unconformably overlain by the Tertiary Claron Formation. (Tc). The Claron Formation is generally divided into the lower pink consisting of pink, pale-orange, light-gray, and white limestone and an upper white unit consisting of white clastic and microcrystalline limestone.

Table 3-S4 - Description of which samples were classified in each rock type group.

Rock Type Group #	# of samples in group	Rock Type Group Topography	Samples included in rock type group
1	n = 8	Vermillion to Pink Cliffs	20, 37, 38, 39, 40, 41, 49, 50
2	n = 5	Vermillion Cliffs	4, 8, 9, 13, 35
3	n = 6	White Cliffs to Pink Cliffs	17, 18, 19, 32, 33, 34
4	n = 5	White Cliffs	1, 2, 10, 21, 29
5	n = 5	Skutumpah Terrace to Pink Cliffs	12, 15, 30, 45, 48
6	n = 4	Only Carmel Formation on Skutumpah Terrace	22, 23, 25, 28
7	n = 3	Skutumpah Terrace and Grey Cliffs	11, 24, 31
8	n = 5	Grey Cliffs (Dakota Formation) to Pink Cliffs	36, 43, 44, 46, 47
9	n = 5	Grey Cliffs (Tropic Shale) to Pink Cliffs	3, 7, 14, 27, 42
10	n = 2	Sevier Basin draining north	51, 52

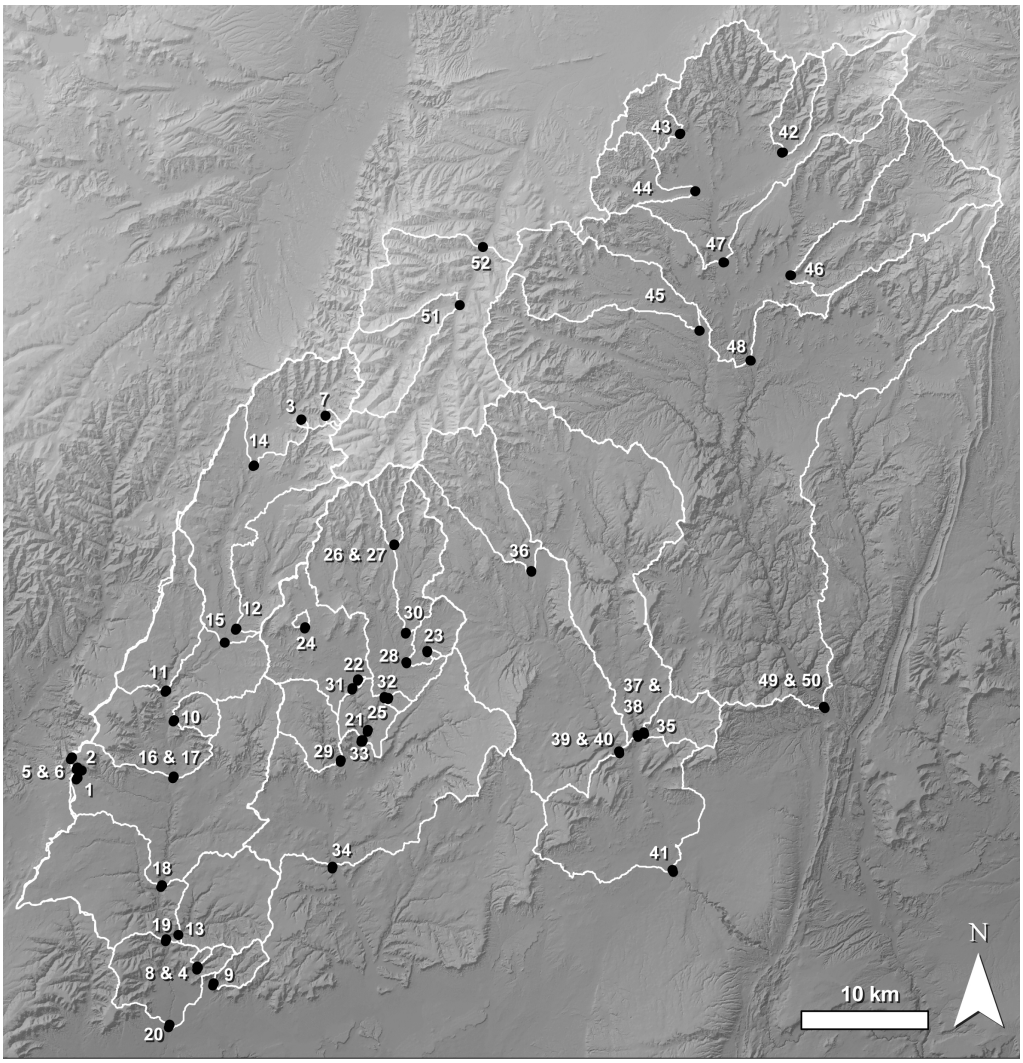

Figure 3S-1 - Map showing alluvial and colluvial sample location and upstream contributing areas. Latitude and Longitude of sample locations are identified in Table DR 1.

References Cited

Balco, G., Stone, J. O., Lifton, N. A., and Dunai, T. J., 2008, A complete and easily accessible means of calculating surface exposure ages or erosion rates from 10Be and 26Al measurements: Quaternary Geochronology, v. 3, no. 3, p. 174-195.

Doelling, H. H., Blackett, R. E., Hamblin, A. H., Powell, J. D., and Pollock, G. L., 2000, Geology of Grand Staircase-Escalante National Monument, Utah, *in* Sprinkel, D. A., Jr., T. C. C., and Anderson, P. B., eds., Geology of Utah's Parks and Monuments, Volume 28, Utah Geological Association.

Granger, D. E., Kirchner, J. W., and Finkel, R., 1996, Spatially Averaged Long-Term Erosion Rates Measured from in Situ-Produced Cosmogenic Nuclides in Alluvial Sediment: The Journal of Geology, v. 104, no. 3, p. 249-257.

Kohl, C., and Nishiizumi, K., 1992, Chemical isolation of quartz for measurement of in-situ-produced cosmogenic nuclides: Geochimica et Cosmochimica Acta;(United States), v. 56, no. 9.

Lal, D., 1991, Cosmic-ray labeling of erosion surfaces - In-situ nuclide production-rates and erosion models: Earth and Planetary Science Letters, v. 104, no. 2-4, p. 424-439.

Riebe, C. S., and Granger, D. E., 2013, Quantifying effects of deep and near-surface chemical erosion on cosmogenic nuclides in soils, saprolite, and sediment: Earth Surface Processes and Landforms, v. 38, no. 5, p. 523-533.

Schwanghart, W., and Scherler, D., 2014, Short Communication: TopoToolbox 2–MATLAB-based software for topographic analysis and modeling in Earth surface sciences: Earth Surface Dynamics, v. 2, no. 1, p. 1-7.

CHAPTER IV

TEMPORAL AND SPATIAL PATTERNS OF EROSION RATES IN A DISEQUILIBRIUM LANDSCAPE OVER 100 KYR OF CLIMATE CHANGE

Abstract

Understanding the coupled response of hillslopes and drainages to climate change requires consideration of the transient response of landscapes adjusting to base-level fall and differential erosion of lithologic units. We evaluate how erosion rates have varied over the Holocene and Pleistocene in three tributaries to the Colorado River in the Grand Staircase region of southern Utah, a landscape characterized by colorful cliffs and benches composed of alternating resistant and less-resistant sedimentary rocks. We compare cosmogenic ^{10}Be derived erosion rates from six late Pleistocene terraces and 15 Holocene-aged valley-fill alluvium with 52 modern alluvial samples. Holocene erosion rates range from 20-420 mm/kyr, integrate over 1.4 to 27 kyr, and show a strong correspondence to nearby bedrock sources. Holocene erosion rates are similar to erosion rates measured in modern stream sediment from analogue alluvial reaches, which vary from 60 to 370 mm/kyr. Late Pleistocene (100-80 ka and 65-50 ka) erosion rates showed less overall variance among the smaller sample population ranging from 100-300 mm/kyr with one outlier of 1300 mm/kyr and are greater than the modern and Holocene analogues in 5 out of 6 samples. Spatially, Pleistocene erosion rates

were greater in the Vermillion Cliffs (lowest topographic escarpment; n = 2) and Pink Cliffs (highest topographic escarpment; n = 3) and slower in the intervening White Cliffs (middle escarpment; n=1) compared to Holocene and modern erosion rates. The temporal and spatial variability of erosion rates over the last 100 kyr is likely influenced by large-scale climate-related changes in sediment production and transport, where Pleistocene climate corresponds to faster erosion rates compared to those recorded during modern and Holocene climate conditions. Coarse gravels indicate deposition during periods of effectively wetter climate conditions during late-Pleistocene conditions relative to fine-grained arroyo deposits. Pleistocene deposits were not in true interglacial times; instead, climate conditions were intermediate, typical of much of the last glacial cycle. An overall cooler climate may have been more conducive to physical weathering processes such as freeze-thaw that produce larger sized clasts.

Introduction

Past dynamics in erosion over space and time can help with predictions of future changes in landscapes. Rates of erosion across a watershed are controlled by climate and lithology, but also may reflect transient signals associated with base-level change. A primary tool used to study erosion-rates based on the concentration of cosmogenic nuclides carried in alluvium. Erosion rates derived from cosmogenic ^{10}Be integrate across catchments and over hundreds to thousands of years (Granger et al., 1996), and analogous sediment stored in

fluvial terraces provides information on erosion rates in the deeper past, once the ^{10}Be concentration acquired after deposition during sediment storage is accounted for (Granger et al., 1997; Granger et al., 2001; Balco and Stone, 2005; Hidy et al., 2013). Schaller and Ehlers (2006) suggest that changes in erosion rates through time can be detected from sediment archives that record orbital-timescale climate signals (41-100 kyr) in landscapes with ^{10}Be-derived denudation rates of 100-500 mm/kyr. In this study, we investigate if and how erosion rates have changed across Pleistocene, Holocene, and modern climate conditions and also across the varied terrain of the Grand Staircase of southern Utah.

While it is well established that climate can be a primary control on erosion rates, few studies have demonstrated the affect of climate change on the longer-term erosion rates of a watershed (e.g., Marshall el al., 2017; Balco and Stone, 2005). Climate change is expected to affect hillslope sediment production and fluvial transport through changes in precipitation, vegetation, runoff, and river discharge regime. Bull (1991) describes a climate-driven biogeomorphic response model wherein, during cooler and wetter glacial periods, in-situ bedrock weathering, vegetation, and sediment storage on hillslopes were greater. This hypothesis predicts lower denudation rates and increased ^{10}Be concentrations in alluvial sediment during glacial intervals. Transitions to interglacial conditions are hypothesized to cause high erosion rates due to vegetation disturbance and high discharge events (Bull, 1991).

Likely related to climate and hydrological changes, many stream channels in the semi-arid southwestern U.S.A. rapidly entrenched into their sediment-filled

valleys at the turn of the 20th century (Cooke and Reeves, 1976; Webb, 1985). This formed arroyos that, in turn, exposed discrete unconformity-bound packages of alluvium representing prehistoric entrenchment and aggradation (Bailey, 1935; Schumm and Hadley, 1957). Stratigraphic evidence suggests that many semi-arid streams transition between end-member conditions of an entrenched arroyo, characteristic of the modern landscape, and an aggraded state with an unconfined channel on a broad floodplain (Fig. 4-1; e.g. Townsend et al., 2019). Previous research has focused on characterizing the timing of mid-late Holocene alluvial cut-fill events (e.g., Hereford, 2002; Mann and Meltzer, 2007; Harvey et al., 2011) and hydrologic-related mechanisms driving incision. While stream power is one control on channel form, the role of sediment supply on arroyo entrenchment and aggradation in semi-arid streams is poorly understood. Dated arroyo-fill sediment combined with cosmogenic derived erosion rate data has the potential to address this research need.

Figure 4-1 - Annotated photograph of an arroyo in Johnson Wash.

This study of ^{10}Be-derived catchment-averaged erosion rates in the Grand Staircase region of the Colorado Plateau in southern Utah is advantageous because active faulting does not influence base-level signals and the semi-arid setting is sensitive to climate change. Furthermore, erosion rates in the region are relatively fast, (average = 360 mm/kyr; Riley et al., 2019), and therefore, changes in ^{10}Be-derived erosion rates could be detectable over Holocene timescales. We compare Holocene and late-Pleistocene paleo-erosion rate data to ^{10}Be-derived erosion rates measured in active channels in the same reach. The modern and paleo-erosion rates are used to address the following questions: 1) did late Pleistocene and Holocene climate change significantly modify the denudation rates of the Grand Staircase over the last 100 kyr? and 2) can ^{10}Be-derived erosion rates over the Holocene inform our understanding of arroyo dynamics?

Study Area

This research investigates catchment-averaged erosion rates in the three mixed alluvial-bedrock streams of Kanab Creek, Johnson Wash, and Kitchen Corral Wash (Fig. 4-2). Streams dissect the Grand Staircase, a region that exhibits colorful cliffs and benches composed of alternating resistant and less-resistant sedimentary rocks and streams drain toward the Colorado River in Grand Canyon. The topographic benches of the Grand Staircase increase in elevation from south to north and influence annual precipitation and vegetation type. Quaternary basalts drape a small proportion of the landscape. The Vermillion Cliffs are the

lowest escarpment in the study area and steps up to the Wygaret Terrace structural bench and extends to the White Cliff escarpment. The Skutumpah Terrace sits on top of the White Cliffs. The Pink Cliffs are the northern boundary of the watershed and culminate at the Paunsaugunt Plateau, the uppermost bench of the Grand Staircase, at an elevation between 2440-2895 m asl. The regional bedrock forms a broad syncline that plunges to the northeast.

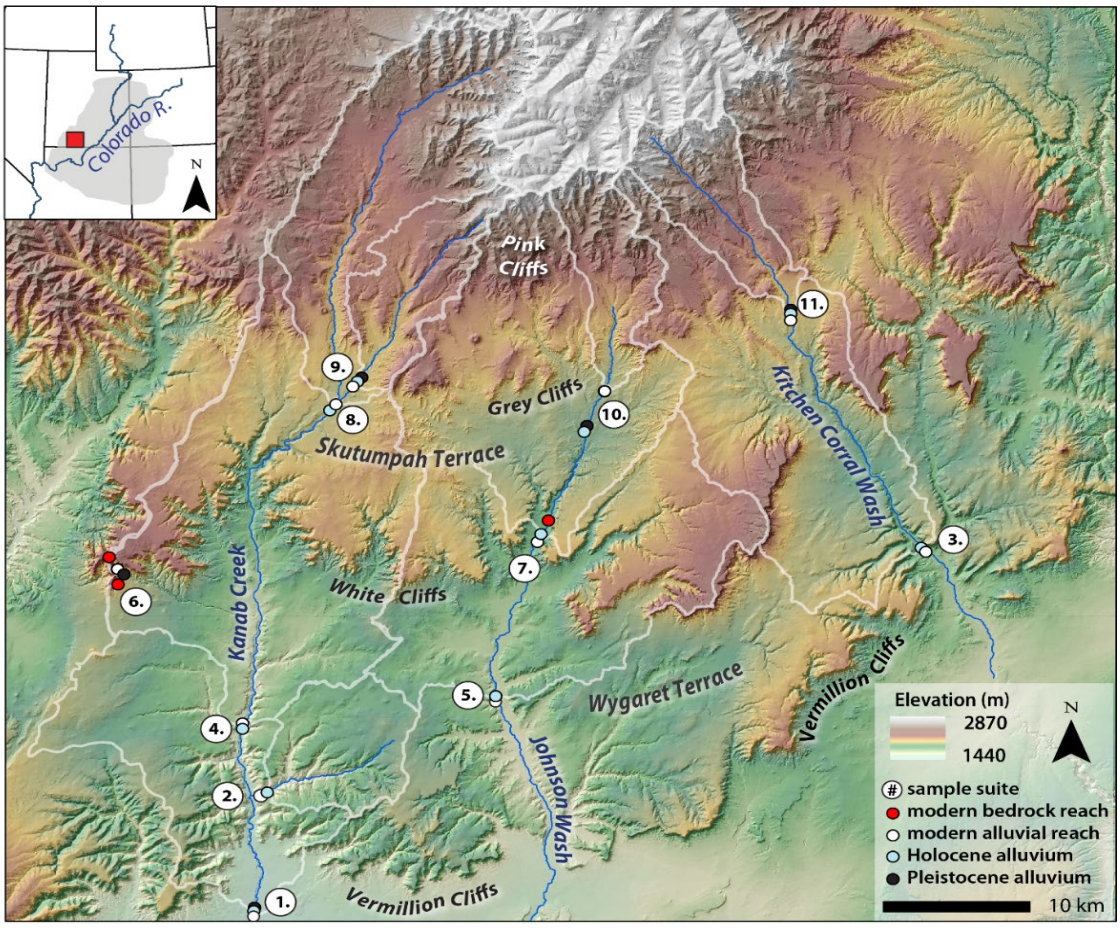

Figure 4-2 – Map of the study area with locations of the eleven sample suites containing modern, Holocene, and Pleistocene sediment analyzed for ^{10}Be concentrations and inferred erosion rates. White outlines are catchment areas for sediment samples.

This landscape is adjusting to base-level-fall associated with the cutting of Grand Canyon over the last 6 Myr and differential erosion of lithologic units as the migration of incision propagates upstream (e.g., Longwell, 1946; Darling and Whipple, 2015; Karlstrom et. al., 2014; Riley et al., 2019). This research expands on a modern alluvial erosion rate inventory in this region (Riley et al., 2019; Ch. III in this dissertation), where cosmogenic ^{10}Be erosion rates were found to vary spatially from 20 to >1000 m/Myr (mm/kyr). This erosion rate variability was interpreted to be related to lithologic-controlled, steep hotspots of erosion located in the upper escarpments of the watershed undergoing headward erosion of the Pink and White Cliffs.

Methods

To evaluate changes in erosion rates through time while minimizing variables, we compared modern, Holocene and Pleistocene alluvial samples collected near each other in selected reaches. For Holocene-age deposits, we measure ^{10}Be-derived erosion rates (n=15) for each discrete alluvial fill package previously described and dated (Chapter II, this dissertation; Huff and Rittenour, 2014; Nelson and Rittenour, 2014; Townsend et al., 2019). Pleistocene terrace samples are limited by preservation and exposure of deposits, but are sampled (n=6) and compared to younger analogous results where possible.

Independent age control for each alluvial deposit was obtained using single grain (Holocene-aged) or small aliquot (Pleistocene-aged) optically

stimulated luminescence (OSL). OSL provides an age estimate of the last time sediment was exposed to light (Huntley et al., 1985). Samples were collected in opaque metal tubes and representative sediment was collected from a 30 cm radius of the sample tube for determination of radio-elemental concentrations for dose rate calculation. OSL dose rate data, equivatlent dose radial and propoability distribution plots are located in the supplemental materials (Tables 4-S1 and Figs. 4-S1, 4-S2). The fine-grained quartz sand fraction (150-250 μm) was isolated for dating at the Utah State University Luminescence Laboratory under safelight, dark room conditions.

Cosmogenic nuclides accumulate in the upper 1-2 m's of Earth's surface and the accumulated concentration can be used to characterize denudation, by physical erosion and chemical weathering (Lal, 1991). However, chemical weathering can largely be ignored in the study area due to semi-arid conditions in the region (Riebe and Granger, 2013). Accumulation of ^{10}Be is proportional to the average production rate and inversely proportional to the average erosion rate over the contributing area (Granger et al., 1996). In paleo-deposits, the ^{10}Be concentration accumulated in the sediment during storage was calculated and subtracted from the measured nuclide concentration of the stored sediment to estimate the initial nuclide concentration when sediment was deposited (Balco and Stone, 2005). Processing for ^{10}Be analysis of quartz sand followed standard techniques. In this study, we limited the effect of grain-size dependence of nuclide concentrations by only analyzing the 250-500 micron grain-size fraction in both modern and paleo samples. Thus, this data set may not fully inventory estimates

of catchment-average erosion rates, but does capture changes in erosion rates from the parts of the basin that are contributing quartz of the target grain size. Each batch of samples contained at least one process blank. BeO targets were prepared at Utah State University and University of Wyoming and sent to PRIME lab at University of Purdue for Accelerator Mass Spectrometry measurements, which yielded measurements of $^{10}Be/^{9}Be$. Shielding correction factors were applied to the sea-level high-latitude (SLHL) production rate (4.0 atoms/g/a; Balco et al., 2008; Borchers et al., 2016) and calculated in Matlab using Topo Toolbox v2 (Schwanghart and Scherler, 2014) based on original work by Dunne et al. (1999). Topographic shielding factors and hypsometric-weighted-average elevation and latitude for each basin were calculated using a 30m DEM and used in the CRONUS-Earth Project $^{10}Be–^{26}Al$ Calculator version 2.3 to calculate catchment averaged erosion rates (Balco et al., 2008). All ^{10}Be data and inputs that were used in the CRONUS Calculator are located in a table in the supplemental material (Table 4-S2 and 4-S3)

To determine the sources of Pleistocene piedmont gravels, pebble to cobble sized clasts were collected (n = 50) at four exposures in upper Kanab, Johnson Wash, and Kitchen Corral drainage basins. Clasts were selected at random and their lithology recorded. Clast count data are in the supplemental materials (Fig 4-S3).

Table 4-1 - Summary of OSL ages for the closest depositional bed to detrital cosmogenic ^{10}Be concentrations. (see footnote [1])

Sample Suite	CRN Sample ID	OSL Lab ID	Field ID	Depth (cm)	Num. of accepted grains [2] / aliquots [3]	Dose Rate[4] ± 2 σ error (Gy / kyr)	De [5] ± 2 σ error (Gy)	Age ± 2 σ error (ka)
1	**KNB 40**	**USU 1631**[8]	**Lower Kanab Creek Arroyo**	**510**	**39 (1100)** [1]	**2.62 ± 0.14**	**7.96 ± 1.73**	**3.03 ± 0.73**
	KNB 29	**USU 1754**	**Lower Kanab Creek Arroyo (white Pleistocene)**	**790**	**19 (51)** [2]	**0.51 ± 0.05**	**35.82 ± 3.14**	**70.83 ± 10.78**
	KNB 41	**USU 1627**	**Lower Kanab Creek (red Pleistocene)**	**1190**	**18 (44) 2**	**0.90 ± 0.04**	**82.29 ± 10.95**	**91.59 ± 15.18**
2	KNB 26	USU 356 [6]	Hog Canyon Arroyo	550	98 (800) [1]	1.30 ± 0.06	6.18 ± 0.70	4.77 ± 0.63
3	KCW 8 & 9	USU 1192 [7]	Kitchen Corral Wash Arroyo (site E)	600	50 (1500) [1]	1.40 ± 0.08	1.60 ± 0.39	1.14 ± 0.19
4	KNB 17	USU 519 [6]	Kanab Creek Arroyo (Best Friends - Qa2)	800	84 (1700) [1]	2.20 ± 0.09	1.86 ± 0.37	0.84 ± 0.18
	KNB 16	USU 1030 [6]	Kanab Creek Arroyo (Best Friends - Qa3)	800	141 (2900) [1]	1.06 ± 0.05	1.61 ± 0.12	1.52 ± 0.16
	KNB 15	USU 363 [6]	Kanab Creek Arroyo (Best Friends - T4)	3000	133 (3000) [1]	0.70 ± 0.04	4.24 ± 1.07	6.05 ± 1.58
5	JW 23	USU 1139	Johnson Wash Arroyo (site M)	4.5	36 (900) [1]	2.69 ± 0.14	7.82 ± 0.93	2.45 ± 0.62
6	**KNB 38**	**USU 2239**	**Upper Red Creek**	**>700**	**18 (27)** [2]	**1.30 ± 0.06**	**68.21 ± 4.76**	**52.42 ± 6.31**
7	JW 2	USU 1394	Johnson Wash Arroyo (site G)	1125	45 (4200) [1]	1.64 ± 0.09	3.13 ± 0.53	1.91 ± 0.37
8	KNB 24	USU 1763 [8]	Upper Kanab Creek Arroyo (waterfall site)	390	42 (2300) [1]	1.35 ± 0.07	7.15 ± 1.21	5.30 ± 1.05
	KNB 25	USU 1428 [8]	Upper Kanab Creek Arroyo (waterfall site)	750	65 (2100) [1]	1.88 ± 0.10	6.27 ± 0.89	3.33 ± 0.58
9	**KNB 42**	**USU 1759**	**Sink Wash (gravel pit)**	**500**	**19 (39)** [2]	**1.45 ± 0.07**	**161.23 ± 25.28**	**111.55 ± 20.5**
	KNB 8	USU 1474 [8]	Sink Wash Arroyo	400	43 (1500) [1]	2.40 ± 0.13	4.56 ± 1.22	1.90 ± 0.54
10	**JW 26**	**USU 2241**	**Skutumpah gravel pit**	**100**	**16 (1427)** [1 2]	**2.21 ± 0.10**	**6.82 ± 1.15**	**3.08 ± 0.6**
		USU 2573	**Skutumpah gravel pit**	**400**	**19 (22)** [2]	**1.95 ± 0.09**	**135.43 ± 12.07**	**69.37 ± 9.03**
	JW 22	**USU 2189**	**Skutumpah gravel pit**	**630**	**21 (34)** [2]	**1.75 ± 0.08**	**150.06 ± 22.93**	**85.83 ± 15.45**
11	**KCW 10**	**USU 2242**	**Kitchen Corral Wash (Meadow Creek gravel)**	**550**	**20 (35)** [2]	**1.62 ± 0.08**	**141.31 ± 18.55**	**87.05 ± 14.17**
	KCW 11	**USU 2243**	**Kitchen Corral Wash (Meadow Creek)**	**400**	**30 (1200)** [1]	**2.23 ± 0.12**	**2.39 ± 0.74**	**1.07 ± 0.35**

[1] OSL data (dose rate chemistry and De distribution data) for new samples (bold) can be found in supplemental material. OSL data for previous published samples can be found in original publication.
[2] Age analysis using the single-aliquot regenerative-dose procedure of Murray and Wintle (2000) on single-grains of quartz sand (Duller, 2008). Number of grains used in age calculation and number of grains analyzed in parentheses.
[3] Age analysis using the single-aliquot regenerative-dose procedure of Murray and Wintle (2000) on small-aliquots of quartz sand. Number of aliquots used in age calculation and number of aliquots analyzed in parentheses.
[4] Dose rates are calculated based on water content, sediment chemistry, and density (1.9g/cm3), and using sample depth, elevation (1.7-1.9 km), and latitude/longitude (~37.2/ ~-112.4) following Prescott and Hutton (1994), Aitken and Xie (1990), Aitken (1998).
[5] Equivalent dose (D_E) calculated using the Minimum Age Model of Galbraith and Roberts (2012) or the Central Age Model of Galbraith and Roberts (2012).
[6] Previous published samples from Nelson and Rittenour (2014)
[7] Previously published ages from Huff and Rittenour (2014)
[8] Previous published samples from Townsend (2015). USU 1631 was preliminary and new data is presented here to make age final.

Table 4-2 – Post deposition depth-averaged ^{10}Be production, measured ^{10}Be concentrations, depth corrected ^{10}Be concentrations, and inferred erosion rates for modern and paleo sample suites.

1

Sample Suite	PRIME ID	Sample ID	Age (ka)	Location / Reach Type	Measured ^{10}Be Conc. (at/g)	Analytical Error	Corrected ^{10}Be Conc. (at/g)	Post Deposition Gain (%)	Erosion Rate [1] (mm/kyr)	Error [2]	T_{ave}[3] (kyr)
1	201603170	KNB 30	0	Vermillion / alluvial	9.09E+04	2.5E+03		0	120	10	5.12
	201603172	KNB 40	2.9	Vermillion / alluvial	4.71E+05	1.1E+04	4.71E+05	0.1	20	10	28.08
	201600328	KNB 29	70.7	Vermillion / alluvial	4.31E+04	1.3E+03	3.84E+04	10.7	270	40	2.28
	201603173	KNB 41	94.6	Vermillion / alluvial	4.90E+04	1.6E+03	4.50E+04	8.2	240	30	2.63
2	201600327	KNB 28	0	Vermillion / alluvial	8.57E+04	4.6E+03		0	110	20	5.54
	201603169	KNB 26	4.8	Vermillion / alluvial	5.72E+04	1.4E+03	5.67E+04	1.0	170	20	3.71
3	201700345	KCW 5	0	Vermillion / alluvial	1.89E+05	4.6E+03		0	60	10	10.13
	201700334	KCW 6	0	Vermillion / alluvial	1.73E+05	4.5E+03		0	65	10	9.25
	201700346	KCW 7	0.2	Vermillion / alluvial	3.60E+05	1.7E+04	3.59E+05	0.3	30	5	19.48
	201700347	KCW 8	1.1	Vermillion / alluvial	3.17E+05	1.4E+04	3.17E+05	0.1	35	5	17.15
	201700348	KCW 9	1.1	Vermillion / alluvial	1.16E+05	6.1E+03	1.15E+05	0.1	100	15	6.13
4	201401587	KNB 19	0	Wygaret / alluvial	3.92E+04	1.5E+03		0	290	25	2.16
	201603168	KNB 17	0.8	Wygaret / alluvial	3.47E+04	1.5E+03	3.46E+04	0.2	330	50	1.89
	201603167	KNB 16	1.5	Wygaret / alluvial	2.67E+04	2.0E+03	2.66E+04	0.4	420	70	1.45
	201401589	KNB 15	6.1	Wygaret / alluvial	3.26E+04	1.2E+03	3.25E+04	0.4	350	50	1.77
5	201600315	JW 20	0	Wygaret / alluvial	4.28E+04	2.1E+03		0	250	40	2.36
	201700342	JW 23	2.5	Wygaret / alluvial	3.58E+04	2.5E+03	3.40E+04	0.2	320	50	1.98

[1] Erosion rates are rounded to the nearest 10 for erosion rates >100 and to the nearest 5 for erosion rates <100 mm ky^{-1}.

[2] Uncertainties in erosion rates are propagated from AMS uncertainties and include a 10% 1σ uncertainty in nuclide production rates including scaling factors for altitude, latitude, and topographic shielding and a 5% 1σ uncertainty in density, attenuation coefficients, and half-lives. Errors are rounded to the nearest 10 for erosion rates >100 and to the nearest 5 for erosion rates <100.

[3] T_{ave} is the interval of time that the catchment-averaged erosion rate is averaged.

Sample Suite	PRIME ID	Sample ID	Age (ka)	Location / Reach Type	Measured ^{10}Be Conc. (at/g)	Analytical Error	Corrected ^{10}Be Conc. (at/g)	Post Deposition Gain (%)	Erosion Rate [1] (mm/kyr)	Error [2]	T_{ave} [3] (kyr)
6	201401583	KNB 12	0	White Cliffs / colluvial	1.96E+04	1.1E+03		0	540	80	1.10
	201501045	KNB 10	0	White Cliffs / alluvial	3.07E+03	7.0E+02		0	3560	990	0.17
	201700337	KNB 10r [4]	0	White Cliffs / alluvial	7.82E+03	1.8E+03		0	1400	400	0.43
	201603171	KNB 36	0	White Cliffs / bedrock	1.89E+04	4.9E+02		0	620	90	0.97
	201700340	KNB 38	52.2	White Cliffs / alluvial	8.57E+04	3.4E+03	8.15E+04	4.8	130	20	4.61
7	201603165	JW 24	0	White Cliffs / colluvial	1.22E+04	8.6E+02		0	710	110	0.84
	201501035	JW 1	0	White Cliffs / alluvial	3.66E+04	2.0E+03		0	310	50	1.93
	201501036	JW 2	1.9	White Cliffs / alluvial	5.14E+04	2.4E+03	5.13E+04	0.2	220	30	2.78
8	201501044	KNB 9	0	Skutumpah / alluvial	3.43E+04	1.5E+03		0	370	50	1.62
	201501047	KNB 25	3.3	Skutumpah / alluvial	3.41E+04	1.6E+03	3.38E+04	0.9	370	50	1.65
	201501046	KNB 24	5.3	Skutumpah / alluvial	4.64E+04	2.0E+03	4.59E+04	1.1	280	40	2.24
9	201700336	KNB 7	0	Skutumpah / alluvial	1.31E+05	3.9E+03		0	90	10	6.58
	201700339	KNB 8	1.9	Skutumpah / alluvial	3.94E+05	1.5E+04	3.94E+05	0.1	30	5	20.58
	201700338	KNB 42	111.6	Skutumpah / alluvial	1.15E+05	3.1E+03	1.14E+05	1.1	120	20	5.43
10	201501039	JW 13	0	Skutumpah / alluvial	3.71E+04	1.7E+03		0	320	50	1.90
	201700335	JW 26	2.2	Skutumpah / alluvial	7.36E+04	6.0E+03	6.43E+04	12.7	290	30	2.05
	201600317	JW 22	87.2	Skutumpah / alluvial	1.73E+04	8.0E+02	9.33E+03	46.1	1300	210	0.54
11	201600325	KCW 4	0	Skutumpah / alluvial	7.05E+04	2.4E+03		0	190	30	3.20
	201700331	KCW 11	1.1	Skutumpah / alluvial	3.61E+05	1.6E+04	3.61E+05	0.1	35	5	17.05
	201700330	KCW 10	79.3	Skutumpah / alluvial	7.29E+04	7.8E+03	6.46E+04	11.3	210	40	3.07

[4] This sample was a lab duplicate from the same field sediment sample.

Results

Temporal Variability in Erosion Rates

Fifteen modern alluvial samples selected from a larger, previously published dataset (Riley et. al., 2019; Chapter III this dissertation) are used here for comparison to the 21 new Holocene and Pleistocene results. Modern detrital ^{10}Be-inferred erosion rates of the larger dataset vary spatially in the study area from 20 to >3500 m/Myr, interpreted to reflect variability from lithologic/steepness and geomorphic transience controls (Riley et al., 2019).

Holocene sediment was collected from five discrete alluvial fill packages located along trunk streams (Kanab Creek, Johnson Wash, and Kitchen Corral Wash) between the Vermillion and the Pink Cliffs and constrained to 6000-3500, 3200-2500, 2200-1550, 1450-750, and 650-100 years old (Chapter II this dissertation; Table 4-1). Resultant Holocene catchment averaged erosion rates range from 20 to 420 mm/kyr and integrate over time intervals (T_{ave}) of 1.5 to 28 kyr (Table 4-2). These integration timescales of erosion rates are equal to or longer than the storage of Holocene sediment, which results in a minimal influence of *in situ* post-deposition cosmogenic nuclide accumulation. These Holocene erosion rates are similar to those measured in analogous modern stream reaches (60 to 370 mm/kyr; Table 4-1, Figs. 4-3, 4-4, 4-5, 4-6).

To determine if Pleistocene erosion rates also span the same range as modern and Holocene rates, we dated and measured the concentration of ^{10}Be in six alluvial deposits. Three Pleistocene gravel deposits on the Skutumpah Terrace were dated, and OSL ages

are 112 ± 21 ka, 87 ± 14 ka, and 86 ± 15 ka. One Pleistocene deposit from a headwater tributary below the White Cliffs is 52 ± 6 ka. Two deposits from lower Kanab Creek below the Vermillion Cliffs, buried within the basin-fill, were dated to 91 ± 15 and 71 ± 11 ka (Table 4-1). These six Pleistocene gravel deposits produce paleo-erosion rates of 100 to 300 mm/kyr (n=5) with an outlier (JW 22) of 1300 mm/kyr (n=1; Table 4-2). These Pleistocene erosion rates average over (T_{ave}) 0.46 to 5.2 ky. In summary, the range of erosion rate values is similar across our modern, Holocene and Pleistocene datasets. However, Pleistocene erosion rates were faster (n = 5; 180 ± 70 mm/kyr) than Holocene analogues (n = 3; 30 ± 10 mm/kyr).

Considering the amount of time buried, depth of burial, and measure Be-concentration, the percent of the measured nuclide concentration gained following deposition is between 0-13 percent with the outlier sample (JW 22) being 46 percent. Significant post-depositional gain in nuclide concentration in the outlier was caused by the age of deposit (86 ± 15 ka), relatively shallow burial depth (6-7 m), and low measured ^{10}Be concertation. The outcrop where the outlier sample was collected features a buried soil with Stage II and III calcium carbonate development 2 m above the sample. The age of the sediment package above the buried soil is ~69 ka (Table 1). Thus, this sample was buried at ~2 m for ~20 ka prior to further deposition and deeper burial.

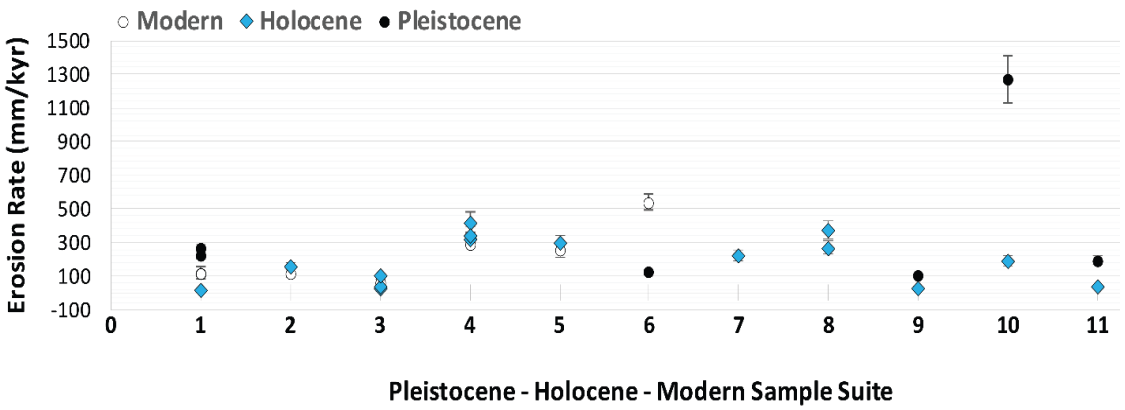

Figure 4-3 - Plot comparing Pleistocene, Holocene, and modern erosion rate estimates from alluvial samples collected in the same stream reach. One modern pair of replicate samples from sample suite 6 were not included in this figure (KNB 10 and KNB 10r; 3560 and 1400 mm/kyr).

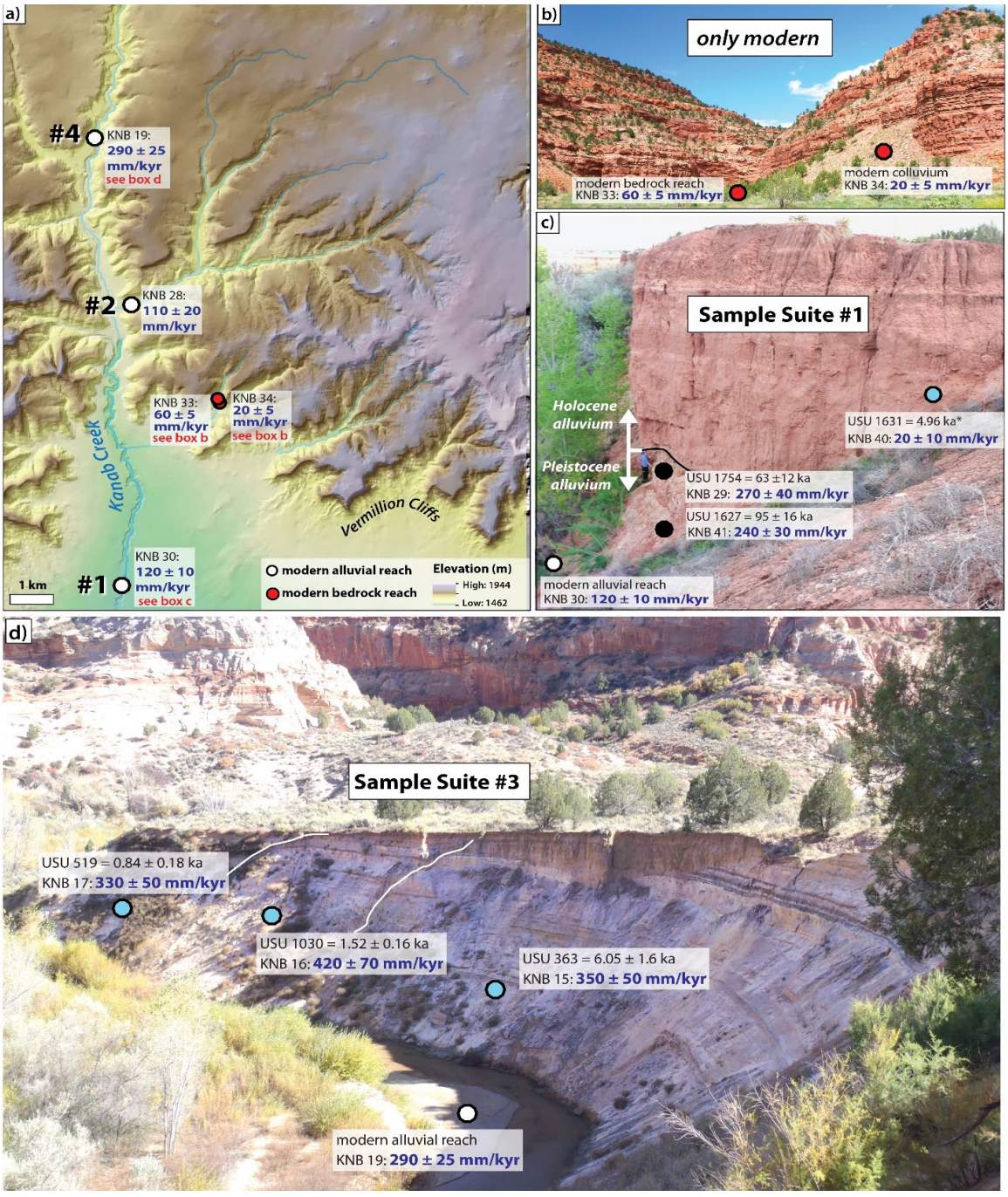

Figure 4-4 – a) Location of samples where Kanab Creek dissects the Vermillion Cliffs. Modern erosion rates sampled in alluvial reaches are identified with white circles and bedrock reaches with red circles. b) Photograph of modern headwater tributaries in the Vermillion Cliffs where modern alluvium and colluvium were sampled. c) The lowest sample location in Kanab Creek where modern, Holocene, and Pleistocene sediment was sampled. d) Arroyo exposure in Kanab Creek where three Holocene-fill packages were dated by OSL and paleo-erosion rates were calculated.

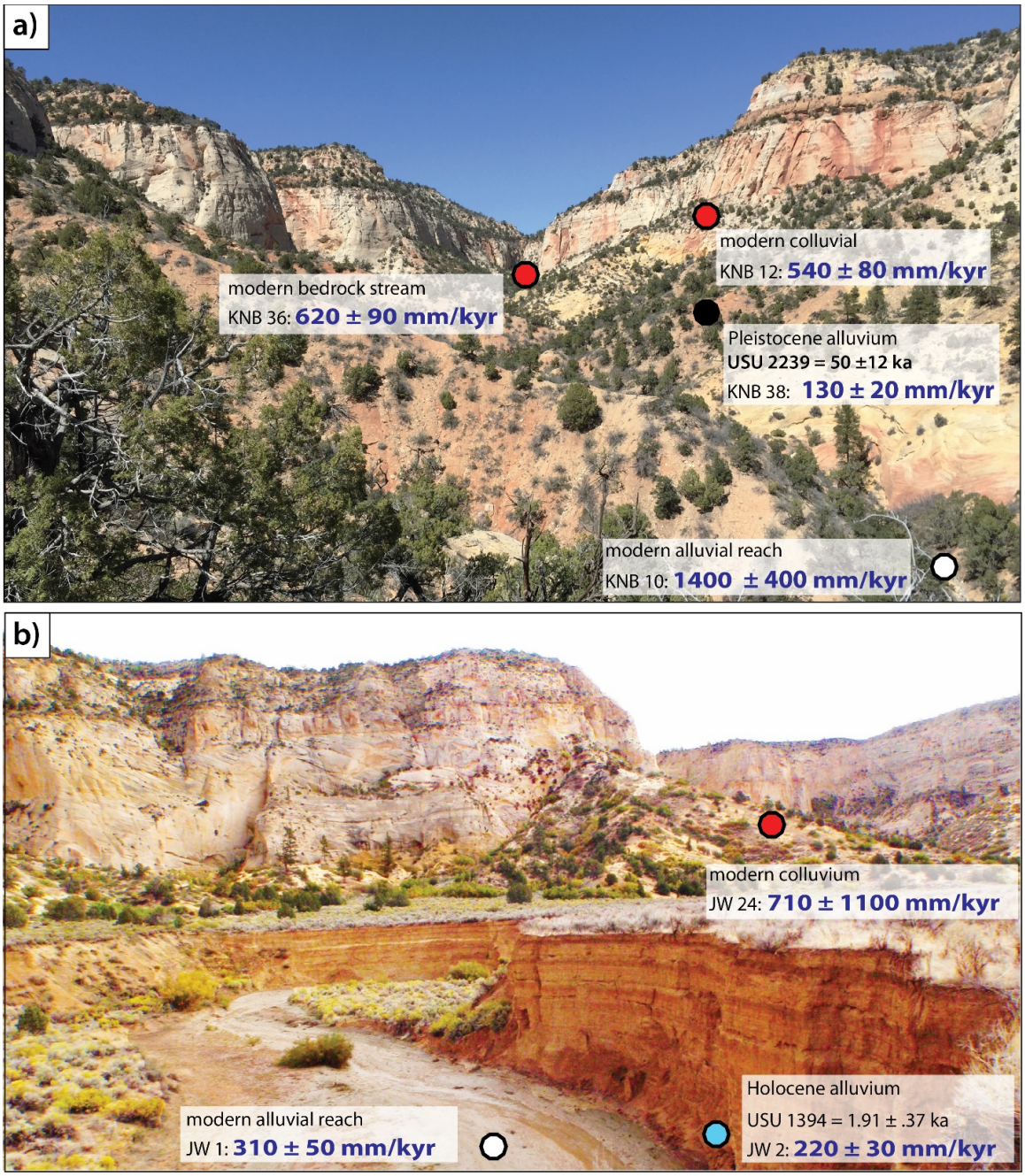

Figure 4-5 - Photographs of the White Cliffs and the different sediment storage reservoirs and their associated erosion rates.

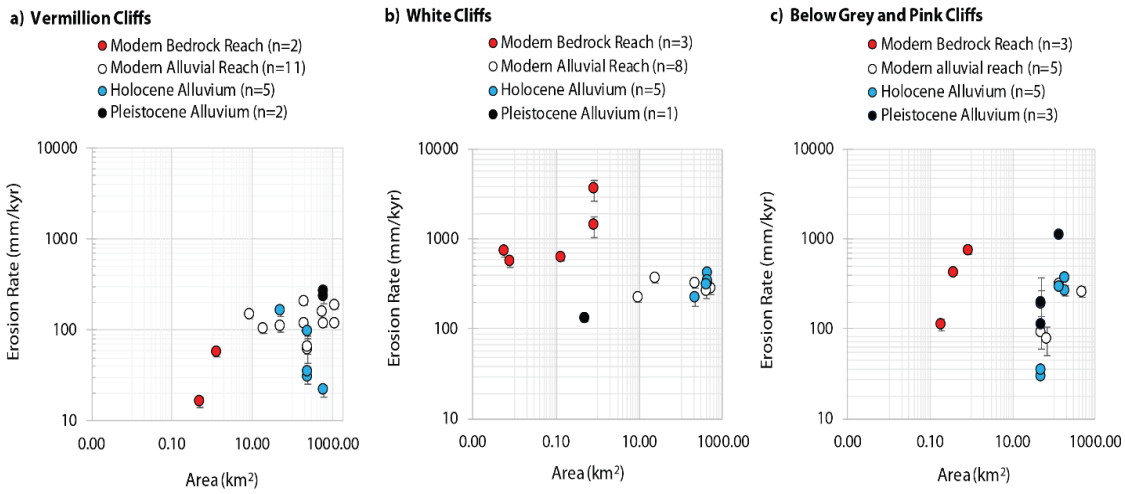

Figure 4-6 - Erosion rates vs. log-area plots classified by age and topographic position on the landscape. Modern alluvial samples are identified by white circles, modern bedrock are red circles, Holocene alluvium are blue circles, and Pleistocene alluvium are black circles. a) Sediment sampled from the trunk stream and colluvium at the base of the Vermillion Cliffs. Note Pleistocene sediment records faster erosion rates than modern and Holocene sediment from the same contributing area. b) Sediment sampled from the trunk stream and colluvium at the base of the White Cliffs. Note the one Pleistocene sample records a slower erosion rate than modern and Holocene sediment from the same contributing area, but it has a much smaller catchment area compared to the other Plesitcoene samples. c) Samples collected on the Skutumpah Terrace below the Grey and Pink Cliffs where Pleistocene erosion rates have about the same range as modern and Holocene sediment.

Spatial Variability in Erosion Rates

A first-order pattern of modern alluvial samples suggests that erosion rates correspond with steepness (i.e., slope; Riley et al., 2019). Small, steep headwater basins of the Pink Cliffs (Tertiary Claron Formation) record faster erosion rates, while gentler headwater basins of the Skutumpah Terrace record lower erosion rates (Table 4.2; Figure

4.6). The highest modern erosion rates are from steep catchments draining the Navajo Sandstone of the White Cliffs. Yet, an exception to this generalization comes from steep catchments of the Vermillion Cliffs that have some of the lowest erosion rates in the study area (Riley et al., 2019).

In contrast, two Pleistocene samples from the same reach in the Vermillion Cliffs, recorded erosion rate results of 240 and 270 mm/kyr, which are more than double the Holocene and modern erosion rates in the same alluvial reach (20 and 110 mm/kyr; 120 mm/kyr) and four times the modern erosion rates of small catchments draining the Vermillion Cliffs (Figs 4-2, 4-4, 4-5a; Riley et al., 2019). Thus, it seems that modern hillslope headwaters produce lower erosion rates than is estimated from sediment stored along the trunk stream in both modern and Holocene alluvium, and even more so compared to higher rates from Pleistocene alluvium (Figure 4-5a).

The single Pleistocene erosion rate result (130 mm/ky) from alluvium at the base of the White Cliffs is considerably slower than rates from modern samples from nearby headwater bedrock catchments (540 - 710 mm/kyr; n=3; Figs 4-3, 4-4, 4-5b). Likewise, this Pleistocene rate estimate is also slower than the rates from Holocene and modern alluvium in the White Cliffs (220-410 mm/ky; n=5 and 220-360 mm/ky; n=8 respectively).

Finally, higher in the study area, on the Skutumpah Terrace below the Grey and Pink Cliffs, three Pleistocene samples (100-80 ka) result in highly variable erosion rates (110, 200, and 1300 mm/kyr), which is similar to the great range of modern headwater erosion rates (110 to 740 mm/kyr; n=3) and perhaps somewhat faster than rates from analogous Holocene samples (30 to 360 mm/kyr; n=5). The variability of results

throughout time in these upper catchments of the Skutumpah Terrace may be tracking the great variability in catchment lithology across this area. Landslide activity in the catchment is an additional potential cause for high variability in erosion rates on the Skutumpah Terrace. Upstream catchment area for the three Pleistocene samples contain the less-resistant part of the Carmel and Temple Cap sandstone, sandstone and shale beds of the Dakota Formation, as well as from the Tropic Shale, Straight Cliffs, Wahweap and Kaiparowits Formations (Fig. 4.S3).

Discussion

Erosion rates from modern (60-370 mm/kyr) and Holocene-aged (20-420 mm/kyr) sediment from arroyo reaches record similar ranges in erosion rates (Figs 4-4 and 4-5). This general match suggests that current sediment is derived in large proportions from Holocene alluvium, or alternatively that erosion rates across the landscape have remained similar across the Holocene. Holocene erosion rates integrate over time intervals (T_{ave}) of 1.5 to 28 kyr (Table 4-2). These integration timescales are equal to or longer than the storage of Holocene sediment between arroyo entrenchment events; thus, these Holocene erosion rates incorporate and average across short-term, high frequency climate signals that occurred during the Holocene. Furthermore, the relatively short timescale of storage (1000's of years) of Holocene alluvium results in minimal influence of in-situ post-deposition cosmogenic nuclide accumulation, which was < 1.1% for all Holocene samples, apart from one outlier (JW 26 (12.7%); Table 4-2). These Holocene erosion rates are similar to those measured in neighboring modern

stream reaches (60 to 370 mm/kyr; Table 4-1, Figs. 4-3, 4-4, 4-5, 4-6). Holocene erosion rates are more similar to modern erosion rates than Pleistocene rates, which is expected given that streams are currerently entrenched into Holoecene-aged sediment-filled valleys and thus directly eroding Holocene sediment from the near-vertical channel banks. Five out of six Pleistocene deposits were perched above modern channel bottoms, which suggest that there was greater sediment supply and valleys were aggraded to higher elevations during their deposition prior to terrace formation.

Pleistocene erosion rates range from 100 to 300 mm/kyr (n=5) with one high outlier (JW 22 = 1300 mm/kyr). These values are greater than modern and Holocene analogues in 5 out of 6 sample sets, with the exception being a sample (KNB 38; Fig 4-4) collected from the base of the White Cliffs with a typical Pleistocene erosion rate associated with a modern alluvial sample with an unusually high erosion rate value (KNB 10r; 1400 mm/kyr). Although we have limited number of samples from Pleistocene alluvium, results indicate Pleistocene erosion rates were generally higher (360 ± 460 mm/kr; n=6) and perhaps more consistent than modern (270 ± 220 mm/kyr; n=5) and Holocene (70 ± 80 mm/kr; n=4) analogue erosion rates measured along streams in the study area. The average erosion rate for all Holocene and modern alluvial samples is 200 ± 190 mm/kyr. It is expected that Pleistocene rates were somewhat elevated in comparison to Holocene and modern rates because enhanced weathering and hillsope sediment transport is predicted during wetter and/or cooler climate conditions of the Pleistocene.

Climate-drivers in sediment production, hillslope erosion, and channel response

Our dataset includes a significant number of samples taken from Holocene alluvium exposed in arroyo walls. Erosion rates vary from 20-420 mm/kyr and climate changes are a logical culprit. In general, it is well known that Holocene climate has been steady compared to the Pleistocene (Figure 4-7). Yet, notable climate Holocene variability has been recorded in regional climate rpoxies. For example, the mid-Holocene (~8-4 ka) was relatively hot and dry in the Southwest (e.g., Davis and Shafer, 1992; Madsen et al., 2001; Waters and Haynes, 2001; Menking and Anderson, 2003). Climate was wetter and/or cooler climate starting ~4 ka (Weng and Jackson, 1999; Polyak and Asmerom, 2001; Asmerom et al., 2007). Climate proxies characterize the Medieval Climatic Anomaly (MCA; 1.5 – .65 ka; Stine, 1998; Cook et al., 2007) as a time with widespread, severe aridity and large decadal to centennial changes in precipitation in the Southwest (Cook et al., 2004; Rasmussen et al., 2006; Jimenez-Moreno et al., 2008). Tree-ring records from the SW indicate wet-dry conditions during The Little Ice Age (~ 0.6 - 0.1 ka). Despite all these documented climate phenomena over the Holocene, an important finding of this study is that, in fact, these high frequency, low magnitude climate changes are not reflected in cosmogenic-derived erosion rates from alluvium preserved and exposed in arroyo walls (Figure 4-8). Holocene erosion rates integrate over 1.5 to 28 kyr (Table 4-2), which are generally longer than the storage of sediment in the valley fills and thus these long-term rates average across short-term, high frequency Holocene climate signals.

The higher magnitude of Pleistocene changes in climate temporally correlates to

Pleistocene erosion rates that are generally greater (ave. = 360 ± 460 mm/kyr) than modern (ave. = 270 ± 220 mm/kyr) and Holocene (ave. = 70 ± 80 mm/kyr) analogue erosion rates. The Pleistocene was overall cooler than Holocene climate (Fig. 4-8), and frost-driven sediment production during cooler intervals has been proposed to increase erosion rates in unglaciated landscapes (Whitney and Harrington, 1993; Pederson et al., 2000; Marshall et al., 2017). Increased biologic activity is also a control on weathering of hillslopes, converting bedrock to sediment that gets transported to channels (Bull, 1991). Also, the coarser gravel of the terrace deposits suggests that sediments were deposited when climate was effectivly wetter, with higher transport competence. In summary, higher weathering rates and sediment transport from hillslopes is broadly predicted during wetter and/or cooler conditions of the Pleistocene—and this matches our small dataset. Five out of our six Pleistocene deposits analyzed date to intermediate climate conditions during late MIS 5 and MIS 3, and not during maximum conditions of interglacial or glacial conditions (Fig. 4-7); and perhaps this is consistent with there being no significant differences observed in rates among different Pleistocene samples. Balco and Stone (2005) reported similar findings in Fisher Valley southeastern Utah, where they found no relation between different mid-Pleistocene erosion rates, but they did find a difference when comparing modern and Pleistocene erosion rates.

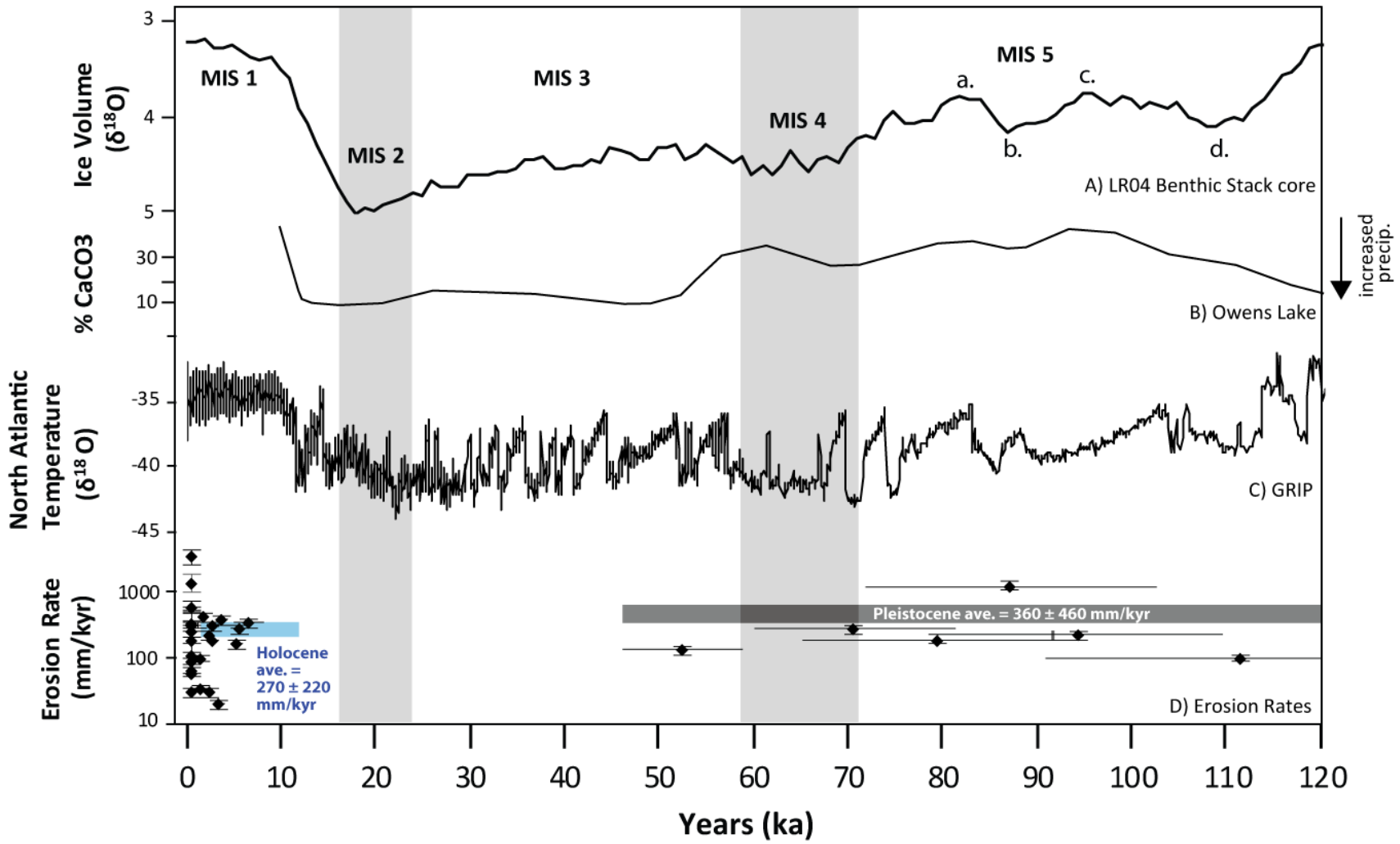

Figure 4-7 – Comparison of paleo-erosion rates with climate time-series shows the average Holocene erosion rates corrosponds with a drier, warmer climate and the average Pleistocene rate generally corroponds with a colder, wetter Pleistocene. Vertical shaded bars indicate major glacial periods. A) Ice volume derived from delta ^{18}O from the LR04 Benthic Stack core (Lisiecki and Raymo, 2005). B) Owens Lake paleoclimate record (Smith et al., 1997). C) Time-series of GRIP $\delta\ ^{18}O$ temperature (Johnsen, 1999). D) Erosion rate data from the study area.

Variance in Sediment Supply: Implications for Arroyo Dynamics

It has been hypothesized that the timing of aggradation and entrenchment in arroyo systems could be related not only to hydrology, but also to an increase or decrease in sediment supply related to bedrock erosion rates (Hereford, 2002). In this study, Holocene sediment did not show a systematic trend in erosion rates related to the timing of aggradation and entrenchment, and in fact modern rates and rates from Holocene fills are the same (Fig. 4-9). Our Holocene erosion rates average over timescales of 1.5 - 28 kyr and periods of arroyo aggradation have been documented to occure over 500-1000 year intervals (Ch. II this dissertation). Even if small scale, high frequency climate signals during the last 6 kyr caused changes in rates of erosion, these changes would likely not be observed in the detrital ^{10}Be record because of the the timescale of integration.

Most alluvial records suggest that arroyo cut-fill dynamics began in the mid-late Holocene. The onset of mid-Holocene arroyo-cut fill dynamics could be related to accelerated erosion of stored Pleistocene hillslope deposits during this time, which could load streams with sediment and cause aggradation and instability. Specifically, during the mid-Holocene, a more arid climate in this region changed vegetation distributions and potentially increased erosion. Morris et al. (2013) show that high elevation forested area decreased on the Aquarius Plateau just northeast of our study area at this time, while more scrub-like pinyon-juniper woodlands increased in range and abundance across the Colorado Plateau (Betancourt, 1987; Mehringer and Wigand, 1990; Jennings and Elliott-Fisk, 1993; Miller and Wigand, 1994; Wigand et al., 1995b). The stripping of hillslope

deposits during this time of vegetation disturbance and high sediment yield may have set the stream systems into the oscillating disequilibrium of arroyo dynamics over the last 6000 years. This interpretation is seemingly contradicted by the Pleistocene erosion rates of our dataset being somewhat faster than erosion rates from sediment in the Holocene alluvial fills.

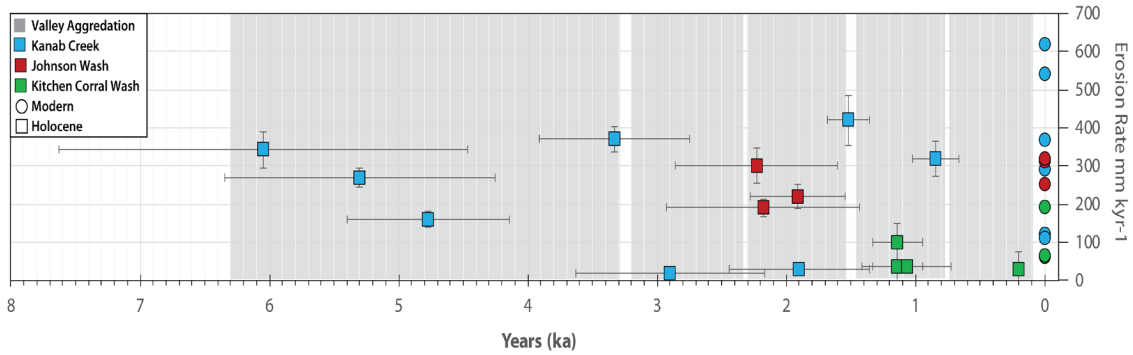

Figure 4-8 – Summary of Holocene cut-fill chronologies from Kanab (Townsend et al., 2019), Johnson Wash (Ch II, this dissertation)), and Kitchen Corral Wash (Huff and Rittenour, 2014). Holocene erosion rates are plotted as markers colored by the topographic position of the channel reach where sediment was sampled. The 2-sigma error in age is shown for sample with errors larger than marker (> 500 years). Grey shading shows periods of regional valley aggrdation.

Conclusions

Modern and paleo erosion rates derived from Beryllium-10 are used to determine if climate change modified denudation rates in the Grand Staircase region of the Colorado Plateau over the last 100 kyr. Paleo-erosion rates sampled from Pleistocene and

Holocene alluvial deposits show overall higher erosion rates during the Pleistocene relative to Holocene and modern analogues. Coarse sediment composing the Pleistocene piedmont and terrace deposits suggest deposition during periods of effectivly wetter climate conditions during interglacial periods. Additionally, the overall cooler Pleistocene may have been more conducive to physical weathering processes such as freeze-thaw that produce larger sized clasts. Five out of six samples showed decreased ^{10}Be concentrations and faster erosion rates across different rock types during overall cooler and wetter climate conditions of the Pleistocene compared to the Holocene.

Over million-year timescales, the Grand Staircase region is a landscape in transience, responding to base-level fall in response to the cutting of Grand Canyon. While preliminary evidence suggests erosion rates may have been depressed in the White Cliffs in the mid-late-Pleistocene, it is important to note this observation is based on one data point and is interpreted with caution. The disparity between Pleistocene and Holocene erosion rates in the White Cliffs is likely not related to a propogating wave of incision. However, to further investigate the temperal shift in erosion rates in the White Cliffs, the Pleistocene dataset could be exapanded on to include stored Pleistocene sediment in small headwater sub-catchments located in the White Cliffs and other escarpments in the study area.

Holoecene-age sediment did not show a systematic trend in erosion rates related to the timing of arroyo aggradation and entrenchment, but did record a strong influence from local lithologic sediment sources. The similarity in erosion rates between modern and Holocene alluvial deposits demonstrates that sediment in aggraded valleys is well mixed and/or erosion rates are relativly similar today as they have been over the last 6000

years. This study provides a robust regional data set of erosion rates that characterizes spatial and temporal variability in sediment supply and is therefore a valuable broad-scale experimental system for understanding landscape evolution. Stream entrenchment destroys agriculture and rangelands, alters stream hydrology, and transports large volumes of sediment downstream impacting water quality, floodplain and riparian habitat, and reservoir storage capacity. Understanding the natural variablity of sediment yields over cenntennial to millenial timescales puts modern seidment yields into perspective allowing for more informed public and private land management.

Acknowledgements

We would like to thank Cliff Riebe and Claire Lukens for expertise and access to the cosmogenic nuclide lab at the University of Wyoming and the PRIME lab at University of Purdue for measurements. We would also like to thank Alan Hidy from Lawrence Livermore National Laboratory for Matlab codes to calculate nuclide production at depth and guidance in cosmogenic methods and assumptions. We would like to thank the National Science Foundation for funding this research (EAR-1057192 and EAR -1536296)

References Cited

Adams, D. K., and Comrie, A. C., 1997, The North American monsoon: Bulletin of the American Meteorological Society, v. 78, no. 10, p. 2197-2213.

Aitken, M.J., 1998. Introduction to optical dating: the dating of Quaternary sediments by the use of photon-stimulated luminescence. Clarendon Press.

Aitken, M.J. and Xie, J., 1992. Optical dating using infrared diodes: young samples. Quaternary Science Reviews, 11(1-2), p.147-152.

Asmerom, Y., Polyak, V., Burns, S., and Rassmussen, J., 2007, Solar forcing of Holocene climate: New insights from a speleothem record, southwestern United States: Geology, v. 35, no. 1, p. 1-4.

Bailey, R. W., 1935, Epicycles of Erosion in the Valleys of the Colorado Plateau Province: The Journal of Geology, v. 43, no. 4, p. 337-355.

Balco, G., Stone, J. O., Lifton, N. A., and Dunai, T. J., 2008, A complete and easily accessible means of calculating surface exposure ages or erosion rates from 10Be and 26Al measurements: Quaternary Geochronology, v. 3, no. 3, p. 174-195.

Balco, G., and Stone, J. O. H., 2005, Measuring middle Pleistocene erosion rates with cosmic-ray-produced nuclides in buried alluvial sediment, Fisher Valley, southeastern Utah: Earth Surface Processes and Landforms, v. 30, no. 8, p. 1051-1067.

Borchers, B., Marrero, S., Balco, G., Caffee, M., Goehring, B., Lifton, N., Nishiizumi, K., Phillips, F., Schaefer, J., and Stone, J., 2016, Geological calibration of spallation production rates in the CRONUS-Earth project: Quaternary Geochronology, v. 31, p. 188-198.

Bull, W. B., 1991, Geomorphic responses to climatic change: Oxford University Press, Oxford.

Bull, W. B., 1997, Discontinuous ephemeral streams: Geomorphology, v. 19, no. 3–4, p. 227-276.

Cook, E. R., Seager, R., Cane, M. A., and Stahle, D. W., 2007, North American drought: Reconstructions, causes, and consequences: Earth-Science Reviews, v. 81, no. 1, p. 93-134.

Cook, E. R., Woodhouse, C. A., Eakin, C. M., Meko, D. M., and Stahle, D. W., 2004, Long-term aridity changes in the western United States: Science, v. 306, no. 5698, p. 1015-1018.

Cook, K. L., Whipple, K. X., Heimsath, A. M., and Hanks, T. C., 2009, Rapid incision of the Colorado River in Glen Canyon–insights from channel profiles, local incision rates, and modeling of lithologic controls: Earth Surface Processes and Landforms, v. 34, no. 7, p. 994-1010.

Cooke, R. U., and Reeves, R. W., 1976, Arroyos and environmental change: Clarendon, Oxford.

Darling, A., and Whipple, K., 2015, Geomorphic constraints on the age of the western Grand Canyon: Geosphere, v. 11, no. 4, p. 958-976.

Davis, O.K. and Shafer, D.S., 1992. An Early-Holocene maximum for the Arizona monsoon recorded at Montezuma Well, central Arizona. Palaeogeogr. Palaeoclimatol. Palaeoecol, 92, pp.107-119.

DeLong, B. D., 2007, Effects of Quaternary climate change on tributary sedimentation and geomorphology in eastern Grand Canyon, Utah State University.

Doelling, H. H., Blackett, R. E., Hamblin, A. H., Powell, J. D., and Pollock, G. L., 2000, Geology of Grand Staircase-Escalante National Monument, Utah, *in* Sprinkel, D. A., Jr., T. C. C., and Anderson, P. B., eds., Geology of Utah's Parks and Monuments, Volume 28, Utah Geological Association.

Duller, G. A., 2008, Single-grain optical dating of Quaternary sediments: why aliquot size matters in luminescence dating: Boreas, v. 37, no. 4, p. 589-612.

Dunne, J., Elmore, D. and Muzikar, P., 1999. Scaling factors for the rates of production of cosmogenic nuclides for geometric shielding and attenuation at depth on sloped surfaces. Geomorphology, 27(1-2), pp.3-11.

Galbraith, R., and Roberts, R. G., 2012, Statistical aspects of equivalent dose and error calculation and display in OSL dating: an overview and some recommendations: Quaternary Geochronology, v. 11, p. 1-27.

Granger, D. E., Fabel, D., and Palmer, A. N., 2001, Pliocene− Pleistocene incision of the Green River, Kentucky, determined from radioactive decay of cosmogenic 26Al and 10Be in Mammoth Cave sediments: Geological Society of America Bulletin, v. 113, no. 7, p. 825-836.

Granger, D. E., Kirchner, J. W., and Finkel, R., 1996, Spatially Averaged Long-Term Erosion Rates Measured from in Situ-Produced Cosmogenic Nuclides in Alluvial Sediment: The Journal of Geology, v. 104, no. 3, p. 249-257.

Granger, D. E., Kirchner, J. W., and Finkel, R. C., 1997, Quaternary downcutting rate of the New River, Virginia, measured from differential decay of cosmogenic 26Al and 10Be in cave-deposited alluvium: Geology, v. 25, no. 2, p. 107-110.

Harvey, J. E., Pederson, J. L., and Rittenour, T. M., 2011, Exploring relations between arroyo cycles and canyon paleoflood records in Buckskin Wash, Utah: Reconciling scientific paradigms: Geological Society of America Bulletin, v. 123, no. 11-12, p. 2266-2276.

Hereford, R., 2002, Valley-fill alluviation during the Little Ice Age (ca. AD 1400-1880), Paria River basin and southern Colorado Plateau, United States: Geological Society of America Bulletin, v. 114, no. 12, p. 1550-1563.

Hidy, A. J., Gosse, J. C., Froese, D. G., Bond, J. D., and Rood, D. H., 2013, A latest Pliocene age for the earliest and most extensive Cordilleran Ice Sheet in northwestern Canada: Quaternary Science Reviews, v. 61, no. 0, p. 77-84.

Huff, W., and Rittenour, T., 2014, Holocene alluvial stratigraphy of Kitchen Corral Wash, southern Utah, *in* MacLean, J. S., Biek, R.F., and Huntoon, J.E., ed., Geology of Utah's Far South: Utah Geological Association Publication 43, p. 77–96.

Huntley, D. J., Godfreysmith, D. I., and Thewalt, M. L. W., 1985, Optical dating of sediments: Nature, v. 313, no. 5998, p. 105-107.

Jimenez-Moreno, G., Fawcett, P. J., and Anderson, R. S., 2008, Millennial- and centennial-scale vegetation and climate changes during the late Pleistocene and Holocene from northern New Mexico (USA): Quaternary Science Reviews, v. 27, no. 13-14, p. 1442-1452.

Jochems, A. P., and Pederson, J. L., 2015, Active salt deformation and rapid, transient incision along the Colorado River near Moab, Utah: Journal of Geophysical Research: Earth Surface, v. 120, no. 4, p. 730-744.

Johnsen, S. J., 1999, GRIP Oxygen Isotopes, PANGAEA.

Karlstrom, Karl E., John P. Lee, Shari A. Kelley, Ryan S. Crow, Laura J. Crossey, Richard A. Young, Greg Lazear et al., 2014. Formation of the Grand Canyon 5 to 6 million years ago through integration of older palaeocanyons. Nature Geoscience 7, no. 3: p. 239-244.

Lal, D., 1991, Cosmic-ray labeling of erosion surfaces - In-situ nuclide production-rates and erosion models: Earth and Planetary Science Letters, v. 104, no. 2-4, p. 424-439.

Lisiecki, L. E., and Raymo, M. E., 2005, A Pliocene-Pleistocene stack of 57 globally distributed benthic δ18O records: Paleoceanography, v. 20, no. 1.

Longwell, C. R., 1946, How old is the Colorado River?: American Journal of Science, v. 244, no. 12, p. 817-835.

Madsen, D.B., Rhode, D., Grayson, D.K., Broughton, J.M., Livingston, S.D., Hunt, J., Quade, J., Schmitt, D.N. and Shaver III, M.W., 2001. Late Quaternary environmental change in the Bonneville basin, western USA. Palaeogeography, Palaeoclimatology, Palaeoecology, 167(3-4), pp.243-271.

Mann, D. H., and Meltzer, D. J., 2007, Millennial-scale dynamics of valley fills over the past 12,000 14C yr in northeastern New Mexico, USA: Geological Society of America Bulletin, v. 119, no. 11-12, p. 1433-1448.

Marshall, J. A., Roering, J. J., Gavin, D. G., and Granger, D. E., 2017, Late Quaternary climatic controls on erosion rates and geomorphic processes in western Oregon, USA: GSA Bulletin, v. 129, no. 5-6, p. 715-731.

Menking, K.M. and Anderson, R.Y., 2003. Contributions of La Niña and El Niño to middle Holocene drought and late Holocene moisture in the American Southwest. Geology, 31(11), pp.937-940.

Murray, A.S. and Wintle, A.G., 2000. Luminescence dating of quartz using an improved single-aliquot regenerative-dose protocol. Radiation measurements, 32(1), pp.57-73.

Nelson, M. S., and Rittenour, T., 2014, Middle to late Holocene chronostratigraphy of alluvial fill deposits along Kanab Creek in southern Utah: Geology of Utah's Far South: Utah Geological Association, Publication, v. 43, p. 97-116.

Pazzaglia, F., Lucas, S., Morgan, G., and Zeigler, K., 2005, River responses to Ice Age (Quaternary) climate in New Mexico: New Mexico's Ice Ages: New Mexico Museum of Natural History and Science Bulletin, v. 28, p. 115-124.

Pederson, Joel, Frank Pazzaglia, and Gary Smith, 2000, Ancient hillslope deposits: Missing links in the study of climate controls on sedimentation: Geology 28, no. 1, p. 27-30.

Pederson, J. L., Mackley, R. D., and Eddleman, J. L., 2002, Colorado Plateau uplift and erosion evaluated using GIS: GSA TODAY, v. 12, no. 8, p. 4-10.

Polyak, V. J., and Asmerom, Y., 2001, Late Holocene climate and cultural changes in the southwestern United States: Science, v. 294, no. 5540, p. 148-151.

Prescott, J.R. and Hutton, J.T., 1994. Cosmic ray contributions to dose rates for luminescence and ESR dating: large depths and long-term time variations. Radiation measurements, 23(2-3), p. 497-500.

Rasmussen, J. B., Polyak, V. J., and Asmerom, Y., 2006, Evidence for Pacific-modulated precipitation variability during the late Holocene from the southwestern USA: Geophysical Research Letters, v. 33, no. 8.

Riebe, C. S., and Granger, D. E., 2013, Quantifying effects of deep and near-surface chemical erosion on cosmogenic nuclides in soils, saprolite, and sediment: Earth Surface Processes and Landforms, v. 38, no. 5, p. 523-533.

Riley, K. E., Rittenour, T. M., Pederson, J. L., and Belmont, P., 2019, Erosion rates and patterns in a transient landscape, Grand Staircase, southern Utah, USA: Geology.

Schaller, M. and Ehlers, T.A., 2006. Limits to quantifying climate driven changes in denudation rates with cosmogenic radionuclides. Earth and Planetary Science Letters, 248(1-2), pp.153-167.

Schumm, S. A., and Hadley, R. F., 1957, Arroyos and the semiarid cycle of erosion [Wyoming and New Mexico]: American Journal of Science, v. 255, no. 3, p. 161-174.

Schwanghart, W., and Scherler, D., 2014, Short Communication: TopoToolbox 2–MATLAB-based software for topographic analysis and modeling in Earth surface sciences: Earth Surface Dynamics, v. 2, no. 1, p. 1-7.

Smith, G.I. and Bischoff, J.L. eds., 1997. An 800,000-year paleoclimatic record from Core OL-92, Owens Lake, southeast California (Vol. 317). Geological Society of America.

Spencer, J., Peters, L., McIntosh, W., Patchett, P., Young, R., and Spamer, E., 2001, 40Ar/39Ar geochronology of the Hualapai Limestone and Bouse Formation and implications for the age of the lower Colorado River: Colorado River: Origin and evolution: Grand Canyon, Arizona, Grand Canyon Association, p. 89-91.

Stine, S., 1998, Water, Environment and Society in Times of Climatic Change.

Townsend, K. F., Nelson, M. S., Rittenour, T. M., and Pederson, J. L., 2019, Anatomy and evolution of a dynamic arroyo system, Kanab Creek, southern Utah, USA: Geological Society of America Bulletin.

Tucker, G. E., and Slingerland, R., 1997, Drainage basin responses to climate change: Water Resources Research, v. 33, no. 8, p. 2031-2047.

Waters, M.R. and Haynes, C.V., 2001. Late Quaternary arroyo formation and climate change in the American Southwest. Geology, 29(5), pp.399-402.

Webb, R. H., 1985, Late Holocene flooding on the Escalante River, south-central Utah [Ph.D. Dissertation: The University of Arizona., 204 p.

Weng, C., and Jackson, S. T., 1999, Late Glacial and Holocene vegetation history and paleoclimate of the Kaibab Plateau, Arizona: Palaeogeography, Palaeoclimatology, Palaeoecology, v. 153, no. 1, p. 179-201.

Whitney, John W., and Charles D. Harrington., 1993. Relict colluvial boulder deposits as paleoclimatic indicators in the Yucca Mountain region, southern Nevada. Geological Society of America Bulletin 105, no. 8: 1008-1018.

Supplemental Material

Table 4-S1. Dose Rate Information

USU num.	In-situ H_2O (%)[1]	Grain size (μm)	K (%)[2]	Rb (ppm)[2]	Th (ppm)[2]	U (ppm)[2]	Cosmic (Gy/ka)
USU-1627	1.6	180-250	0.67±0.02	22.7±0.9	1.4±0.2	0.5±0.1	0.07±0.01
USU-1631	1.3	125-212	1.86±0.05	71.9±2.9	5.3±0.5	1.4±0.1	0.15±0.01
USU-1754	0.22	180-250	0.30±0.01	9.5±0.4	0.8±0.2	0.3±0.1	0.11±0.01
USU-1759	1.8	180-250	0.92±0.02	37.3±1.5	3.0±0.3	1.0±0.1	0.17±0.02
USU-2189	-	125-250	1.15±0.03	45.4±1.8	4.4±0.4	1.1±0.1	0.14±0.01
USU-2238	8.8	150-250	1.19±0.03	42.4±1.7	3.0±0.3	1.0±0.1	0.16±0.02
USU-2239	0.8	150-250	0.97±0.02	35.2±1.4	2.0±0.2	0.6±0.1	0.13±0.01
USU-2241	5.1	150-250	1.36±0.03	59.8±2.4	5.0±0.5	1.6±0.1	0.26±0.03
USU-2242	7.0	150-250	0.84±0.02	39.1±1.6	5.3±0.5	1.7±0.1	0.15±0.01
USU-2243	-	150-250	1.41±0.04	58.7±2.3	5.6±0.5	1.4±0.1	0.18±0.02

[1] Assumed 3±3% for moisture content over burial history for Holocene samples with in-situ values <3%, and 5% for Pleistocene samples.

[2] Radioelemental concentrations determined by ALS Chemex using ICP-MS and ICP-AES techniques; dose rate is derived from concentrations by conversion factors from Guérin et al. (2011).

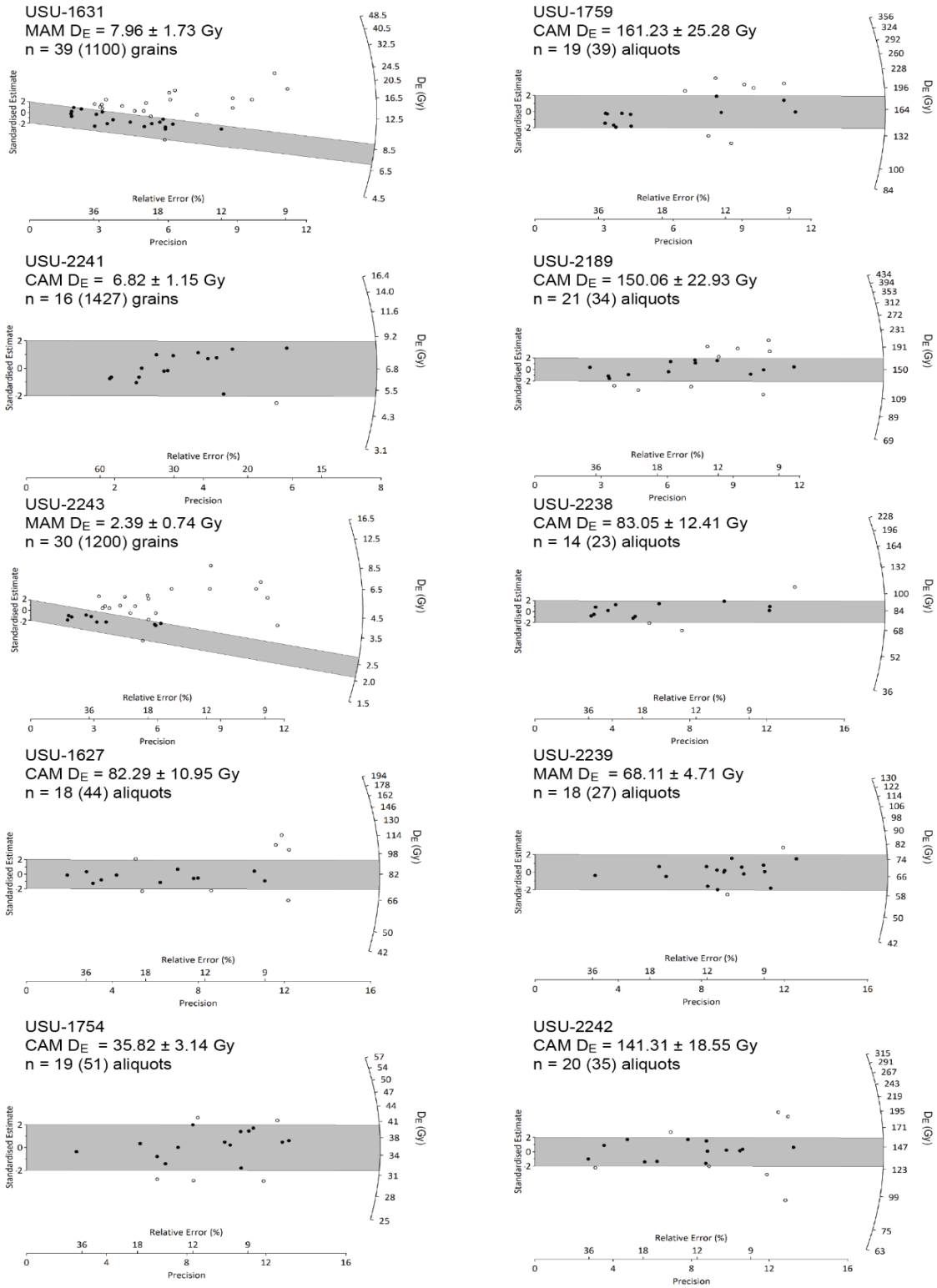

Figure 4-S1 – Equivalent dose (De) radial plots.

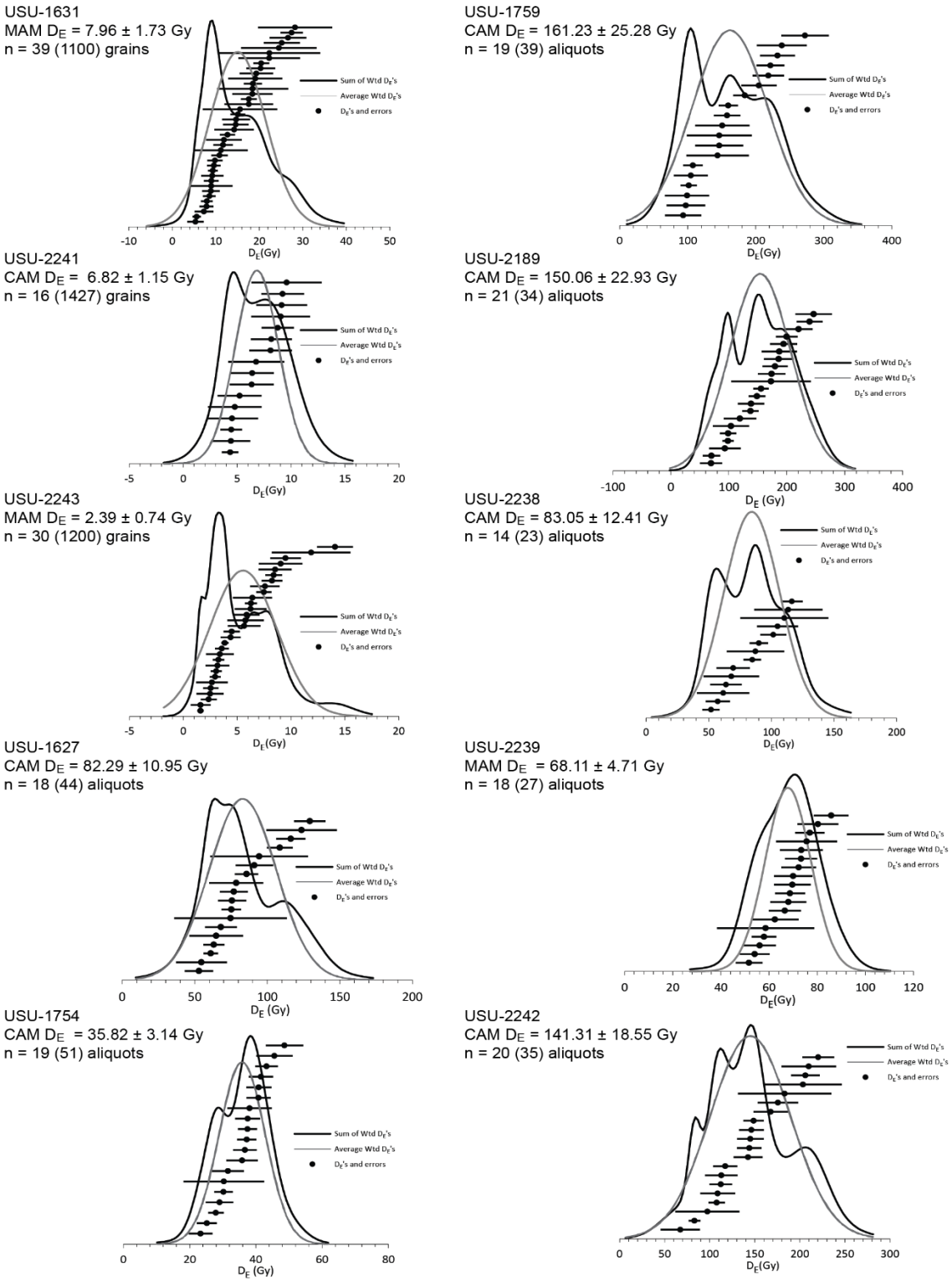

Figure 4-S2 – Equivalent dose (De) probability density functions.

Table 4-S2 – Paleo-sample locations and data used to calculate burial-corrected ^{10}Be production and measured ^{10}Be concentrations. Samples are ordered from downstream to upstream.

Sample ID	Age (ka)	Sample Depth (cm)	Sample Latitude (dd)	Sample Longitude (dd)	Sample Elev. (m)	Topo Shield. Factor	Spallogenic Production at Depth (atoms/g/a)	Muogenic Production at Depth (atoms/g/a)	Total Production at Depth [1] (atoms/g/a)	Post Deposit. ^{10}Be Conc. (at/g)	Post-Deposit. Gain (%)	Measured ^{10}Be Conc. (at/g)	Anal. Error	% Error	Depth Corrected ^{10}Be Conc. (at/g)
KNB 40	2.90	510	37.018549	-112.537484	1476	0.986	2.260E-02	1.055E-01	1.280E-01	371	0.08	4.71E+05	1.1E+04	2	4.71E+05
KNB 29	70.73	790	37.018549	-112.537484	1476	0.986	2.369E-04	6.630E-02	6.650 E-02	4623	10.7	4.31E+04	1.3E+03	3	3.84E+04
KNB 41	94.55	1190	37.018549	-112.537484	1476	0.986	9.630E-07	4.330E-02	4.330E-02	3997	8.16	4.90E+04	1.6E+03	3	4.50E+04
KNB 26	4.77	550	37.083084	-112.526285	1532	0.992	1.530E-02	1.009E-01	1.162E-01	554	0.97	5.72E+04	1.4E+03	2	5.67E+04
KCW 7	0.2	100	37.216930	-112.140588	1691	0.987	3.014E+00	1.925E-01	3.207E+00	971	0.27	3.60E+05	1.7E+04	5	3.59E+05
KCW 8	1.14	550	37.216930	-112.140588	1691	0.987	1.910E-02	1.065E-01	1.256E-01	143	0.05	3.17E+05	1.4E+04	4	3.17E+05
KCW 9	1.14	690	37.216930	-112.140588	1691	0.987	3.600E-03	8.930E-02	9.290E-02	106	0.09	1.16E+05	6.1E+03	5	1.15E+05
KNB 17	0.84	800	37.118644	-112.543931	1549	0.986	9.247E-04	7.690E-02	7.790E-02	65	0.19	3.47E+04	1.5E+03	4	3.46E+04
KNB 16	1.52	800	37.118644	-112.543931	1549	0.986	8.431E-04	7.700E-02	7.780E-02	118	0.44	2.67E+04	2.0E+03	7	2.66E+04
KNB 15	6.05	2500	37.118644	-112.543931	1549	0.986	1.473E-12	2.160E-02	2.160 E-02	131	0.40	3.26E+04	1.2E+03	4	1.15E+05
JW 23	2.45	2500	37.132096	-112.390823	1664	0.985	1.469E-12	2.190E-01	2.190E-01	54	0.15	3.58E+04	2.5E+03	7	3.57E+04
KNB 38	52.23	700	37.198340	-112.618030	1900	0.947	1.100E-03	7.910E-02	8.020E-02	4133	4.82	8.57E+04	3.4E+03	4	8.15E+04
JW 2	1.91	1100	37.223542	-112.371094	1513	0.987	2.256E-05	5.580E-02	5.580E-02	107	0.21	5.14E+04	2.4E+03	5	5.13E+04
KNB 25	3.33	700	37.399200	-112.455670	1887	0.985	3.200E-03	8.950E-02	9.270E-02	308	0.90	3.41E+04	1.6E+03	5	3.38E+04
KNB 24	5.3	700	37.399200	-112.455670	1887	0.985	3.500E-03	8.980E-02	9.330E-02	494	1.06	4.64E+04	2.0E+03	4	4.59E+04
KNB 8	1.9	400	37.302623	-112.484102	1910	0.991	3.810E-02	1.173E-01	1.554E-01	295	0.07	3.94E+05	1.5E+04	4	3.94E+05
KNB 42	111.55	500	37.302623	-112.484102	1910	0.991	1.670 E-02	1.035E-01	1.202 E-01	1304	1.13	1.15E+05	3.1E+03	3	1.14E+05
JW 26	2.24	100	37.282793	-112.340496	1810	0.981	3.973E+00	2.076E-01	4.181E+00	9360	12.71	7.36E+04	6.0E+03	8	6.43E+04
JW 22	87.23	600	37.282793	-112.340496	1810	0.981	4.200E-03	8.950E-02	9.360E-02	7992	46.14	1.73E+04	8.0E+02	5	9.33E+03
KCW 11	1.07	400	37.344637	-112.216949	1894	0.984	1.346E-01	1.361E-01	2.707E-01	290	0.08	3.61E+05	1.6E+04	4	3.61E+05
KCW 10	79.32	550	37.344637	-112.216949	1894	0.984	8.900E-03	9.750E-02	1.063E-01	8270	11.34	7.29E+04	7.8E+03	11	6.46E+04

[1] The average density of material above sandy-gravel Pleistocene samples was assumed 2.2 g /cm^3 and the average density of material above fine-grained sandy Holocene samples was 1.9 g /cm^3. Neutron attenuation length was assumed to 160 g / cm^2 following Balco et al., (2008). Reference spallogenic production was assumed 4.0 atoms/g/yr following Borchers et al. (2016) and scaled by topographic shielding factor.

Table 4-S3 – CRONUS inputs and outputs for paleo-samples.

Sample ID	Basin Area (km^2)	Basin Mean Lat. (dd)	Basin Mean Long. (dd)	Eff. Elev. (m)	Topo. Shield Factor	Depth Corrected ^{10}Be Conc. (at/g)	Basin Mean Production Rate (muons) (at/g/yr)	Basin Mean Production Rate (spallation) (at/g/yr)	Total Basin Mean Production Rate (at/g/yr)	Erosion Rate and Error (mm/kyr)
KNB 40	616	37.2441	112.5116	1957	0.986	4.71E+05 ± 1.1E+04	0.142	16.54	16.682	21.87 ± 1.85
KNB 29	616	37.2441	112.5116	1957	0.986	3.84E+04 ± 1.3E+03	0.142	16.54	16.682	273.48 ± 23.24
KNB 41	616	37.2441	112.5116	1957	0.986	4.50E+04 ± 1.6E+03	0.142	16.54	16.682	236.84 ± 20.36
KNB 26	51	37.1068	112.4866	1751	0.992	5.67E+04 ± 1.4E+03	0.133	14.35	14.483	164.54 ± 13.41
KCW 7	238	37.3118	112.2333	2050	0.987	3.59E+05 ± 1.7E+04	0.146	17.67	17.816	30.8 ± 2.9
KCW 8	238	37.3118	112.2333	2050	0.987	3.17E+05 ± 1.4E+04	0.146	17.67	17.816	34.98 ± 3.22
KCW 9	238	37.3118	112.2333	2050	0.987	1.15E+05 ± 6.1E+03	0.146	17.67	17.816	97.89 ± 9.35
KNB 17	440	37.2999	112.4968	2038	0.986	3.46E+04 ± 1.5E+03	0.146	17.51	17.656	325.26 ± 29.15
KNB 16	440	37.2999	112.4968	2038	0.986	2.66E+04 ± 2.0E+03	0.146	17.51	17.656	423.48 ± 46.12
KNB 15	440	37.2999	112.4968	2038	0.986	3.25E+04 ± 1.2E+03	0.146	17.51	17.656	346.36 ± 30.01
JW 23	412	37.2625	112.3637	1982	0.985	3.40E+04 ± 2.5E+03	0.143	16.81	16.953	318.73 ± 34.32
KNB 38	0.29	37.2036	112.6231	2057	0.947	8.15E+04 ± 3.4E+03	0.147	17.00	17.147	133.76 ± 11.92
JW 2	213	37.3185	112.3664	2050	0.987	5.13E+04 ± 2.4E+03	0.146	17.67	17.816	220.89 ± 20.22
KNB 25	190	37.3991	112.4553	2217	0.985	3.38E+04 ± 1.6E+03	0.154	19.79	19.944	373.42 ± 34.4
KNB 24	190	37.3991	112.4553	2217	0.985	4.59E+04 ± 2.0E+03	0.154	19.79	19.944	274.67 ± 24.81
KNB 8	50	37.3579	112.4461	2137	0.991	3.94E+05 ± 1.5E+04	0.150	18.85	19.00	29.82 ± 2.68
KNB 42	50	37.3579	112.4461	2137	0.991	1.14E+05 ± 3.1E+03	0.150	18.85	19.00	116.3 ± 9.87
JW 26	54	37.3574	112.3319	2164	0.981	6.53E+04 ± 6.0E+03	0.152	19.00	19.152	185.46 ± 22.62
JW 22	54	37.3574	112.3319	2164	0.981	9.33E+03 ± 8.0E+02	0.152	19.00	19.152	1305.44 ± 152.41
KCW 11	50	37.4022	112.2669	2302	0.984	3.61E+05 ± 1.6E+04	0.158	20.92	21.078	36.16 ± 3.35
KCW 10	50	37.4022	112.2669	2302	0.984	6.46E+04 ± 7.8E+03	0.158	20.92	21.078	205.27 ± 30.02

Clast Count Methods and Data

Clast count data was collected by Alexander Short for his MS Thesis at Utah State University from the three Pleistocene deposits sampled on the Skutumpah Terrace (KNB 42, JW 22, and KCW 10) to determine the lithologic source of the deposit (Supplemental Material). In all three deposits, the dominant sediment source was from the Claron Formation comprising the Pink Cliffs. Upper Kanab Creek contained 46% and upper Johnson Wash and Kitchen Corral Wash both contained 62% clasts from the Pink Cliffs. The remainder of clasts came from different lithologies between the Pink Cliffs and the location of deposit.

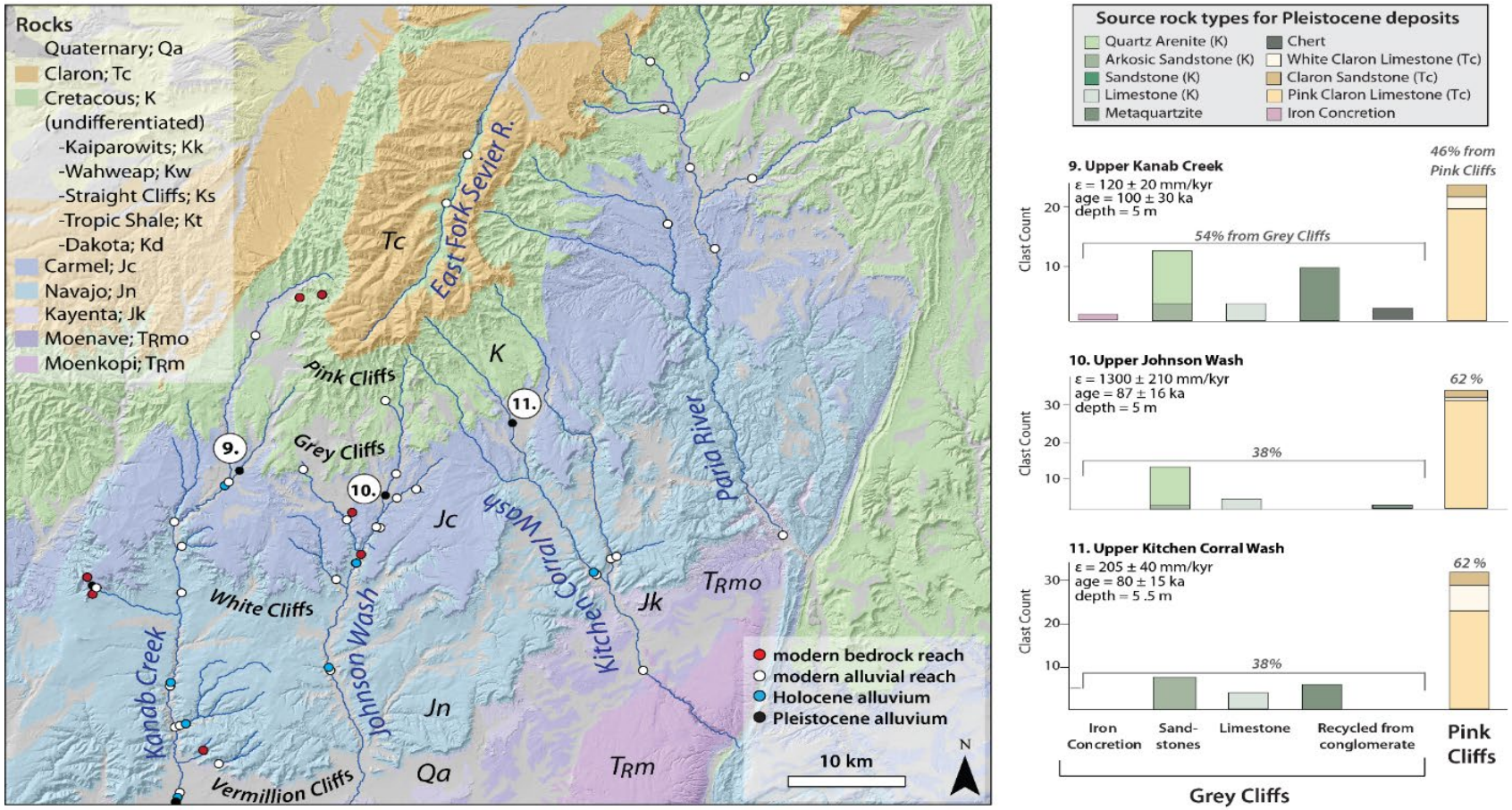

Figure 4-S3 – Overview of the geology of the region. Circles show locations of all modern (red and white), Holocene (blue), and Pleistocene (black) sediment samples containing ^{10}Be concentration inventories and inferred erosion rates in the study area. Locations of sample suites containing Pleistocene erosion rates and clast count data are identified in numbered white circles. Erosion rates (ε) and age of deposit are annotated for each clast count deposit.

References Cited

Balco, G., Stone, J. O., Lifton, N. A., and Dunai, T. J., 2008, A complete and easily accessible means of calculating surface exposure ages or erosion rates from 10Be and 26Al measurements: Quaternary Geochronology, v. 3, no. 3, p. 174-195.

Borchers, B., Marrero, S., Balco, G., Caffee, M., Goehring, B., Lifton, N., Nishiizumi, K., Phillips, F., Schaefer, J., and Stone, J., 2016, Geological calibration of spallation production rates in the CRONUS-Earth project: Quaternary Geochronology, v. 31, p. 188-198.

Guérin, G., Mercier, N. and Adamiec, G., 2011. Dose-rate conversion factors: update. Ancient TL, 29(1), pp.5-8.

CHAPTER V

MID-LATE HOLOCENE CLIMATE-FIRE RELATIONSHIPS ON THE COLORADO PLATEAU, USA

Abstract

Decadal to millennial scale fire activity was reconstructed from 7,500 to 300 cal yr BP using alluvial charcoal from four large watersheds that drain the Grand Staircase region of the Colorado Plateau in southern Utah. The study area is located along a forest-woodland-shrub ecosystem gradient consisting of mixed-conifer forests, ponderosa pine, pinyon-juniper woodlands, and desert scrub. We interpreted 179 charcoal-derived radiocarbon-ages as discrete fires and investigated similarities among cumulative fire probabilities for each watershed to examine possible relationships between fire activity and climate. The fire record extends to 7500 cal yr BP in two watersheds and 5000 cal yr BP in all four watersheds. We identified 22 regionally synchronous fires between 5000 and 300 cal yr BP, where three out of the four watersheds contained statistically similar radiocarbon age distributions. The frequency of regionally synchronous fires increased dramatically ~2800 cal yr BP. Over millennial timescales, we interpret regionally widespread fires to be related to hydroclimate-driven changes in the abundance and distribution of fuel. Over shorter timescales, we interpret regional fires to be related to the timing of drought. In semi-arid ecosystems, fuel accumulates during wet decades and is subsequently consumed during stand-replacing fires that follow discrete, annual droughts.

Our results suggest climate-driven changes in vegetation productivity and the frequency and intensity of drought controlled mid- to late- Holocene fire activity.

Introduction

Analyses of changes in wildfire activity over the last two to three decades indicate an increase in the number of fires, fire season length, total area burned, and fire severity in the southwestern United States (Westerling, 2016) and globally (Holden et al., 2018; Jolly et al., 2015; Abatzoglou and Williams, 2016). Forests in the Southwest are vulnerable to fire during periods of drought and warming, particularly in dense forest stands where fuel build-up is high (Williams et al., 2010). Recent increases in fire activity, as a result of anthropogenic climate change, has been a major driver of changes in vegetation structure and species distributions (Overpeck et al., 1990; Dale et al., 2001; Williams et al., 2010), which in turn have affected the size and severity of wildfires (Power et al., 2008). In order to understand future effects of fire, it is important to place recent trends in fire activity in context by understanding how past centennial- to millennial-scale climatic change has influenced regional fire activity and vegetation patterns across the landscape during the Holocene.

Tree-ring-based studies have indicated that regionally synchronous fires in the Southwest are linked to short-term seasonal to inter-annual climate variability (Swetnam and Betancourt, 1990; Swetnam and Betancourt, 1998) and fire activity is regulated by effective moisture and fuel accumulation (Littell et al., 2009). Tree-ring reconstructions suggest that over the last 500-years, in southwest shrub steppe, pinyon-juniper woodlands

(*Pinus edulis* Engelm. and *Juniperus osteosperma* (Torr.) Little, and J. *monosperma* (Engelm.)), and across forest ecosystem gradients (pinyon-juniper, ponderosa pine (*Pinus ponderosa* Lawson and C. Lawson), and mixed-conifer), large fires burned during average precipitation years that were preceded by one or two wetter than average years (Baisan and Swetnam, 1990; Baisan and Swetnam, 1997; Brown et al., 2001). Above-average antecedent precipitation (Swetnam and Betancourt, 1998) and/or cooler temperatures (Veblen et al., 2000) in fuel-limited ecosystems result in fuel accumulation and are related to the year(s) prior to widespread fire (Littell et al., 2009).

The Southwest has experienced rapid warming, decreased precipitation, and intense droughts since the mid-1970's (Williams et al., 2010). Models suggest future climate conditions will be outside the natural range of variability observed during the last few centuries (Marlon et al., 2012) and the Southwest might experience a long-term shift to warmer and more arid conditions, e.g., mega-droughts similar to those of the Medieval Warm Period (Schwinning et al., 2008). An additional complicating factor is that relationships among climate, vegetation, and fire frequency/intensity involve lag times that can span years, decades, and centuries (Whitlock et al., 2010). While the cause of recent increases in fire activity has been attributed to increased temperatures and length of the fire season, climate-vegetation feedbacks likely play an important role.

While tree-ring-based studies are able to resolve annual and seasonal relationships between climate, vegetation, and fire activity over many centuries, they often lack context for broad-scale, regional patterns, and long-term (centennial-to-millennial) changes. Different forest types occur along ecological gradients with attendant natural fire regimes, but have similar fire history patterns because differences in physical

environments, vegetation characteristics, and site histories can overprint the tree-ring record (Brown et al., 2001). Thus, large-scale, regional fire histories are invaluable records for better understanding the natural range of variability in fire regimes over longer time periods (e.g., millennia). Centuries-to-millennia climatic change likely influences regional fire activity through its control on precipitation and temperature variability (i.e., the hydroclimate), and therefore drought and vegetation patterns and abundance across the landscape.

Alluvial charcoal can provide a millennial-scale record of wildfire activity that extends through the Holocene in environments where lake records are not present. Importantly, alluvial records are abundant throughout the Southwest and provide a valuable record of Holocene wildfire activity that is otherwise unavailable from other fire proxy records. At the turn of the twentieth century, streams throughout the Southwest rapidly entrenched up to forty meters below their floodplains exposing Holocene-aged alluvium. This widespread change in stream dynamics stimulated research investigating geomorphic change of these streams and arroyo and paleo-flood studies in the region produced hundreds of radiocarbon ages dating depositional events. Some long-term millennial-scale fire records from the western U.S. have been derived from alluvial charcoal collected in depositional systems such as alluvial fans (e.g., Meyer et al., 1995; Pierce et al., 2004; Bigio et al., 2010; Riley et al., 2015; Fitch and Meyer, 2016).

In this study, we take advantage of the rich alluvial charcoal data, collected from valley-fill sediment exposed in channel banks of arroyos and paleo-flood deposits in southern Utah, to investigate how climate change has influenced regional fire activity in the west-central Colorado Plateau. This study provides millennial scale records of fire

from what is now dominantly pinon-juniper forest. We compare fire records from across a large geographic region to determine synchronous periods of fire activity, evaluate their timing, and the associated climatic conditions. The primary research questions are: 1) When were periods of increased regional fire activity in a Pinyon-Juniper Woodland during the Holocene and 2) What is the relationship between increased regional fire activity and hyrdroclimate?

By extending the record of regional fire activity to the mid-Holocene, the currently century-scale, tree-ring-based understanding of fire in the Southwest (e.g., Swetnam and Baisan, 1996; Grissino-Mayer and Swetnam, 2000; Westerling et al., 2003) can be extended. More importantly, large-scale and longer-term fire histories can provide regional context to the sparse number of semi-arid system fire histories (e.g., Floyd et al., 2004; Weppner et al., 2013). They may also improve understanding of fire regimes in pinyon-juniper woodlands where limited numbers of fire scarred trees, and slow post-fire re-establishment make tree-ring-based reconstructions rare (Baker and Shinneman, 2004; Floyd et al., 2004).

Study Area

We reconstructed wildfire activity in four watersheds that drain the Grand Staircase region of the Colorado Plateau physiographic province in southern Utah and northern Arizona (Figure 5-1). Watersheds included the upper portions of Kanab Creek (615 km^2), Johnson Wash (692 km^2), a tributary to the Paria River (769 km^2), and the Escalante River (5,245 km^2). The region is characterized by cliff and bench topography

composed of gently northward dipping Mesozoic and Tertiary sedimentary rocks. Elevations range from 970 to 3500 m asl, that increase to the north from Grand Canyon. Precipitation increases with elevation observed at Lee's Ferry, AZ (978 m asl elevation; 155 ± 59 mm/yr), Kanab, UT (1494 m; 336 ± 95 mm/yr), Escalante, UT (1770 m; 264 ± 2mm/yr), Bryce Canyon, UT (2413 m; 397 ± 110 mm/yr; Climate Center Data accessed November, 2017, all MAP data span 1960-2010 unless record had a missing monthly value and no annual value was calculated). Precipitation is bimodal; with peaks in the winter months of January through March and in the late summer between July and September. The study area is on the northwest boundary of influence from the North American Monsoon (NAM), which is characterized by a prominent increase in precipitation from July through September (Figure 5-1) that originates from the Gulf of Mexico (Adams and Comrie, 1997). The influence of NAM and the proportion of mean annual precipitation received between July and September generally decreases from south to north across the Southwest. Winter precipitation is derived from Pacific Ocean westerlies produced by low-pressure systems of the jet stream. Hydroclimatic variability in the Southwest is associated with the El Niño Southern Oscillation (ENSO), a naturally occurring phenomenon where anomalous warming and cooling in the tropical Pacific (Capotondi et al., 2015) influences variability in the delivery of precipitation to the Southwest. El Niño conditions are related to enhanced winter precipitation in the Southwest, while La Niña conditions drier winter conditions (Cayan et al., 1999). ENSO has been shown to influence droughts, vegetation conditions (i.e., fuel accumulation and moisture content) and fire activity (Swetnam and Betancourt, 1990; Brown et al., 2001). In general, winter precipitation influences plant growth by recharging soil moisture and

summer ‘monsoon’ precipitation wets surface layers and controls annual grass production (Swetnam and Betancourt, 1998; Williams and Ehleringer, 2000).

The Southwest encompasses a broad range of ecosystems including subalpine, mixed-conifer, ponderosa pine, and pinyon-juniper woodlands, as well as lower elevation sagebrush steppe (*Artemisia* spp.) and grasslands. Over the past 150 years, Pinon-juniper woodland species are thought to have increased in density and distribution in some locations throughout the West, but have not changed or declined in others (Romme et al., 2009). Expansion has been attributed to fire exclusion, grazing, recovery from past disturbance, natural range expansion over millennia, CO_2 fertilization, and climate change (Miller and Rose, 1999; Miller and Tausch, 2001; Romme et al., 2009; Marlon et al., 2012). While substantial research, time, and money has been dedicated to combatting woody encroachment, our understanding of historical conditions and ecological processes in pinyon-juniper woodlands remains unclear (Romme et al., 2009). Pinyon-juniper woodlands have experienced recent large, severe (stand-replacing) fires that may be extraordinary over the past 100 years, but are likely within the natural range of variability of fire in these ecosystems over century- to millennial-timescales (Romme et al., 2009).

The dominant forest type within the study catchments was pinyon-juniper woodland, which constituted 40% of the total study area and 83% of the total forested area (Table 5-1; Table 5-S1; Table 5-S2). Non-forest communities that consist of desert scrub (sagebrush), blackbrush *(Coleogyne* spp.), Mormon tea (*Ephedra* spp.), saltbush (*Atriplex* spp.), and winterfat (*Ceratoides* spp.) occupied the lowest elevations and ~40% of the total study area. Pinyon-juniper woodlands and sagebrush steppe combined characterized ~80% of the study area. Higher-elevation subalpine, mixed-conifer, and

ponderosa pine forest communities make up the remaining forested area. Species included Engelmann spruce (Picea engelmannii Parry Ex. Engelm.), subalpine fir (Abies lasiocarpa (Hook.) Nutt), Douglas-fir (*Pseudotsuga menziesii* (Mirb.) Franco), white fir (*Abies concolor* Gord. & Glend), limber pine (*Pinus flexilis* James), quaking aspen (*Populus tremuloides* Michx.), and ponderosa pine.

Table 5-1. Percentage of area in different ecosystems types in the study area. High elevation forests include subalpine, mixed conifer, and ponderosa pine forests (Table 5-S1 and Table 5-S2)

Watershed	**Area (km^2)**	**Shrub and Grassland (%)**	**Pinyon-Juniper Woodland (%)**	**High-elevation Forested Area (%)**
Kanab Creek	600	29	62	9
Johnson Wash	400	33	59	8
Paria River	770	21	73	6
Escalante River	5250	45	29	26
Total Study Area	**7020**	40%	41%	19%

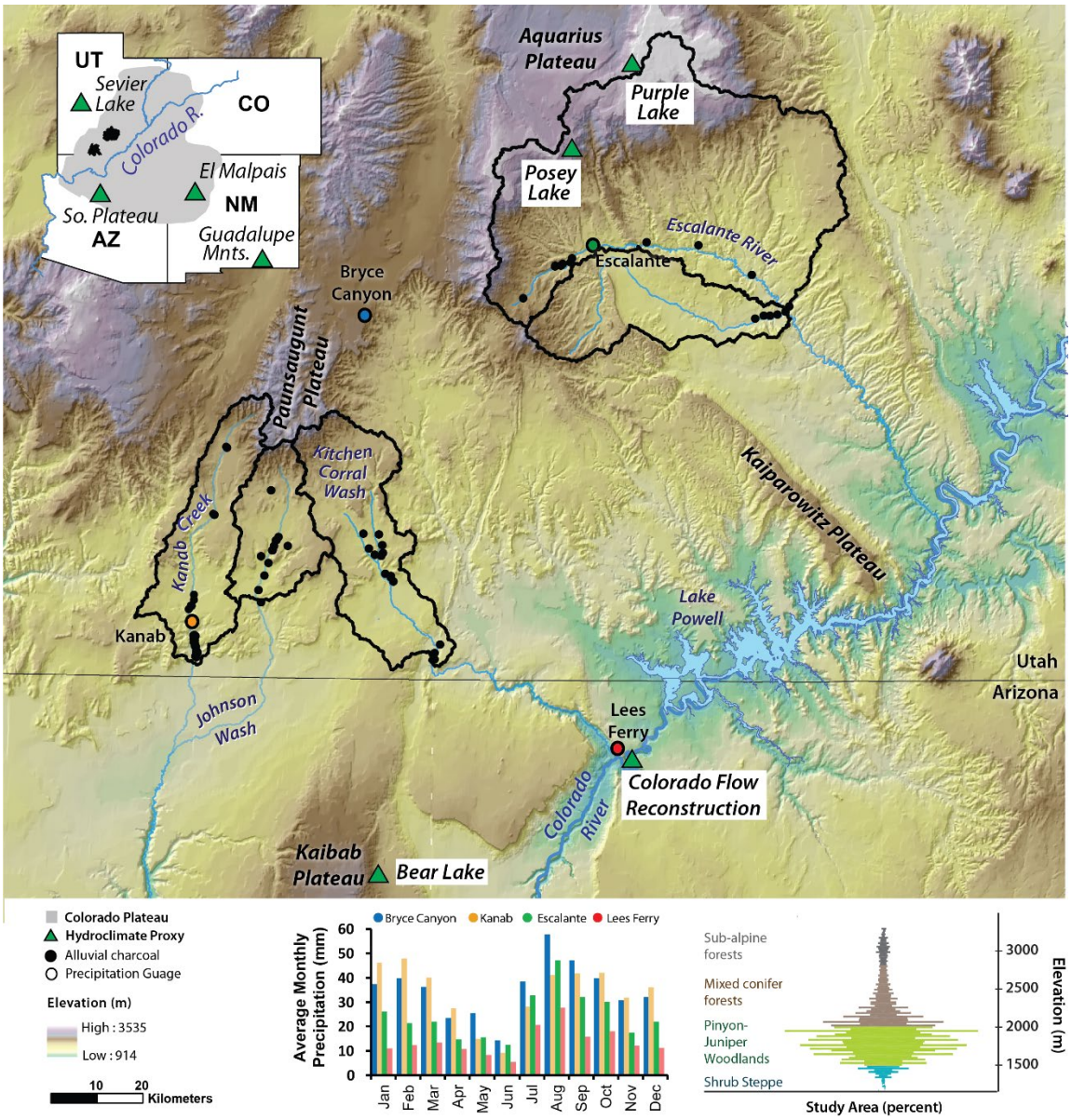

Figure 5-1. Map of regional catchments used in the study with black dots representing locations of dated alluvial charcoal. Precipitation gauge sites are identified with colored circles and weather station average monthly precipitation records are shown in the middle bottom graph (CCD, 2017). Climate proxies discussed in text are annotated and marked with green triangles (see text for citations). The relationship among ecosystem type, elevation, and percent contributing area of the study area is illustrated in the bottom-right violin plot.

Previous fire studies have suggested that pinyon-juniper forests have natural fire regimes dominated by infrequent (fire rotations on the order of >400 years), high-severity, crown fires (Wangler and Minnich, 1996; Romme et al., 2003; Baker and Shinneman, 2004; Floyd et al., 2004; Bauer, 2006; Shinneman and Baker, 2009). Furthermore, the fuel structure in pinyon-juniper forests is not conducive to low-severity surface fires. Specifically, fine fuels are discontinuous and most of the fuel components are in the crowns of shrubs and trees, which tend to burn completely and kill all of the trees and top-kill all of the shrubs and herbs (Baker and Shinneman, 2004; Floyd et al., 2004; Romme et al., 2009). Pinyon and juniper trees have thin bark and low crowns making them intolerant to fire (Romme et al., 2009).

Pre-settlement fire regimes in sagebrush steppe communities were characterized by generally frequent surface fires (Miller and Rose, 1999). In SW ponderosa pine and mixed-conifer forests, low-severity fire that reoccurred every 5-20 years helped shape forest structure conducive to frequent burning, and fires were associated with ENSO activity (Brown et al., 2008). Small, stand-replacing fires were rare in these lower elevation forest types, and were more likely to occur at the higher elevation subalpine sites at frequencies of many centuries (Morris et al., 2013b).

While there is general agreement that humans have influenced fire regimes following Euro-American settlement, Native Americans likely did not did not alter vegetation and fire on a regional scale (Parker, 2002). Natural (lightening) ignitions are frequent in the Southwest (Hostetler et al., 2006) and are not a limiting factor. Past human ignitions were likely not a big influence on fire regimes.

Methods

Radiocarbon-dated alluvial charcoal (n=193) was assembled from previous regional arroyo and paleo-flood studies (Table 5-2; Table 5-S3; Table 5-S4; Table 5-S5; Table 5-S6) and used to construct a history of fire activity in the Grand Staircase region of the Colorado Plateau. Alluvial charcoal ages were derived from 77 different sites in Kanab Creek, Johnson Wash, Paria River, and Escalante River watersheds, with some sites containing multiple charcoal samples (Figure 5-1). All radiocarbon ages used in this study were derived from alluvial charcoal from burned wood from non-cultural settings. We assume alluvial charcoal originated from large-scale burning of woody (forested) types.

Original radiocarbon ages were calibrated to calendar year BP at the one-sigma level using CALIB 7.0.4 (Reimer et al., 2004) and the IntCal13 calibration curve (Reimer et al., 2013). Ages were reported in calibrated years before present (cal yr BP), where present represents 1950 CE. Probability distributions for each calibrated ^{14}C-age were summed (Meyer et al., 1995) and classified to reconstruct the timing of wildfire in each watershed and then combined to create proxy for fire activity in the Grand Staircase region of the Colorado Plateau. Fire probability curves were detrended and corrected for taphonomic bias (Figure 5-S1) associated with the loss of preservation in the geologic record through time and lack of exposure of older sediments using the method of Surovell et al. (2009). The record was truncated at 300 cal yr BP due to the large analytical error associated with young ^{14}C-ages and the biased sampling strategy toward older ages. Thus, 13 samples were not included from the original dataset because the ^{14}C-age was less than

300 years old. Finally, the summed probability curves were smoothed with a 20-year running mean and standardized by dividing each probability by the maximum probability. While the record extended back ~7500 years, only two of the four watersheds contained alluvial charcoal records that extend into the mid-Holocene, therefore we interpreted the fire record during the mid-Holocene with caution and acknowledged that the effects of the fading record potentially caused a decreased probability of exposure, preservation, and number of samples with time.

The resolution of radiocarbon ages precluded identification of individual fire years, but did reveal changes in fire activity. Significant regional fire-events were identified as times when three out of the four watersheds contained charcoal with statistically similar ages and are thus limited to the last 5000 years when we have a fire record for all four watersheds. While we defined regional fires as 'events', they are interpreted as regional fire activity. Synchronous regional fire activity was determined by identifying statistically similar charcoal ages from multiple watersheds using the T-Test tool in CALIB 7.0.4. OxCal 4.3.2 was used to perform a Bayesian analysis (Ramsey, 2009) on statistically similar radiocarbon ages from at least three watersheds. The calibrated radiocarbon age ranges for each statistically similar age comprising each regional fire event was combined and then modelled to produce one probability density function that represented the timing of the regional fire event. This method was used to provide the best age estimate for the timing of regionally synchronous fire events within dating resolution.

Calibrated radiocarbon ages can have asymmetric, multi-modal distributions; thus annually resolved ages are problematic and discouraged (Telford et al., 2004;

Michczyński, 2007). While it is well known that there is no good point estimate for a calibrated radiocarbon age, previous research has shown that the mode of the probability distribution is a more accurate estimate of the true age of the sample (Michczyński, 2007). Many of the combined calibrated radiocarbon ages that we identified as regional fire events were multi-modal (14 out of 21). Other options include using the weighted mean or median of the calibrated age ranges; however, these could over-estimate the true age of the fire event. The minimum mode for the modelled regional fire age distributions could under-estimate of the age of the regional fire event. However, it is likely the best estimate, due to the requirement that the age of the charcoal must precedes the timing of the fire. Due to uncertainties in interpretation of the calibrated age ranges, regional fire events were calculated and analyzed in three ways: median, weighted mean, and the value of the minimum (youngest) local mode of the combined density distributions with 1-sigma errors.

Annually resolved hyrdroclimate records derived from tree-rings are difficult to pair with charcoal-derived fire histories because of the difference in temporal resolution. We addressed this problem using methods modified from Dunnette et al., (2014). In order to compare the non-annual record of wildfire reconstructed in this study to climate reconstructions we truncated all hydroclimate records to the commonly used radiocarbon datum of 1950 CE and we smoothed the annual resolution data with a 30-year moving average and decreased the resolution (increased the time-interval) of the climate time-series to 30-year bins. We identified long-term non-stationarity trends with a low frequency (100-yr) locally weighted regression robust to outliers. We subtracted the low-frequency trend from the binned time-series to obtain a 30-year binned residual time-

series. Hydroclimate reconstructions included a Colorado River flow reconstruction from Lees Ferry (Woodhouse et al., 2010), two independent precipitation reconstructions from the southern Colorado Plateau in northern New Mexico and El Malpais National Monument in Arizona (Grissino-Mayer, 1996; Salzer and Kipfmueller, 2005). The three calibrated age estimates (median, weighted mean, and minimum local mode) of regional fire events were compared to tree-ring-derived hydro-climate records. We also compared our charcoal record with the North American Drought Atlas (e.g., June-July-August Palmer Drought Severity Index reconstruction) using the average of the two closest gridpoints (gridpoints 87 and 88; Cook, 2004; Figure S7).

Table 5-2. Previously published charcoal-derived radiocarbon ages used in this study.

River	n	References
Kanab Creek	48	(Smith, 1990; Nelson and Rittenour, 2014; Townsend, 2015)
Johnson Wash	48	(Chapter II this dissertation)
Paria River		
Kitchen Corral Wash	34	(Hereford, 2002; Harvey, 2009; Huff and Rittenour, 2014)
Buckskin Wash	4	(Ely, 1992; Harvey, 2009)
Coyote Gulch	1	(Harvey, 2009)
Escalante		
Upper	40	(Webb and Hasbargen, 1997; Hayden-Lesmeister and Rittenour, 2014)
Middle	10	(Webb, 1985)
Harris Wash	8	(Patton and Boison, 1986)
Coyote Wash	2	(Boison and Patton, 1985)

Results

The final regional dataset contained 175 radiocarbon-dated fires. Fire records from Kanab Creek and Escalante River extended to 7500 cal ya BP and fire records from Johnson Wash and the Paria River extended back 5000 years (Figure 5-2). Twenty-two regional fire events were identified in the fire record (Table 5-3); twenty of which burned during the last 3000 cal yr BP. The time of greatest regional fire activity recording the greatest number fire ages and the highest peak in fire activity was between 550-650 cal ya BP. This fire peak consisted of 11 statistically similar fire ages that occurred in all four watersheds. The next two largest regional fires occurred at 835-925 and 1000-1060 cal ya BP and together these events consisted of 15 statistically similar fire ages from all four watersheds. Six regional fire events occurred at 325-480, 1060-1180, 1200-1260, 1350-1400, 1620-1720, and 2150-2300 cal ya BP and contained seven statically similar aged fires within each age range. Thirteen additional regional fire events were identified that consisted of three to six statistically similar aged fires from at least three watersheds (Table 5-3).

The two longest records (Kanab Creek and Paria River) contained 12 discretely dated fires between 7500-5000 cal ya BP (under the assumption that each ^{14}C-dated piece of charcoal represents a fire event). The reconstructed (apparent) fire activity was low, with an average of only two fires per 200-year interval. Fire frequency was elevated between 5800-5600 cal yr BP relative the preceding and following time periods, and recorded three fires per 200-year interval (Figure 5-2). After 5000 cal yr BP, all four watersheds (n=171) recorded fires. The reconstructed fire activity between 5000-2700 cal

yr BP varied between one and seven fires per 200-year interval. Four intervals of increased fire activity (defined here as ≥ 4 fires per 200-year interval) are recorded between 5000-4800, 4200-4000, 3800-3500, and 3200-3000 cal yr BP. The reconstructed fire activity increased ~2700 cal yr BP, and varied between 5 and 15 dated fires per 200-year interval. Intervals of elevated fire activity (defined as ≥ 10 fires per 200-year interval) were recorded between 2350-2550, 2200- 1800, 1450-950, and 650-450 cal yr BP. We focus here on 'fire activity' based on concurrent dates and the absolute number of fires recorded indicates not just large regional fires, but likely several independent fires in each drainage at various times.

No strong systematic relationship between the timing of regional fire events and 30-year binned time-series of regional climatic variability was found, however, three out of the nine youngest modelled regional fires occurred during low Colorado River flows, four fires occurred during average flow and two fires occurred during above average flows (5-4A). Six out of the ten youngest modelled regional fires over the last 1350 years occurred during drier than average precipitation on the southern Colorado Plateau (Figure 5-4B). Eleven out of the 16 youngest regional fires were related to below average precipitation at El Malpais National Monument over the last 2000-years (Figure 5-4C). Ten out of the 15 youngest regional fires occurred during drier than average drought conditions over the last 2000 years (Figure 5-4D).

Table 5-3. Measures of central tendency for combined modelled age distributions inferred to represent regional fire activity. The last five columns show the number of samples derived from each watershed contributing to the combined age model. The regional events with the greatest number of dated charcoal are highlighted in grey. Individual and combined modelled age distributions are in Figures 5-S2 through 5-S4.

Regional Fire	Minimum Mode cal yr BP_{1950}	Median cal yr BP_{1950}	Weighted Mean cal yr BP_{1950}	KNB	JW	PAR	ESC	TOTAL
1	**335 ± 10**	**390**	**400 ± 50**	**0**	**2**	**1**	**4**	**7**
2	480 ± 15	475	455 ± 50	1	1	1	1	4
3	505 ± 5	505	505 ± 5	1	1	1	3	6
4	**550 ± 5**	**610**	**595 ± 35**	**2**	**2**	**2**	**6**	**11**
5	660 ± 5	660	650 ± 25	2	0	1	1	4
6	735 ± 10	735	735 ± 15	3	1	1	1	6
7	**835 ± 5**	**865**	**880 ± 40**	**3**	**1**	**3**	**1**	**7**
8	**1005 ± 15**	**1010**	**1015 ± 20**	**1**	**2**	**3**	**2**	**8**
9	**1095 ± 10**	**1125**	**1125 ± 30**	**1**	**2**	**2**	**2**	**7**
10	**1215 ± 10**	**1215**	**1215 ± 20**	**1**	**2**	**3**	**1**	**7**
11	**1375 ± 15**	**1370**	**1370 ± 10**	**0**	**3**	**3**	**1**	**7**
12	1410 ± 5	1475	1475 ± 35	1	1	0	1	3
13	**1640 ± 10**	**1660**	**1670 ± 30**	**1**	**2**	**3**	**1**	**7**
14	1835 ± 5	1850	1850 ± 15	2	1	0	3	6
15	1910 ± 10	1940	1940 ± 25	0	1	1	1	3
16	1955 ± 5	1975	1970 ± 15	0	2	1	1	4
17	**2170 ± 15**	**2240**	**2225 ± 50**	**0**	**3**	**2**	**2**	**7**
18	2375 ± 15	2405	2410 ± 40	1	2	1	0	4
19	2500 ± 40	2585	2585 ± 65	2	3	1	0	6
20	2725 ± 15	2725	2710 ± 45	2	1	1	1	5
21	3645 ± 5	3665	3665 ± 20	2	0	1	1	4
22	4875 ± 85	5010	4925 ± 50	3	1	1	0	5

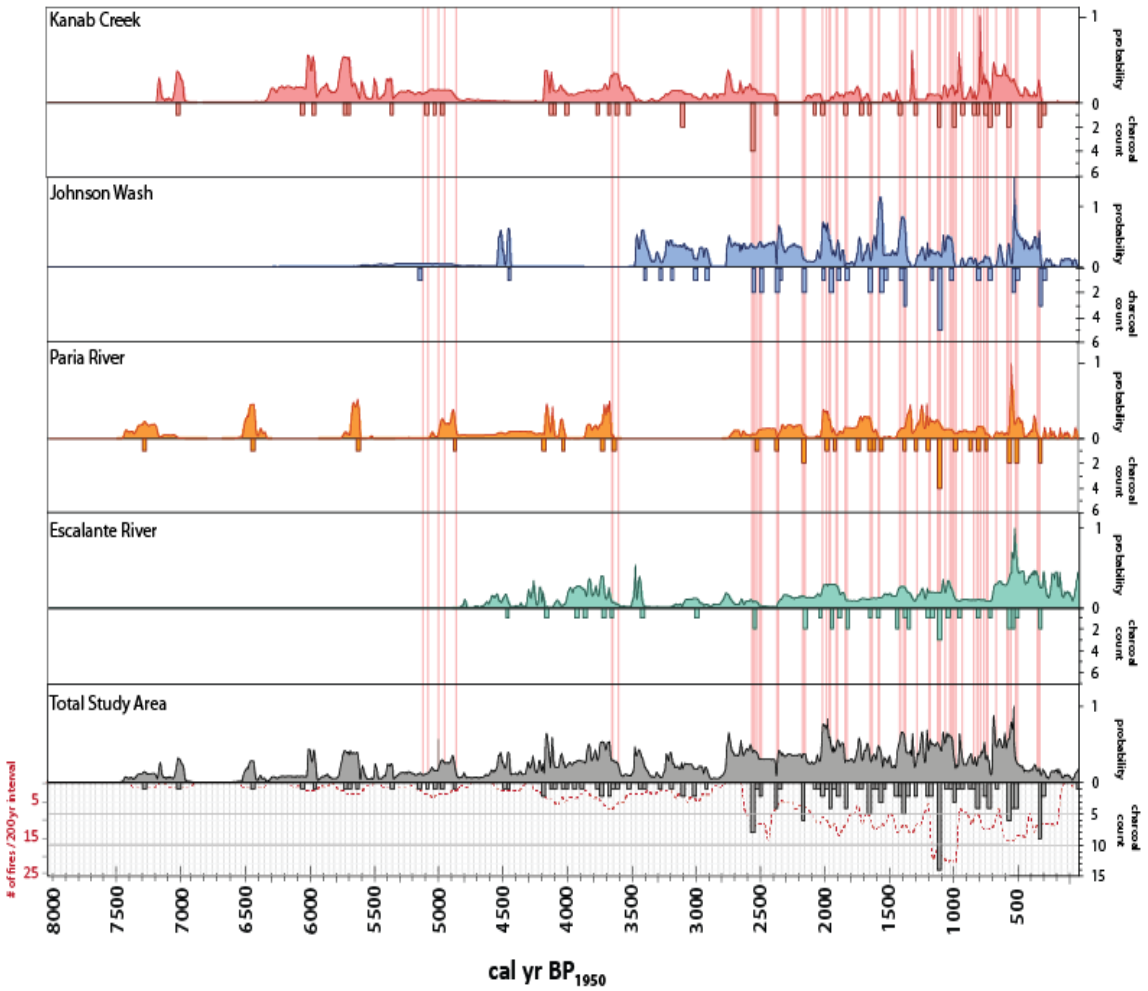

Figure 5-2. Fire reconstructions derived from radiocarbon-dated alluvial charcoal from Kanab Creek (red), Johnson Wash (blue), Kitchen Corral Wash and Paria River (green), and the Escalante River (orange). The sum of all radiocarbon age distributions is in black. All data was smoothed using a 20-year moving average, standardized, and detrended. The minimum mode of the calibrated probability density distributions were rounded to the nearest decade and plotted as inverted histograms (Telford et al., 2004), which represent the number of samples used in the summed curves. Statistically similar age distributions of fires burning in three or more watersheds representing regional fires and are identified with red vertical lines. The red inverted dashed line represents the apparent fire frequency (activity), which is the number of fires per 200-year interval.

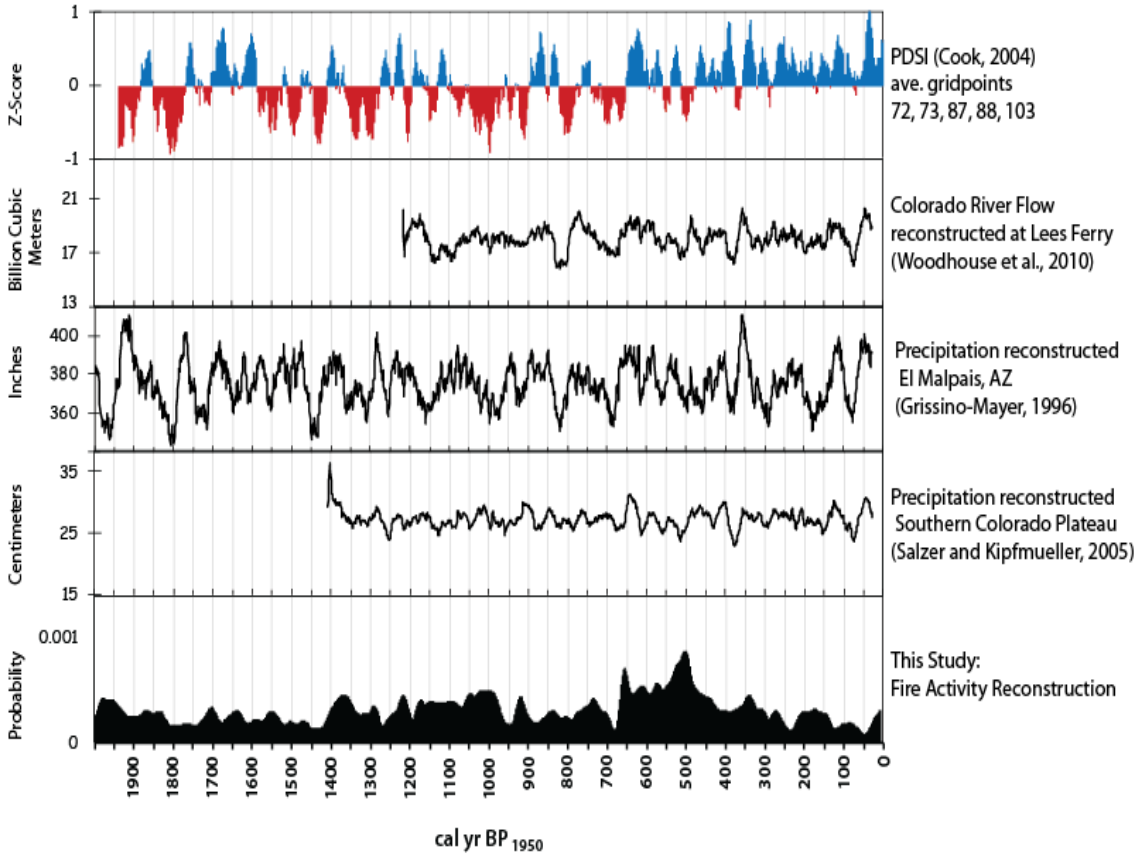

Figure 5-3 – Summary of time series of tree-ring derived climate proxy data from top to bottom: z-score of the 30-year moving average reconstructed summer PDSI for the average of gridpoints 72, 73, 87, 88, and 103 (Cook, 2004), Colorado Flow Reconstruction smoothed with 30-year moving average (Woodhouse et al., 2010), and precipitation reconstruction from southern Colorado Plateau with 30-year moving average, New Mexico (Salzer and Kipfmueller, 2005). The black curve represents the detrended summed probability distributions for all charcoal samples between 2,000 and 0 cal yr BP. Note the date of 0 cal yr BP represents the 1950 datum in all records.

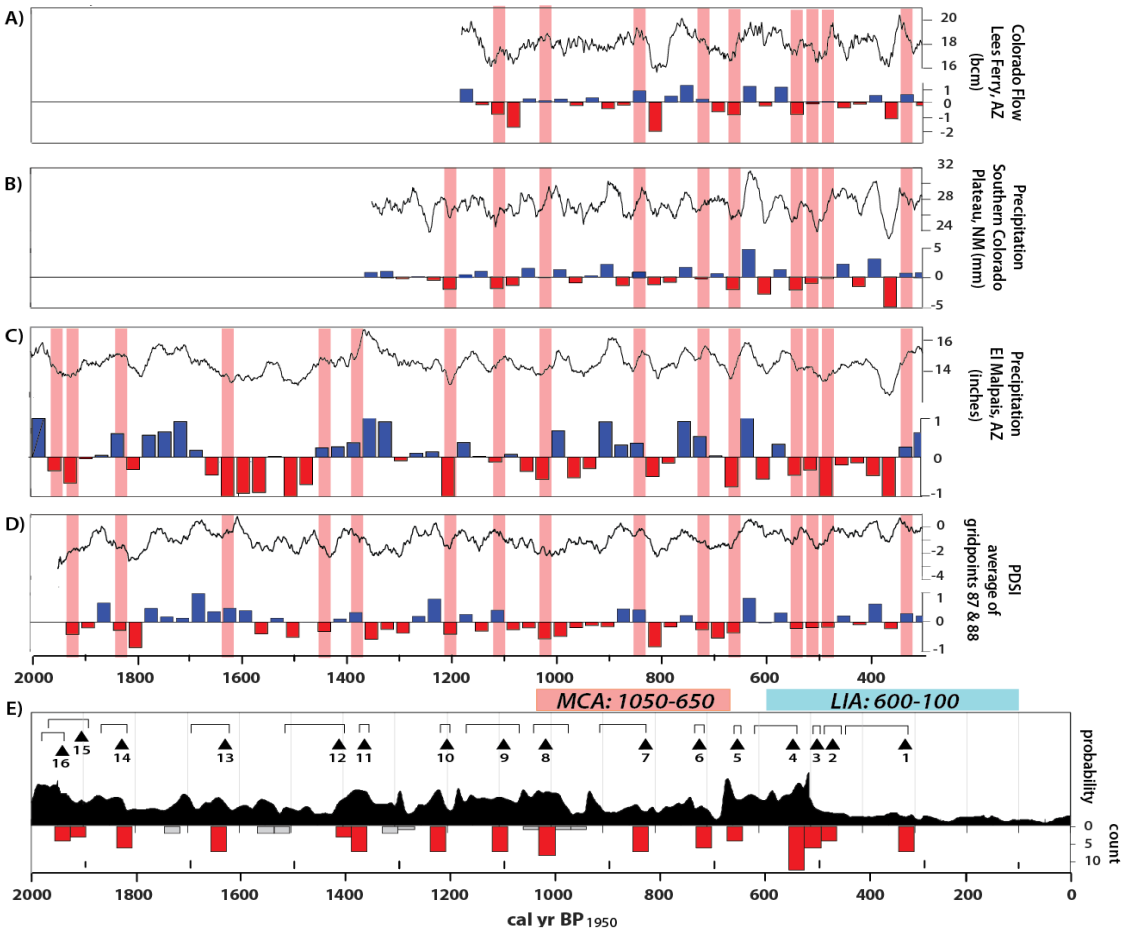

Figure 5-4– Time series of tree-ring derived climate proxy data from top to bottom: A) Colorado Flow Reconstruction (Woodhouse et al., 2010), B) precipitation reconstruction from southern Colorado Plateau, New Mexico (Salzer and Kipfmueller, 2005), C) precipitation reconstruction from El Malpais National Monument, Arizona (Grissino-Mayer, 1996) and D) the reconstructed summer PDSI for the average of gridpoints 87 and 88 (Cook, 2004). Each record shows a smoothed (30-year trend; bold black line) time-series at the top and the residual time-series as a histogram at the bottom. The residual time series is in 30-year bins and annotated to show red as drier and blue as wetter than average conditions. The thick red vertical bars are the regional fire events. E) The black curve represents the detrended summed probability distributions for all charcoal samples between 2,000 and 300 cal yr BP. The inverted histogram (30-year bins) at the bottom is the number of ^{14}C samples creating the above distribution. Black triangles and red bars identify the minimum mode for regional fires defined by statistically similar radiocarbon-dated fires from three or more watersheds. The black error bars represent the 1-sigma confidence intervals for the regional fire event.

Discussion

A 7500-year alluvial charcoal-derived fire record was used to reconstruct the timing, frequency, and climatic control of wildfires across four watersheds in the Grand Staircase region of the Colorado Plateau. During the Holocene, ENSO caused shifts in the North American Monsoon and Pacific storm systems influenced hydroclimate and the structure and function of ecosystems by modifying vegetation productivity (Van Devender and Spaulding, 1979; Neilson, 1986; Spaulding and Graumlich, 1986; Stine, 1994; Williams and Ehleringer, 2000). The earliest synchronous fire activity in the study area recorded in alluvial charcoal was ~5000 cal yr BP and appears contemporaneous with large-scale climate shifts from mid- to late- Holocene climate conditions (Fig. 5-4). Ninety-one percent of identified regional (i.e., widespread) fire activity occurred during the last 3000 years (Table 5-3). Greatest regional fire activity (greatest number fire ages and the highest peak in fire activity) was interpreted from 11 statistically similar fire ages that burned in all four watersheds and was estimated to have occurred between 550-650 cal ya BP during the LIA.

The next two periods of greatest regional fire activity (15 statistically similar fire ages from four watersheds) occurred at 835-925 cal ya BP and 1000-1060 cal ya BP during the MCA. There is an apparent link between fires and wet/dry climate conditions. High variability in hydroclimate is a potential cause of increased fire activity leading to the accumulation and drying out of biomass. Between 1250 and 1050 cal yr BP, high variability between pluvial and drought conditions recorded on the Tavaputs Plateau (Knight et al., 2010) resulted in one of the highest peaks in fire activity in this record.

Furthermore, fires that burned during last 2000 years appear to have primarily burned during dry conditions (Fig. 5-4). This trend is most apparent when comparing regional fire ages with the PDSI climate record (5-S8).

Mid-Holocene (8000–4000 cal yr BP)

Alluvial charcoal in Kanab Creek and Paria River contained 12 dated fires between 7500-5000 cal ya BP, apparent fire activity was relatively low, and fire activity was slightly elevated between 5800-5600 cal yr BP (Figure 5-2). Two additional intervals of increased fire activity were recorded between 5000-4800 and 4200-4000 cal ya BP. A regional fire record from a lake on the Markagunt Plateau in southwestern Utah showed the lowest amount of biomass burning of the record between 6200-4200 cal yr BP and authors concluded that the landscape moving from mesic toward xeric growing conditions resulting in a fuel-limited fire regime (Morris et al., 2013a). Climate proxy records are in general agreement that in the mid-Holocene (~8000–4000 cal yr BP), the Southwest experienced hot and dry conditions (e.g., Davis and Shafer, 1992; Dean et al., 1996; Madsen et al., 2001; Waters and Haynes, 2001; Menking and Anderson, 2003). Pinyon-juniper woodlands rapidly increased in range and abundance, migrating north, east, and up 500 meters in elevation compared to modern distributions (Betancourt, 1987; Mehringer and Wigand, 1990; Jennings and Elliott-Fisk, 1993; Miller and Wigand, 1994; Wigand et al., 1995). High-elevation forested area decreased on the Aquarius Plateau immediately to the north at this time (Morris et al., 2013a). Thus, Pinyon-juniper woodlands likely expanded in the study area during the mid-Holocene, while higher

elevation subalpine and mixed conifer forests contracted (Morris et al., 2013a).

Studies suggest that the strength of El Niño events were reduced during the middle Holocene and La Niña events (dry winters) were enhanced (e.g., Ely, 1992; Rodbell et al., 1999; Riedinger et al., 2002; Menking and Anderson, 2003). Warmer and drier climate conditions in the mid-Holocene would have increased the extent, but not necessarily the abundance of biomass in pinyon-juniper ecosystems. The structure of pinyon-juniper woodlands was thought to have been open woodlands, probably similar to wooded shrubland or pinyon-juniper savannas. Ponderosa pine and gamble oak also expanded their distributions and two-needle pinyon expanded to its northern most limit (Betancourt, 1987). Fire regimes in these types of ecosystems would have been fuel-limited because of scattered trees among sparse understories of low shrubs and grasses (Romme et al., 2009). The fires that burned during the mid-Holocene might have been frequent, low-severity and/or moderately frequent, high severity, shrub and crown fires. Pinyon-juniper wooded shrubland would have been favored in conditions with greater winter precipitation, while a pinyon-juniper savanna would have been favored with greater summer precipitation, but both ecosystems would have had less overall available seasonal moisture available for trees (Romme et al., 2009).

Neoglacial (4000–2000 cal yr BP)

Most of the fires reconstructed in this study (93%) burned during the last 5000 years, which includes the neoglacial climate interval. Fire activity was recorded in all four watersheds and ENSO activity strengthened in the tropical Pacific (e.g., Rodbell et

al., 1999; Conroy et al., 2008)**.** The neoglacial period was characterized by a climatic shift to cooler and wetter conditions with increased winter precipitation in the Great Basin (Wigand, 1987; Wigand et al., 1995). Five regional fire peaks were recorded during this time at ~3645, 2725, 2500, 2375, and 2170 cal yr BP and were likely associated with increased density of biomass associated with increased available moisture. Regional primary productivity in perennials is largely determined by winter precipitation (Caldwell, 1985), whereas late-summer precipitation supplies moisture for shallow-rooted plant species such as grasses and late-summer annuals (Ehleringer et al., 1991; Lin et al., 1996; Schwinning et al., 2003). Fire activity on the high elevation Markagunt Plateau was interpreted to be a frequent, low severity fire regime, where fire severity was probably limited by increased moisture (Morris et al., 2013a)

Eolian landform stability in the southern Colorado Plateau suggest wetter climatic conditions around 4000-3700 cal yr BP, indicating increased vegetative cover and ground-moisture (Wells et al., 1990). Speleothem records from southwest New Mexico and pollen and macrofossils from Bear Lake on the Kaibab Plateau in northern Arizona suggests a wetter and/or cooler climate starting ~4000 yr BP (Weng and Jackson, 1999; Polyak and Asmerom, 2001; Asmerom et al., 2007). Pinyon also reached their current range in Utah during the neoglacial (Nowak et al., 1994; Wigand et al., 1995; Miller and Tausch, 2001).

Low fire activity between 3600-2700 suggests conditions were potentially too wet to burn in dense pinyon-juniper forests and there were no significant droughts (Figure 5-4). Alternatively, decreased fire activity between 3500 and 2700 cal yr BP could be related to a lack of accommodation space and therefore lack of preservation in the

alluvial valleys to store sediment (and charcoal) at this time. Arroyo chronologies from Kanab Creek constrain arroyo entrenchment between 3600-3200 cal yr BP (Nelson and Rittenour, 2014; Townsend, 2015) and chronologies from Kitchen Corral Wash, a tributary to the Paria River constrain entrenchment between 3400–3200 cal yr BP (Huff and Rittenour, 2014). These records provide evidence for a change in stream dynamics and a hiatus in alluvial charcoal deposition during this time.

Sevier Lake in the Great Basin recorded a high-stand between 3000-2000 cal yr BP (Oviatt, 1988) and lake levels increased to near modern levels around 3000 yr BP on the Kaibab Plateau to the south (Enzel et al., 1992; Anderson, 1993; Weng and Jackson, 1999). El Nino conditions strengthened ~3000 yr BP (Riedinger et al., 2002) and ~2800 cal yr BP corresponds to the greatest increase in relative frequency of regional fire activity of the record.

Late Holocene (2000–300 cal yr BP)

Paleo-climate records suggest climate became warmer and drier in the Great Basin following the neoglacial (Wigand et al., 1995) and peaks in fire activity in southern Utah generally correspond to intervals of drought during this time. Fires that burned at the end of the neoglacial potentially helped to transition forest ecosystems to shrub and grasslands. Pinyon maintained their neoglacial extent until 1900 cal yr BP, after which desert scrub increased until ~1000 cal yr BP (Wigand, 1987). Maximum Holocene ENSO variability was recorded between 2000-1500 cal yr BP (Conroy et al., 2008). Regional synchronous fires burned around 1955, 1910, 1835, 1640, 1410, 1375, 1215, 1095, and

1005 cal yr BP and generally correspond to drought in the Great Basin between 1900-1500 cal yr BP (Wigand et al., 1995) and below average rainfall between 1692-1430, and 1289-927 recorded in tree-rings from El Malpais in northwest New Mexico (Grissino-Mayer, 1996). Pinyon decreased in extent between 1900-1500 cal yr BP, mortality was probably partially caused by high-severity, stand-replacing fires that transitioned to grasslands, shrublands, and less dense, open woodlands; pinyon re-expanded north and down in elevation at ~1500 cal yr BP (Wigand et al., 1995).

Climate proxies characterize the Medieval Climatic Anomaly (MCA; 1050 – 650 cal yr BP; Stine, 1998; Cook et al., 2007) as a time with widespread, severe aridity and large decadal to centennial changes in precipitation in the Southwest (Cook et al., 2004; Rasmussen et al., 2006; Jimenez-Moreno et al., 2008). The MCA contains four regional fire peaks at ~1005, 835, 735 and 660 cal yr BP, all of which correspond to periods of drought in the region (Figure 3). The regional fire event at 660 cal yr BP corresponds to the "Great Drought" of 674-653 cal yr BP in the four corners area, which was preceded by two decades of pluvial conditions (Salzer and Kipfmueller, 2005; Cook et al., 2007; Woodhouse et al., 2010). The Great Basin recorded drought and fire between 900-500 cal yr BP (Holmes et al., 1986) and reduced pinyon-juniper pollen in southern Great Basin (Wigand and Rose, 1990). Drought conditions persisted until 927 yr BP (Grissino-Mayer, 1996) and a wet interval was recorded in tree-rings between 900-700 yr BP (Adams, 2003). Lakes in the Sierra Mountains record drought 1038-838 and 740-600 cal yr BP and highstand 838-740 cal yr BP (Stine, 1994). Synchronous regional fire peaks at this time likely represent high severity, stand-replacing fires during annual or seasonal drought that followed years to centuries of relatively wet conditions and fuel

accumulation.

The Little Ice Age (~600-100 cal yr BP) is the time-period with highly variable climate in southwest tree-ring records with periods of wet and dry conditions. Annually resolved fire records over the last 500 years from southwest forests and Utah suggest that regionally synchronous fires were coincident with droughts (Swetnam and Betancourt, 1998; Floyd et al., 2004; Schoennagel et al., 2004; Brown et al., 2008; Williams et al., 2013; Williams et al., 2015). The alluvial charcoal fire record from the Grand Staircase region of the Colorado Plateau is consistent with widespread fire activity between 500-350 cal yr BP throughout fuel-limited sites in the west. This result contrasts to findings from subalpine forests on the nearby Aquarius Plateau, where low fire activity during the late Holocene was attributed to high fuel moisture conditions that restricted ignition and fire spread (Morris et al., 2013b). Four regional fires burned at ~550, 505, 480, and 335 cal yr BP. These fires were preceded by a multi-decadal wet interval between 600-550 cal yr BP, which likely helped fuel build up (Cook, 2004; Meko et al., 2007; Williams et al., 2013). Tree-ring records from the southwest record drought ~500-460 cal yr BP and a mega-drought ~375 cal yr BP (Salzer and Kipfmueller, 2005; Cook et al., 2007; Stahle et al., 2007; Woodhouse et al., 2010; Williams et al., 2013) corresponding to regional fire peaks in this fire record and extensive mortality of pinyon-juniper woodlands in the southwest.

While fire severity was likely decreased in higher elevation forested ecosystems in the region because of moist conditions that maintained high fuel moisture (Morris et al., 2013b; Fitch and Meyer, 2016), pinyon-juniper woodlands likely became denser during wet periods in the Little Ice Age. Given their lower-elevation occurrence in the

ecosystem, pinyon-juniper woodlands would be more likely to burn in high-severity stand-replacing fires during droughts that decreased fuel moisture. Fire scars found in tree rings have been used to demonstrate that wet winters and springs followed by dry years increase fine fuels needed to carry low-severity fire in the Southwest (Swetnam and Betancourt, 1990; Swetnam and Betancourt, 1998). However, fuel accumulation over decadal- to centennial-timescales followed by drought likely lead to high-severity fire events on the Grand Staircase. This supposition has been observed in modern records and tree-ring records from pinyon-juniper woodlands on Mesa Verde, where canopy fuels built during protracted wet periods and subsequently burned in high-severity fires during drought (Floyd et al., 2004). We then infer that the largest widespread fire events in this study were likely associated with drought conditions. Wetter than average years promote tree densification, major shrub components, and ultimately fuel accumulation and drought is the primary driver of regionally synchronous fire activity.

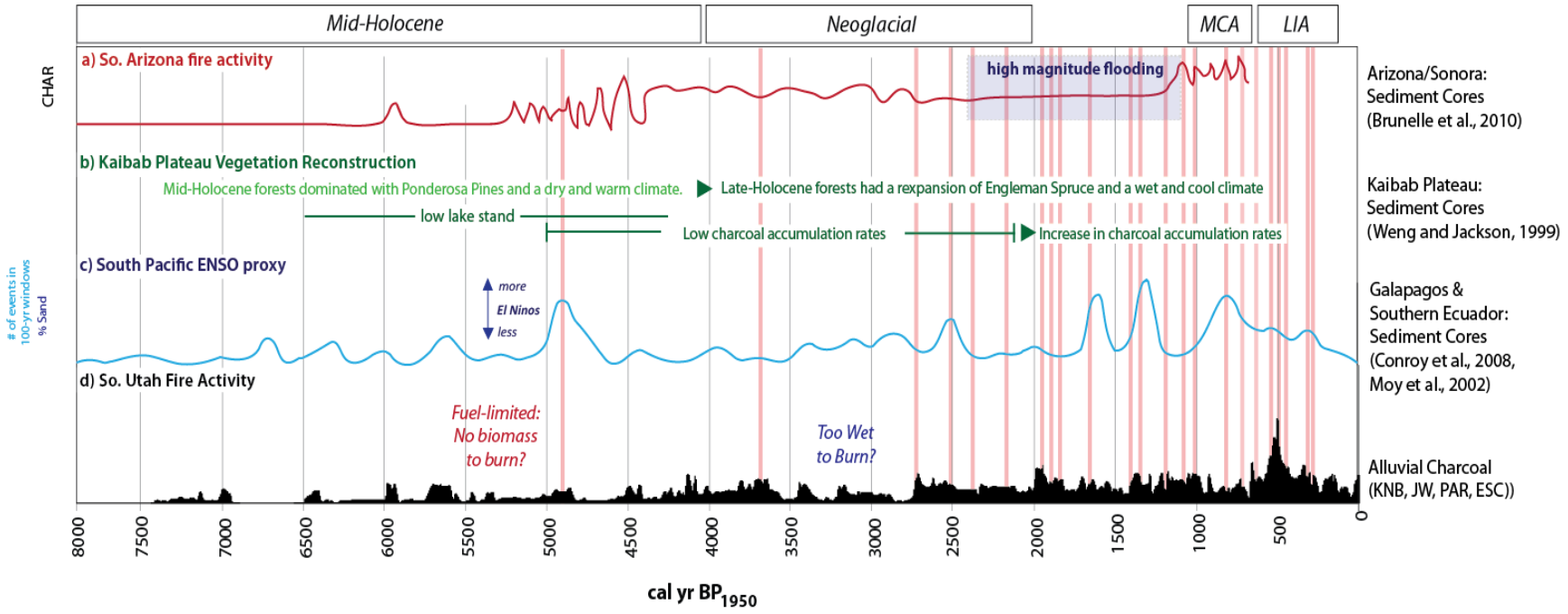

Figure 5-5 – Time series of the last 8000 years comparing climate-proxy data with the alluvial charcoal fire record.

Conclusion

Alluvial charcoal is a useful paleoecological proxy of fire activity that is comparable with long-term lake records and annually resolved tree-ring records and enables long-term changes in fire regimes to be interpreted across regional scales to place modern changes in fire activity in context. Decadal to millennial scale fire activity was reconstructed from 7,500 to 300 cal yr BP in the Grand Staircase region of the Colorado Plateau in southern Utah. We identified 22 regionally synchronous fires between 5000 and 300 cal yr BP. The frequency of regionally synchronous fires increased dramatically 2800 cal yr BP. We interpret this record to suggest that over centennial to millennial timescales, regional fire activity was controlled by hydroclimate-driven changes in the abundance of woody fuel in this semi-arid ecosystems. Over shorter timescales, regional fires were likely related to the timing of drought. We suggest that climate-driven changes in vegetation productivity and the frequency and intensity of drought controlled fire activity during the mid- to late-Holocene on the Grand Staircase.

These findings have significant management implications for pinyon-juniper woodlands. We found large widespread fires often followed decades or centuries of wet climatic conditions that would have naturally promoted the building of fuel, consistent with recent suggestions that modern expansion and densification in pinyon-juniper woodland ecosystems is partly a natural response to climate change that is likely within the natural range of fire regime variability (Floyd et al. 2014). Furthermore, when woodland trees build-up fuels during these wet decades or centuries they exhibit the characteristics of a climate-limited system, and burn at high-severity following annual

drought. Consequently, this climate-vegetation-fire dynamic would have driven the expansion and contraction of pinyon-juniper woodlands throughout the Holocene.

The radiocarbon record presented here is conditioned by Holocene alluviation dynamics. Arroyo cut-fill dynamics are expected to have effects on the preservation of alluvial charcoal deposits and the interpretation of the regional fire history. Episodes of arroyo entrenchment have been recorded multiple times over the last 6000 years in the study area catchments (Harvey et al., 2011; Huff and Rittenour, 2014; Nelson and Rittenour, 2014; Townsend, 2015). There is little preservation potential for charcoal produced and deposited during arroyo entrenchment episodes. Fortunately, entrenchment occurs relatively quickly over decadal to centennial timescales. For this reason, the fire reconstruction produced here should be interpreted as a conservative record that is biased toward more recent fires and those that burned during periods of aggradation due to loss of records over time, and in particular during entrenchment.

Acknowledgements

All Johnson Wash radiocarbon samples were processed at the Keck Accelerator Mass Spectrometer Lab at the University of California, Irvine with assistance from John Southon. We used radiocarbon dates from previous theses by Kirk Townsend (2015), Will Huff (2013), Ann Hayden (2011), Michelle Summa-Nelson (2009), Jon Harvey (2009), Smith (1990), and dissertations by Lisa Ely (1992) and Robert Webb (1985), and peer-reviewed publications by Hereford (2002), Webb and Hasbargen (1997), Patton and Boison 1986), and Boison and Patton (1985). Scripts for the statistical analysis were

modified from original code published by Dunnette et al., (2014). The bulk of this material was derived from work supported by NSF Career Grant EAR-1057192 awarded to Tammy Rittenour. This paper was prepared in part by an employee of the US Forest Service as part of official duties and is therefore in the public domain.

References Cited

Adams, K.D., 2003. Age and paleoclimatic significance of late Holocene lakes in the Carson Sink, NV, USA. Quaternary Research, 60(3), pp.294-306.

Adams, D. K., and Comrie, A. C., 1997, The North American monsoon: Bulletin of the American Meteorological Society, v. 78, no. 10, p. 2197-2213.

Anderson, R. S., 1993, A 35,000 year vegetation and climate history from Potato Lake, Mogollon Rim, Arizona: Quaternary Research, v. 40, no. 3, p. 351-359.

Asmerom, Y., Polyak, V., Burns, S., and Rassmussen, J., 2007, Solar forcing of Holocene climate: New insights from a speleothem record, southwestern United States: Geology, v. 35, no. 1, p. 1-4.

Baker, W.L. and Shinneman, D.J., 2004. Fire and restoration of pinon–juniper woodlands in the western United States: a review. Forest Ecology and Management, 189(1-3), pp.1-21.

Baisan, C.H. and Swetnam, T.W., 1990. Fire history on a desert mountain range: Rincon Mountain Wilderness, Arizona, USA. Canadian Journal of Forest Research, 20(10), pp.1559-1569.

Baisan, C.H. and Swetnam, T.W., 1997. Interactions of fire regimes and land use in the Central Rio Grande Valley. Research Paper RM-RP-330. US Department of Agriculture, Forest Service, Rocky Mountain Forest and Range Experiment Station, Fort Collins, CO.

Bauer, J.M., 2006. Fire history and stand structure of a central Nevada pinyon-juniper woodland. University of Nevada, Reno.

Bechtold, W. A., and Patterson, P. L., 2005, The enhanced forest inventory and analysis program-national sampling design and estimation procedures.

Betancourt, J. L., 1987, Paleoecology of pinyon-juniper woodlands: summary: General technical report INT-US Department of Agriculture, Forest Service, Intermountain Research Station (USA).

Bigio, E., Swetnam, T.W. and Baisan, C.H., 2010. A comparison and integration of tree-ring and alluvial records of fire history at the Missionary Ridge Fire, Durango, Colorado, USA. The Holocene, 20(7), pp.1047-1061.

Boison, P. J., and Patton, P. C., 1985, Sediment storage and terrace formation in Coyote Gulch basin, south-central Utah: Geology, v. 13, no. 1, p. 31-34.

Brown, P. M., Heyerdahl, E. K., Kitchen, S. G., and Weber, M. H., 2008, Climate effects on historical fires (1630-1900) in Utah: International Journal of Wildland Fire, v. 17, no. 1, p. 28-39.

Brown, P. M., Kaye, M. W., Huckaby, L. S., and Baisan, C. H., 2001, Fire history along environmental gradients in the Sacramento Mountains, New Mexico: Influences of local patterns and regional processes: Ecoscience, v. 8, no. 1, p. 115-126.

Capotondi, A., Wittenberg, A. T., Newman, M., Di Lorenzo, E., Yu, J.-Y., Braconnot, P., Cole, J., Dewitte, B., Giese, B., and Guilyardi, E., 2015, Understanding ENSO diversity: Bulletin of the American Meteorological Society, v. 96, no. 6, p. 921-938.

Cayan, D. R., Redmond, K. T., and Riddle, L. G., 1999, ENSO and hydrologic extremes in the western United States: Journal of Climate, v. 12, no. 9, p. 2881-2893.

Conroy, J. L., Overpeck, J. T., Cole, J. E., Shanahan, T. M., and Steinitz-Kannan, M., 2008, Holocene changes in eastern tropical Pacific climate inferred from a Galápagos lake sediment record: Quaternary Science Reviews, v. 27, no. 11–12, p. 1166-1180.

Cook, E., 2004, North American Summer PDSI Reconstructions, NOAA/NGDC Paleoclimatology Program: Boulder CO, World Data Center for Paleoclimatology

Cook, E. R., Seager, R., Cane, M. A., and Stahle, D. W., 2007, North American drought: Reconstructions, causes, and consequences: Earth-Science Reviews, v. 81, no. 1, p. 93-134.

Cook, E. R., Woodhouse, C. A., Eakin, C. M., Meko, D. M., and Stahle, D. W., 2004, Long-term aridity changes in the western United States: Science, v. 306, no. 5698, p. 1015-1018.

Dale, V.H., Joyce, L.A., McNulty, S., Neilson, R.P., Ayres, M.P., Flannigan, M.D., Hanson, P.J., Irland, L.C., Lugo, A.E., Peterson, C.J. and Simberloff, D., 2001. Climate change and forest disturbances: climate change can affect forests by altering the frequency, intensity, duration, and timing of fire, drought, introduced species, insect and pathogen outbreaks, hurricanes, windstorms, ice storms, or landslides. BioScience, 51(9), pp.723-734.

Davis, O. K., and Shafer, D. S., 1992, A Holocene climatic record for the Sonoran Desert from pollen analysis of Montezuma Well, Arizona, USA: Palaeogeography, Palaeoclimatology, Palaeoecology, v. 92, no. 1, p. 107-119.

Dean, W. E., Ahlbrandt, T. S., Anderson, R. Y., and Bradbury, J. P., 1996, Regional aridity in North America during the middle Holocene: The Holocene, v. 6, no. 2, p. 145-155.

Dunnette, P.V., Higuera, P.E., McLauchlan, K.K., Derr, K.M., Briles, C.E. and Keefe, M.H., 2014. Biogeochemical impacts of wildfires over four millennia in a R ocky M ountain subalpine watershed. New Phytologist, 203(3), pp.900-912.

Ely, L. L., 1992, Large floods in the southwestern United States in relation to late-Holocene climatic variations [PhD Diseration] [PhD: The University of Arizona.

Enzel, Y., Brown, W. J., Anderson, R. Y., McFadden, L. D., and Wells, S. G., 1992, Short-duration Holocene lakes in the Mojave River drainage basin, Southern California: Quaternary Research, v. 38, no. 1, p. 60-73.

Fitch, E. P., and Meyer, G. A., 2016, Temporal and spatial climatic controls on Holocene fire-related erosion and sedimentation, Jemez Mountains, New Mexico: Quaternary Research, v. 85, no. 1, p. 75-86.

Floyd, M. L., Hanna, D. D., and Romme, W. H., 2004, Historical and recent fire regimes in Piñon–Juniper woodlands on Mesa Verde, Colorado, USA: Forest Ecology and Management, v. 198, no. 1, p. 269-289.

Grissino-Mayer, H. D., 1996, A 2129-year reconstruction of precipitation for northwestern New Mexico, USA: Tree rings, environment, and humanity, p. 191-204.

Grissino Mayer, H.D. and Swetnam, T.W., 2000. Century scale climate forcing of fire regimes in the American Southwest. The Holocene, 10(2), pp.213-220.

Harvey, J., 2009, Reconciling Holocene alluvial records in Buckskin Wash, southern Utah [MS: University of Utah, 157 p.

Harvey, J. E., Pederson, J. L., and Rittenour, T. M., 2011, Exploring relations between arroyo cycles and canyon paleoflood records in Buckskin Wash, Utah: Reconciling scientific paradigms: Geological Society of America Bulletin, v. 123, no. 11-12, p. 2266-2276.

Hayden-Lesmeister, A., and Rittenour, T. R., 2014, Chronostratigraphy of Holocene valley-fill alluvium and arroyo cut-fill events in the upper Escalante River, southern Utah, *in* MacLean, J. S., Biek, R.F., and Huntoon, J.E., ed., Geology of Utah's Far South Volume 43, Utah Geological Association Publication, p. 57–76.

Hereford, R., 2002, Valley-fill alluviation during the Little Ice Age (ca. AD 1400-1880), Paria River basin and southern Colorado Plateau, United States: Geological Society of America Bulletin, v. 114, no. 12, p. 1550-1563.

Holden, Z.A., Swanson, A., Luce, C.H., Jolly, W.M., Maneta, M., Oyler, J.W., Warren, D.A., Parsons, R. and Affleck, D., 2018. Decreasing fire season precipitation increased recent western US forest wildfire activity. Proceedings of the National Academy of Sciences, 115(36), pp.E8349-E8357.

Holmes, R.L., Adams, R.K. and Fritts, H.C., 1986. Tree-ring chronologies of western North America: California, eastern Oregon and northern Great Basin with procedures used in the chronology development work including users manuals for computer programs COFECHA and ARSTAN.

Hostetler, S.W., Bartlein, P.J. and Holman, J.O., 2006. Atlas of climatic controls of wildfire in the western United States. US Geological Survey.

Huff, W., and Rittenour, T., 2014, Holocene alluvial stratigraphy of Kitchen Corral Wash, southern Utah, *in* MacLean, J. S., Biek, R.F., and Huntoon, J.E., ed., Geology of Utah's Far South: Utah Geological Association Publication 43, p. 77–96.

Jennings, S. A., and Elliott-Fisk, D. L., 1993, Packrat Midden Evidence of Late Quaternary Vegetation Change in the White Mountains, California-Nevada: Quaternary Research, v. 39, no. 2, p. 214-221.

Jimenez-Moreno, G., Fawcett, P. J., and Anderson, R. S., 2008, Millennial- and centennial-scale vegetation and climate changes during the late Pleistocene and Holocene from northern New Mexico (USA): Quaternary Science Reviews, v. 27, no. 13-14, p. 1442-1452.

Jolly, W.M., Cochrane, M.A., Freeborn, P.H., Holden, Z.A., Brown, T.J., Williamson, G.J. and Bowman, D.M., 2015. Climate-induced variations in global wildfire danger from 1979 to 2013. Nature communications, 6(1), pp.1-11.

Knight, T. A., Meko, D. M., and Baisan, C. H., 2010, A bimillennial-length tree-ring reconstruction of precipitation for the Tavaputs Plateau, Northeastern Utah: Quaternary Research, v. 73, no. 1, p. 107-117.

Littell, J.S., McKenzie, D., Peterson, D.L. and Westerling, A.L., 2009. Climate and wildfire area burned in western US ecoprovinces, 1916–2003. Ecological Applications, 19(4), pp.1003-1021.

Madsen, D. B., Rhode, D., Grayson, D. K., Broughton, J. M., Livingston, S. D., Hunt, J., Quade, J., Schmitt, D. N., and Shaver, M., 2001, Late Quaternary environmental change in the Bonneville basin, western USA: Palaeogeography, Palaeoclimatology, Palaeoecology, v. 167, no. 3, p. 243-271.

Marlon, J. R., Bartlein, P. J., Gavin, D. G., Long, C. J., Anderson, R. S., Briles, C. E., Brown, K. J., Colombaroli, D., Hallett, D. J., Power, M. J., Scharf, E. A., and Walsh, M. K., 2012, Long-term perspective on wildfires in the western USA: Proceedings of the National Academy of Sciences, v. 109, no. 9, p. E535-E543.

Mehringer, P., and Wigand, P. E., 1990, Comparison of late Holocene environments from woodrat middens and pollen: Diamond Craters, Oregon: Fossil packrat middens: the last, v. 40, p. 294-325.

Meko, D. M., Woodhouse, C. A., Baisan, C. A., Knight, T., Lukas, J. J., Hughes, M. K., and Salzer, M. W., 2007, Medieval drought in the upper Colorado River Basin: Geophysical Research Letters, v. 34, no. 10, p. L10705.

Menking, K. M., and Anderson, R. Y., 2003, Contributions of La Nina and El Nino to middle holocene drought and late Holocene moisture in the American Southwest: Geology, v. 31, no. 11, p. 937-940.

Meyer, G. A., Wells, S. G., and Jull, A. J. T., 1995, Fire and alluvial chronology in Yellowstone National Park: Climatic and intrinsic controls on Holocene geomorphic processes: Geol. Soc. Am. Bull., v. 107, p. 1211-1230.

Michczyński, A., 2007, Is it possible to find a good point estimate of a calibrated radiocarbon date?: Radiocarbon, v. 49, no. 02, p. 393-401.

Miller, R., and Tausch, R., The role of fire in pinyon and juniper woodlands: a descriptive analysis, *in* Proceedings Proceedings of the invasive species workshop: the role of fire in the control and spread of invasive species. Tall Timbers Research Station Miscellaneous Publication2001, Volume 11, p. 15-30.

Miller, R. F., and Rose, J. A., 1999, Fire history and western juniper encroachment in sagebrush steppe: Journal of Range Management, p. 550-559.

Miller, R. F., and Wigand, P. E., 1994, Holocene changes in semiarid pinyon-juniper woodlands: BioScience, v. 44, no. 7, p. 465-474.

Morris, J. L., Brunelle, A., DeRose, R. J., Seppä, H., Power, M. J., Carter, V., and Bares, R., 2013a, Using fire regimes to delineate zones in a high-resolution lake sediment record from the western United States: Quaternary Research, v. 79, no. 1, p. 24-36.

Morris, J. L., Brunelle, A., Munson, A. S., Spencer, J., and Power, M. J., 2013b, Holocene vegetation and fire reconstructions from the Aquarius Plateau, Utah, USA: Quaternary International, v. 310, p. 111-123.

Neilson, R. P., 1986, High-Resolution Climatic Analysis and Southwest Biogeography: Science, v. 232, no. 4746, p. 27-34.

Nelson, M. S., and Rittenour, T. R., 2014, Middle to late Holocene chronostratigraphy of alluvial fill deposits along Kanab Creek in southern Utah, *in* MacLean, J. S., Biek, R.F., and Huntoon, J.E., ed., Geology of Utah's Far South, Volume 43, Utah Geological Association Publication p. 97–116.

Nowak, C. L., Nowak, R. S., Tausch, R. J., and Wigand, P. E., 1994, Tree and shrub dynamics in northwestern Great Basin woodland and shrub steppe during the Late-Pleistocene and Holocene: American Journal of Botany, p. 265-277.

Overpeck, J.T., Rind, D. and Goldberg, R., 1990. Climate-induced changes in forest disturbance and vegetation. Nature, 343(6253), pp.51-53.

Oviatt, C. G., 1988, Late Pleistocene and Holocene lake fluctuations in the Sevier Lake basin, Utah, USA: Journal of Paleolimnology, v. 1, no. 1, p. 9-21.

Parker, K.C., 2002. Fire in the pre-European lowlands of the American Southwest. Fire, Native Peoples, and the Natural Landscape, pp.101-141.

Patton, P. C., and Boison, P. J., 1986, Processes and rates of formation of Holocene alluvial terraces in Harris Wash, Escalante River Basin, South-Central Utah: Geological Society of America Bulletin, v. 97, no. 3, p. 369-378.

Pierce, J.L., Meyer, G.A. and Jull, A.T., 2004. Fire-induced erosion and millennial-scale climate change in northern ponderosa pine forests. Nature, 432(7013), pp.87-90.

Polyak, V. J., and Asmerom, Y., 2001, Late Holocene climate and cultural changes in the southwestern United States: Science, v. 294, no. 5540, p. 148-151.

Ramsey, C. B., 2009, Bayesian analysis of radiocarbon dates: Radiocarbon, v. 51, no. 01, p. 337-360.

Rasmussen, J. B., Polyak, V. J., and Asmerom, Y., 2006, Evidence for Pacific-modulated precipitation variability during the late Holocene from the southwestern USA: Geophysical Research Letters, v. 33, no. 8.

Reimer, P. J., Baillie, M. G. L., Bard, E., Bayliss, A., Beck, J. W., Bertrand, C. J. H., Blackwell, P. G., Buck, C. E., Burr, G. S., Cutler, K. B., Damon, P. E., Edwards, R. L., Fairbanks, R. G., Friedrich, M., Guilderson, T. P., Hogg, A. G., Hughen, K. A., Kromer, B., McCormac, G., Manning, S., Ramsey, C. B., Reimer, R. W., Remmele, S., Southon, J. R., Stuiver, M., Talamo, S., Taylor, F. W., van der Plicht, J., and Weyhenmeyer, C. E., 2004, IntCal04 terrestrial radiocarbon age calibration, 0-26 cal kyr BP: Radiocarbon, v. 46, no. 3, p. 1029-1058.

Reimer, P.J., Bard, E., Bayliss, A., Beck, J.W., Blackwell, P.G., Ramsey, C.B., Buck, C.E., Cheng, H., Edwards, R.L., Friedrich, M. and Grootes, P.M., 2013. IntCal13 and Marine13 radiocarbon age calibration curves 0–50,000 years cal BP. Radiocarbon, 55(4), pp.1869-1887.

Riedinger, M. A., Steinitz-Kannan, M., Last, W. M., and Brenner, M., 2002, A~ 6100 14C yr record of El Niño activity from the Galápagos Islands: Journal of Paleolimnology, v. 27, no. 1, p. 1-7.

Riley, K., Pierce, J. and Meyer, G.A., 2015. Vegetative and climatic controls on Holocene wildfire and erosion recorded in alluvial fans of the Middle Fork Salmon River, Idaho. The Holocene, 25(5), pp.857-871.

Rodbell, D. T., Seltzer, G. O., Anderson, D. M., Abbott, M. B., Enfield, D. B., and Newman, J. H., 1999, An~ 15,000-year record of El Niño-driven alluviation in southwestern Ecuador: Science, v. 283, no. 5401, p. 516-520.

Romme, W. H., Allen, C. D., Bailey, J. D., Baker, W. L., Bestelmeyer, B. T., Brown, P. M., Eisenhart, K. S., Floyd, M. L., Huffman, D. W., and Jacobs, B. F., 2009, Historical and modern disturbance regimes, stand structures, and landscape dynamics in pinon–juniper vegetation of the western United States: Rangeland Ecology & Management, v. 62, no. 3, p. 203-222.

Salzer, M. W., and Kipfmueller, K. F., 2005, Reconstructed temperature and precipitation on a millennial timescale from tree-rings in the Southern Colorado Plateau, USA: Climatic Change, v. 70, no. 3, p. 465-487.

Schoennagel, T., Veblen, T. T., and Romme, W. H., 2004, The Interaction of Fire, Fuels, and Climate across Rocky Mountain Forests: BioScience, v. 54, no. 7, p. 661-676.

Schwinning, S., Belnap, J., Bowling, D.R. and Ehleringer, J.R., 2008. Sensitivity of the Colorado Plateau to change: climate, ecosystems, and society. Ecology and Society, 13(2).

Shinneman, D.J. and Baker, W.L., 2009. Historical fire and multidecadal drought as context for pinon–juniper woodland restoration in western Colorado. Ecological Applications, 19(5), pp.1231-1245.

Smith, S., 1990, Large floods and rapid entrenchment Kanab Creek, southern Utah [MS Thesis]: University of Arizona, 82 p. p.

Spaulding, W. G., and Graumlich, L. J., 1986, The last pluvial climatic episodes in the deserts of southwestern North America: Nature, v. 320, no. 6061, p. 441-444.

Stahle, D. W., Fye, F. K., Cook, E. R., and Griffin, R. D., 2007, Tree-ring reconstructed megadroughts over North America since AD 1300: Climatic change, v. 83, no. 1-2, p. 133.

Stine, S., 1994, Extreme and Persistent Drought in California and Patagonia During Medieval Time Nature, v. 369, no. 6481, p. 546-549.

-, 1998, Water, Environment and Society in Times of Climatic Change.

Surovell, T.A., Finley, J.B., Smith, G.M., Brantingham, P.J. and Kelly, R., 2009. Correcting temporal frequency distributions for taphonomic bias. Journal of archaeological Science, 36(8), pp.1715-1724.

Swetnam, T.W. and Baisan, C.H., 1996. Fire histories of montane forests in the Madrean Borderlands. United States Department of Agriculture Forest Service General Technical Report, pp.15-36.

Swetnam, T. W., and Betancourt, J. L., 1990, Fire-southern oscillation relations in the southwestern United States: Science(Washington), v. 249, no. 4972, p. 1017-1020.

Swetnam, T. W., and Betancourt, J. L., 1998, Mesoscale disturbance and ecological response to decadal climatic variability in the American Southwest: J. Clim., v. 11, p. 3128-3147.

Telford, R. J., Heegaard, E., and Birks, H. J. B., 2004, The intercept is a poor estimate of a calibrated radiocarbon age: The Holocene, v. 14, no. 2, p. 296-298.

Townsend, K. F., 2015, A Chronostratigraphic Record of Arroyo Entrenchment and Aggradation in Kanab Creek, Southern Utah.

Van Devender, T. R., and Spaulding, W. G., 1979, Development of vegetation and climate in the southwestern United States: Science, v. 204, no. 4394, p. 701-710.

Veblen, T.T., Kitzberger, T. and Donnegan, J., 2000. Climatic and human influences on fire regimes in ponderosa pine forests in the Colorado Front Range. Ecological applications, 10(4), pp.1178-1195.

Wangler, M.J. and Minnich, R.A., 1996. Fire and succession in pinyon-juniper woodlands of the San Bernardino Mountains, California. Madrono, pp.493-514.

Waters, M. R., and Haynes, C. V., 2001, Late Quaternary arroyo formation and climate change in the American Southwest: Geology, v. 29, no. 5, p. 399-402.

Webb, R., and Hasbargen, J., 1997, Floods, ground-water levels, and arroyo formation on the Escalante River, southcentral Utah, *in* Hill, L. M., ed., Learning from the Land:Grand Staircase-Escalante National Monument Science Symposium Proceedings.

Webb, R. H., 1985, Late Holocene flooding on the Escalante River, south-central Utah [Ph.D. Dissertation: The University of Arizona., 204 p.

Wells, S. G., McFadden, L. D., and Schultz, J. D., 1990, Eolian landscape evolution and soil formation in the Chaco dune field, southern Colorado Plateau, New Mexico: Geomorphology, v. 3, no. 3, p. 517-546.

Weng, C., and Jackson, S. T., 1999, Late Glacial and Holocene vegetation history and paleoclimate of the Kaibab Plateau, Arizona: Palaeogeography, Palaeoclimatology, Palaeoecology, v. 153, no. 1, p. 179-201.

Weppner, K.N., Pierce, J.L. and Betancourt, J.L., 2013. Holocene fire occurrence and alluvial responses at the leading edge of pinyon–juniper migration in the Northern Great Basin, USA. Quaternary Research, 80(2), pp.143-157.

Westerling, A.L., Gershunov, A., Brown, T.J., Cayan, D.R. and Dettinger, M.D., 2003. Climate and wildfire in the western United States. Bulletin of the American Meteorological Society, 84(5), pp.595-604.

Westerling, A.L., 2016. Increasing western US forest wildfire activity: sensitivity to changes in the timing of spring. Philosophical Transactions of the Royal Society B: Biological Sciences, 371(1696), p.20150178.

Whitlock, C., Higuera, P.E., McWethy, D.B. and Briles, C.E., 2010. Paleoecological perspectives on fire ecology: revisiting the fire-regime concept. The Open Ecology Journal, 3(1).

Wigand, P. E., 1987, Diamond Pond, Harney County, Oregon: vegetation history and water table in the eastern Oregon desert: The Great Basin Naturalist, p. 427-458.

Wigand, P. E., Hemphill, M., and Sharpe, S., 1995, Great Basin semi-arid woodland dynamics during the late Quaternary: Rust Geotech, Inc., Grand Junction, CO (United States).

Wigand, P.E. and Rose, M.R., 1990. Calibration of high frequency pollen sequences and tree-ring records. In High level radioactive waste management.

Williams, A. P., Allen, C. D., Macalady, A. K., Griffin, D., Woodhouse, C. A., Meko, D. M., Swetnam, T. W., Rauscher, S. A., Seager, R., and Grissino-Mayer, H. D., 2013, Temperature as a potent driver of regional forest drought stress and tree mortality: Nature climate change, v. 3, no. 3, p. 292-297.

Williams, A.P., Allen, C.D., Millar, C.I., Swetnam, T.W., Michaelsen, J., Still, C.J. and Leavitt, S.W., 2010. Forest responses to increasing aridity and warmth in the southwestern United States. Proceedings of the National Academy of Sciences, 107(50), pp.21289-21294.

Williams, A.P. and Abatzoglou, J.T., 2016. Recent advances and remaining uncertainties in resolving past and future climate effects on global fire activity. Current Climate Change Reports, 2(1), pp.1-14.

Williams, A. P., Seager, R., Macalady, A. K., Berkelhammer, M., Crimmins, M. A., Swetnam, T. W., Trugman, A. T., Buenning, N., Noone, D., and McDowell, N. G., 2015, Correlations between components of the water balance and burned area reveal new insights for predicting forest fire area in the southwest United States: International Journal of Wildland Fire, v. 24, no. 1, p. 14-26.

Williams, D. G., and Ehleringer, J. R., 2000, Intra- and interspecific variation for summer precipitation use in pinyon-juniper woodlands: Ecological Monographs, v. 70, no. 4, p. 517-537.

Woodhouse, C. A., Meko, D. M., MacDonald, G. M., Stahle, D. W., and Cook, E. R., 2010, A 1,200-year perspective of 21st century drought in southwestern North America: Proceedings of the National Academy of Sciences, v. 107, no. 50, p. 21283-21288.

Supplemental Material

Table 5-S1. Percentage of current watershed covered by forest, defined as greater than 10% canopy cover. Area calculated from one full cycle of USFS Forest Inventory and Analysis (2006-2015) plots that fall within the four study area basins. Plots were established on a geographically unbiased sampling grid designed to characterize all land and ownerships (i.e, forest and non-forest; Bechtold and Patterson, 2005)

Watershed	**Upstream Catchment Area** (km^2)	**Non-Forested Area** (km^2)	**Percent**	**Forested Area** (km^2))	**Percent**
Kanab Creek	615	178	29	437	71
Johnson Wash	412	231	33	461	67
Paria River	769	162	21	607	79
Escalante River	5245	2380	45	2865	55
Total Study Area	**7321**	**2951**	**40%**	**4370**	**60%**

Table 5-S2. Percentage of forested area by forest type occurring in each watershed. Percentage by forest type calculated from one full cycle of Forest Inventory and Analysis (2006-2015) forested plots (greater than 10% canopy cover) that fell within the four study area basins. Forest types were defined in the field by crews, and verified by algorithm upon data compilation.

Watershed	Forest Type	Percentage
Escalante River	Pinyon/Juniper	72
	Engelmann spruce/subalpine fir	6
	Ponderosa pine	5
	Quaking aspen	5
	Non-stocked [1]	4
	Gambel oak	3
	White fir	3
	Cottonwood	8
	Limber pine	< 1
Johnson Wash	Pinyon/Juniper	94
	Gamble oak	6
Paria River	Pinyon/Juniper	96
	Douglas-fir	4
Kanab Creek	Pinyon/Juniper	94
	Douglas-fir	6
Total Study Area	Pinyon/Juniper	83
	Engelmann spruce/subalpine fir	3
	Ponderosa pine	3
	Quaking aspen	3
	White fir	3
	Douglas-Fir	2
	Gambel oak	2
	Cottonwood	2
	Limber pine	< 1
	Non-stocked [1]	< 1

[1] Non-stocked means that the field crew knows it is (or was, or will be) a forest, it just currently doesn't have enough stems or canopy cover. For example, if there was a fire and all the trees are dead, but there are clearly trees everywhere it would be non-stocked. That is, forest with little or no live trees. Regenerating forests are the same, as aspen thicket of millions of trees 5 feet tall is a 'forest' but has no stocking.

Table 5-S3. Alluvial charcoal samples (n = 48) from 20 sites along Kanab Creek.

Lab Code [1]	Sample ID	^{14}C-age *± 1 sigma*	Median Age [2] *cal yr BP ± 1 sigma*			Latitude *(dd)*	Longitude *(dd)*	Citation
UCIAMS - 113991	KNB: 15	200 ± 15	170	120	-170	37.12900	-112.54000	Summa-Nelson and Rittenour, 2014
UCIAMS - 147402	KNB: 73	280 ± 25	370	50	-80	37.2849	-112.49954	Townsend, 2015
Beta-256843	KNB: 16	420 ± 40	480	35	-145	37.11793	-112.54416	Summa-Nelson and Rittenour, 2014
NR	KNB: S-2	485 ± 90	520	120	-180	37.11793	-112.54416	Smith, 1990
NR	KNB: S-1	570 ± 70	590	55	-60	37.06120	-112.53941	Smith, 1990
NR	KNB: S-3	625 ± 70	600	55	-50	37.11793	-112.54416	Smith, 1990
UCIAMS - 147399	KNB: 37	670 ± 25	650	20	-80	37.03761	-112.53304	Townsend, 2015
UCIAMS - 136401	KNB: 15	690 ± 15	660	5	-5	37.06754	-112.54047	Townsend, 2015
UCIAMS - 151642	KNB: 9	820 ± 20	720	25	-15	37.06835	-112.53742	Townsend, 2015
UCIAMS - 113890	KNB: 20	835 ± 15	740	25	-30	37.13800	-112.54000	Summa-Nelson and Rittenour, 2014
UCIAMS - 147398	KNB: 26	860 ± 30	760	25	-35	37.05524	-112.53898	Townsend, 2015
UCIAMS - 151639	KNB: 2	955 ± 20	850	70	-50	37.07377	-112.24256	Townsend, 2015
UCIAMS - 151644	KNB: 30	985 ± 20	920	15	-85	37.03973	-112.53311	Townsend, 2015
UCIAMS - 136382	KNB: 11	1005 ± 20	930	20	-10	37.06754	-112.54047	Townsend, 2015
UCIAMS - 151641	KNB: 8	1095 ± 20	1000	50	-35	37.06835	-112.53742	Townsend, 2015
UCIAMS - 147393	KNB: 33	1100 ± 25	1010	45	-35	37.03973	-112.53311	Townsend, 2015
UCIAMS - 136383	KNB: 14	1195 ± 15	1120	50	-40	37.06754	-112.54047	Townsend, 2015
UCIAMS - 113992	KNB: 12	1280 ± 90	1200	95	-110	37.12900	-112.54000	Summa-Nelson and Rittenour, 2014
UCIAMS - 105786	KNB: 13	1360 ± 15	1290	5	-5	37.11767	-112.54508	Summa-Nelson and Rittenour, 2014
UCIAMS - 105785	KNB: 14	1545 ± 15	1470	45	-70	37.11767	-112.54508	Summa-Nelson and Rittenour, 2014
UCIAMS - 147392	KNB: 28	1785 ± 25	1710	35	-80	37.03973	-112.53311	Townsend, 2015
UCIAMS - 151638	KNB: 45	1815 ± 25	1760	25	-45	37.03041	-112.53501	Townsend, 2015
UCIAMS - 136385	KNB: 21	1885 ± 15	1840	20	-25	37.13800	-112.54000	Summa-Nelson and Rittenour, 2014
UCIAMS - 136381	KNB: 10	1925 ± 35	1870	40	-50	37.06754	-112.54047	Townsend, 2015
UCIAMS - 147395	KNB: 6	2080 ± 25	2050	50	-50	37.06835	-112.53742	Townsend, 2015
UCIAMS - 113993	KNB:DN-1	2135 ± 15	2130	25	-56	37.16875	-112.59300	Rittenour Dunes - unpublished
NR	KNB: S-5	2420 ± 60	2490	195	-135	37.0612	-112.53941	Smith, 1990
UCIAMS - 147394	KNB: 5	2495 ± 25	2580	125	-85	37.06835	-112.53742	Townsend, 2015
UCIAMS - 147397	KNB: 22	2500 ± 25	2580	130	-80	37.05524	-112.53898	Townsend, 2015
UCIAMS - 151643	KNB: 18	2535 ± 20	2700	35	-160	37.06094	-112.53942	Townsend, 2015
UCIAMS - 151637	KNB: 43	2690 ± 180	2810	250	-310	37.03041	-112.53501	Townsend, 2015
Not Reported	KNB: S-4	2955 ± 60	3110	105	-110	37.0612	-112.53941	Smith, 1990
Not Reported	KNB: S-7	3320 ± 50	3550	75	-75	37.11793	-112.54416	Smith, 1990
UCIAMS - 151640	KNB: 4	3365 ± 30	3610	20	-35	37.06835	-112.53742	Townsend, 2015
Beta-256844	KNB: 2	3460 ± 40	3730	95	-85	37.11828	-112.54576	Summa-Nelson and Rittenour, 2014
NR	KNB: S-8	3560 ± 50	3860	75	-125	37.11793	-112.54416	Smith, 1990
Beta-256845	KNB: 4	3690 ± 40	4030	45	-55	37.11217	-112.55107	Summa-Nelson and Rittenour, 2014
UCIAMS - 136384	KNB: 48	3745 ± 15	4120	30	-30	37.4052	-112.47348	Townsend, 2015
Not Reported	KNB: 5401b	3810 ± 80	4210	160	-120	Not reported	Not reported	Smith, 1990
Not Reported	KNB: S-11	4360 ± 90	4970	245	-135	37.11793	-112.54416	Smith, 1990
Not Reported	KNB: S-10	4460 ± 390	5060	520	-500	37.0612	-112.53941	Smith, 1990
Not Reported	KNB: S-9	4460 ± 90	5110	180	-135	37.11793	-112.54416	Smith, 1990
UCIAMS - 151645	KNB: 27	4710 ± 20	5390	180	-55	37.04865	-112.53661	Townsend, 2015
UCIAMS - 147396	KNB: 17	4970 ± 25	5690	25	-35	37.06094	-112.53942	Townsend, 2015
Not Reported	KNB: S-13	4980 ± 85	5730	145	-115	37.0612	-112.53941	Smith, 1990
UCIAMS - 128122	KNB: 52	5215 ± 20	5960	25	-30	37.28783	-112.49551	Townsend, 2015
NR	KNB: S-12	5345 ± 90	6120	145	-120	37.0612	-112.53941	Smith, 1990
UCIAMS -128123	KNB: 56	6125 ± 20	7000	145	-45	37.28783	-112.49551	Townsend, 2015

1 UCIAMS is the lab ID for the University of California Irvine Accelerator Mass Spectrometry Lab, Beta is the lab ID for Beta Analytic, and NR stands for lab ID's that were not reported in the publication.

2 The calibrated median age was calculated with CALIB 7.1 (Reimer et al., 2004) and the IntCal13 calibration curve (Reimer et al., 2013). Ages reported are in calibrated years before 1950 (cal yr BP).

Table 5-S4. Charcoal samples (n=48) collected from 14 sites along Johnson Wash.

Lab Code [1]	Sample ID	^{14}C-age *± 1 sigma*	Median Age [2] *cal yr BP ± 1 sigma*			Latitude (deg)	Longitude (deg)	Citation
UCIAMS -137319	JW: 11	115 ± 25	120	+ 145	- 85	37.24049	-112.36064	Ch 2; Riley and Rittenour, in prep.
UCIAMS - 147088	JW: 51	285 ± 20	390	+ 35	- 85	37.15202	-112.39815	Ch 2; Riley and Rittenour, in prep.
UCIAMS - 128115	JW: 26	350 ± 15	390	+ 75	- 60	37.22302	-112.36850	Ch 2; Riley and Rittenour, in prep.
UCIAMS - 137320	JW: 12	355 ± 35	400	+ 75	- 80	37.24049	-112.36064	Ch 2; Riley and Rittenour, in prep.
UCIAMS - 147086	JW: 56	400 ± 25	480	+ 55	- 135	37.23133	-112.33472	Ch 2; Riley and Rittenour, in prep.
UCIAMS - 128117	JW: 27	440 ± 15	510	+ 5	- 10	37.22302	-112.36850	Ch 2; Riley and Rittenour, in prep.
UCIAMS - 137317	JW: 39	555 ± 30	560	+ 65	- 30	37.22312	-112.36949	Ch 2; Riley and Rittenour, in prep.
UCIAMS - 147065	JW: 13	570 ± 25	600	+ 25	- 65	37.24049	-112.36064	Ch 2; Riley and Rittenour, in prep.
UCIAMS - 137311	JW: 10	820 ± 30	730	+ 30	- 35	37.24154	-112.35978	Ch 2; Riley and Rittenour, in prep.
UCIAMS - 128114	JW: 55	945 ± 15	850	+ 65	- 50	37.21200	-112.39400	Ch 2; Riley and Rittenour, in prep.
UCIAMS - 128118	JW: 28	1125 ± 15	1020	+ 40	- 35	37.22302	-112.36850	Ch 2; Riley and Rittenour, in prep.
UCIAMS - 147087	JW: 52	1125 ± 20	1020	+ 35	- 35	37.15202	-112.39815	Ch 2; Riley and Rittenour, in prep.
UCIAMS - 147064	JW: 4	1135 ± 25	1030	+ 35	- 45	37.24154	-112.35978	Ch 2; Riley and Rittenour, in prep.
UCIAMS - 147080	JW: 42	1205 ± 20	1130	+ 50	- 45	37.20069	-112.37725	Ch 2; Riley and Rittenour, in prep.
UCIAMS - 151647	JW: 23	1210 ± 45	1140	+ 85	- 70	37.23106	-112.36467	Ch 2; Riley and Rittenour, in prep.
UCIAMS - 147066	JW: 14	1230 ± 25	1170	+ 65	- 80	37.24049	-112.36064	Ch 2; Riley and Rittenour, in prep.
UCIAMS - 137318	JW: 40	1260 ± 25	1220	+ 35	- 40	37.22312	-112.36949	Ch 2; Riley and Rittenour, in prep.
UCIAMS - 128120	JW: 57	1485 ± 15	1370	+ 15	- 20	37.23133	-112.33472	Ch 2; Riley and Rittenour, in prep.
UCIAMS - 147067	JW: 15	1495 ± 20	1380	+ 20	- 20	37.24049	-112.36064	Ch 2; Riley and Rittenour, in prep.
UCIAMS - 137314	JW: 16	1495 ± 30	1380	+ 25	- 30	37.24049	-112.36064	Ch 2; Riley and Rittenour, in prep.
UCIAMS - 147084	JW: 46	1560 ± 20	1470	+ 49	- 61	37.17746	-112.38585	Ch 2; Riley and Rittenour, in prep.
UCIAMS - 147075	JW: 34	1630 ± 20	1540	+ 20	- 15	37.22396	-112.36855	Ch 2; Riley and Rittenour, in prep.
UCIAMS - 147060	JW: 1	1660 ± 20	1560	+ 35	- 25	37.33053	-112.37371	Ch 2; Riley and Rittenour, in prep.
UCIAMS - 136386	JW: 47	1680 ± 15	1580	+ 20	- 25	37.17746	-112.38585	Ch 2; Riley and Rittenour, in prep.
UCIAMS - 147079	JW: 41	1770 ± 25	1670	+ 45	- 45	37.22312	-112.36949	Ch 2; Riley and Rittenour, in prep.
UCIAMS - 147070	JW: 24	1785 ± 20	1710	+ 25	- 75	37.23106	-112.36467	Ch 2; Riley and Rittenour, in prep.
UCIAMS - 128112	JW: 25	1915 ± 15	1870	+ 40	- 65	37.23106	-112.36467	Ch 2; Riley and Rittenour, in prep.
UCIAMS - 147062	JW: 6	1990 ± 20	1940	+ 100	- 115	37.24154	-112.35978	Ch 2; Riley and Rittenour, in prep.
UCIAMS - 151648	JW: 19	2030 ± 20	1980	+ 20	- 30	37.23106	-112.36467	Ch 2; Riley and Rittenour, in prep.
UCIAMS - 151650	JW: 2	2035 ± 20	1980	+ 20	- 35	37.33053	-112.37371	Ch 2; Riley and Rittenour, in prep.
UCIAMS - 151651	JW: 8	2140 ± 60	2130	+ 165	- 125	37.24154	-112.35978	Ch 2; Riley and Rittenour, in prep.
UCIAMS - 147083	JW: 50	2230 ± 25	2220	+ 90	- 65	37.17746	-112.38585	Ch 2; Riley and Rittenour, in prep.
UCIAMS - 137315	JW: 17	2195 ± 25	2240	+ 65	- 90	37.24049	-112.36064	Ch 2; Riley and Rittenour, in prep.
UCIAMS - 147076	JW: 29	2280 ± 20	2330	+ 15	- 10	37.22302	-112.36850	Ch 2; Riley and Rittenour, in prep.
UCIAMS - 147061	JW: 3	2400 ± 25	2410	+ 40	- 60	37.33053	-112.37371	Ch 2; Riley and Rittenour, in prep.
UCIAMS - 147068	JW: 18	2415 ± 25	2410	+ 30	- 70	37.25070	-112.36153	Ch 2; Riley and Rittenour, in prep.
UCIAMS - 137312	JW: 7	2475 ± 25	2590	+ 115	- 95	37.24154	-112.35978	Ch 2; Riley and Rittenour, in prep.
UCIAMS - 137316	JW: 37	2505 ± 30	2590	+ 140	- 120	37.22396	-112.36855	Ch 2; Riley and Rittenour, in prep.
UCIAMS - 128113	JW: 22	2460 ± 15	2600	+ 90	- 140	37.23106	-112.36467	Ch 2; Riley and Rittenour, in prep.
UCIAMS - 147081	JW: 44	2535 ± 20	2700	+ 35	- 160	37.20069	-112.37725	Ch 2; Riley and Rittenour, in prep.
UCIAMS - 147073	JW: 36	2825 ± 20	2920	+ 70	- 60	37.22396	-112.36855	Ch 2; Riley and Rittenour, in prep.
UCIAMS - 147072	JW: 38	2910 ± 20	3040	+ 30	- 45	37.22396	-112.36855	Ch 2; Riley and Rittenour, in prep.
UCIAMS - 147078	JW: 33	2985 ± 20	3160	+ 45	- 85	37.22302	-112.36850	Ch 2; Riley and Rittenour, in prep.
UCIAMS - 151649	JW: 43	3000 ± 20	3190	+ 30	- 30	37.20069	-112.37725	Ch 2; Riley and Rittenour, in prep.
UCIAMS - 147063	JW: 9	3125 ± 35	3350	+ 40	- 85	37.24154	-112.35978	Ch 2; Riley and Rittenour, in prep.
UCIAMS - 113994	JW: 53	3185 ± 20	3410	+ 35	- 25	37.13059	-112.39248	Ch 2; Riley and Rittenour, in prep.
UCIAMS - 113901	JW: 54	3985 ± 20	4480	+ 55	- 30	37.13059	-112.39248	Ch 2; Riley and Rittenour, in prep.
UCIAMS - 147074	JW: 35	4480 ± 230	5120	+ 340	- 275	37.22396	-112.36855	Ch 2; Riley and Rittenour, in prep.

[1] UCIAMS is the lab ID for the University of California Irvine Accelerator Mass Spectrometry Lab

[2] The calibrated median age was calculated with CALIB 7.1 (Reimer et al., 2004) and the IntCal13 calibration curve (Reimer et al., 2013). Ages reported are in calibrated years before 1950 (cal yr BP).

Table 5-S5. Charcoal samples (n = 37) from 16 sites along arroyo walls and in flood deposits along the main-stem Paria River and its tributary Kitchen Corral Wash and Buckskin Wash.

Lab Code [1]	Sample ID	^{14}C-age *± 1 sigma*	Median Age [2] *cal yr BP ± 1 sigma*	Latitude (deg)	Longitude (deg)	Citation
UCIAMS - 113988	PAR: 13	140 ± 15	140 + 125 - 130	37.21745	-112.13931	Huff and Rittenour, 2014
UCIAMS - 113986	PAR: 2	365 ± 15	440 + 35 - 110	37.25507	-112.16564	Huff and Rittenour, 2014
X-24131	PAR: 36	368 ± 37	430 + 70 - 95	37.14164	-112.09405	Huff and Rittenour, 2014
X-24133	PAR: 8	466 ± 37	510 + 15 - 15	37.23512	-112.12296	Huff and Rittenour, 2014
UCIAMS - 113981	PAR: 3	500 ± 15	530 + 5 - 10	37.25423	-112.13139	Huff and Rittenour, 2014
X-24140	PAR: 15	609 ± 37	600 + 45 - 50	37.22137	-112.12116	Huff and Rittenour, 2014
UCIAMS - 113982	PAR: 18	665 ± 15	650 + 30 - 5	37.21581	-112.12551	Huff and Rittenour, 2014
X-24142	PAR: 27	849 ± 40	760 + 30 - 55	37.18361	-112.1155	Huff and Rittenour, 2014
X-24138	PAR: 12	879 ± 38	790 + 110 - 55	37.21745	-112.13931	Huff and Rittenour, 2014
X-24129	PAR: 34	993 ± 46	900 + 55 - 100	37.14164	-112.09405	Huff and Rittenour, 2014
UCIAMS - 105793	PAR: 24	1115 ± 30	1020 + 40 - 40	37.18361	-112.1155	Huff and Rittenour, 2014
X-24134	PAR: 17	1194 ± 38	1120 + 55 - 50	37.21581	-112.12551	Huff and Rittenour, 2014
X-24135	PAR: 9	1208 ± 38	1130 + 45 - 65	37.23512	-112.12296	Huff and Rittenour, 2014
UCIAMS - 113989	PAR: 4	1235 ± 15	1210 + 30 - 110	37.25423	-112.13139	Huff and Rittenour, 2014
Beta-256836	PAR: RCBG6	1250 ± 40	1200 + 70 - 105	37.03129	-112.00464	Harvey et al., 2010
GX-16582	PAR: BSR-30	1330 ± 80	1250 + 75 - 70	37.04470	-112.0178	Ely, 1992
UCIAMS - 113987	PAR: 11	1420 ± 15	1320 + 10 - 15	37.21745	-112.13931	Huff and Rittenour, 2014
X-24132	PAR: 7	1488 ± 38	1370 + 35 - 40	37.23512	-112.12296	Huff and Rittenour, 2014
UCIAMS - 105790	PAR: 31	1730 ± 30	1640 + 55 - 70	37.17012	-112.09731	Huff and Rittenour, 2014
UCIAMS - 105788	PAR: 28	1755 ± 30	1660 + 45 - 40	37.17752	-112.10266	Huff and Rittenour, 2014
Beta-256835	PAR: RCBG5	1780 ± 40	1700 + 75 - 80	37.03129	-112.00464	Harvey et al., 2010
UCIAMS - 105791	PAR: 32	1860 ± 30	1800 + 65 - 60	37.17012	-112.09731	Huff and Rittenour, 2014
X-24130	PAR: 35	2002 ± 40	1950 + 40 - 55	37.14164	-112.09405	Huff and Rittenour, 2014
UCIAMS - 113985	PAR: 1	2015 ± 15	1960 + 25 - 15	37.25507	-112.16564	Huff and Rittenour, 2014
UCIAMS - 105794	PAR: 25	2200 ± 40	2230 + 75 - 80	37.18361	-112.1155	Huff and Rittenour, 2014
Beta-256840	PAR: RCKCW4	2220 ± 40	2230 + 80 - 75	37.17752	-112.10266	Harvey et al., 2010
X-24143	PAR: 33	2395 ± 40	2430 + 50 - 80	37.17012	-112.09731	Huff and Rittenour, 2014
X-24136	PAR: 5	2460 ± 40	2550 + 145 - 115	37.22864	-112.15267	Huff and Rittenour, 2014
UCIAMS - 113984	PAR: 21	3420 ± 15	3670 + 25 - 25	37.21581	-112.12551	Huff and Rittenour, 2014
UCIAMS - 105792	PAR: 22	3480 ± 30	3760 + 65 - 60	37.18361	-112.1155	Huff and Rittenour, 2014
UCIAMS - 113983	PAR: 26	3735 ± 15	4090 + 50 - 85	37.18361	-112.1155	Huff and Rittenour, 2014
A-5721	PAR: BSR-29	3895 ± 95	4320 + 115 - 160	37.04470	-112.0178	Ely, 1992
NR	PAR: P-9 BA	4130 ± 200	4640 + 305 - 345	36.95420	-111.7830	Webb, 1985
Not published	PAR: PW 1	4330 ± 40	4900 + 55 - 55	37.18000	-112.10361	Hereford, 2002
Beta-244295	PAR: RCCW1	4890 ± 40	5630 + 20 - 30	36.93595	-112.04021	Harvey et al., 2010
Not published	PAR: PW 2	5650 ± 35	6430 + 40 - 30	37.18000	-112.10361	Hereford, 2002
Not published	PAR: PW 3	6320 ± 80	7250 + 160 - 85	37.18000	-112.10361	Hereford, 2002

[1] UCIAMS is the lab ID for the University of California Irvine Accelerator Mass Spectrometry Lab, Beta is the lab ID for Beta Analytic, GX, X, and A refer to University of Arizona Radiocarbon Lab, and NR stands for lab ID's that were not reported in the publication.

[2] The calibrated median age was calculated with CALIB 7.1 (Reimer et al., 2004) and the IntCal13 calibration curve (Reimer et al., 2013). Ages reported are in calibrated years before 1950 (cal yr BP).

Table 5-S6. Charcoal samples (n = 60) from 26 sites in the Escalante River watershed.

Lab Code [1]	Sample ID	^{14}C-age ± 1 sigma	Median Age [2] cal yr BP ± 1 sigma	Latitude (deg)	Longitude (deg)	Citation
AA-87507	ESC: E1	173 ± 35	180 + 105 - 75	37.739	-111.727	Hayden-Lesmeister and Rittenour, 2014
UCIAMS -113978	ESC: T13	175 ± 15	190 + 95 - 180	37.73	-111.7575	Rittenour - unpublished
A-3792	ESC: UV 1-1	190 ± 90	190 + 114 - 190	37.7625	-111.6889	Webb, 1985
A-3461	ESC: OC	230 ± 100	250 + 185 - 250	37.7227	-111.3005	Webb, 1985
TX-4425	ESC: HW-2	270 ± 90	320 + 150 - 315	37.6687	-111.2151	Patton and Boison 1986
TX-5104	ESC: AA 1	310 ± 70	380 + 80 - 80	37.778	-111.5751	Webb, 1985
TX-4424	ESC: HW-3	320 ± 70	380 + 75 - 80	37.6687	-111.2151	Patton and Boison 1986
UCIAMS -113975	ESC: T9	345 ± 15	380 + 80 - 60	37.73	-111.7575	Rittenour - unpublished
AA-87505	ESC: F1	357 ± 35	400 + 75 - 80	37.741	-111.725	Hayden-Lesmeister and Rittenour, 2014
UCIAMS -113979	ESC: T14	415 ± 15	500 + 10 - 10	37.73	-111.7575	Rittenour - unpublished
NR	ESC: WH 2-2	420 ± 90	450 + 85 - 125	37.7605	-111.6989	Webb and Hasbargen, 1998
NR	ESC: WH 2-3	470 ± 120	490 + 145 - 165	37.7605	-111.6989	Webb and Hasbargen, 1998
NR	ESC: WH 2-1	470 ± 60	510 + 40 - 167	37.7605	-111.6989	Webb and Hasbargen, 1998
NR	ESC: WH 1-1	500 ± 45	530 + 15 - 25	37.7365	-111.749	Webb and Hasbargen, 1998
NR	ESC: WH 2-4	530 ± 60	550 + 76 - 44	37.7605	-111.6989	Webb and Hasbargen, 1998
NR	ESC: WH 3-2	570 ± 120	580 + 85 - 70	37.7624	-111.6914	Webb and Hasbargen, 1998
NR	ESC: WH 1-2	580 ± 55	600 + 45 - 59	37.7365	-111.749	Webb and Hasbargen, 1998
NR	ESC: WH 2-5	620 ± 110	600 + 65 - 65	37.7605	-111.6989	Webb and Hasbargen, 1998
NR	ESC: WH 1-3	640 ± 60	610 + 55 - 50	37.7365	-111.749	Webb and Hasbargen, 1998
Beta-261342	ESC: B2	670 ± 40	630 + 40 - 70	37.736	-111.742	Hayden-Lesmeister and Rittenour, 2014
TX-5103	ESC: AA 2	830 ± 60	750 + 35 - 65	37.7805	-111.5369	Webb, 1985
A-4108	ESC: SA	930 ± 60	840 + 70 - 50	37.6676	-111.2143	Webb, 1985
AA-87515	ESC: A1	1215 ± 36	1140 + 80 - 65	37.679	-111.813	Hayden-Lesmeister and Rittenour, 2014
TX-4414	ESC: HW-4	1050 ± 150	980 + 195 - 180	37.65104	-111.25925	Patton and Boison 1986
TX-4120	ESC: CG	1070 ± 180	1000 + 180 - 205	37.41568	--111.0296	Boison and Patton, 1985
A-3791	ESC: UV 1-2	1090 ± 100	1020 + 155 - 95	37.7625	-111.6889	Webb, 1985
AA-87511	ESC: I2	1121 ± 36	1020 + 35 - 45	37.751	-111.704	Hayden-Lesmeister and Rittenour, 2014
UCIAMS -113977	ESC-T11	1140 ± 15	1020 + 40 - 25	37.73	-111.7575	Rittenour - unpublished
A-3464	ESC: AB	1170 ± 60	1100 + 80 - 95	37.7762	-111.4203	Webb, 1985
UCIAMS -113976	ESC: T10	1245 ± 25	1210 + 50 - 35	37.73	-111.7575	Rittenour - unpublished
TX-5105	ESC: AA 3	1400 ± 90	1320 + 85 - 130	37.7805	-111.5369	Webb, 1985
A-3468	ESC: Alcove 1	1480 ± 100	1390 + 125 - 95	37.778	-111.5751	Webb, 1985
AA-87504	ESC: D1	1494 ± 37	1380 + 30 - 40	37.738	-111.729	Hayden-Lesmeister and Rittenour, 2014
A-4057	ESC: AA 4	1500 ± 110	1410 + 110 - 105	37.7805	-111.5369	Webb, 1985
NR	ESC: WH 3-5	1590 ± 110	149 + 110 - 130	37.7624	-111.6914	Webb and Hasbargen, 1997
AA-993	ESC: UV 1-3	1640 ± 90	1540 + 145 - 130	37.7625	-111.6889	Webb, 1985
NR	ESC: WH 2-6	1750 ± 65	1670 + 60 - 100	37.7605	-111.6989	Webb and Hasbargen, 1997
TX-4103	ESC: HW-5	1910 ± 150	1850 + 180 - 225	37.65025	-111.27364	Patton and Boison 1986
AA-87508	ESC: D2	1940 ± 43	1890 + 40 - 65	37.738	-111.729	Hayden-Lesmeister and Rittenour, 2014
NR	ESC: WH 1-4	1945 ± 65	1890 + 90 - 70	37.7365	-111.749	Webb and Hasbargen, 1997
TX-4399	ESC: Dry Fork	1980 ± 80	1940 + 100 - 115	37.4397	-111.1276	Boison and Patton, 1985
AA-87506	ESC: D3	2022 ± 37	1970 + 60 - 70	37.738	-111.729	Hayden-Lesmeister and Rittenour, 2014
A-3794	ESC: Alcove 2	2080 ± 70	2060 + 85 -105	37.778	-111.5751	Webb, 1985
AA-87509	ESC: H3	2170 ± 38	2200 + 105 - 75	37.744	-111.707	Hayden-Lesmeister and Rittenour, 2014
NR	ESC: WH 1-5	2250 ± 50	2240 + 100 - 75	37.7365	-111.749	Webb and Hasbargen, 1997
TX-4411	ESC: HW-6	2570 ± 70	2630 + 130 - 130	37.669	-111.215	Patton and Boison 1986
NR	ESC: WH 1-6	2605 ± 80	2710 + 130 - 210	37.7365	-111.749	Webb and Hasbargen, 1997
AA-87514	ESC: A2	2880 ± 39	3010 + 60 - 55	37.679	-111.813	Hayden-Lesmeister and Rittenour, 2014
UCIAMS -113973	ECT-T4	3225 ± 15	3430 + 25 - 25	37.73	-111.7575	Rittenour - unpublished
TX-3938	ESC: HW-7	3280 ± 430	3540 + 540 - 580	37.6510	-111.2592	Patton and Boison 1986
AA-87503	ESC: C1	3440 ± 48	3700 + 120 - 65	37.738	-111.741	Hayden-Lesmeister and Rittenour, 2014
UCIAMS -113974	ESC-T6	3465 ± 15	3730 + 85 - 40	37.73	-111.7575	Rittenour - unpublished
Beta-281705	ESC: A3	3570 ± 40	3870 + 90 - 40	37.679	-111.813	Hayden-Lesmeister and Rittenour, 2014
AA-87512	ESC: B3	3627 ± 40	3940 + 45 - 65	37.736	-111.742	Hayden-Lesmeister and Rittenour, 2014
UCIAMS -113972	ESC-T1	3840 ± 15	4240 + 45 - 80	37.73	-111.7575	Rittenour - unpublished
AA-87502	ESC: C2	4053 ± 40	4530 + 245 - 95	37.738	-111.741	Hayden-Lesmeister and Rittenour, 2014
TX-4101	ESC: HW 8	8160 ± 380	9080 + 405 - 475	37.65025	-111.2736	Patton and Boison 1986

[1] UCIAMS is the lab ID for the University of California Irvine Accelerator Mass Spectrometry Lab, Beta is the lab ID for Beta Analytic, TX is Radiocarbon Laboratory, Balcones Research Center, University of Texas at Austin , AA and A refer to University of Arizona Radiocarbon lab, and NR stands for lab ID's that were not reported in the publication.

[2] The calibrated median age was calculated with CALIB 7.1 (Reimer et al., 2004) and the IntCal13 calibration curve (Reimer et al., 2013). Ages reported are in calibrated years before 1950 (cal yr BP).

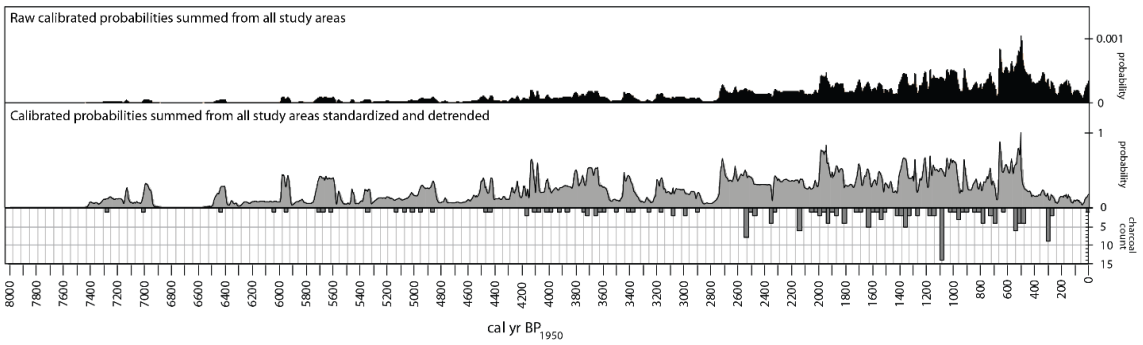

Figure 5-S1. Detrended, standardized, and calibrated radiocarbon age distributions.

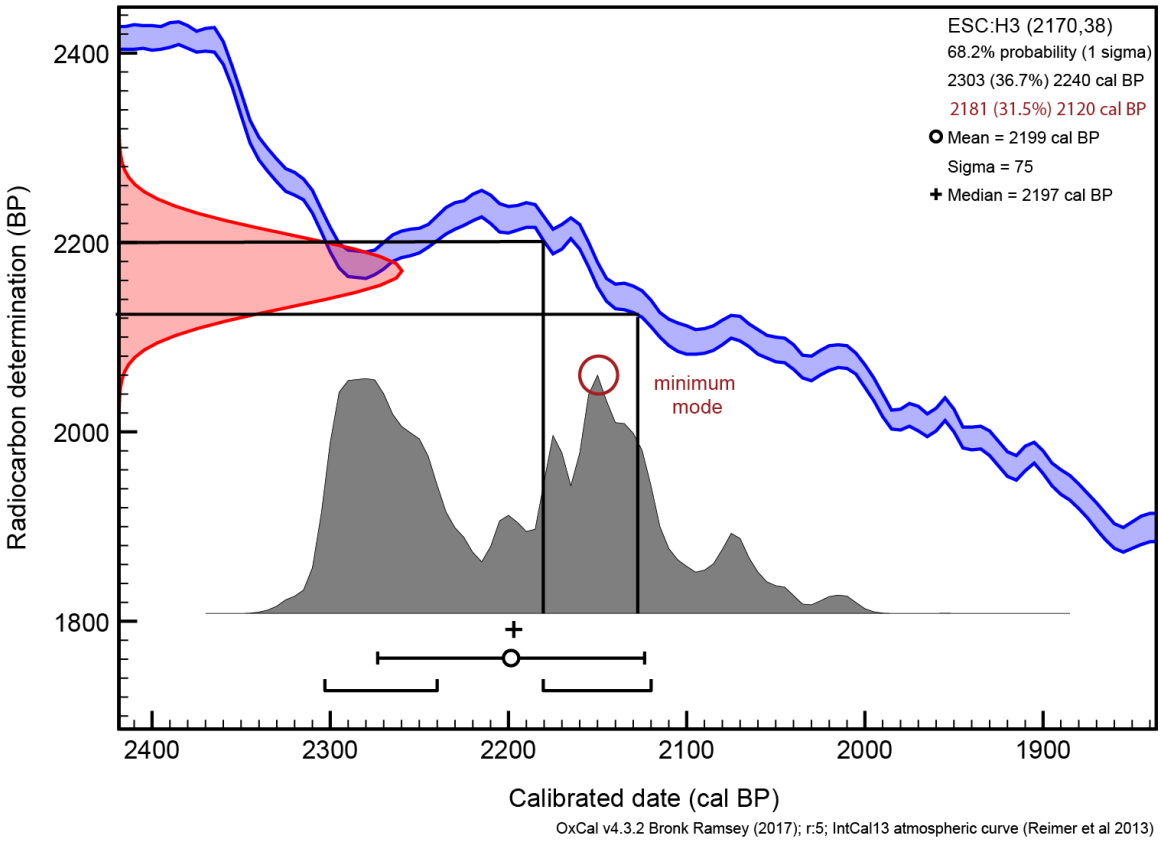

Figure 5-S2. Example of multi-modal calibrated age distribution.

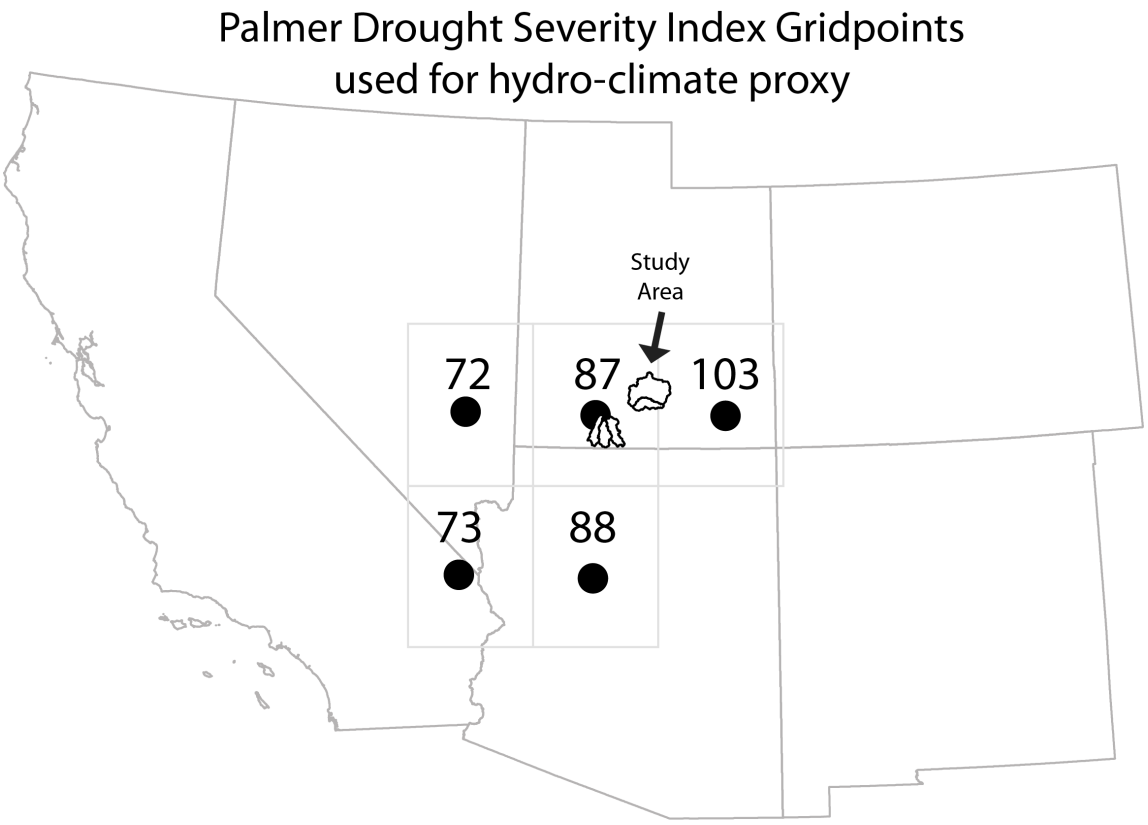

Figure 5- S3. Map with the locations of the 5 gridpoints averaged and used for a regional estimate of the Palmer Drought Severity Index (PDSI) over the last 2000 years (Cook, 2004).

Regional Fire Analysis

The following four figures show the original calibrated probability distributions for each sample used to calculate the combined modelled regional fire age distributions. Each regional fire number represents statistically similar distributions of discrete sampled charcoal ages. The modelled regional fire distribution for each cluster is in black. The original published ^{14}C-age and 1-sigma error is annotated under each sample identification. The median (black triangle), weighted mean (white circle), and local modes (black squares; minimum mode = red square) of the combined modelled distribution are identified. The 1-sigma confidence intervals of the combined modelled distribution is identified with brackets below each distribution.

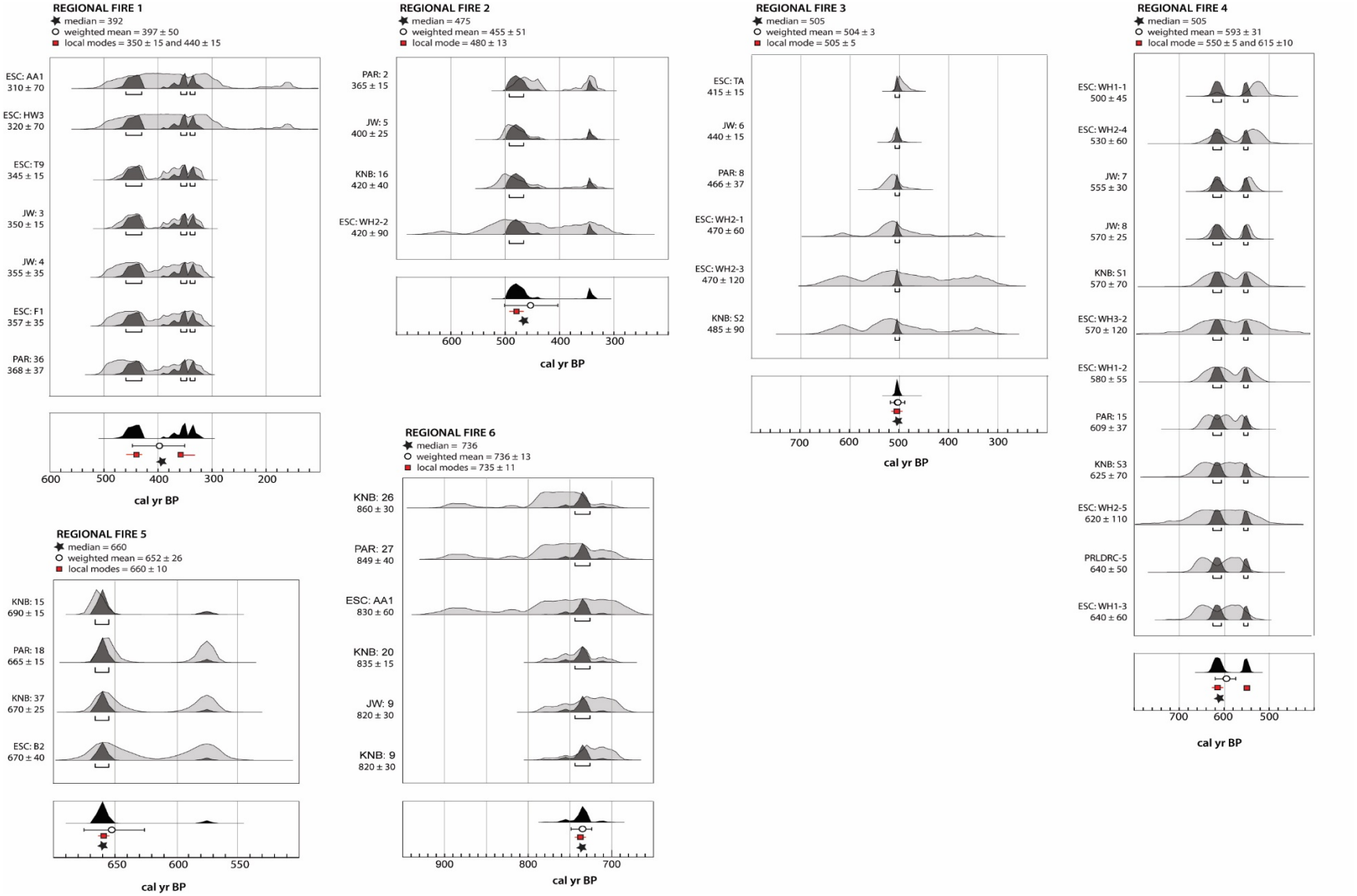

Figure 5-S4 - Regional fire distributions 1 through 6.

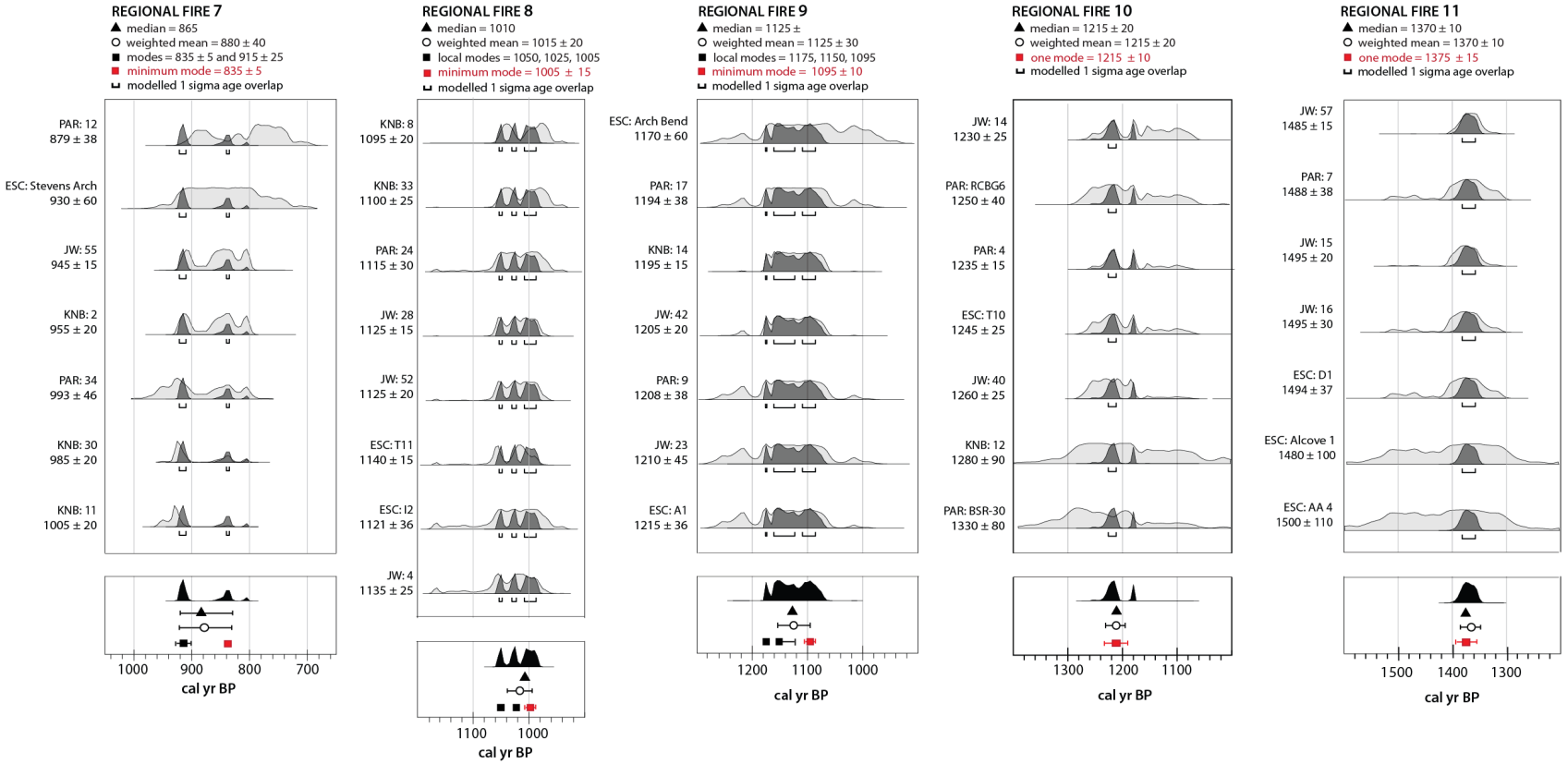

Figure 5-S5 - Regional fire distributions 7 through 11.

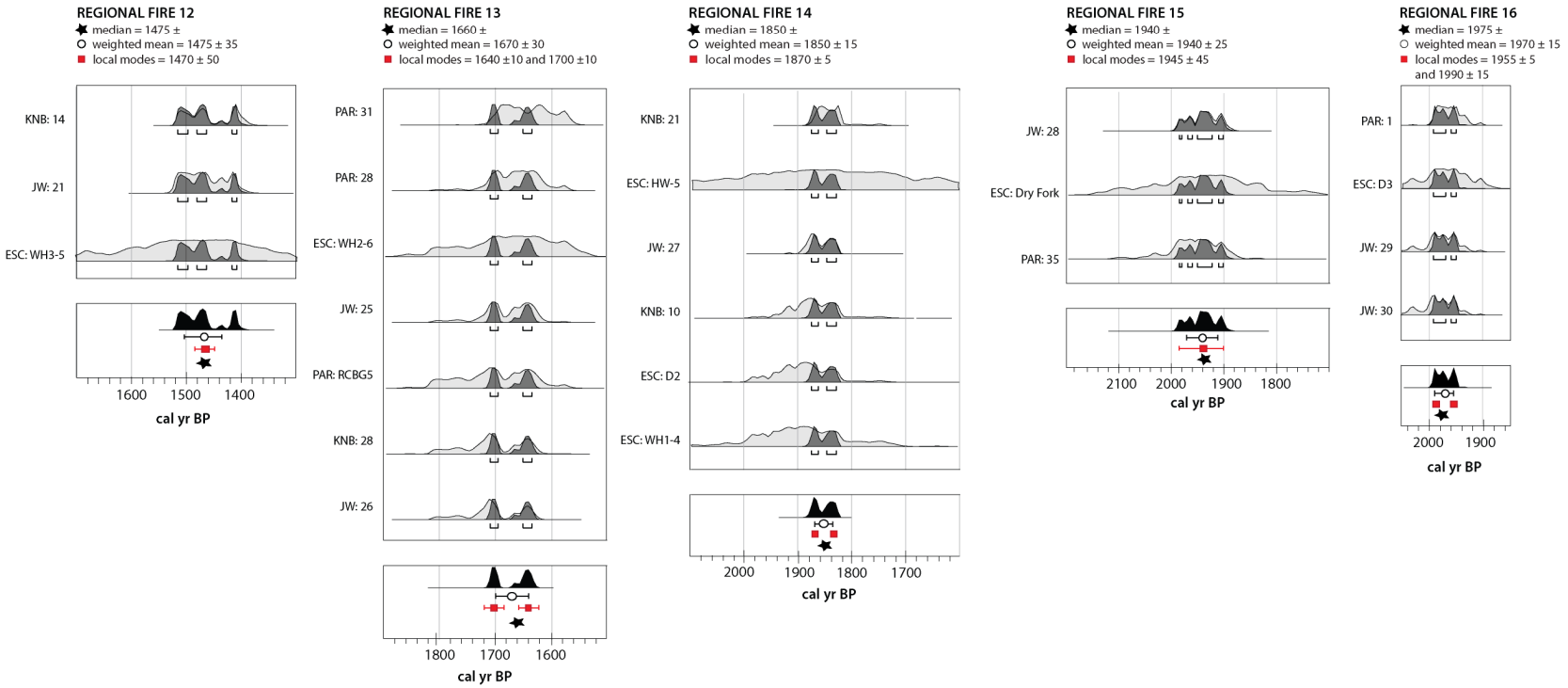

Figure 5-S6- Regional fire distributions 12 through 16.

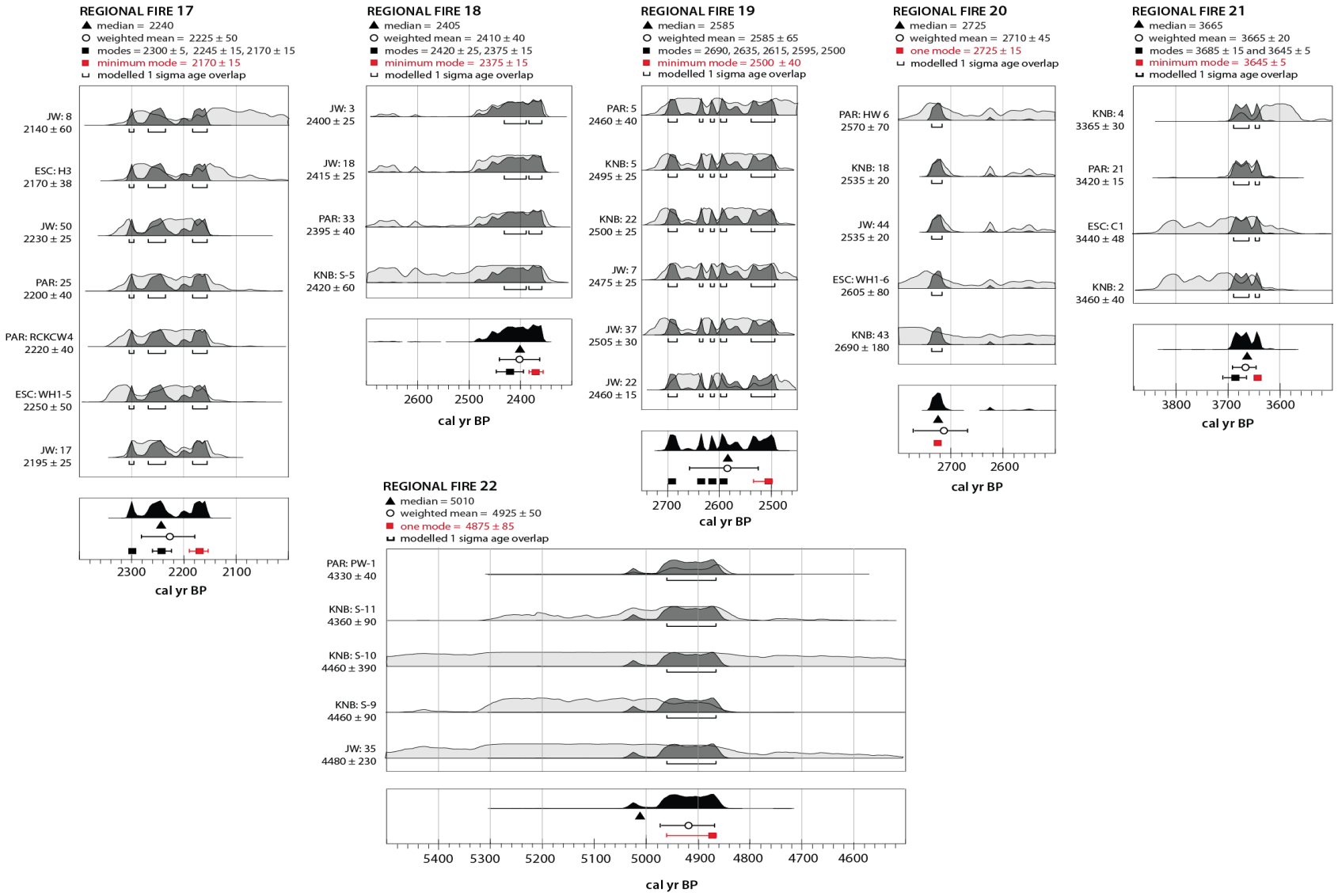

Figure 5-S7. Regional fire distributions 17 through 22.

SEA Methods

In order to compare the non-annual record of wildfire reconstructed in this study to climate reconstructions we truncated all hydroclimate records to the commonly used radiocarbon datum of 1950 CE and we smoothed the annual resolution data with a 30-year moving average and decreased the resolution (increased the time-interval) of the climate time-series to 30-year bins. Hydroclimate reconstructions included a Colorado River flow reconstruction from Lees Ferry (Meko et al., 2007), two independent precipitation reconstructions from the southern Colorado Plateau in northern New Mexico and El Malpais National Monument in Arizona (Grissino-Mayer, 1996; Salzer and Kipfmueller, 2005). The three calibrated age estimates (median, weighted mean, and minimum local mode) of regional fire events were compared to tree-ring-derived hydro-climate records. We also compared our charcoal record with the North American Drought Atlas. The Superposed Epoch Analysis (SEA) was completed in Matlab using script modified from Higuera and Dunnette (2014) and the preliminary results for the minimum mode for regional fire event ages are located in Figures 5-S9, 5-S11, and 5-S13). We tested for non-stationarity in the records by using three different methods to delineate time intervals: apriori climate intervals (i.e., MCA and LIA), 300-year and 200-year intervals. We also evaluate the entire time series for non-stationarity in a climate-fire signal.

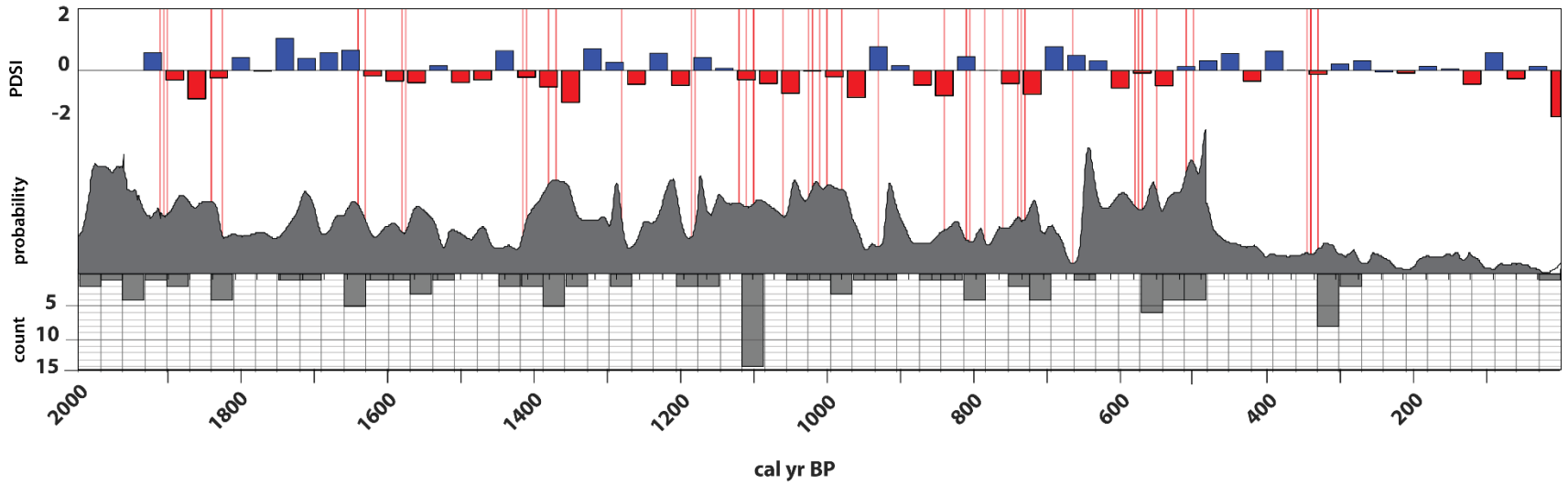

Figure 5-S8. Summary figure illustrating simplified data of PDSI and the minimum mode of fire events used for superposed epoch analysis. The PDSI record shows the residual time-series as a histogram. The residual time series is in 30-year bins and annotated to show red as drier and blue as wetter than average conditions. The black curve represents the detrended summed probability distributions for all charcoal samples between 2,000 and 0 cal yr BP. The inverted histogram (30-year bins) at the bottom is the number of samples creating the above distribution. Red bars identify the minimum mode for regional fires defined by statistically similar radiocarbon-dated fires from three or more watersheds.

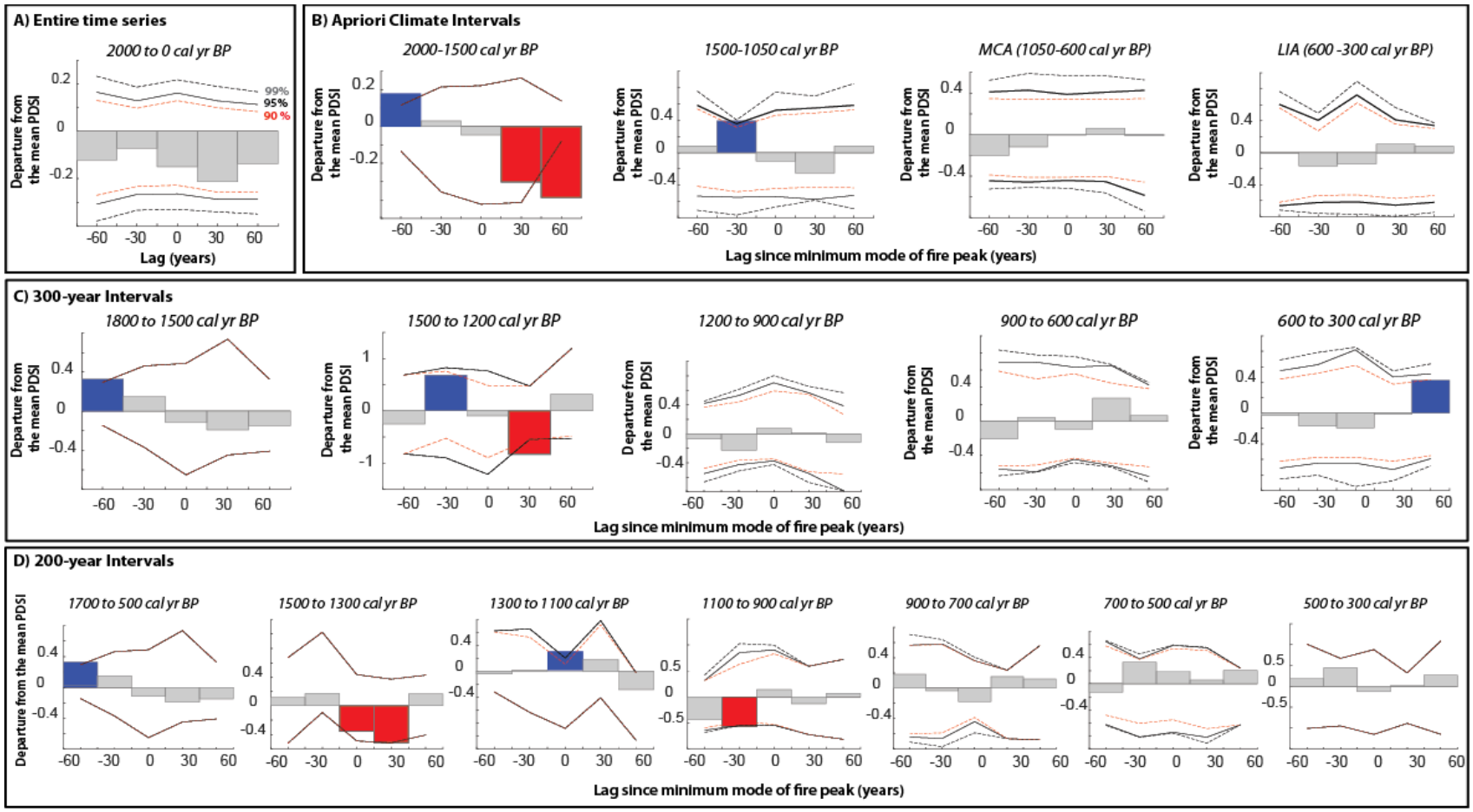

Figure 5-S9. Summary figure of superposed epoch analysis of the relationship between the PDSI and the minimum mode of fire activity for (A) the entire time series, 1188–0 cal yr BP, (B) Apriori climate intervals including the Medieval Climatic Anomaly (1050-600 cal yr BP) and the Little Ice Age (600 – 300 cal yr BP), (C) 300-year intervals, and (D) 200-year intervals. The x-axis indicates the years before (-) and after (+) a fire activity peak (year 0). Bar length (y-axis) indicates the mean departure of that year's PDSI from the mean PDSI for the entire sampling period. Lines represent the 90%, 95% and 99% confidence intervals, respectively.

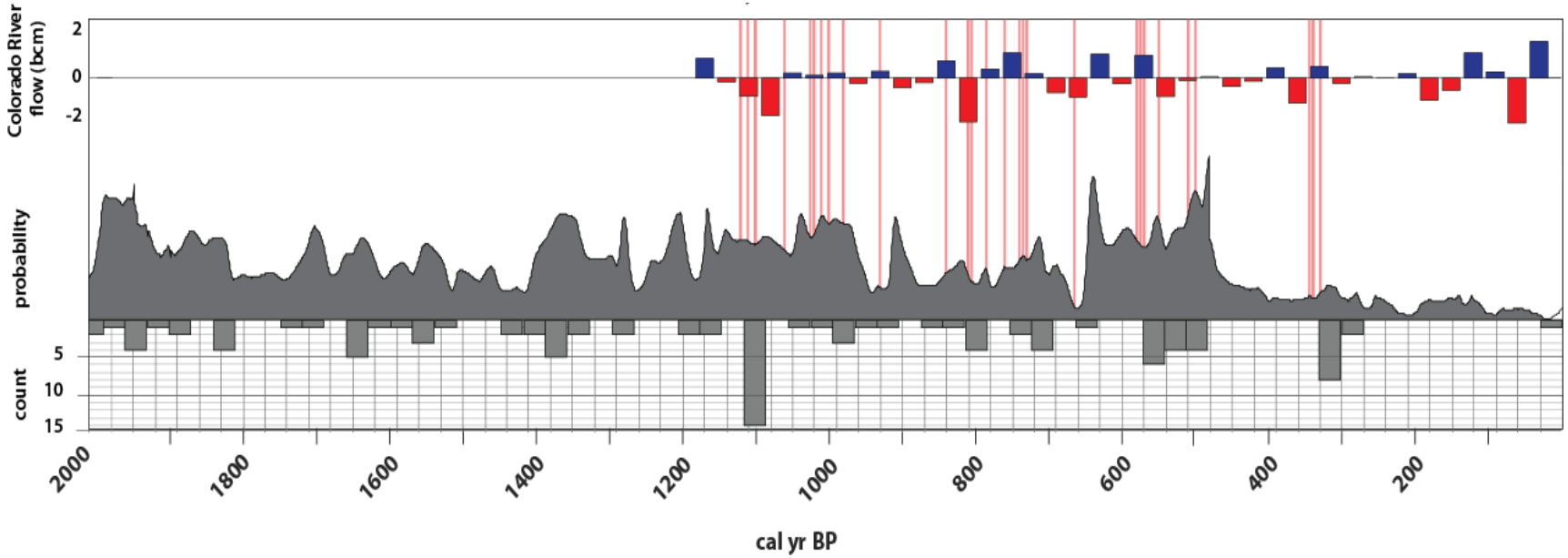

Figure 5-S10. Summary figure illustrating simplified data from the Colorado River reconstructed flow at Lees Ferry (Woodhouse et al., 2010) and the minimum mode of fire events used for superposed epoch analysis. The Colorado River record shows the residual time-series as a histogram. The residual time series is in 30-year bins and annotated to show red as drier and blue as wetter than average conditions. The black curve represents the detrended summed probability distributions for all charcoal samples between 2,000 and 0 cal yr BP. The inverted histogram (30-year bins) at the bottom is the number of samples creating the above distribution. Red bars identify the minimum mode for regional fires defined by statistically similar radiocarbon-dated fires from three or more watersheds.

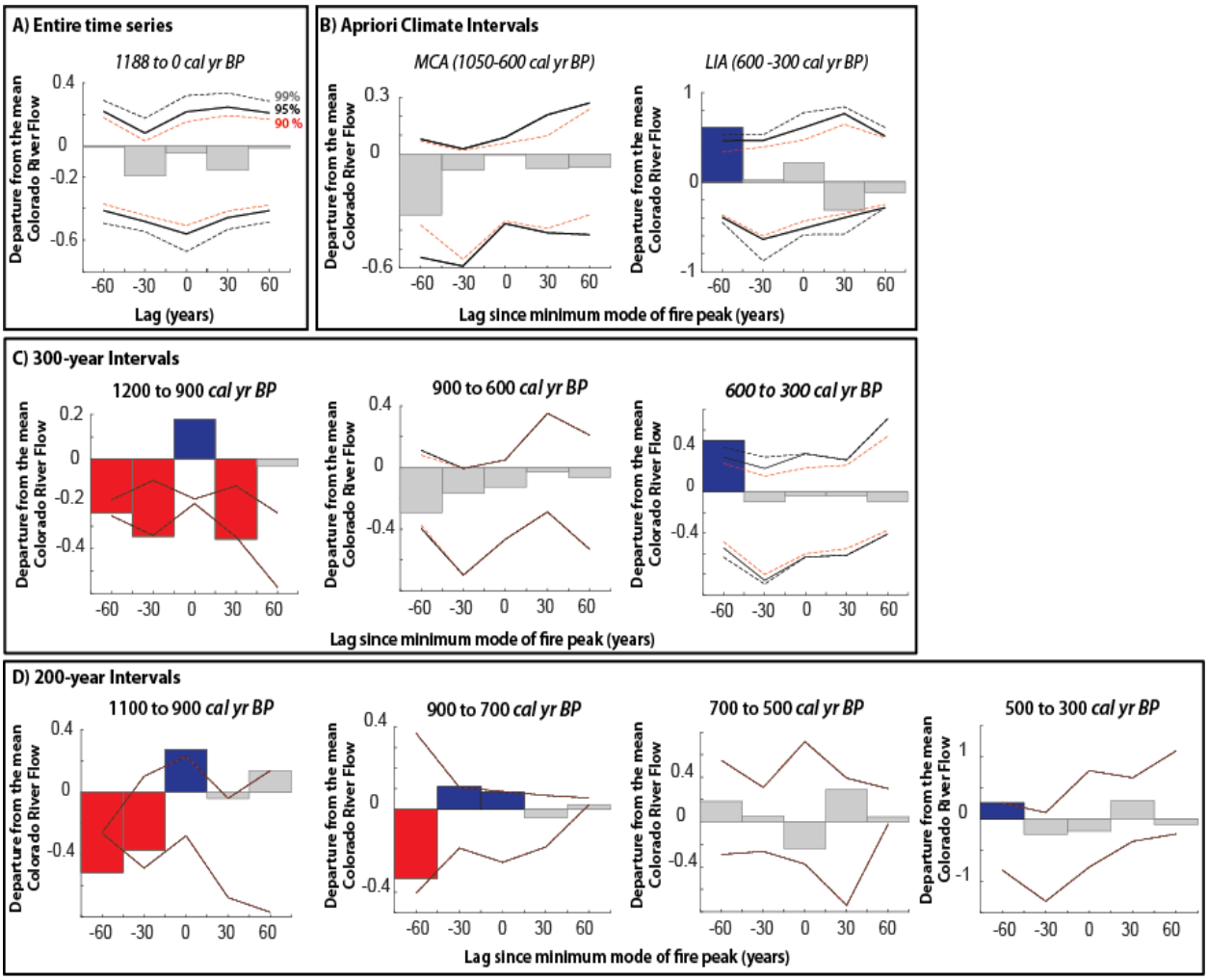

Figure 5-S11. Summary figure of superposed epoch analysis of the relationship between the Colorado River reconstructed flow at Lees Ferry (Woodhouse et al., 2010) and the minimum mode of fire activity for (A) the entire time series, 1188–0 cal yr BP, (B) Apriori climate intervals including the Medieval Climatic Anomaly (1050-600 cal yr BP) and the Little Ice Age (600 – 300 cal yr BP), (C) 300-year intervals, and (D) 200-year intervals. The x-axis indicates the years before (-) and after (+) a fire activity peak (year 0). Bar length (y-axis) indicates the mean departure of that year's flow from the mean flow for the entire sampling period. Lines represent the 90%, 95% and 99% confidence intervals, respectively.

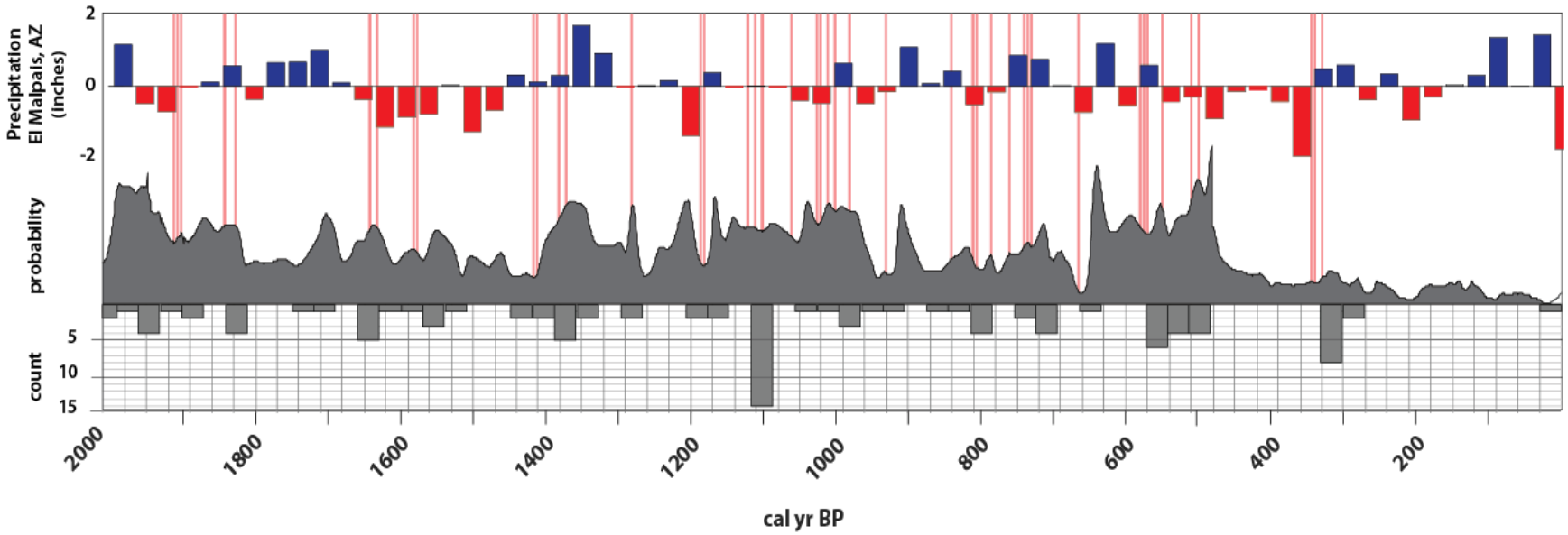

Figure 5-S12. Summary figure illustrating simplified data from the El Malpais Precipitation Record from New Mexico and the minimum mode of fire events used for superposed epoch analysis. The El Malpais record shows the residual time-series as a histogram. The residual time series is in 30-year bins and annotated to show red as drier and blue as wetter than average conditions. The black curve represents the detrended summed probability distributions for all charcoal samples between 2,000 and 0 cal yr BP. The inverted histogram (30-year bins) at the bottom is the number of samples creating the above distribution. Red bars identify the minimum mode for regional fires defined by statistically similar radiocarbon-dated fires from three or more watersheds.

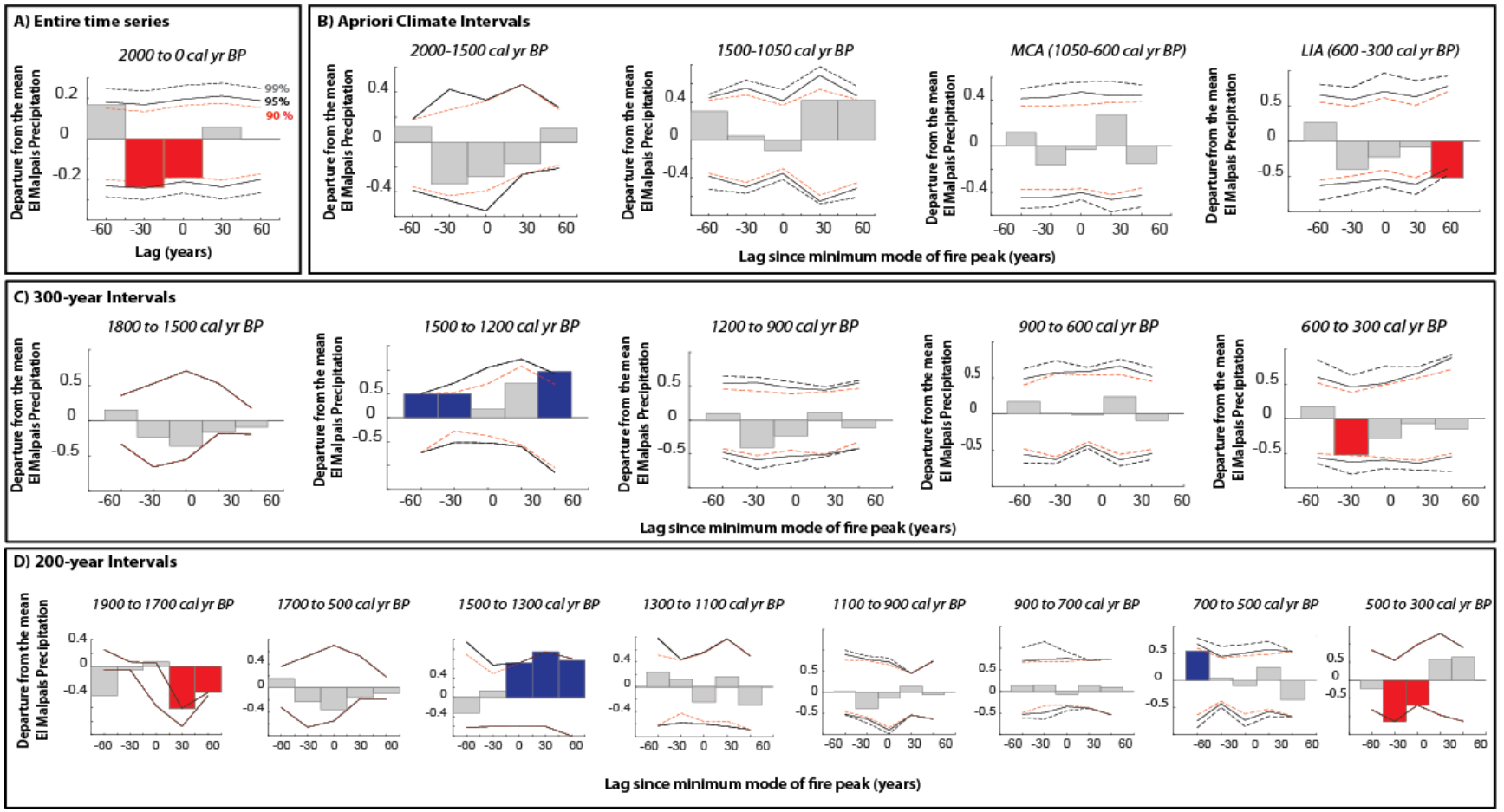

Figure 5-S13. Summary figure of superposed epoch analysis of the relationship between the El Malpais Precipitation Record from New Mexico and the minimum mode of fire activity for (A) the entire time series, 2000–0 cal yr BP, (B) Apriori climate intervals including the Medieval Climatic Anomaly (1050-600 cal yr BP) and the Little Ice Age (600 – 300 cal yr BP), (C) 300-year intervals, and (D) 200-year intervals. The x-axis indicates the years before (-) and after (+) a fire activity peak (year 0). Bar length (y-axis) indicates the mean departure of that year's precipitation from the mean precipitation for the entire sampling period. Lines represent the 90%, 95% and 99% confidence intervals, respectively.

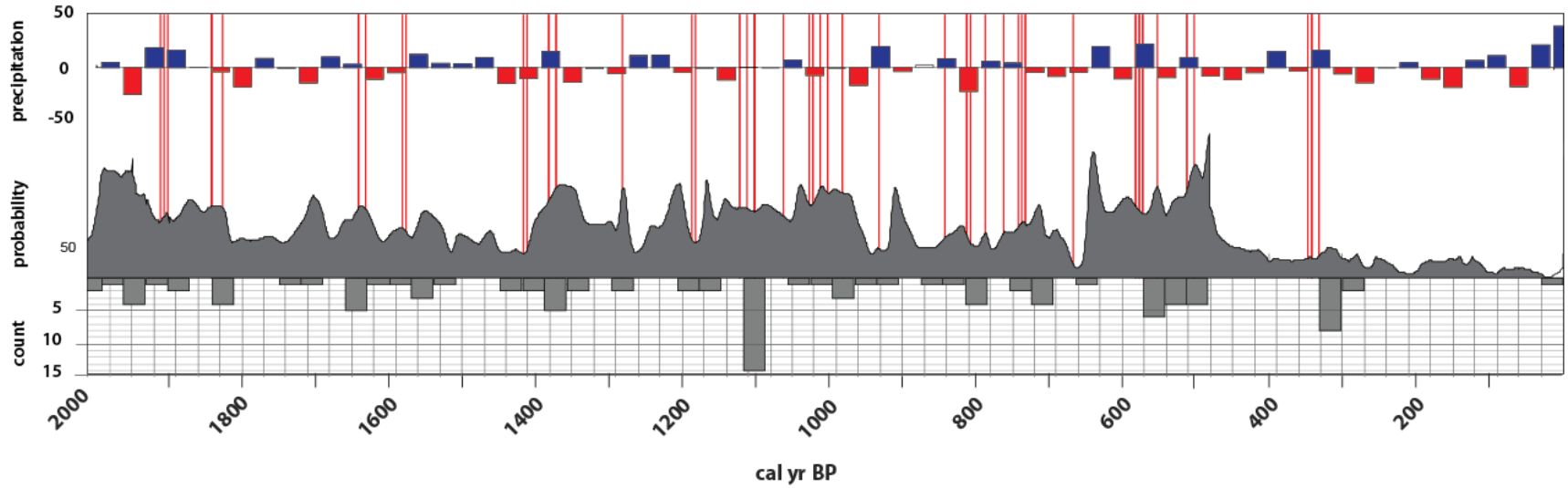

Figure 5-S14. Summary figure illustrating simplified data from the Tavaputs Precipitation Record from New Mexico and the minimum mode of fire events used for superposed epoch analysis. The Tavaputs record shows the residual time-series as a histogram. The residual time series is in 30-year bins and annotated to show red as drier and blue as wetter than average conditions. The black curve represents the detrended summed probability distributions for all charcoal samples between 2,000 and 0 cal yr BP. The inverted histogram (30-year bins) at the bottom is the number of samples creating the above distribution. Red bars identify the minimum mode for regional fires defined by statistically similar radiocarbon-dated fires from three or more watersheds.

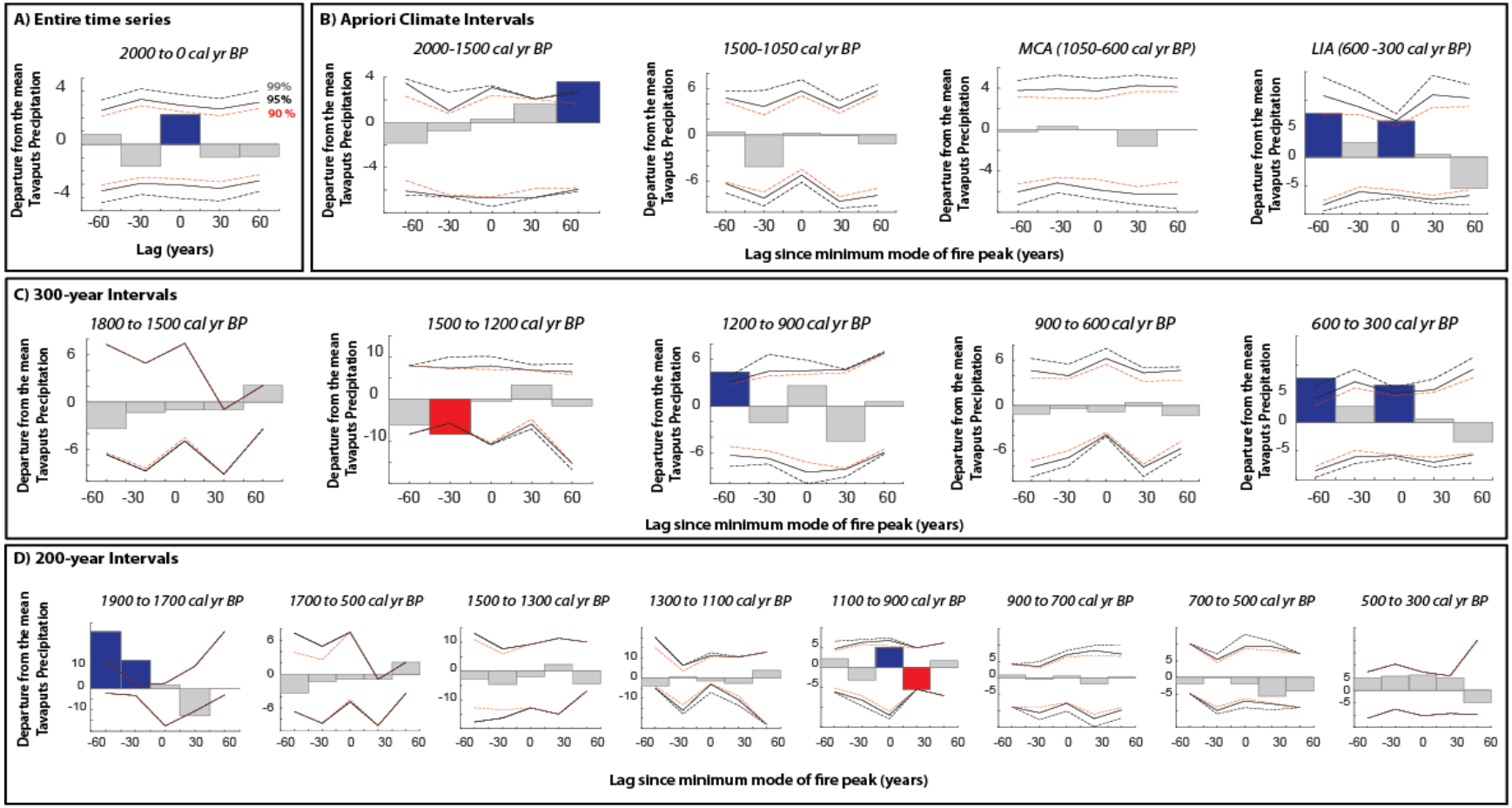

Figure 5-S15. Summary figure of superposed epoch analysis of the relationship between the Tavaputs Precipitation Record from New Mexico and the minimum mode of fire activity for (A) the entire time series, 2000–0 cal yr BP, (B) Apriori climate intervals including the Medieval Climatic Anomaly (1050-600 cal yr BP) and the Little Ice Age (600 – 300 cal yr BP), (C) 300-year intervals, and (D) 200-year intervals. The x-axis indicates the years before (-) and after (+) a fire activity peak (year 0). Bar length (y-axis) indicates the mean departure of that year's precipitation from the mean precipitation for the entire sampling period. Lines represent the 90%, 95% and 99% confidence intervals, respectively.

References Cited

Bechtold, W. A., and Patterson, P. L., 2005, The enhanced forest inventory and analysis program-national sampling design and estimation procedures.

Cook, E., 2004, North American Summer PDSI Reconstructions, NOAA/NGDC Paleoclimatology Program: Boulder CO, World Data Center for Paleoclimatology

Grissino-Mayer, H. D., 1996, A 2129-year reconstruction of precipitation for northwestern New Mexico, USA: Tree rings, environment, and humanity, p. 191-204.

Harvey, J., 2009, Reconciling Holocene alluvial records in Buckskin Wash, southern Utah [MS: University of Utah, 157 p.

Harvey, J. E., Pederson, J. L., and Rittenour, T. M., 2011, Exploring relations between arroyo cycles and canyon paleoflood records in Buckskin Wash, Utah: Reconciling scientific paradigms: Geological Society of America Bulletin, v. 123, no. 11-12, p. 2266-2276.

Hayden-Lesmeister, A., and Rittenour, T. R., 2014, Chronostratigraphy of Holocene valley-fill alluvium and arroyo cut-fill events in the upper Escalante River, southern Utah, in MacLean, J. S., Biek, R.F., and Huntoon, J.E., ed., Geology of Utah's Far South Volume 43, Utah Geological Association Publication, p. 57–76.

Hereford, R., 2002, Valley-fill alluviation during the Little Ice Age (ca. AD 1400-1880), Paria River basin and southern Colorado Plateau, United States: Geological Society of America Bulletin, v. 114, no. 12, p. 1550-1563.

Huff, W., and Rittenour, T., 2014, Holocene alluvial stratigraphy of Kitchen Corral Wash, southern Utah, in MacLean, J. S., Biek, R.F., and Huntoon, J.E., ed., Geology of Utah's Far South: Utah Geological Association Publication 43, p. 77–96.

Meko, D. M., Woodhouse, C. A., Baisan, C. A., Knight, T., Lukas, J. J., Hughes, M. K., and Salzer, M. W., 2007, Medieval drought in the upper Colorado River Basin: Geophysical Research Letters, v. 34, no. 10, p. L10705.

Nelson, M. S., and Rittenour, T., 2014, Middle to late Holocene chronostratigraphy of alluvial fill deposits along Kanab Creek in southern Utah: Geology of Utah's Far South: Utah Geological Association, Publication, v. 43, p. 97-116.

Reimer, P. J., Baillie, M. G. L., Bard, E., Bayliss, A., Beck, J. W., Bertrand, C. J. H., Blackwell, P. G., Buck, C. E., Burr, G. S., Cutler, K. B., Damon, P. E., Edwards, R. L., Fairbanks, R. G., Friedrich, M., Guilderson, T. P., Hogg, A. G., Hughen, K. A., Kromer, B., McCormac, G., Manning, S., Ramsey, C. B., Reimer, R. W.,

Remmele, S., Southon, J. R., Stuiver, M., Talamo, S., Taylor, F. W., van der Plicht, J., and Weyhenmeyer, C. E., 2004, IntCal04 terrestrial radiocarbon age calibration, 0-26 cal kyr BP: Radiocarbon, v. 46, no. 3, p. 1029-1058.

Reimer, P. J., Bard, E., Bayliss, A., Beck, J. W., Blackwell, P. G., Bronk Ramsey, C., Buck, C. E., Cheng, H., Edwards, R. L., and Friedrich, M., 2013, IntCal13 and Marine13 radiocarbon age calibration curves 0-50,000 years cal BP.

Salzer, M. W., and Kipfmueller, K. F., 2005, Reconstructed temperature and precipitation on a millennial timescale from tree-rings in the Southern Colorado Plateau, USA: Climatic Change, v. 70, no. 3, p. 465-487.

Smith, S., 1990, Large floods and rapid entrenchment Kanab Creek, southern Utah [MS Thesis]: University of Arizona, 82 p. p.

Townsend, K. F., 2015, A Chronostratigraphic Record of Arroyo Entrenchment and Aggradation in Kanab Creek, Southern Utah.

Townsend, K. F., Nelson, M. S., Rittenour, T. M., and Pederson, J. L., 2019, Anatomy and evolution of a dynamic arroyo system, Kanab Creek, southern Utah, USA: Geological Society of America Bulletin.

Webb, R. H., 1985, Late Holocene flooding on the Escalante River, south-central Utah [Ph.D. Dissertation: The University of Arizona., 204 p.

CHAPTER VI

SUMMARY AND CONCLUSIONS

> "In many places, canyons have cut the terrace platform deeply, and open in magnificent gateways upon the broad desert plain in front. We look into them from afar, wonderingly and questioningly, with a fancy pleased to follow their windings until their sudden turns carry them into distant, unseen depths."
>
> Clarence E. Dutton, Surveyor, Powell Expedition Tertiary

The Grand Staircase region of the Colorado Plateau is a colorful stair-stepped landscape sculpted by millions of years of erosion. Climate variability and sediment supply have influenced channel change, rates of landscape evolution, and the wildfire history of the region over late Pleistocene and Holocene timescales. Quaternary alluvial sedimentary records preserved in watersheds draining this region contain valuable information for understanding arroyo cut-fill dynamics, sediment supply variability, and wildfire activity in the region.

Stratigraphic records from the three adjacent drainages show these streams as primarily aggradational during the last 2500 years and near synchronous regional arroyo entrenchment support climate (allogenic) controlled channel change, while systematic changes in longitudinal profile concavity support autogenic controls on arroyo entrenchment. Thus, arroyo formation likely involves a combination of allogenic forcing and autogenic processes. High sediment supply produced by high erosion rates of retreating bedrock escarpments combined with limited transport capacity of ephemeral

and flashy watersheds seasonally influenced by atmospheric circulation associated with the North American Monsoon (NAM), characterized by a prominent increase in precipitation from July through September and the El Niño Southern Oscillation (ENSO) related to either El Nino conditions related to enhanced winter precipitation in the Southwest or La Niña conditions related to drier winter conditions (Cayan et al., 1999). The timing of regional alluvial entrenchment over the last 2200 corresponded to dry-to-wet hydro-climate variability. Geomorphic and stratigraphic observations indicating repeated aggradation to similar fill positions suggest a geometric threshold of stability. Unstable geometric threshold conditions associated with decreased concavity is likely, also, a requirement for entrenchment. Results and observations of this research suggest valley fills are reaching critical instability thresholds at similar times recording a quasi-synchronous geomorphic response.

In the stair-stepped landscape of the Grand Staircase, cosmogenic ^{10}Be erosion rates varied spatially by three orders of magnitude and hotspots of erosion were focused in the two upper escarpments, the White and Pink Cliffs. The escarpments produced high sediment yields by cliff retreat and caused valley-fill sediment storage on low-relief benches downstream. Paleo-cosmogenic ^{10}Be inventories from Holocene alluvium and Pleistocene terraces suggest climate change during the Holocene did not influence erosion rates. Holocene-aged sediment did not show a systematic trend in erosion rates related to the timing of aggradation and entrenchment, but did record a strong influence from local lithologic sediment sources. Paleo-erosion rates derived from Be-10 sampled from Pleistocene alluvial deposits in terraces and piedmonts were generally higher than modern and Holocene samples from similar alluvial reaches. Future research could

expand the Pleistocene erosion rate record to test the influence of glacial-interglacial climates. Alluvial samples from known glacial periods are missing in the current dataset. Furthermore, the sample population for each topographic position could be expanded to develop a more robust spatial dataset in the complex landscape.

The fire record in the region extends to 7500 cal yr BP and the frequency of regionally synchronous fires increased 2800 cal yr BP. Results support that climate-driven changes in vegetation productivity and the frequency and intensity of drought influences Holocene fire activity. Alluvial charcoal is a useful paleoecological proxy of fire activity that is comparable with long-term lake records and annually resolved tree-ring records and enables long-term changes in fire regimes to be interpreted across regional scales to place modern changes in fire activity in context. Over centennial to millennial timescales, regionally widespread fires appear to be controlled by hydroclimate-driven changes in the density and species distribution of fuel in semi-arid ecosystems. Over shorter timescales, regional fires are likely related to the timing of drought.

Future research related to fire regime should incorporate these longer-term fire records into shorter fire models used to predict wildfire hazards. It is important to encompasses the long-term natural range in variability of climate-fire relations to plan for future scenarios that we may not have observed in human history.

References Cited

Cayan, D. R., Redmond, K. T., and Riddle, L. G., 1999, ENSO and hydrologic extremes in the western United States: Journal of Climate, v. 12, no. 9, p. 2881-2893.